

# **“Structural Investigations of Capillary Suspensions using Rheology and Confocal Microscopy”**

zur Erlangung des akademischen Grades eines  
DOKTORS DER INGENIEURWISSENSCHAFTEN (Dr.-Ing.)

der Fakultät für Chemieingenieurwesen und Verfahrenstechnik des  
Karlsruher Instituts für Technologie (KIT)

genehmigte  
DISSERTATION

von  
Dipl.-Ing. Frank Bossler  
aus Biberach an der Riß

Referent: Prof. Dr. Erin Koos  
Korreferenten: Prof. Dr. Matthias Franzreb,  
Prof. Dr. Norbert Willenbacher

Tag der mündlichen Prüfung: 14.05.2018





# Acknowledgments

The research and final writing of this thesis took place from July 2013 until January 2018, supervised by Prof. Dr. Erin Koos, in the Applied Mechanics Group of Prof. Dr. Norbert Willenbacher at the Institute for Mechanical Process Engineering and Mechanics (MVM), Karlsruhe Institute of Technology. This also included a research stay of half a year in the Soft Matter, Rheology and Technology Group at the Department of Chemical Engineering, KU Leuven, Belgium. At this point, I want to thank everybody who contributed to the success of this thesis. Especially I want to offer a big thank-you to:

- Prof. Dr. Erin Koos for her excellent supervision of this thesis project, for offering me the possibility to investigate all of these interesting topics, for the advice and encouraging support over all the years – during her time in the work group in Karlsruhe as well as later during her time at KU Leuven in Belgium. Apart from the willingness of always listening to any arising research issues and good advices on how to solve these, I'm also grateful for making funding for my research available over many years, and last but not least also for the invaluable help in further improving my scientific writing abilities.
- Prof. Dr. Norbert Willenbacher for offering me the possibility to work in his group over so many years, for a lot of constructive discussions and advice on any scientific topics, for his support over all the time, for providing funding, and for being an additional reviewer of this thesis.
- Prof. Dr. Matthias Franzreb for his interest in my research and kindly taking charge as the second reviewer of my thesis.
- My students Katrin Dyhr, Robert Schmidt and Lydia Weyrauch. The experiments that they performed during their Bachelor's theses and/or as student assistant in lab have provided inestimably important contributions to the big picture of my research project. Many of these experiments found their way into two of my (our!) journal publications, and therefore in the end also contributed to the results summarized in this thesis.
- My colleagues Johannes Maurath for the very fruitful collaboration on elucidating the structure of aluminum-oxide-based capillary suspensions, Irene Natalia for working out the cumbersome details of chemical particle treatments together with me, and to Sebastian Bindgen for his help in computational evaluations of my confocal images.
- Dr. Günter Auernhammer (Max Planck Institute for Polymer Research, Mainz) for providing a lot of practical knowledge on confocal microscopy of suspensions and Dr. Jennifer Wenzl for providing many helpful details on how to fluorescently dye the Kromasil glass beads.

- The technical staff of the MVM group, especially Thomas Lebe for the SEM images, Astrid Huber, Regina Mall and Klaus Hirsch for particle characterizations and Karsten Sasso for his technical support.
- Dr. Bernhard Hochstein for his help concerning a lot of organizational questions over all the years, particularly for his input on how to officially buy a confocal microscope.
- All my colleagues, in Karlsruhe as well as in Leuven, for a fantastic time together, a lot of wonderful scientific and less scientific discussions, a lot of help and guidance, a great atmosphere while working in the offices, but on manifold occasions also out of office, for proofreading some of my written drafts, for your helping hands during several moves, for even letting me live in your apartments for some periods, and for countless other things not mentioned here. Indeed, nearly everybody of you should be named here in person as he would deserve this for a lot of different reasons!
- My good friends and even more my family, especially my parents, for the priceless support and the willingness to listen to any of my problems anytime – not only during this thesis, but also during the many years before. Without you and your support, doing my PhD studies never would have been possible that way.

# Abstract

A vast number of industrial consumer products are based on suspensions of particles in a bulk liquid, e.g. paints, inks, mortar, cosmetics, pharmaceuticals and fruit juices. The flow properties during production and of the end product are crucial for processability as well as customer acceptance. Capillary suspensions offer a relatively new option to tune the suspension flow properties. Since 2011, when benefits of the capillary suspensions concept were first demonstrated by Koos and Willenbacher, this class of materials has become a topic of increasing interest. Studies have concentrated on their structure and physical properties as well as their application in developing new products. Amongst these applications are the usage as precursors for ceramic or glass filters with high porosity and simultaneously small pore size, slurries for printable electronics with accurately molded edge shapes, the preparation of novel food products, 3D printing paste formulations, and many more.

Capillary suspensions are suspensions where a small amount of a secondary fluid, that is immiscible with the bulk phase, is added. Apart from an induced or increased yield stress, many other rheological properties, like low-shear viscosity or viscoelastic properties, are also modified. These changes arise due to the capillary forces induced by the added liquid leading to a percolating particle network by bridging the particles. The network formation appears when the secondary fluid wets the particles better than does the bulk fluid, which is termed the pendular state, but is also possible when the secondary fluid wets the particles worse, termed the capillary state. Both of these states have distinctly different microstructures. Details of the microstructure must be unraveled to gain knowledge of the origin of their rheological fingerprint, which is necessary for an adequate tailoring of product properties. Particularly, the structure is influenced by several physical key properties, such as particle size, volume fractions of particles and secondary fluid and the three-phase contact angle that captures the wetting behavior of both fluids on the particles. Additionally, the microstructure of capillary suspensions is also strongly influenced by their preparation process.

Heretofore, an observation of the microstructure of capillary suspensions was only possible when samples were first solidified, either by polymerization of the interparticulate secondary fluid bridges or by sintering of the particles. These approaches were limited to imaging fractured, two-dimensional surfaces of the solidified samples. Additionally, the solidification processes almost certainly changed the microstructure of the samples to an unknown extent. An acquisition of capillary suspension microstructures, in 3D, without the need for any sample alterations is, therefore, of utmost interest. One main motivation of this thesis is to accomplish this task using confocal microscopy, which is a powerful method for the visualization of three-dimensional sample structures in situ. In addition to establishing the necessary methods and sample systems to make confo-

cal microscopy of capillary suspensions feasible, the primary concern of the present thesis is to determine physical properties of capillary suspensions as well as illuminate the processing parameter variations. A broad variety of sample compositions is investigated, ranging from glass-bead-based model systems, designed for fundamental research, to application-relevant aluminum-oxide-based systems. The research focus of this thesis addresses the following issues:

- Determination of the influence of sample preparation procedure variations on the rheology and microstructure of several representative capillary suspension sample systems.
- Design and development of a suitable model capillary suspension system as well as of an image analysis method to enable in situ structural studies using 3D confocal microscopy.
- Elucidation of the influence of variations in the contact angle, particle porosity, secondary fluid volume fraction, particle size, and particle volume fraction on microstructural and rheological key parameters.
- Evaluation of the connection between microstructure and rheology.
- Use of the knowledge gained from the microstructural studies to generate a generalized yield stress master curve to facilitate directed product design.

Regarding the sample preparation procedures, an enhanced droplet breakup of the secondary fluid is found to lead to stronger particle networks with more homogeneous network structures. Using a dissolver stirrer in capillary state systems, this is achieved by increasing the energy input by either applying faster mixing speeds or longer mixing times using turbulent mixing. In the pendular state, increased mixing speed also leads to better droplet breakup using the same stirrer, but spherical agglomeration is found to be favored at longer times. This agglomeration decreases the yield stress and leads to severe sample inhomogeneities. The additional use of a ball mill after turbulent stirring is beneficial as it leads to a minimization of spherical agglomerates. Emulsification of the secondary fluid before particle addition can also cause stronger particle networks, if coalescence of the secondary fluid droplets before the particles are well-distributed is sufficiently slow. Using ultrasound for sample preparation enables superlative droplet breakup, leading to very small droplets of secondary fluid. On the other hand, sonication is limited to very small sample sizes due to the highly localized energy input of the ultrasonic horn. Additional experiments with a model system containing viscosity-matched fluids show that the capillary state competes with the formation of large Pickering emulsion droplets and is often more difficult to achieve than the pendular state.

For the confocal experiments, model capillary suspensions are prepared with matched refractive indices of particles and both liquids. The particles used – porous glass beads – can be chemically treated to cover a wide range of three-phase contact angles as well as differences in particle porosity. Confocal experiments using these model samples make it possible, for the first time, to image entire unmodified volumes of capillary suspensions and gain insight into the 3D network structure. Structural differences that occur with the variation in the contact angle are elucidated. For nonporous particles, the confocal images prove the existence of the capillary state for contact angles  $\theta$  slightly higher than  $90^\circ$ . Images of such structures clearly show a sample-spanning, clustered network, as was previously proposed only using simulations. The pendular state is imaged for samples with contact angles less than  $90^\circ$ . The images demonstrate a transition be-

tween systems consisting of only binary bridges to systems with bridges binding more than two particles, a state that is analogous to the funicular state in wet granular media. A contact-angle-dependent criterion to calculate the amount of secondary fluid needed for this transition is derived. Calculations of individual secondary fluid droplet sphericities additionally offer a possibility to quantify the structural differences observed in the confocal images.

For highly porous particles, the transition from pendular to capillary state changes from  $90^\circ$  to a much higher apparent contact angle near  $130^\circ$ . This shift is attributed to contact angle hysteresis, most likely caused by surface roughness. For samples with porous particles and contact angles below  $90^\circ$ , a strong network caused by the capillary force is not formed as the added secondary fluid is rapidly absorbed into the particle pores. At  $\theta = 115^\circ$ , confocal images show numerous pendular bridges in samples containing these porous particles and the elastic modulus is increased by three decades compared to the suspension without secondary fluid. Samples that are confocally identified as being in the capillary state ( $\theta > 130^\circ$ ) also show an increase in shear modulus when compared to the pure suspensions, but have a modulus one decade lower than the maximal pendular state samples.

In another set of experiments, the amount of secondary fluid is varied for sample systems containing porous particles with contact angles of either  $87^\circ$  or  $115^\circ$ . The rheology of these systems is governed by the effective – rather than the set – volume fractions of secondary fluid and solid particles, where the effective volume fractions incorporate the imbibition of some secondary and bulk fluid into the particle pores. The effective volume fractions are directly calculated from 3D confocal images. Representative stress values, i.e. the elastic modulus plateau value and apparent yield stress, show a dependence on the effective secondary fluid volume fraction that is known to be characteristic for capillary suspensions. With addition of secondary fluid, the stress first increases due to the formation of bridges in the pendular state that transmit forces, then goes through a maximum denoting funicular state structures, and finally decreases again when the amount of secondary fluid is large enough that the samples agglomerate even under optimized sample preparation conditions. Confocal images are used to directly visualize each of these structures. Overall, the  $115^\circ$  samples show lower stress values than for  $87^\circ$ , which is related to the difference in energy needed to detach particles from the fluid-fluid interface.

Using a primarily self-programmed algorithm to analyze the 3D confocal images, the particle positions are detected at varying effective amounts of secondary fluid for the two apparent contact angles of  $87^\circ$  and  $115^\circ$ . With the ascertained particle positions and sizes, different structural parameters, namely pair correlation functions, coordination numbers and apparent fractal dimensions, are calculated. The pair correlation functions show a well defined first peak at particle surface contact distance. For capillary suspensions, the height of this peak increases with the amount of secondary fluid for both contact angles. This is related to the increased attraction between particles, which is also reflected in the rheological data. The same correlation is found for the coordination numbers. The mean coordination number of capillary suspensions also is found to increase with the amount of added secondary fluid. Differences in the slopes of the coordination number rise with increasing secondary fluid volume between samples with  $87^\circ$  and  $115^\circ$  are found and these differences closely resemble similar variations in the rheological data. The determination of fractal dimensions as a function of the secondary fluid volume fraction

provides unsatisfactory results. While the fractal dimension can be calculated, the data is accompanied by very large error bars that impede the deduction of any significant trends. However, an increase in the fractal dimension with increasing solid volume fraction is found.

Due to the difficulties in determining meaningful values for the fractal dimension solely from confocal imaging, two additional approaches are performed. Both of these rely on rheological scaling laws that are based on different structural and aggregation models. These rheological studies are performed with  $\text{CaCO}_3$ - and  $\text{Al}_2\text{O}_3$ -based capillary suspensions as the small sample volumes available for the glass-bead-based confocal microscopy model system are insufficient. Fractal dimensions in the range from 1.86 to 2.05 are determined from a yield stress scaling model, while distinctly higher values in the range from 2.57 to 2.74 are obtained for the same capillary suspensions from a scaling model applied to critical strain amplitudes and elastic moduli obtained from oscillatory measurements. This marked difference is explained by an inhomogeneous microstructure where relatively dense agglomerates are linked together to form a relatively sparse backbone transmitting the forces. This hypothesis is confirmed by 3D confocal images. Taking into account the origin of the two applied rheological scaling models, the fractal dimensions calculated are then expected to be a measure for the backbone and internal aggregate structure, respectively. Fractal dimensions directly determined from confocal image analysis can only provide an apparent fractal dimension containing mixed contributions of backbone and aggregates. Accordingly, the confocally determined fractal dimensions lie between the results obtained from the different rheological approaches. This mixed contribution with two length scales also explains the large error bars found using the optical measurements of the fractal dimension. Regardless of the method used, the fractal dimension of capillary suspensions increases with increasing particle size. This trend is confirmed by all of the sample systems at the various length scales provided by each method. Therefore, capillary suspensions with larger particles exhibit more compact particle arrangements. This can be explained by the weakening of the capillary force in comparison to both the inertial and hydrodynamic forces with increasing particle size.

Finally, a master curve for the yield stress as function of the secondary fluid content is constructed. This master curve is a very helpful tool to predict the sample yield stress for any given combination of secondary fluid volume, particle size and solid volume fraction for a given composition, as is demonstrated for the  $\text{Al}_2\text{O}_3$ -based system. The master curve is further generalized, including the interfacial tension as well as the contact angle and the obtained transition criterion from pendular to funicular-like microstructures. The generalized master curve then enables the yield stress of samples with different composition to also be predicted, as was shown by including systems based on  $\text{CaCO}_3$  and on the glass beads of the confocal model system. This generalized master curve is a clear representation of how the knowledge gained from the microstructure imparts a deeper understanding of the rheology and, thereby, aids in the future design of capillary suspensions. This research, thus, highlights the importance and usefulness obtained by understanding the influence of basic physical properties on possible applications for such samples. Hopefully, this will encourage continuing, fruitful research on capillary suspension microstructures.

# Kurzfassung

Eine sehr große Anzahl von Verbrauchsgütern basiert auf Suspensionen von Feststoffpartikeln in einer Flüssigkeit, z.B. Farben, Tinten, Mörtel, Kosmetika, Pharmazeutika oder Fruchtsäfte. Die Fließeigenschaften, sowohl während der Herstellung, als auch des Endprodukts, sind entscheidend für die Prozessierbarkeit und die Kundenakzeptanz. Hierbei stellen Kapillarsuspensionen eine innovative Möglichkeit dar, um die Fließeigenschaften einer Suspension gezielt einzustellen. Das Interesse an der Materialklasse der Kapillarsuspensionen ist stark gestiegen, seit *Koos* und *Willenbacher* im Jahr 2011 Vorteile ihrer Nutzung aufgezeigt haben. Untersuchungen von Kapillarsuspensionen konzentrieren sich seither sowohl auf die Erforschung ihrer Struktur und physikalischen Eigenschaften, als auch auf ihre Anwendbarkeit auf die Entwicklung neuer Produkte. Mögliche Anwendungen umfassen die Nutzung als Precursor bei der Herstellung keramischer Filter mit hoher Porosität bei gleichzeitig kleiner Porengröße, Suspensionen zur Herstellung druckbarer Elektronik mit präzise geformter Kantenkontur des Drucks, neuartig formulierter Lebensmittel, Pasten für den 3D-Druck, und viele weitere.

Kapillarsuspensionen sind Suspensionen, denen eine kleine Menge einer zweiten Flüssigkeit zugegeben wird, welche mit der Hauptflüssigkeit nicht mischbar ist. Neben dem Auftreten einer stark ausgeprägten Fließgrenze unterscheiden sie sich in vielen weiteren rheologischen Eigenschaften von reinen Suspensionen, z.B. in der Viskosität bei niedrigen Scherraten oder in den viskoelastischen Eigenschaften. Diese Änderungen beruhen auf Kapillarkräften, die durch die zugegebene Zweitflüssigkeit hervorgerufen werden. Die zugegebene Zweitphase bildet Flüssigkeitsbrücken zwischen den Partikeln wodurch ein perkolierendes Partikelnetzwerk entsteht. Die Netzbildung tritt sowohl im sogenannten *pendular state* auf, wenn die Zweitphase die Partikel besser benetzt als die Hauptphase, aber ist ebenso im *capillary state* möglich, wenn die Zweitphase schlechter benetzt. *Pendular* und *capillary state* weisen hierbei zwei grundverschiedene Mikrostrukturen auf. Ein detailliertes Verständnis der Mikrostruktur ist notwendig, um die rheologischen Charakteristika von Kapillarsuspensionen zu verstehen. Letzteres ist zur gezielten Einstellung von Produkteigenschaften unerlässlich. Die Struktur wird insbesondere von einigen entscheidenden physikalischen Stoffparametern beeinflusst. Dazu gehören die Partikelgröße, der Feststoff- und Zweitphasenanteil, sowie der Dreiphasen-Kontaktwinkel, welcher die Benetzungseigenschaften beider Flüssigkeiten auf den Partikeln erfasst. Darüber hinaus wird die Mikrostruktur durch den Herstellungsprozess der Kapillarsuspension beeinflusst.

Bisher konnte die Mikrostruktur von Kapillarsuspensionen nur nach Verfestigung der Proben durch Polymerisation der Flüssigkeitsbrücken oder durch Sintern der gesamten Probe beobachtet und charakterisiert werden. Diese Experimente waren auf die optische Abbildung zweidimensionaler Oberflächen der verfestigten Proben beschränkt. Darüber-

hinaus ist davon auszugehen, dass der Verfestigungsprozess die Mikrostruktur der Proben in unbekanntem Ausmaß verändert. Eine optische Erfassung der Mikrostruktur von Kapillarsuspensionen in 3D und ohne die Notwendigkeit jedweder Probenverfestigung oder sonstiger Veränderung ist daher von großem Interesse. Eine zentrale Motivation dieser Dissertationsschrift ist es, diese Problemstellung mittels konfokaler Mikroskopie anzugehen. Konfokale Mikroskopie ermöglicht die in-situ-Visualisierung dreidimensionaler Strukturen. Zum einen befasst sich diese Dissertation mit der Entwicklung der notwendigen Methoden und Stoffsysteme zur Ermöglichung konfokaler Mikroskopie an Kapillarsuspensionen. Zum anderen wird der Einfluss der Variation sowohl diverser physikalischer Eigenschaften, als auch von Prozessierungsparametern ermittelt. Es wird eine große Bandbreite verschiedener Probenzusammensetzungen untersucht. Diese reicht von Proben basierend auf sphärischen Glaspartikeln, welche speziell auf Anforderungen der Grundlagenforschung ausgerichtet sind, bis zu anwendungsrelevanten Proben, welche auf Aluminiumoxid-Partikeln basieren. Der Fokus der Forschung liegt dabei auf folgenden Punkten:

- Ermittlung des Einflusses von Variationen im Probenherstellungsprozess auf die Rheologie und die Mikrostruktur anhand verschiedener repräsentativer Kapillarsuspensionsproben.
- Auswahl und Entwicklung einer geeigneten Modell-Kapillarsuspension sowie von Bildauswertungsmethoden, um Strukturuntersuchungen mittels konfokaler Mikroskopie in situ und in 3D zu ermöglichen.
- Aufklärung des Einflusses von Variationen des Kontaktwinkels, der Partikelporosität, der Partikelgröße, der Konzentration der Zweitphase und der Konzentration der Partikel auf mikrostrukturelle und rheologische Kenngrößen.
- Evaluierung des Zusammenhangs zwischen Mikrostruktur und Rheologie.
- Nutzung des gewonnenen Wissens zur Erstellung einer Masterkurve für die Fließgrenze, welche die zielgerichtete Produktentwicklung unterstützen kann.

In Hinsicht auf die Probenherstellungsprozesse zeigt sich, dass eine Verbesserung des Tropfenaufbruchs der Zweitphase zur Ausbildung stärkerer Partikelnetzwerke mit homogenerer Netzwerkstruktur führt. Bei der Nutzung eines Dissolver-Rührers für Systeme im *capillary state* lässt sich dies unter turbulenten Rührbedingungen durch einen erhöhten Energieeintrag erreichen, was entweder durch eine höhere Rührerdrehzahl oder eine längere Rührzeit realisiert werden kann. Im *pendular state* führen – bei Nutzung des selben Rührwerkzeugs – erhöhte Drehzahlen ebenfalls zu einem verbesserten Tropfenaufbruch der Zweitphase, wohingegen längere Rührzeiten bevorzugt sphärische Agglomeration der Proben hervorrufen. Eine derartige Agglomeration senkt die Fließgrenze und ruft starke Probeninhomogenitäten hervor. Die zusätzliche Verwendung einer Kugelmühle nach vorhergehendem turbulentem Rühren minimiert die Größe der sphärischen Agglomerate. Ein Emulgieren der Zweitphase in der Hauptflüssigkeit bevor die Partikel zugegeben werden, kann ebenfalls zur Ausbildung stärkerer Partikelnetzwerke führen, falls die Koaleszenz der Zweitphasentropfen hinreichend verlangsamt werden kann. Die Nutzung von Ultraschall zur Probenvorbereitung führt zu einem noch besseren Tropfenaufbruch und ermöglicht so die Herstellung sehr kleiner Zweitphasentropfen. Allerdings ist diese Methode auf sehr kleine Probengrößen limitiert, da der Energieeintrag der Ultraschall-Sonotrode stark lokal beschränkt ist. Zusätzliche Experimente mit einem Modellsystem,



bei dem die Viskosität von Haupt- und Zweitflüssigkeit identisch sind, zeigen, dass die Ausbildung des *capillary state* mit der Entstehung von *Pickering*-Emulsionen konkurriert.

Für die konfokalmikroskopischen Experimente werden Modell-Kapillarsuspensionen hergestellt, bei denen die Brechungsindizes der Partikel und beider Flüssigkeiten identisch sind. Die hierfür genutzten Partikel – poröse sphärische Glaspartikel – können chemisch modifiziert werden, was umfassende Variationen des Kontaktwinkels und der Partikelporosität ermöglicht. Konfokalmikroskopische Experimente mit derartigen Modell-Kapillarsuspensionen ermöglichen es zum ersten Mal vollständige unmodifizierte Volumina von Kapillarsuspensionen in situ abzubilden und aus diesen Bildern Einblicke in die 3D-Netzwerkstruktur zu gewinnen. Strukturunterschiede, die sich unter Variation des Kontaktwinkels ergeben, werden hierbei aufgeklärt. Für unporöse Partikel weisen die konfokalmikroskopischen Bilder die Existenz des *capillary state* bei Kontaktwinkeln knapp über  $90^\circ$  nach. Die Bilder der entsprechenden Strukturen zeigen ein perkolierendes, auf Mikro-Clustern beruhendes Netzwerk, welches zuvor lediglich auf Basis von Simulationen postuliert worden war. Die Struktur des *pendular state* wird für Proben mit Kontaktwinkeln kleiner als  $90^\circ$  bildlich erfasst. Diese Bilder zeigen einen Übergang zwischen Netzwerkstrukturen, die nur binäre Brücken zwischen zwei Partikeln aufweisen, zu Systemen, bei denen die Brücken mehr als zwei Partikel verbinden. Letztere Konfiguration ist analog zum *funicular state*, d.h. einer Mikrostruktur welche klassischerweise bei feuchten Schüttgütern auftritt. Ein kontaktwinkelabhängiges Kriterium zur Berechnung der Menge an Zweitflüssigkeit, die für den Übergang zwischen *pendular* und *funicular state* notwendig ist, wird abgeleitet. Darüber hinaus wird die Sphärizität individueller Zweitphasentropfen in der Probe berechnet, was eine zusätzliche Quantifizierung der strukturellen Unterschiede ermöglicht, welche in den konfokalmikroskopischen Bildern qualitativ sichtbar sind.

Werden poröse Partikel genutzt, verschiebt sich der Übergang zwischen *pendular* und *capillary state* von  $90^\circ$  zu einem scheinbaren höheren Kontaktwinkel von circa  $130^\circ$ . Diese Verschiebung wird auf eine Kontaktwinkelhysterese zurückgeführt, welche höchstwahrscheinlich durch Oberflächenrauigkeiten der Partikel hervorgerufen wird. In Proben mit porösen Partikeln und einem Kontaktwinkel kleiner als  $90^\circ$  bildet sich kein stabiles auf Kapillarkräften beruhendes Netzwerk aus, da die hinzugefügte Zweitphase unmittelbar in die Partikelporen absorbiert wird. Bei einem Kontaktwinkel von  $115^\circ$  zeigen konfokalmikroskopische Bilder einer Probe, die poröse Partikel enthält, hingegen eine Vielzahl an binären Kapillarbrücken auf. Der Speichermodul dieser Probe ist gegenüber einer entsprechenden Suspension ohne Zweitphase um drei Dekaden erhöht. Proben, die konfokalmikroskopisch als *capillary state* klassifiziert werden können (Kontaktwinkel über  $130^\circ$ ), zeigen ebenfalls einen deutlich erhöhten Speichermodul gegenüber einer reinen Suspension. Der Speichermodul liegt hier allerdings um ca. eine Dekade niedriger als der Maximalwert des *pendular state*.

In einer weiteren Versuchsreihe wird die Menge an zugegebener Zweitphase für Systeme mit porösen Partikeln bei zwei verschiedenen Kontaktwinkeln ( $87^\circ$  oder  $115^\circ$ ) variiert. Die Rheologie dieser Systeme wird durch effektive Anteile an Zweitphase und Partikeln bestimmt, nicht durch die real bei der Probenherstellung eingewogenen Anteile. Die effektiven Anteile berücksichtigen hierbei die anteilige Absorption von Haupt- und Zweitphase in die Partikelporen. Die effektiven Anteile werden aus dreidimensionalen konfokalmikroskopischen Bildern berechnet. Repräsentative Spannungen, nament-

lich der Plateauwert des Speichermoduls sowie die scheinbare Fließgrenze, zeigen eine Abhängigkeit vom effektiven Zweitphasenanteil, die für Kapillarsuspensionen bereits als charakteristisch bekannt ist. Mit der Zugabe von Zweitflüssigkeit steigt die jeweilige Spannung zunächst aufgrund der Ausbildung von Kapillarbrücken im *pendular state* an und erreicht ein Maximum, welches auf der Struktur des *funicular state* beruht. Schließlich nimmt die Spannung wieder ab, sobald der Zweitphasenanteil hoch genug ist, dass sich – auch unter optimierten Probenherstellungsmethoden – Agglomeratstrukturen ausbilden. Konfokalmikroskopische Bilder werden genutzt um all diese Strukturen direkt in 3D zu visualisieren. Insgesamt zeigen die Proben mit 115° niedrigere Spannungswerte als die Proben mit 87°, was mit der kontaktwinkelabhängigen Energie, die benötigt wird um Partikel aus der Grenzfläche zwischen Zweit- und Hauptflüssigkeit zu entfernen, erklärt wird.

Die exakten Positionen der sphärischen Partikel in den 3D-Bildern werden mithilfe eines überwiegend selbstprogrammierten Bildauswertungs-Algorithmus ermittelt. Entsprechende Partikelpositionen werden für Proben mit 87° und 115° bei verschiedenen Zweitphasenanteilen bestimmt. Auf Basis der festgestellten Partikelpositionen und -radien werden die Mikrostrukturparameter Paarkorrelationsfunktion, Koordinationszahl und scheinbare fraktale Dimension berechnet. Die Paarkorrelationsfunktionen zeigen ein ausgeprägtes Maximum bei einem Abstandswert der einem direkten Oberflächenkontakt der Partikel entspricht. Bei Kapillarsuspensionen steigt dieses Maximum bei beiden untersuchten Kontaktwinkeln mit zunehmender Menge an Zweitphase an. Dies wird mit der zunehmenden Anziehungskraft der Partikel begründet, welche sich auch in den rheologischen Daten widerspiegelt. Die selbe Korrelation wird zudem für die Koordinationszahlen aufgefunden – die mittlere Koordinationszahl steigt bei Kapillarsuspensionen mit der Menge an zugegebener Zweitphase an. Zwischen Proben mit 87° und 115° treten Unterschiede in der Steigung dieser Koordinationszahlzunahme auf, welche mit entsprechenden Unterschieden in den rheologischen Daten korrelieren. Die berechneten fraktalen Dimensionen der Proben sind mit großen Fehlerbalken behaftet, welche die Ableitung signifikanter Trends als Funktion des Zweitphasenanteils verhindern. Jedoch lässt sich eine klare Zunahme der fraktalen Dimension mit zunehmendem Feststoffanteil aufzeigen.

Aufgrund der Schwierigkeiten bei der Ermittlung aussagekräftiger Werte der fraktalen Dimension ausschließlich aus konfokalmikroskopischer Bildauswertung werden zwei weitere Ansätze verfolgt. Beide beruhen auf rheologischen Potenzgesetzen, welche sich auf verschiedene Struktur- und Aggregations-Modelle zurückführen lassen. Die für konfokalmikroskopische Experimente optimierten glasbasierten Kapillarsuspensionen können nur in unzureichend kleinen Volumina hergestellt werden. Daher werden die entsprechenden rheologischen Studien mit auf  $\text{Al}_2\text{O}_3$  und auf  $\text{CaCO}_3$  basierenden Kapillarsuspensionen durchgeführt. Fraktale Dimensionen zwischen 1.86 und 2.05 werden aus einem Potenzgesetz ermittelt, welches auf Fließgrenzenmessungen angewandt wird. Hingegen ergeben sich für die gleichen Proben deutlich höhere Werte zwischen 2.57 und 2.74 aus einem Modell, welches Potenzgesetze der kritischen Deformationsamplituden und des Plateauwerts des Speichermoduls nutzt. Der Unterschied in den ermittelten fraktalen Dimensionen lässt sich durch eine inhomogene Mikrostruktur erklären, bei der dichter gepackte Agglomerate durch ein vergleichsweise weitmaschiges partikuläres Rückgrat miteinander verknüpft sind, welches die Kräfte im Netzwerk überträgt. Die

Hypothese einer derartigen Struktur wird durch konfokalmikroskopische 3D-Bilder bestätigt. Bei Betrachtung des jeweiligen physikalischen Ursprungs beider genutzter rheologischer Modelle, können die verschiedenen berechneten fraktalen Dimensionen einerseits als Maß für die Rückgratstruktur und andererseits als Maß für die Aggregate selbst angenommen werden. Fraktale Dimensionen, die optisch aus den konfokalmikroskopischen Bildern ermittelt werden, können nur scheinbare Werte liefern, die gemischte Beiträge von Rückgrat und Aggregaten enthalten. Entsprechend liegen die konfokalmikroskopisch ermittelten fraktalen Dimensionen zwischen den Ergebnissen der beiden rheologischen Modelle. Diese gemischten Beiträge auf zwei verschiedenen Längenskalen erklären auch die großen Fehlerbalken, die bei der optischen Methode der Ermittlung der fraktalen Dimension zuvor aufgefunden wurden. Unabhängig von der genutzten Methode ergibt sich ein Anstieg der fraktalen Dimension von Kapillarsuspensionen mit zunehmender Partikelgröße. Dieser Trend bestätigt sich in allen untersuchten Stoffsystemen und auf allen verschiedenen Längenskalen, die sich aus den jeweiligen Methoden ergeben. Dementsprechend weisen Kapillarsuspensionen mit größeren Partikeln eine kompaktere Partikelanordnung auf. Dies lässt sich aufgrund einer Schwächung des Beitrags der Kapillarkraft im Vergleich mit Trägheits- und hydrodynamischen Kräften bei zunehmender Partikelgröße erklären.

Zuletzt wird eine Masterkurve für die Fließgrenze als Funktion des Zweitphasenanteils erstellt. Diese Masterkurve kann genutzt werden, um die Fließgrenze einer Probe für eine beliebige Kombination von Zweitphasenanteil, Partikelgröße und Feststoffanteil für eine stofflich vorgegebene Probenrezeptur vorauszusagen. Dies wird am Beispiel der  $\text{Al}_2\text{O}_3$ -Proben aufgezeigt. Die Masterkurve wird darüber hinaus um die Grenzflächenspannung, den Kontaktwinkel, sowie das ermittelte Übergangskriterium zwischen *pendular* und *funicular state* erweitert. Die derart generalisierte Masterkurve ermöglicht auf diese Weise die materialunabhängige Vorhersage der Fließgrenze bei Proben stofflich verschiedener Zusammensetzung. Dies wird durch Einbeziehung der Stoffsysteme gezeigt, die auf  $\text{CaCO}_3$  sowie auf den für konfokale Mikroskopie genutzten sphärischen Glaspartikeln beruhen. Diese generalisierte Masterkurve ist ein eindeutiges Beispiel dafür, wie die aus der Mikrostruktur gewonnenen Erkenntnisse ein tiefergehendes Verständnis der Rheologie ermöglichen und hierbei die zukünftige Entwicklung von Kapillarsuspensionen unterstützen. Somit zeigt diese Forschung die Wichtigkeit und den Nutzen des Verständnisses physikalischer Grundeigenschaften auf mögliche Anwendungen solcher Proben auf. Die Ergebnisse liefern den Grundstein für weitere strukturelle Untersuchungen. Dies soll als Ermutigung zu zukünftig fortgeführter, erfolgreicher Erforschung der Mikrostruktur von Kapillarsuspensionen dienen.



# Contents

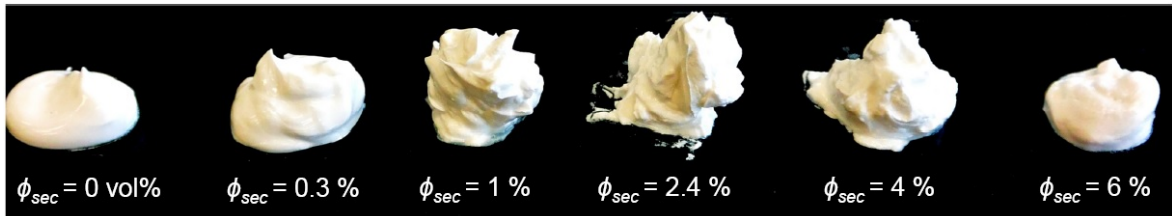
<b>1</b>	<b>Introduction and Motivation</b>	<b>1</b>
<b>2</b>	<b>Theoretical Background</b>	<b>5</b>
2.1	Basic concepts of shear rheology . . . . .	5
2.1.1	Laminar shear flow . . . . .	5
2.1.2	Yield stress . . . . .	6
2.1.3	Rotational rheometry . . . . .	7
2.1.4	Oscillatory rheology . . . . .	7
2.2	Particle suspensions . . . . .	9
2.2.1	Van der Waals force . . . . .	9
2.2.2	Electrostatic interaction . . . . .	11
2.2.3	Gravity and diffusion . . . . .	12
2.2.4	Colloidal gels – fractal particle networks . . . . .	13
2.3	Wetting on a solid . . . . .	16
2.3.1	Interfacial tensions and the three-phase contact angle . . . . .	16
2.3.2	Capillary forces . . . . .	19
2.3.3	Wet granular materials . . . . .	21
2.4	Capillary suspensions . . . . .	25
2.4.1	Pendular and capillary state . . . . .	25
2.4.2	A system between wet granular materials and colloidal gels . . . . .	27
2.4.3	Mechanical features . . . . .	29
2.5	Droplet breakup . . . . .	32
<b>3</b>	<b>Material Systems</b>	<b>37</b>
3.1	Raw materials and capillary suspension compositions . . . . .	37
3.1.1	Basic physical characterization of particles and fluids . . . . .	38
3.1.2	Composition C1 – the confocal microscopy sample systems . . . . .	38
3.1.3	Compositions C2 and C3 – pendular and capillary state model system . . . . .	43
3.1.4	Composition C4 – a viscosity matched model system . . . . .	44
3.1.5	Composition C5 – $\text{Al}_2\text{O}_3$ -based capillary suspensions . . . . .	45
3.1.6	Composition C6 – $\text{CaCO}_3$ -based capillary suspensions . . . . .	46
3.2	Chemical modification of Kromasil silica particles . . . . .	47
3.2.1	Particle dyeing and porosity modification . . . . .	47
3.2.2	Particle hydrophobization . . . . .	50
3.3	Capillary suspension sample preparation . . . . .	51
3.3.1	Preparation protocols for compositions C1 to C6 . . . . .	51

3.3.2	Set and effective solid and secondary fluid volume fractions . . . . .	54
<b>4</b>	<b>Experimental Techniques and Devices</b>	<b>55</b>
4.1	Rheological measurements . . . . .	55
4.2	Confocal microscopy . . . . .	57
4.3	Contact angle and interfacial tension determination . . . . .	61
4.4	Computational image evaluation . . . . .	63
<b>5</b>	<b>Influence of Sample Preparation</b>	<b>69</b>
5.1	Turbulent mixing with a dissolver stirrer . . . . .	69
5.1.1	Choice of a pendular and capillary state reference sample . . . . .	69
5.1.2	Influence of stirring speed . . . . .	70
5.1.3	Influence of stirring time . . . . .	72
5.2	Alternative sample preparation methods . . . . .	75
5.2.1	Mixing on a ball mill . . . . .	75
5.2.2	Secondary fluid emulsification before particle addition . . . . .	77
5.2.3	Emulsification and mixing using ultrasound . . . . .	79
5.3	Viscosity-matched model system . . . . .	80
<b>6</b>	<b>Microstructural Features and Transitions</b>	<b>85</b>
6.1	Variation of wetting and validation of methods . . . . .	86
6.1.1	Structure of systems with nonporous particles . . . . .	86
6.1.2	Structure of systems with porous particles . . . . .	95
6.1.3	Coupling structure and rheology . . . . .	99
6.1.4	A short contemplation on the confocal method and composition C1 . . . . .	103
6.2	Variation of secondary fluid volume fraction . . . . .	105
6.2.1	Confocal images and basic sample properties . . . . .	106
6.2.2	Oscillatory rheometry . . . . .	113
6.2.3	Computational structure evaluations . . . . .	119
6.3	Variation of solid volume fraction and particle size . . . . .	127
6.3.1	Yield stress master curve for $\text{Al}_2\text{O}_3$ -based system . . . . .	128
6.3.2	Fractal dimension from rheological scaling laws . . . . .	131
6.3.3	$\text{CaCO}_3$ -based system – further extending the master curve . . . . .	136
6.3.4	Reassessing the fractal dimensions using confocal microscopy . . . . .	141
<b>7</b>	<b>Conclusion</b>	<b>147</b>
7.1	Summary . . . . .	147
7.2	Outlook . . . . .	152
<b>8</b>	<b>Bibliography</b>	<b>155</b>
<b>9</b>	<b>Appendix</b>	<b>169</b>
9.1	Calculations of partial sphere volumes inside a box . . . . .	169
9.2	Additional figures to chapter 6.2 . . . . .	171
9.3	List of symbols and abbreviations . . . . .	175
<b>10</b>	<b>Academic CV (shortened version)</b>	<b>181</b>

# 1 Introduction and Motivation

Suspensions consist of solid particles that are dispersed in a bulk fluid. They are ubiquitous. A vast number of industrial consumer products are suspensions, or at least are based on them, e.g. paints, inks, mortar, cosmetics, pharmaceuticals and fruit juices. The flow properties during production and of the end product are crucial for processability as well as customer acceptance. Thus, knowledge of the suspension's rheological properties, as well as the structural origin thereof, is needed. Often, it is desirable to produce suspensions that exhibit a yield stress, which prevents sedimentation of the particles and spreading of the suspension over long time scales. Classically, this necessitates the addition of polymeric binders or other rheology control agents.

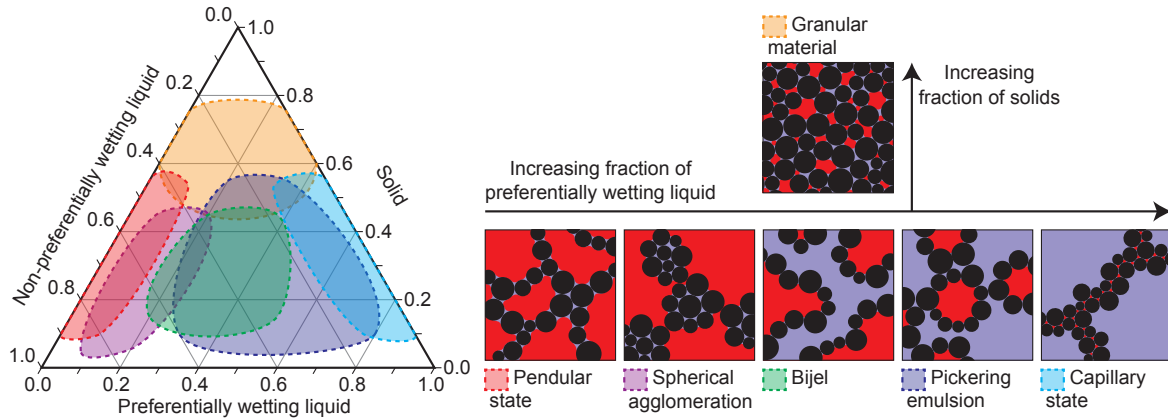
A different, relatively new option to easily induce a yield stress is to formulate suspension products as capillary suspensions. These consist of particle suspensions with a small amount of added secondary fluid that is immiscible with the bulk liquid [1]. Therefore, capillary suspensions are ternary solid-liquid-liquid systems that do not require the addition of any additional rheology control agents apart from the secondary fluid. For an oil-based suspension, this secondary fluid is just water in the easiest case. The added liquid causes a sample-spanning particle network to form, which leads to dramatic alterations of the suspension rheology and stability [1–6]. This effect can be used as a simple method to tune the flow behavior of suspensions [7] that is not only limited to inducing a yield stress to prevent sedimentation, as many other rheological properties, like low-shear viscosity or viscoelastic properties, are also modified. An example demonstrating how the addition of small amounts of an aqueous liquid to an oil-based suspension influences the appearance of the sample is shown in Fig. 1.1. Differences in the samples flow properties directly are evident by eye.



**Figure 1.1:** Suspensions of  $\alpha$ - $\text{Al}_2\text{O}_3$  particles in paraffin oil with the addition of small amounts of aqueous sucrose solution (50 vol %) as an immiscible secondary fluid. The amount of added sucrose solution is given by  $\phi_{\text{sec}}$ , which is defined as the ratio of added secondary fluid volume to total sample volume. The solid volume fraction is  $\phi_{\text{solid}} = 20$  %.

The buildup of a percolating particle network arises when the secondary fluid wets the particles better than the bulk fluid does, which is termed the pendular state, but is also

possible when the secondary fluid wets the particles worse, termed capillary state. In the pendular state, binary bridges of secondary fluid connect adjacent particles and cause attractive capillary forces. In the capillary state, particles assemble around droplets of secondary fluid and form an energetically favored percolating structure of micro-cluster based building blocks [8]. The classification of the pendular and capillary states, amongst other ternary solid-liquid-liquid structures, is presented in the ternary diagram of Fig. 1.2 as a function of the sample composition.



**Figure 1.2:** A possible ternary diagram of solid-liquid-liquid systems. Reprinted from [2] ([hyper-link](#)) with permission from Elsevier. The diagram includes capillary suspensions in the pendular state (red) and capillary state (cyan), represented by one of the two fluid amounts being much smaller than the other one and amounts of solid volume being in a possible range of  $\approx 10 - 55$  %. Also included are other common systems, namely spherical agglomerated structures (purple), Pickering emulsions (blue) and bijels (green). At very high solid volume fractions, the various systems are subsumed by wet granular materials (orange), which also show a variety of different microstructures in reality.

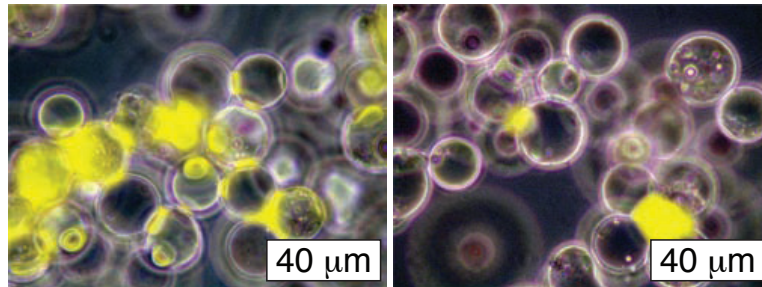
Due to the ease of tuning the suspension rheology, capillary suspensions can be used for various applications. In the last years, many different possible industrial applications have been researched. Amongst these are: the usage as precursors for ceramic or glass filters with high porosity and simultaneously small pore size [9–11]; porous polymeric or hybrid membranes [12, 13]; improved polymer blends [5, 14, 15]; slurries for printable electronics with accurately molded edge shape, good charge transfer properties and reduced resistivity [16–18]; crack-free films [19]; thermal interface materials [20]; slurries of renewable carbon sources used for energy generation [21]; the preparation of novel food products [22]; and 3D printing paste formulations [23, 24]. On the other hand, modified rheological properties also can be detrimental, for example when capillary suspensions appear as hydrate slurries formed from water in mineral oil emulsions during oil recovery [25, 26]. In these cases, an understanding of capillary suspension formation is needed to prevent or at least minimize their appearance.

For industrial applications of capillary suspensions, tunable, reproducible and predictable rheological features are of outstanding interest. The rheological properties are closely related to the microstructure of the samples. Therefore, a detailed analysis of the microstructure, under a broad variation of parameters, and simultaneous acquisition of both structure and rheology is a fundamental aim to further understand and improve capillary suspension products. In recent works, the strength of capillary suspensions has



been characterized by rheological measurements, e.g. [1–7, 9, 16, 21, 22]. These papers show the impact of the secondary fluid on the flow behavior. A marked increase in the yield stress occurs when the particle network is formed. The low frequency complex shear modulus shows the same increasing trend due to addition of the secondary fluid [1]. Capillary suspensions are shear-thinning, with the low-shear viscosity showing a marked increase, while the high-shear viscosity remains unchanged [7]. This also offers many advantages during processing, which often takes place at high shear rates, e.g. during atomization of capillary suspensions [21] or coating with a doctor blade [16].

Heretofore, an observation of the microstructure of capillary suspensions was only possible when samples were solidified first, either by polymerization of the bridges, e.g. [5, 14, 27–29], or by sintering of the particles, e.g. [10–12]. While these approaches are extremely helpful and valuable to our understanding of many structural properties of capillary suspensions, imaging is limited to fractured, two-dimensional surfaces of the solidified samples. Additionally, the solidification processes almost certainly change the microstructure of the samples to an unknown extent. Also, all of these imaged samples were limited to pendular state structures. The capillary state was never imaged directly, but merely was hypothesized by observed changes in the rheology and by simulations [30]. While one of the earliest studies on capillary suspensions does provide microscopy images representing pendular and capillary state samples [1], the samples had to be heavily diluted for imaging. Furthermore the image resolution is unsatisfactory. These images are reproduced in Fig. 1.3. Unambiguous structural insights from these images are not



**Figure 1.3:** Bright field microscopy images of glass-bead-based capillary suspensions with fluorescent overlay. The images are reproduced from *E. Koos and N. Willenbacher, Capillary Forces in Suspension Rheology, Science 331(6019), 897-900, 2011* [1] ([hyperlink](#)), reprinted with permission from AAAS. The image shows diluted capillary suspension samples in the pendular state (left) and in the capillary state (right). The fluorescently dyed secondary fluid is shown in yellow. The precise position of secondary fluid and interfaces between both fluids are difficult to localize due to the refraction of light.

possible. An acquisition of capillary suspension microstructures in 3D without the need of any solidification, dilution or other sample alterations is therefore of utmost interest. One of the main motivations of this thesis is to accomplish this task using confocal microscopy, which is a powerful method for the visualization of three-dimensional sample structures in situ [31]. Spatial imaging deep within the sample is possible using confocal microscopy, if the refractive indexes of the components are matched.

A plethora of examples for the application of confocal microscopy to elucidate the structure in classical two-phase solid-liquid particle suspensions can be found in literature [cf. 32]. Recently, several confocal studies on different ternary solid-liquid-liquid systems have also been performed. For example, Gögelein et al. imaged the buildup of

capillary bridges in wet granular media [33]. Lee et al. clarified the structure of colloidal gels that arise due to bridging of Pickering emulsion droplets and compared this gelled structure to van der Waals colloidal gels [34]. Leunissen et al. examined Pickering emulsions by means of dyeing the particles and the droplet phase with two fluorescent dyes with different emission wavelengths while leaving the bulk phase undyed [35]. Wenzl studied the influence of shear and compression forces on particle clusters held together by a secondary fluid immersed in another bulk fluid also using two different dyes for particles and droplets [36]. Thus, confocal microscopy appears to be a very promising tool to evaluate the structure of capillary suspensions and to relate the observed structural characteristics to the samples' rheological properties. The approach of using two different dyes for particles and secondary fluid seems to be especially worthwhile and is indeed applied to capillary suspensions in this thesis. Such high-resolution, 3D images enable the evaluation of in-situ structural properties. Therefore, the structure can be described quantitatively. Consequently, a much more straightforward relation between structural parameters and rheological properties is enabled.

In addition to establishing the necessary methods and sample systems to make confocal microscopy of capillary suspensions possible, the primary concern of the present thesis is to determine physical properties of capillary suspensions as well as illuminate the processing parameter variations. Following an overview of the theoretical background in chapter 2, a description of the various samples, their modifications, and preparations is included in chapter 3. The experimental and analytical methods, as designed and used, are described in chapter 4. Finally, the main results are presented in chapters 5 and 6, with a short summary and outlook in chapter 7.

In chapter 5, the focus is on the processing of capillary suspensions, using different preparation methods and variations in the energy input, mixing times and mixing speeds. As capillary suspension structures are not in thermodynamic equilibrium [37], differences in preparation will always lead to a different structure and rheology. Acknowledging these results, chapter 6 then investigates the influence of several different physical properties of capillary suspensions on their structure and rheology. This chapter consists of three parts. First, the confocal method is established while the influence of the secondary fluid wetting as well as particle porosity is evaluated. Secondly, the influence of different amounts of secondary fluid on the structure and rheology is examined in detail. Finally, the fractal dimension, which is a core parameter to describe a percolating particle network, is investigated by confocal and rheological methods. At the same time, the influence of particle size and the amount of solid particles are analyzed. This allows a master curve for the yield stress to be constructed, while the other physical parameters are incorporated into a rescaled yield stress or into the amount of secondary fluid. This master curve is a very powerful tool for the directed design of capillary suspension based products.

The master curve is clear representation of how the knowledge gained from the microstructure imparts a deeper understanding of the rheology and thereby aids in the future design of capillary suspensions. This research, thus, highlights the importance and usefulness obtained by understanding the influence of basic physical properties on possible applications for such samples. This will then encourage continuing, fruitful research on capillary suspension microstructures. While this thesis achieves several key structural insights, there also remain promising research options, some of which are outlined in chapter 7.

## 2 Theoretical Background

### 2.1 Basic concepts of shear rheology

Rheology investigates the deformation and flow of matter. These are in general described by a stress tensor  $\sigma$  and a strain-rate tensor  $D$ , given as

$$\sigma = \begin{pmatrix} \sigma_{xx} & \sigma_{xy} & \sigma_{xz} \\ \sigma_{yx} & \sigma_{yy} & \sigma_{yz} \\ \sigma_{zx} & \sigma_{zy} & \sigma_{zz} \end{pmatrix} \quad (2.1)$$

$$D = \begin{pmatrix} D_{xx} & D_{xy} & D_{xz} \\ D_{yx} & D_{yy} & D_{yz} \\ D_{zx} & D_{zy} & D_{zz} \end{pmatrix} = \begin{pmatrix} \frac{\partial v_x}{\partial x} & \frac{1}{2} \left( \frac{\partial v_x}{\partial y} + \frac{\partial v_y}{\partial x} \right) & \frac{1}{2} \left( \frac{\partial v_x}{\partial z} + \frac{\partial v_z}{\partial x} \right) \\ \frac{1}{2} \left( \frac{\partial v_y}{\partial x} + \frac{\partial v_x}{\partial y} \right) & \frac{\partial v_y}{\partial y} & \frac{1}{2} \left( \frac{\partial v_y}{\partial z} + \frac{\partial v_z}{\partial y} \right) \\ \frac{1}{2} \left( \frac{\partial v_z}{\partial x} + \frac{\partial v_x}{\partial z} \right) & \frac{1}{2} \left( \frac{\partial v_z}{\partial y} + \frac{\partial v_y}{\partial z} \right) & \frac{\partial v_z}{\partial z} \end{pmatrix} \quad (2.2)$$

with the flow velocities  $v_x$ ,  $v_y$  and  $v_z$  in the spatial  $x$ ,  $y$  and  $z$  directions.

#### 2.1.1 Laminar shear flow

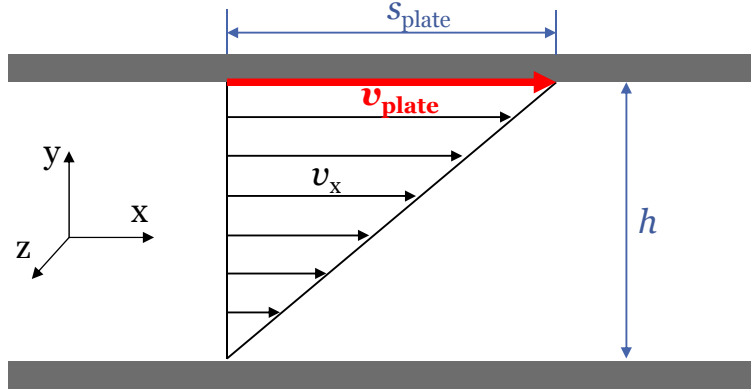
One special case derived from general flow is simple laminar shear flow, which is characterized by parallel velocity vectors (i.e.  $v_x \neq 0$ ,  $v_y = 0$ ,  $v_z = 0$ ) with a velocity field gradient in another direction (i.e.  $\partial v_x / \partial x = 0$ ,  $\partial v_x / \partial y \neq 0$  and  $\partial v_x / \partial z = 0$ ). In this easy model case, the strain-rate tensor (equation 2.2) contains  $D_{xy} = D_{yx} = 1/2 \cdot \partial v_x / \partial y$  as only non-zero components, where the shear rate  $\dot{\gamma}$  is defined as  $\dot{\gamma} = \partial v_x / \partial y$ . The dynamic viscosity  $\eta$  relates the stress to the strain rate tensor, thus  $\sigma_{xy} = 2\eta D_{xy} = \eta \dot{\gamma}$  for simple shear flow, where  $\eta$  is the shear viscosity [38].

Laminar shear flow between two plates is sketched in Fig. 2.1. The bottom plate is at rest while the top plate moves with velocity  $v_{\text{plate}}$  in the  $x$ -direction. If there is a fluid in the gap between the plates, the fluid is sheared and moves with velocity  $v_x$ , which is only a function of position  $y$  in the gap. No-slip conditions are assumed, which means that the liquid sticks to the plate. Thus, the liquid at the bottom plate does not move ( $v_x = 0$ ) and at the top plate translates with the same velocity as the plate ( $v_x = v_{\text{plate}}$ ). The strain  $\gamma$  is defined as

$$\gamma = \frac{s_{\text{plate}}}{h} \quad (2.3)$$

with the gap height  $h$  and the distance  $s_{\text{plate}}$  that the top plate has moved from its original position. For Newtonian liquids, the shear rate is constant. Thus

$$\dot{\gamma} = \frac{d\gamma}{dt} = \frac{dv_x}{dy} \quad (2.4)$$



**Figure 2.1:** Model for simple shear flow between two plates.

where the shear rate, representing the time derivative  $d/dt$  of the strain, is used as previously defined. The shear stress  $\sigma \equiv \sigma_{xy}$  can be determined, if the area  $A$  of the top plate in contact with the liquid and the force  $F$  moving the plate is known. Then

$$\sigma = \frac{F}{A} = \eta \dot{\gamma} \quad (2.5)$$

where the shear viscosity also is used as previously defined. Equation 2.5 is the rheological constitutive equation, i.e. an equation relating stress and flow kinematics [38], for the Newtonian fluid in simple shear flow. For non-Newtonian fluids, the viscosity, amongst others, is a function of the shear rate. Various, more complex constitutive equations exist for different types of non-Newtonian behaviors and have to be chosen depending on the particular flow behavior of the sample, which in case of suspensions to a large extent (but not solely) is governed by the particle interactions outlined in chapter 2.2.

### 2.1.2 Yield stress

Some samples may show only elastic deformation (solid-like behavior) for low applied stresses and only start to flow when a critical stress value is exceeded. This critical stress is called the yield stress  $\sigma_y$ . For an applied stress  $\sigma < \sigma_y$ , the shear rate essentially is zero, apart from the elastic deformation leading to some creep. In the easiest case, such a yield stress fluid shows Newtonian flow after the yield stress is exceeded, thus the constitutive equation for flow ( $\sigma > \sigma_y$ ) becomes

$$\sigma = \sigma_y + \eta \dot{\gamma} \quad (2.6)$$

which is called the Bingham model. If non-Newtonian flow behavior appears for  $\sigma > \sigma_y$  the second term on the right hand side of equation 2.6 has to be replaced by a different appropriate constitutive term.

The yield stress is a slightly ambiguous and sometimes controversially discussed property [39], as it may depend on the applied deformation, flow field and timescales of observation and additionally the start-up of flow in many cases appears transiently with increasing stress and not instantaneously as the Bingham model predicts [40]. There exist several different methods to measure the yield stress and yield stress values measured with different methods should not be directly compared with each others [41]. The

yield stress often is understood in the context of a failure in the sample microstructure, which generates a sufficient resistance against flow by any sample-dependent interactions and at some point is ruptured or otherwise forced to move, while the type of failure may depend on the way the external force is applied and thus on the method of yield stress measurement.

### 2.1.3 Rotational rheometry

Shear rheological properties are typically obtained using rotational rheometers. Classical shear rheology depends on the principles of continuum mechanics. Due to the continuum assumption any sample length scales, especially gap widths, have to be much larger than for any features in the sample, i.e. the size of particles or particle aggregates in the case of suspensions. Either shear rate or shear stress is applied to the sample in rotational shear rheometers, while the other property is detected. Therefore, rheometers are classified as stress- or strain-controlled. In stress-controlled devices, the shear stress is calculated from the torque  $M_R$  measured by the rotating component of the rheometer, while the shear rate is obtained from its angular velocity  $\Omega$ . In strain-controlled rheometers, the force to keep the non-rotating component stationary is measured to obtain  $M_R$  and, thus, the force sensor kept separate from the motor.

Three types of geometries are commonly used: a combination of two plates (plate-plate geometry); a combination of an upper cone and a lower plate (cone-plate geometry); and a combination of an inner cylinder and an outer cup (Searle or Couette geometry, with either the cylinder or cup rotating, respectively) [38]. A more specialized geometry mainly used for yield stress determination is the vane geometry, where the cylinder of the Searle system is replaced by a vane with four to eight blades [42]. Fig. 2.2 shows schematic drawings of all these types of rotational rheometer geometries. All of them have individual advantages as well as pitfalls. Details about these, as well as the geometry-dependent determination and calculations of  $\dot{\gamma}$ ,  $\sigma$  and  $\eta$  from  $M_R$ ,  $\Omega$  and the geometrical parameters charted in Fig. 2.2 can be found in various textbooks, eg. [38].

### 2.1.4 Oscillatory rheology

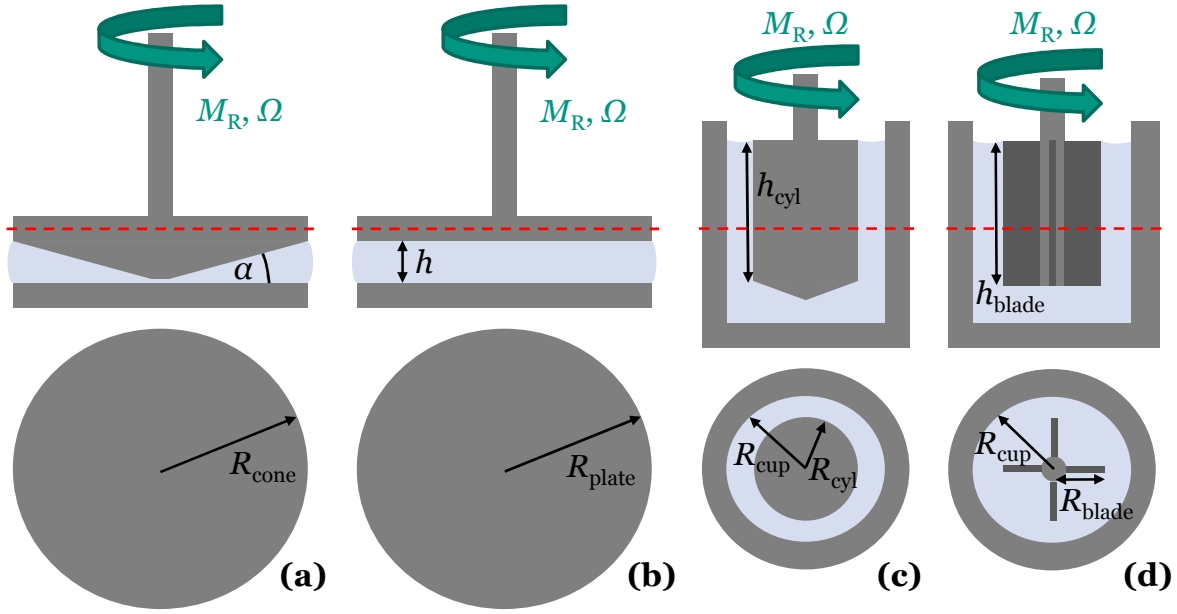
Instead of steady shear experiments, where the geometry of the rheometer monotonically retains one direction of rotation, the sample can also be characterized by applying a sinusoidal oscillation of the geometry around its rest position, where either the stress amplitude or the strain amplitude is prescribed while the other one is detected. The strain oscillation as function of the time  $t$  is characterized by the strain amplitude  $\hat{\gamma}$  and the frequency  $f = 2\pi\omega$  with

$$\gamma(t, \omega) = \hat{\gamma}(\omega) \sin(\omega t). \quad (2.7)$$

The stress in the sample responds with an oscillation of same angular frequency  $\omega$ , but with the oscillation shifted by an angle  $\delta$ , so that

$$\begin{aligned} \sigma(t, \omega) &= \hat{\sigma}(\omega) \sin(\omega t + \delta) \\ &= \hat{\sigma}(\omega) [\sin(\omega t) \cos(\delta) + \cos(\omega t) \sin(\delta)] \end{aligned} \quad (2.8)$$

with the stress amplitude  $\hat{\sigma}$ . The phase shift  $\delta$  can take values between 0 and  $\pi/2$ . The limiting case of  $\delta = \pi/2$  corresponds to a purely viscous sample (i.e. a Newtonian fluid)



**Figure 2.2:** Schematic side view (top row) and cross-sectional area along the red dashed line (bottom row) of rotational rheometer types used for determining shear rheological properties from measurements of torque  $M_R$  and angular velocity  $\Omega$ . (a) Cone-plate geometry with cone angle  $\alpha$  and cone radius  $R_{\text{cone}}$ , (b) plate-plate geometry with gap width  $h$  and plate radius  $R_{\text{plate}}$ , (c) Searle system with cup and cylinder radii  $R_{\text{cup}}$  and  $R_{\text{cyl}}$ , respectively, and cylinder height  $h_{\text{cyl}}$  and (d) vane geometry with a four-bladed vane with blade radius  $R_{\text{blade}}$  and blade height  $h_{\text{blade}}$ . The sample is denoted by the light blue filled areas.

with  $\sigma(t) \propto d\gamma/dt$  and the viscosity  $\eta$  as the proportionality constant. The other limiting case of  $\delta = 0$  represents a purely elastic sample, i.e. a Hookean solid characterized by  $\sigma(t) \propto \gamma(t)$  with the shear modulus  $G$  as the proportionality constant. Intermediate phase shifts represent viscoelastic liquids, which possess viscous as well as elastic properties.

The fraction of stress and strain amplitude in the viscoelastic case is the magnitude of the complex shear modulus  $|G^*|$  with

$$|G^*(\omega)| = \frac{\hat{\sigma}(\omega)}{\hat{\gamma}(\omega)} \quad (2.9)$$

which in combination with equation 2.8 leads to

$$\sigma(t, \omega) = \hat{\gamma}(\omega) |G^*(\omega)| [\sin(\omega t) \cos(\delta) + \cos(\omega t) \sin(\delta)]. \quad (2.10)$$

$G^*$  is separated into its real and imaginary part,  $G^* = G' + iG''$  with

$$|G^*(\omega)| = \sqrt{G'(\omega)^2 + G''(\omega)^2} \quad (2.11)$$

$$G'(\omega) = |G^*(\omega)| \cos \delta \quad (2.12)$$

$$G''(\omega) = |G^*(\omega)| \sin \delta \quad (2.13)$$



$$\begin{aligned}\sigma(t, \omega) &= \hat{\gamma}(\omega) [G'(\omega) \sin(\omega t) + G''(\omega) \cos(\omega t)] \\ &= \hat{\gamma}(\omega) [G'(\omega) \sin(\omega t) + G''(\omega) \sin(\omega t + \pi/2)].\end{aligned}\quad (2.14)$$

Direct comparison of equations 2.8 and 2.14 helps to clarify that the storage modulus  $G'$  is a measure for the magnitude of elastic sample properties and the loss modulus  $G''$  represents the magnitude of viscous properties. The tangent of the phase shift

$$\tan(\delta) = \frac{G''(\omega)}{G'(\omega)} \quad (2.15)$$

as calculated from equations 2.12 and 2.13, identifies the relative magnitude of viscous to elastic sample properties.

If oscillations are performed at small amplitudes, the stress and strain are directly proportional,  $\hat{\sigma} \propto \hat{\gamma}$ . As a consequence,  $G'$ ,  $G''$ ,  $|G^*|$  and  $\tan(\delta)$  are independent of both stress and strain amplitudes in this linear-viscoelastic (LVE) region. When a critical amplitude  $\hat{\gamma}_{\text{crit}}$  (or equivalently  $\hat{\sigma}_{\text{crit}}$ ) is exceeded, the proportionality no longer holds and, thus, all oscillatory properties also become a function of the applied amplitudes. As both amplitudes themselves are a function of frequency  $\omega$ , this transition away from the LVE region can also be frequency-dependent.

## 2.2 Particle suspensions

The rheology of regular, two-phase suspensions of particles in a bulk liquid is primarily determined by the amount of particles, characterized by the solid volume fraction  $\phi_{\text{solid}}$ , and by particle interactions at the relevant timescale. The solid volume fraction is defined as the ratio of the summed volume of all solid particles to the total sample volume. Common particle interactions are the attractive van der Waals force, repulsive electrostatic interactions, steric interactions, depletion interactions and capillary forces. Additionally, the rheology may be influenced by particle motion induced by Brownian diffusion, gravity and hydrodynamic forces. Hydrodynamic forces dominate the rheological properties under flow at high shear rates, while particle interactions dominate at low shear rates or at rest where hydrodynamic forces are absent [38].

Steric and depletion interactions will not be discussed here as they are not relevant for the particles used in this thesis. As the scope of the thesis is on the structure at rest rather than under fast flows, hydrodynamic forces are also not detailed further. Capillary forces require a secondary liquid phase that is not present in two-phase suspensions and, therefore, are explained separately later. The other heretofore mentioned particle interactions and motions are detailed in this section. Each of these interactions depends on the particle radius  $a$ . Suspensions of particles approximately smaller than 1  $\mu\text{m}$  are commonly termed colloidal suspensions.

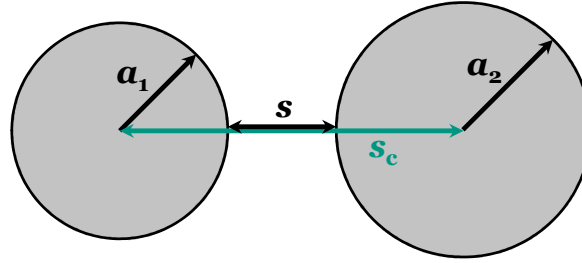
### 2.2.1 Van der Waals force

Van der Waals forces are ubiquitously present between all particles and result from local fluctuations (polarizations) in electron clouds on the atomic level. On a colloidal particle

scale, the atoms of any particle polarize the atoms of any adjacent particle. This interaction between two induced dipoles in both particles is called the London interaction. Additional contributions originate from permanent dipoles in both particles (Keesom interaction) and permanent dipoles in one and induced dipoles in the other particle (Debye interaction). These effects ordinarily lead to net attractive forces between the particles [38]. Particle interactions are not typically expressed in terms of forces  $F$  directly, but rather in terms of potentials  $\Psi(s_c)$  as function of the particle center distance  $s_c$ . The force is calculated as the negative derivative of the potential [38]

$$F(s_c) = -\frac{d\Psi(s_c)}{ds_c}. \quad (2.16)$$

The van der Waals interaction depends on the geometry of the two interacting bodies. The model case of two interacting spheres of radii  $a_1$  and  $a_2$  is sketched in Fig. 2.3. In



**Figure 2.3:** Schematic image of two spherical particles with radii  $a_1$  and  $a_2$ , surface distance  $s$  and particle center distance  $s_c$ .

this case, the potential of the van der Waals interaction is given by [38]

$$\Psi_{\text{vdW}}(s_c) = -\frac{A_H}{6} \left( \frac{2a_1a_2}{s_c^2 - (a_1 + a_2)^2} + \frac{2a_1a_2}{s_c^2 - (a_1 - a_2)^2} + \ln \frac{s_c^2 - (a_1 + a_2)^2}{s_c^2 - (a_1 - a_2)^2} \right) \quad (2.17)$$

where the coefficient  $A_H$  is called the Hamaker constant. However,  $A_H$  is indeed not a constant, but depends strongly on the material properties of the particles and the suspending liquid [38]. If both particles consist of the same material, the Hamaker constant can be expressed as [43]

$$A_H \cong \frac{3}{4} k_B T \left( \frac{\epsilon_p - \epsilon_b}{\epsilon_p + \epsilon_b} \right)^2 + \frac{3h\nu_e}{16\sqrt{2}} \frac{(n_p^2 - n_b^2)^2}{(n_p^2 + n_b^2)^{3/2}} \quad (2.18)$$

with the thermal energy  $k_B T$  (Boltzmann constant times temperature), the mean ionization potential  $h\nu_e$  (Planck's constant times the main ultraviolet absorption frequency), the dielectric constants  $\epsilon_p$  of the particles and  $\epsilon_b$  of the bulk liquid, respectively, and the refractive indices  $n_p$  of particles and  $n_b$  of the bulk liquid. In many cases, the second term (London dispersion) on the right hand side of eq. 2.18 contributes more significantly to the Hamaker constant than the first term (Keesom and Debye), as typically  $k_B T \ll h\nu_e$  [43]. This means that the Hamaker constant will be reduced significantly if the suspension is index-matched, i.e. particles and bulk liquid have the same refractive index  $n_p = n_b$  as the second term of the equation vanishes. As the van der Waals potential is a linear



function of the Hamaker constant (eq. 2.17), the potential and consequently the van der Waals force via eq. 2.16 will be significantly reduced in these index-matched cases.

Assuming non-deformable spheres ( $s_c \geq a_1 + a_2$ , i.e. particle surface distance  $s \geq 0$ ), the van der Waals potential of equation 2.17 becomes monotonically more negative when the surface distance is decreased, tending towards negative infinity for zero surface distance. Under the condition  $s \ll a_1$ , and by replacing the distance variable  $s = s_c - (a_1 + a_2)$ , the potential equation 2.17 simplifies to

$$\Psi_{\text{vdW}}(s) = -\frac{A_H}{6s} \frac{a_1 a_2}{a_1 + a_2}. \quad (2.19)$$

Using eq. 2.16 to calculate the van der Waals force, substituting the distance variable, leads to

$$F_{\text{vdW}}(s) = -\frac{A_H}{12s^2} \frac{a_1 a_2}{a_1 + a_2}. \quad (2.20)$$

For equisized particles with radius  $a \equiv a_1 = a_2$ , this further simplifies to

$$F_{\text{vdW}}(s) = -\frac{A_H a}{12s^2} \quad (2.21)$$

and, thus, the van der Waals force for small relative particle separations  $\tilde{s} \equiv s/a \ll 1$  scales linearly with the particle size  $a$ .

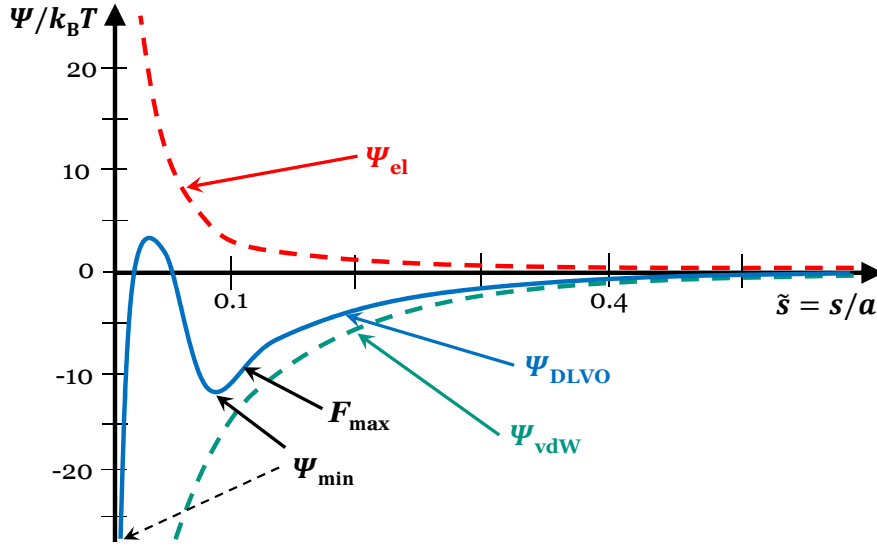
### 2.2.2 Electrostatic interaction

Repulsive electrostatic interactions occur due to a surface charging of particles, which appears when particles are dissolved in a bulk liquid, e.g. by dissociation of surface acids or bases or adsorption of free ions. The electrostatic interaction potential between equisized particles, as function of the particle surface distance, in the presence of an electrolyte can be expressed as [38]

$$\Psi_{\text{el}}(s) \approx 32\pi a \epsilon_b \epsilon_0 \left( \frac{k_B T}{z_{\text{el}} e} \right)^2 \tanh^2 \left( \frac{\Psi_{\text{surf}} e z_{\text{el}}}{4 k_B T} \right) \exp(-\kappa s) \quad (2.22)$$

with the dielectric constant of the surrounding bulk fluid  $\epsilon_b$ , the vacuum permittivity  $\epsilon_0$ , electronic charge  $e$ , electrolyte valence  $z_{\text{el}}$ , the particle surface potential  $\Psi_{\text{surf}}$  and the inverse Debye length  $\kappa$ . Details about these parameters and their influence on the electrostatic interaction can be found in various textbooks [e.g. 38, 44]. The positive sign of the electrostatic potential denotes a repulsive interaction, in contrast to the van der Waals potential (eq. 2.17). Linear addition of electrostatic and van der Waals potentials provides the DLVO potential  $\Psi_{\text{DLVO}} = \Psi_{\text{vdW}} + \Psi_{\text{el}}$ , named after the initials of Derjaguin, Landau, Verwey and Overbeek who first postulated the theory [38]. A schematic representation of the van der Waals, electrostatic and DLVO potentials is given in Fig. 2.4. Minima in the potential denote energetically stable particle separations. The depth (and width) of these minima is related to the interaction strength. Forces become maximal where the slope of the potentials is steepest, see eq. 2.16.

In the present thesis, particles with dissociable surface groups will be used, e.g. silica with surface  $-\text{OH}$  groups. However, only oil-based bulk liquids will be used, which should avoid or minimize dissociations. The typical dielectric constant of oils  $\epsilon_b \approx 1 - 10$  is also



**Figure 2.4:** Schematic drawing of an example van der Waals, electrostatic and DLVO potential as a function of the normalized particle surface distance  $\tilde{s} = s/a$ . The potentials are normalized by thermal energy  $k_B T$ . Thermodynamically stable particle distances are at a local potential minimum  $\Psi_{\min}$  (here  $\tilde{s} \approx 0.08$  and  $\tilde{s} \approx 0$ ). Maxima in the particle separation force  $F_{\max}$  occur at the positions of the steepest slopes (here  $\tilde{s} \approx 0.11$  and  $\tilde{s} \approx 0$ ).

much lower than for water  $\epsilon_b \approx 80$ . Therefore, electrostatic interactions are expected to be negligible here – an assumption that has always been made for capillary suspension studies up to now. However, a recent paper investigated possible electrostatic interactions in the presence of aqueous pendular bridges influencing the sample strength [45]. Therefore, the hypothesis of electrostatic interactions always being negligible in capillary suspensions should be checked in the future. That said, the assumption for vanishing electrostatic interactions should hold in the present work.

### 2.2.3 Gravity and diffusion

The diffusion of a particle due to Brownian motion is directly related to thermal energy  $k_B T$  and is described by the Stokes-Einstein equation

$$D_{\text{diff}} = \frac{k_B T}{6\pi\eta_b a} \quad (2.23)$$

with the diffusion coefficient  $D_{\text{diff}}$  and surrounding bulk liquid viscosity  $\eta_b$  [38]. The time  $t_{\text{diff}}$  that a particle needs to diffuse over a distance equal to its own radius can be calculated as

$$t_{\text{diff}} = \frac{a^2}{D_{\text{diff}}} = \frac{6\pi\eta_b a^3}{k_B T}. \quad (2.24)$$

Sedimentation of particles is a direct result of gravity and the density difference  $\Delta\rho$  between the particle and surrounding liquid. The sedimentation velocity  $v_{\text{sed}}$  of a single particle due to gravity is given by Stokes' law

$$v_{\text{sed}} = \frac{2a^2 g \Delta\rho}{9\eta_b}, \quad (2.25)$$

with the acceleration of gravity  $g$ . The time  $t_{\text{sed}}$  that a particle needs to move over a distance equal to its own radius due to sedimentation also is easily obtained as

$$t_{\text{sed}} = \frac{a}{v_{\text{sed}}} = \frac{9\eta_b}{2ag\Delta\rho}. \quad (2.26)$$

The relative contribution of gravity and diffusion to single particle movement is captured by defining a Péclet number of gravity  $\text{Pe}_{\text{gravity}}$

$$\text{Pe}_{\text{gravity}} = \frac{t_{\text{diff}}}{t_{\text{sed}}} = \frac{4\pi a^4 g \Delta\rho}{3k_B T}, \quad (2.27)$$

which relates both timescales to each other and is a very strong function of the particle size. For  $\text{Pe}_{\text{gravity}} \ll 1$ , particles are able to diffuse freely with no (or negligible) sedimentation occurring due to gravity. For  $\text{Pe}_{\text{gravity}} \gg 1$ , gravity dominates and the particles will settle very quickly without the ability to form a homogeneous suspension assuming that there are no additional stabilizing particle interactions.

#### 2.2.4 Colloidal gels – fractal particle networks

Colloidal suspensions with net attractive interactions, e.g. dominating van der Waals interactions, can form a percolating network of particles spanning the entire sample. Such samples may form through self-assembly by particle aggregation induced purely by particle diffusion, as long as the Péclet number of eq. 2.27 is sufficiently small, but can naturally also be prepared by external mixing. Depending on the depth of the attractive interaction potential minimum (see Fig. 2.4), these colloidal suspensions are either classified as weakly flocculated ( $-\Psi/(k_B T) < 20$ ) or strongly flocculated ( $-\Psi/(k_B T) \geq 20$ ) attractive particle gels [44]. The deeper the potential minimum, the steeper is its slope and, thus, the force necessary to separate attractively bound particles. Rheologically, colloidal particle gels predominantly demonstrate a yield stress and their elastic modulus  $G'$  dominates over the viscous modulus  $G''$ .

To understand the rheology of these attractive networks, the spatial arrangement of particles has to be considered. The remainder of this subsection, dealing with the structure of particle gels, was already published as the theory section in “Fractal approaches to characterize the structure of capillary suspensions using rheology and confocal microscopy” by Frank Bossler, Johannes Maurath, Katrin Dyhr, Norbert Willenbacher and Erin Koos, Journal of Rheology, 62(1), 183-196, 2018 ([hyperlink](#)), copyright SOR, reproduced with permission from SOR [46].

The fractal dimension  $D$  is a parameter used to describe the internal geometry of particle clusters. When fractal clusters consisting of  $N$  particles are formed by aggregation, the cluster radius  $R_c$  scales as

$$N \propto R_c^D \quad (2.28)$$

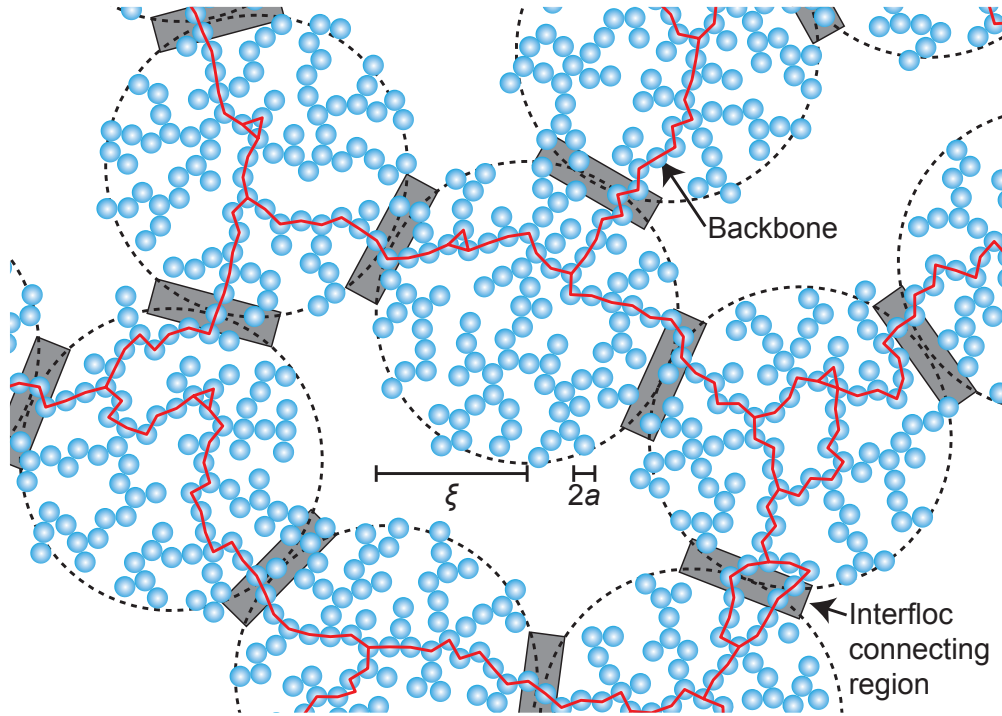
where  $D$  in three-dimensional space can take values of  $1 \leq D \leq 3$  [47, 48]. Counting the number of particles inside a sphere of radius  $R$  and transforming eq. 2.28 to non-dimensional form by normalizing the radial coordinate  $R$  by the particle radius  $a$  directly leads to

$$N\left(\frac{R}{a}\right) \propto \left(\frac{R}{a}\right)^D \quad (2.29)$$

where  $N(R/a)$  is the particle number as function of the normalized radial coordinate  $R/a$  and the center of gyration of the cluster is defined as  $R = 0$  [49].

Different models have classically been used to describe cluster formation kinetics. The diffusion limited (DLCA) and reaction limited cluster aggregation (RLCA) models are distinguished by the sticking probability of each additional particle contacting the cluster. The sticking probability is 1 (every particle sticks to the cluster upon first contact) for DLCA, while it is close to 0 for RLCA (a particle can contact the cluster many times before it finally adheres) [50]. Thus, RLCA clusters have a more densely packed structure than DLCA which is captured by their fractal dimension values. Typically, DLCA clusters have  $D \approx 1.85 \pm 0.1$ , while  $D \approx 2.1 \pm 0.1$  for RLCA in three-dimensional space [50, 51].

Experimental determination of  $D$  by eq. 2.29 is quite straightforward using 3D confocal images of the clustered particles from which the particle positions can be calculated [52]. There are some caveats, however, when a percolated particle network instead of a single particle cluster is evaluated. In this case, different fractal clusters touch and merge into each other. Thus, adjacent clusters that were initially grown separately share particles with each other and the corresponding structure in the overlap regions can no longer be well described by the cluster fractal dimension. The correlation length  $\xi$ , which denotes the maximum length scale before a cluster loses its internal fractality, is a helpful tool to capture this critical overlap. Therefore, eqs. 2.28 and 2.29 are limited to  $R \leq \xi$ . Fig. 2.5 shows an idealized drawing of a particle gel originating from merged clusters where  $\xi$



**Figure 2.5:** Schematic drawing of a percolated network consisting of interconnected clusters (flocs) of particles having radius  $a$ . The large dashed-line circles denote flocs with correlation length  $\xi$  and inter-floc connecting regions are highlighted by the gray shaded areas. A backbone transmitting forces in the particle network is indicated by the thick red lines. While most inter-floc links are part of the backbone, only a minor amount of the total particles inside of a floc contributes to the backbone. Figure reproduced with permission from SOR [46].

is labeled. The correlation length decreases as the number density of particles is increased. For attractive particle gels,  $\xi$  can be directly related to the volume fraction of particles  $\phi_{\text{solid}}$ , defined as the total particle volume divided by the total sample volume, with

$$\frac{\xi}{a} = \phi_{\text{solid}}^{\frac{1}{D-3}} \quad (2.30)$$

which also includes changes to the correlation length with the cluster structure via the dependence on  $D$  [53, 54]. While the cluster fractal dimension  $D$  is often treated as identical to the overall percolated gel fractal dimension, such fractality only holds for length scales smaller than  $\xi$  and the gel appears non-fractal and homogeneous at larger length scales [55]. Using the aforementioned approaches on larger length scales identifies an uncorrelated structure, resulting in  $D = 3$  [54, 55].

Since the concept of fractality was introduced to characterize clustered structures of particles about three decades ago [56], a plethora of scaling theories have emerged that relate the fractal dimension to the rheological properties of attractive particle gels as a function of the particle volume fraction  $\phi_{\text{solid}}$  (e.g. [49, 55, 57–64]). All of these scalings are of a power law type, such that

$$X(\phi_{\text{solid}}) \propto \phi_{\text{solid}}^{f(D)} \quad (2.31)$$

where  $X$  serves here as a placeholder for a rheological property, e.g. yield stress  $\sigma_y$  or elastic modulus plateau  $G_0$ , and the scaling theories mostly differ in the exponent  $f(D)$ , commonly denoted by  $m$ . Piau et al. [58] have proposed a model for the yield stress scaling of particle gels with

$$f(D) \equiv m = \frac{4}{3 - D} \quad (2.32)$$

The model of Piau et al. relates the yielding behavior of the particle gel to the free energy stored in a volume with scale  $\xi$ , which is not related to  $\phi_{\text{solid}}$  via eq. 2.30, but instead via a scaling argument following the method of de Gennes designed for mesh size determinations of semi-dilute polymer gels [65]. While this derivation seems to be somewhat arbitrary, Piau et al. have compared fractal dimensions calculated with their model to fractal dimensions experimentally determined by light scattering methods and found very good agreement. The Piau model has also been successfully applied to particle gels with a broad diversity of material compositions [58, 66–68].

Shih et al. [57] proposed a very different model relating the network structure to the elastic properties of the particle gel, which are represented by two different elastic constants  $K_f$  and  $K_b$ .  $K_f$  is the intra-floc constant characterizing the elasticity inside a cluster of size  $\xi$  and  $K_b$  characterizes the inter-floc or backbone connections between different flocs. The inter-floc connecting regions are highlighted by the gray boxes in Fig. 2.5. Such an inhomogeneous gel structure is specifically expected for intermediate particle volume fraction ranges ( $\phi_{\text{solid}} \approx 0.2\text{--}0.5$ ) [69, 70], which is often the relevant range for capillary suspensions. Following Shih et al., the relative contribution of both elastic constants determines the sign and slope of a scaling exponent  $f(D) \equiv m_\gamma$  where the rheological property  $X$  in eq. 2.31 is the critical strain amplitude  $\hat{\gamma}_{\text{crit}}$  from oscillatory shear rheometry that denotes the end of the linear viscoelastic deformation regime at a given frequency. A second scaling proposed for  $G_0$ , the frequency-independent plateau value of the elastic

modulus  $G'$  in the linear viscoelastic regime, has a scaling exponent  $f(D) \equiv m_G$ . The model of Shih et al. has been further evaluated and extended by Wu and Morbidelli [59], who derived the two scaling exponents as

$$m_\gamma = \frac{2 - \beta_{Wu}}{3 - D} \quad (2.33)$$

$$m_G = \frac{\beta_{Wu}}{3 - D} \quad (2.34)$$

with the parameter  $\beta_{Wu}$  containing information about the relative contributions of intra-floc and backbone elasticities. Eliminating  $\beta_{Wu}$  by combining eqs. 2.33 and 2.34 leads to an expression of  $D$  as a function of both scaling exponents

$$D = \frac{3(m_\gamma + m_G) - 2}{m_\gamma + m_G} \quad (2.35)$$

where  $D$ , following the definitions of eqs. 2.28 to 2.30, is the internal fractal dimension of the flocs.

The model of Piau et al., on the other hand, does not differentiate between the flocs and backbone as this theory originates from semi-dilute polymer network mesh sizes (i.e. small  $\phi_{solid}$  for particle gels). Ergo, this model assumes the presence of a homogeneous backbone that resembles the structure of such polymer gels rather than densely packed flocs. Therefore, the corresponding fractal dimension calculated from Piau's model is not expected to be the same  $D$  as calculated from the other rheological models, but should rather correspond to a “backbone dimensionality” on larger length scales. This implies, then, a fractal network of clusters where the clusters of size  $\xi$  are the basic building blocks. Thus,  $\xi$  is the lower instead of the upper length scale for the fractal structure of the network backbone [71].

## 2.3 Wetting on a solid

The formation of capillary bridges between particles and the shape that these will form can be understood based on some fundamental concepts of wetting of a liquid on a solid surface. The main physical properties involved in wetting are the different interfacial energies per wetted area, i.e. the interfacial tensions  $\Gamma$ , between two fluids as well as between each fluid and the solid. These energies determine the contact angle  $\theta$ .

### 2.3.1 Interfacial tensions and the three-phase contact angle

The Gibbs free energy  $G$  of a two-phase system is given by its exact differential

$$dG = Vdp - SdT + \sum_k \mu_k dn_k + \Gamma dA \quad (2.36)$$

with volume  $V$ , pressure  $p$ , entropy  $S$ , temperature  $T$ , chemical potential  $\mu$  of component  $k$ , amount of substance  $n$ , interfacial energy  $\Gamma$  and area  $A$  of the interface between both phases. Therefore, the interfacial energy is the partial derivative of the Gibbs free



energy with respect to the interfacial area at constant pressure, temperature and amount of substance

$$\Gamma = \left( \frac{\partial G}{\partial A} \right)_{p,T,n} \quad (2.37)$$

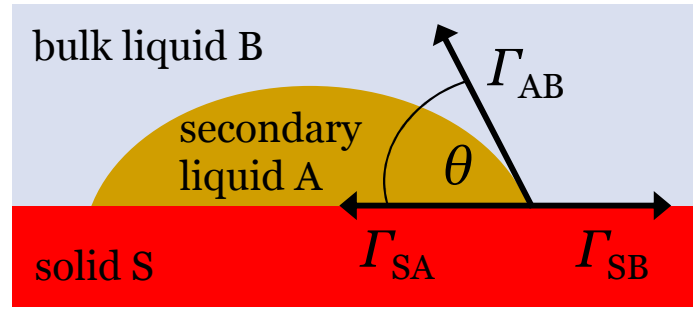
and is a measure for the amount of work necessary to increase the interfacial area. In the case of a liquid-liquid interface, the interfacial energy more commonly is termed interfacial tension. For the case of curved interfaces with principle curvatures  $R_1$  and  $R_2$ , a pressure difference between the phases occurs,

$$\Delta p = \Gamma \left( \frac{1}{R_1} + \frac{1}{R_2} \right) \quad (2.38)$$

where the pressure difference  $\Delta p$  is termed Laplace pressure. For spherical droplets with radius  $a_{\text{drop}} \equiv R_1 = R_2$  the Laplace pressure simplifies to

$$\Delta p = \frac{2\Gamma}{a_{\text{drop}}}. \quad (2.39)$$

In a three-phase system, three different interfacial energies exist from the pairwise combinations between the phases. A schematic drawing of a solid-liquid-liquid arrangement is shown in Fig. 2.6 where the three interfacial energies are also depicted. A balance



**Figure 2.6:** Schematic drawing of a solid-liquid-liquid arrangement of a droplet of secondary fluid “A” residing on a flat surface of the solid “S” surrounded by a bulk liquid “B”. The secondary fluid droplet forms the three-phase contact angle  $\theta$  towards the solid. Also depicted are the interfacial energies  $\Gamma_{SB}$  between solid and bulk liquid,  $\Gamma_{SA}$  between solid and secondary liquid and  $\Gamma_{AB}$  between both liquids. The latter is commonly termed the interfacial tension  $\Gamma \equiv \Gamma_{AB}$ . The bulk liquid may also be air. In this case,  $\Gamma_{AB}$  is called the surface tension of the liquid A.

of the three interfacial energies at the three-phase contact line directly leads to

$$\Gamma_{SB} = \Gamma_{SA} + \Gamma_{AB} \cos \theta \quad (2.40)$$

with definitions as given in Fig. 2.6, including the three-phase contact angle  $\theta$ . Converting this balance leads to

$$\cos \theta = \frac{\Gamma_{SB} - \Gamma_{SA}}{\Gamma_{AB}}, \quad (2.41)$$

which is commonly known as Young equation [72].

The Young equation is only valid for an ideal solid surface that is defined as rigid, smooth, chemically homogeneous, insoluble and non-reactive [72]. For non-ideal surfaces, corrections to the Young equation have to be applied, which leads to contact angles

different from the thermodynamically predicted Young contact angle  $\theta_{\text{Young}}$  of equation 2.41.

For rough, solid surfaces the actual surface  $A_{\text{actual}}$  is increased compared to its projection (i.e. the ideal flat surface  $A_{\text{flat}}$ ). The equation of Wenzel takes this effect into account,

$$\cos\theta_{\text{Wenzel}} = \frac{A_{\text{actual}}}{A_{\text{flat}}} \cos\theta_{\text{Young}} \quad (2.42)$$

where the Wenzel contact angle  $\theta_{\text{Wenzel}}$  is the apparent contact angle that forms on the rough surface [73]. The Wenzel equation assumes homogeneous wetting, i.e. full wetting of the entire surface area and all asperities of the rough surface. In case of heterogeneous wetting (i.e. some air or other fluid “2” being trapped in some asperities, which are not wet by the main wetting fluid “1”) the equation of Cassie-Baxter has to be used instead [74]. The same equation also has to be used for wetting on chemically inhomogeneous surfaces. For the case of the surface showing two different chemical properties with partial areas  $A_1$  and  $A_2$ , respectively, the Cassie-Baxter equation reads

$$\cos\theta_{\text{CB}} = \frac{A_1}{A_{\text{actual}}} \cos\theta_1 + \frac{A_2}{A_{\text{actual}}} \cos\theta_2 \quad (2.43)$$

with the apparent Cassie-Baxter angle  $\theta_{\text{CB}}$  and the respective Young contact angles  $\theta_1$  and  $\theta_2$  of the liquid on homogeneous surfaces of chemical type “1” or “2” [75].

While  $\theta_{\text{Young}}$ ,  $\theta_{\text{Wenzel}}$  and  $\theta_{\text{CB}}$  denote thermodynamic equilibrium angles at rest, different contact angles will appear during the process of wetting or de-wetting of a solid [76], which also strongly depend on the local surface geometry [77]. The angle during wetting, termed the advancing contact angle  $\theta_{\text{adv}}$ , is higher than the equilibrium angle  $\theta_{\text{eq}}$ , while the angle during de-wetting, termed the receding contact angle  $\theta_{\text{rec}}$ , is lower than the equilibrium angle. The most stable apparent contact angle may be calculated as the mean angle between advancing and receding angles,  $(\theta_{\text{adv}} + \theta_{\text{rec}})/2$  [72], but this approach is not valid in all cases [78]. While the most stable apparent contact angle should also be the equilibrium angle  $\theta_{\text{eq}}$ , there also exist some other energetically metastable contact angles where the Gibbs energy exhibits a local, but not global minimum. These local minima, however, will lead to the appearance of a variety of such metastable contact angles  $\neq \theta_{\text{eq}}$  in the range of the hysteresis for a real system even when the system is at rest [72]. The angles  $\theta_{\text{Young}}$ ,  $\theta_{\text{Wenzel}}$  and  $\theta_{\text{CB}}$  are all equilibrium angles in the global Gibbs energy minimum. Therefore, they are not directly affected by the contact angle hysteresis, but without information on the hysteresis, they alone will not be sufficient to explain the whole appearance of a wetted structure [72]. The range of the hysteresis can be fairly large. Hystereses in the range of  $\theta_{\text{eq}} \pm 20^\circ$  are easily found in literature [e.g. 79].

In addition to the aforementioned effects, contact line pinning, i.e. an increased resistance of the three-phase contact line against moving, can appear. Besides the surface inhomogeneities and roughness, this line pinning is also related to the contact line energy itself [78, 80]. The main effects of contact line pinning are a broadening of the contact angle hysteresis and a shift in the value of the most stable contact angle.

Further, the contact angle that forms on a particle length scale may be different to the macroscopic contact angle measured for a large drop and flat surface of identical materials. This is due to an effect of the solid surface curvature on the line tension [81], but also due to the Wenzel and Cassie-Baxter equations losing validity if the length scale

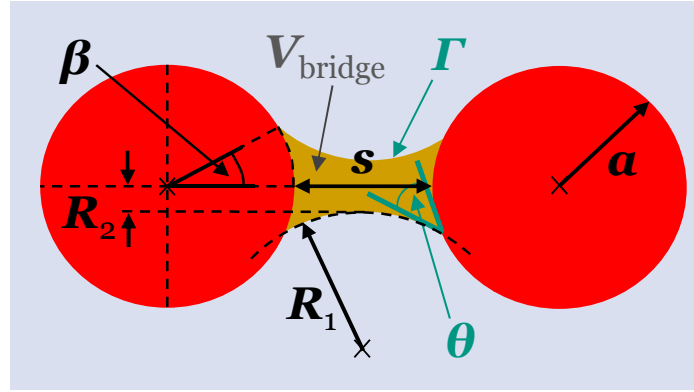


of roughness or chemical heterogeneity approaches the length scale of total wetted area [82]. In this case, the path of the contact line, not just the contact area, must be considered [82, 83].

Practically, all of these issues have to be taken as a caveat when measuring contact angles with common methods, e.g. sessile drop measurements on a millimeter length scale, and then attempting to directly transfer the measured contact angles to angles appearing in, e.g., a tiny capillary bridge between two micron-sized particles. In such capillary bridges, the bridges' individual contact angles will influence the particle interaction, as will be described in the following subsection.

### 2.3.2 Capillary forces

To calculate the capillary force between two particles connected by a pendular bridge, it is necessary to be acquainted with the bridge geometry. Fig. 2.7 shows a schematic drawing of a capillary bridge between two equisized spherical particles. The capillary force



**Figure 2.7:** Geometry of a rotationally symmetric concave capillary bridge (dark yellow) between two equisized spherical particles (red). The bridge volume  $V_{\text{bridge}}$  and the resulting capillary force between the particles are determined by wetting properties, namely the three-phase contact angle  $\theta$  and interfacial tension  $\Gamma$  as well as geometric parameters, namely particle radius  $a$ , particle surface distance  $s$ , the half-filling angle  $\beta$  that defines the position of the three-phase contact line and the principle radii of curvature of the bridge,  $R_1$  and  $R_2$ .

depends on the particle radius, the interfacial tension between the fluids, the wetting properties of both liquids, comprised by the three-phase contact angle that the secondary fluid forms towards the particles in a bulk liquid environment and the geometry of the bridge. The capillary force  $F_c$  in a concave bridge of volume  $V_{\text{bridge}}$  between two equally sized spherical particles with surface separation  $s$  can be computed either by solving the Young-Laplace equation or by assuming a certain bridge shape. Typically, the attraction energy between such particles connected by the capillary force is many times higher than thermal energy  $k_B T$  [84]. Accordingly, the capillary force is then orders of magnitude higher than the van der Waals force [2], as well as gravity [85].

Predominantly, a toroidal bridge shape is assumed, which enables the bridge surface shape to be described solely by two principal radii of curvature,  $R_1$  and  $R_2$ , as depicted in Fig. 2.7. While the exact expected surface shape of a pendular bridge is rather nodoidal [86], the toroidal shape assumption is very commonly applied as it makes calculations

more comfortable without introducing serious errors. The toroidal approximation leads to errors in the calculation smaller than 10 % for concave bridges [87]. A straightforward equation to calculate the capillary force  $F_c$  in a toroidally-shaped bridge was proposed by Pietsch and Rumpf [88]

$$F_c = -2\pi\Gamma a \sin\beta \left[ \sin(\beta + \theta) + \frac{a}{2} \left( \frac{1}{R_1} - \frac{1}{R_2} \right) \sin\beta \right] \quad (2.44)$$

with the parameters used as labeled in Fig. 2.7. This equation is only valid for zero particle distance  $s = 0$ . The attractive capillary force is comprised of two contributions, which can be distinguished in equation 2.44. The first summand on the right hand side of the equation results from the interfacial tension of the bridge acting at the three-phase contact line and is always attractive. The second summand results from the Laplace pressure, the sign of which depends mainly on the sign of the curvature  $R_1$ . For convex bridges, the pressure in the bridge is negative as long as  $1/R_1 > 1/R_2$ . This leads to an additional attractive contribution to the capillary force between the particles. For  $1/R_1 < 1/R_2$ , the pressure in the bridge is larger than outside and thus its contribution to the force will become repulsive. This is especially true for all convex bridges, which only can induce attractive inter-particle forces in cases where the interfacial tension term dominates over the Laplace pressure term [89]. Usually, the Laplace pressure term, however, is significantly larger than the interfacial tension term.

A different equation to calculate the capillary force in good approximation, including the particle surface separation  $s$  and also based on assuming a toroidal bridge shape, is given by [90, 91]

$$F_c = -f(V_{\text{bridge}}, s, a) \cdot 2\pi\Gamma a \cos\theta = -\frac{2\pi\Gamma a \cos\theta}{\left(1 + 1.05s\sqrt{\frac{a}{V_{\text{bridge}}}} + 2.5s^2\frac{a}{V_{\text{bridge}}}\right)}, \quad (2.45)$$

where the interfacial tension term acting at the three-phase contact line is neglected. The geometric function  $f(V_{\text{bridge}}, s, a)$  can also be converted by using the relative bridge volume  $\tilde{V}_{\text{bridge}} = V_{\text{bridge}}/a^3$  and relative particle separation  $\tilde{s} = s/a$ , leading to

$$f(V_{\text{bridge}}, s, a) = f(\tilde{V}_{\text{bridge}}, \tilde{s}) = \frac{1}{1 + 1.05\sqrt{\frac{\tilde{s}^2}{\tilde{V}_{\text{bridge}}}} + 2.5\frac{\tilde{s}^2}{\tilde{V}_{\text{bridge}}}}. \quad (2.46)$$

From this equation, it is obvious that  $f(\tilde{V}_{\text{bridge}}, \tilde{s})$  monotonically decreases with increasing  $\tilde{s}$  and, thus, becomes maximal for  $\tilde{s} = 0$ . Following eq. 2.45, the capillary force is also largest when the particle surface distance is zero. In this case,  $f(\tilde{V}_{\text{bridge}}, 0) = 1$  and the force equation 2.45 simplifies to

$$F_c = -2\pi\Gamma a \cos\theta, \quad (2.47)$$

which denotes the maximum possible capillary force that will appear if full surface contact of the particle pair is not otherwise constricted, e.g. by other adjacent particles. The equations for the force may, with slight modification, also be applied for spheres of different size using a Derjaguin approximation [90]. Furthermore, different particle shapes or surface roughnesses can be introduced into the calculations [92, 93].

Calculations of the bridge volume are feasible using a set of equations by Megias-Alguacil et al. [94]. Using the nomenclature of parameters as in Fig. 2.7, the volume is given by

$$\begin{aligned} \frac{V_{\text{bridge}}}{2\pi} = & [(R_1 + R_2)^2 + R_1^2] x_a - \frac{x_a^3}{3} - (R_1 + R_2) \left[ x_a \sqrt{R_1^2 - x_a^2} + R_1^2 \arcsin \frac{x_a}{R_1} \right] \\ & - \frac{(x_a - \frac{s}{2})^2}{3} \left[ 3a - \left( x_a - \frac{s}{2} \right) \right] \end{aligned} \quad (2.48)$$

where  $x_a$  is the length of the spherical cap formed by the bridge on the particle

$$x_a = \frac{s}{2} + a - a \cos \beta, \quad (2.49)$$

and the radii of curvature  $R_1$  and  $R_2$  needed to solve the equation are calculated as

$$R_1 = \frac{ax_a}{\left(\frac{s}{2} + a - x_a\right) \cos \theta - \sqrt{a^2 - \left(x_a - \frac{s}{2} - a\right)^2} \sin \theta} \quad (2.50)$$

$$R_2 = \sqrt{a^2 - \left(x_a - \frac{s}{2} - a\right)^2} + x_a \frac{\sqrt{a^2 - \left(x_a - \frac{s}{2} - a\right)^2} \cos \theta + \left(\frac{s}{2} + a - x_a\right) \sin \theta - a}{\left(\frac{s}{2} + a - x_a\right) \cos \theta - \sqrt{a^2 - \left(x_a - \frac{s}{2} - a\right)^2} \sin \theta}. \quad (2.51)$$

Therefore, eqs. 2.48 to 2.51 enable the toroidal capillary bridge volume to be calculated as a function of the particle radius, particle surface separation, the half-filling angle and the contact angle. If the normalized bridge volume  $\tilde{V}_{\text{bridge}}$  is calculated, with an appropriate modification of these equations, the only three remaining independent parameters are the relative surface separation  $\tilde{s}$  and the angles  $\beta$  and  $\theta$ .

### 2.3.3 Wet granular materials

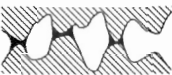
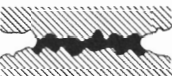
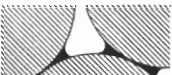

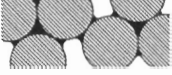
One popular class of materials whose properties are dominated by the capillary force are wet granular materials. They typically consist of a pile of particles, surrounded by air, to which a wetting fluid is added. One of the most well-known examples is sand castles, which can be formed when water is added to a dry pile of sand grains [91]. The effect of the water on the material strength is obvious. It is a direct result from the formation of capillary bridges and related structures, which induce attractive capillary forces between the grains. While there are some special cases of wet granular matter where the surrounding bulk medium is another liquid instead of air, the added fluid is preferentially wetting ( $\theta < 90^\circ$ ) in all cases, independent of the bulk medium. Most theories on wet granular material physics just assume perfect wetting, i.e.  $\theta = 0^\circ$  [85].

Due to their typical particle sizes in the millimeter or upper micrometer range and the large density difference between these grains and the surrounding air, granular materials are strongly dominated by gravity and always have very high solid volume fractions a few percent below random close packing, which for spherical particles is at  $\phi_{\text{solid}} \approx 0.64$  [85]. Their mean coordination number  $z$ , i.e. the number of contact points of zero surface distance that an average particle forms with any adjacent particles, is typically around  $z = 6$

or slightly larger [95]. The exact solid volume fraction and coordination number depends on the particle shape, size distribution and on the friction coefficient  $\mu$  between the grains [85]. Additionally, compaction by tapping or other external forces is possible. Random close packing of  $\phi_{\text{solid}} = 0.64$  only appears for quasi-frictionless particles. An increase in the friction coefficient to more physically realistic values around  $\mu = 0.5$  reduces the particle packing density and, thus, also particle volume fraction of samples made with monodisperse spherical particles to lower random loose packing values around  $\phi_{\text{solid}} = 0.58$  [96]. The same is true for the coordination number, which is similarly reduced to values around 4.5–5 [96]. For wet granular materials, packing fractions are slightly lower than for dry granular piles, but still are very high at the same coordination number. Typical values are  $0.52 < \phi_{\text{solid}} < 0.61$  and  $5.5 < z < 7.5$  for wet and  $0.58 < \phi_{\text{solid}} < 0.61$  and  $5.5 < z < 7$  for dry granular matter [97].

The morphology of wet granular matter depends on the amount of added wetting fluid, captured by  $W$ , which is the ratio of the volume of added wetting fluid to the total volume of the wet granular pile that encompasses the volumes of grains, added liquid and interstitial air. Accordingly,  $W$  can take values in the range  $0 < W < 1 - \phi_{\text{solid}}$ , where the sample at  $W = 0$  is a dry granular pile and  $W = 1 - \phi_{\text{solid}}$  is a densely packed two-phase particle suspension with no remaining interstitial air. Figure 2.8 shows a schematic overview of the different regimes of wetness of a granular pile as function of  $W$ . The following explanation uses the definitions and nomenclature of these systems as proposed by Herminghaus [85].

In the humidity regime, only very small amounts of wetting liquid are present. This

wetness regime		morphology	liquid content
humidity	asperities		$W = 0.0$ to 0.026
	roughness		
pendular			clusters 0.026 to 0.08 bicontinuous 0.08 to 0.28 0.28 to saturation
funicular			
bubbles			

**Figure 2.8:** The different regimes of wetness of a granular pile using the nomenclature of Herminghaus. The figure has been reproduced from [85] with permissions from Stephan Herminghaus and from World Scientific Publishing Co., Inc.

leads to micro-bridges of fluid between contacting grains, where the peaks of any asperities (asperity regime) or larger regions of the rough surface between the grains (roughness regime) are wetted, but no fully established capillary bridges of relevant volume and defined shape can be optically detected yet. The asperity and roughness regime cannot be experimentally discriminated. At some fluid content  $W_{cb}$ , capillary bridges start to form. The number and volume of the bridges increases with increasing fluid content in this pendular regime [98] until the transition to the so-called funicular regime is reached at a critical fluid content  $W^* \approx 0.026$ , as can be calculated from capillary bridge volume equations assuming  $\phi_{solid} = 0.6$  [85] and as also will be shown below in Fig. 2.9. In the funicular regime, particles are not solely interconnected by binary capillary bridges, but also by larger fluid volumes connecting more than two particles. The funicular regime itself can be split into a cluster regime and a bicontinuous regime, the latter one denoting that the whole amount of added wetting liquid becomes interconnected to form just a single, large fluid entity spanning the entire sample, while the interstitial air is also fully percolating through the sample as one single interconnected volume entity at the same time. In the bubble regime, the air no longer spans the sample, but is separated into several smaller bubbles. In the classical theories of Rumpf, the bubble regime is followed by the so-called capillary state, where the whole interstitial space between the particles is filled with the liquid, but the outer surface of some larger, wet agglomerates still exhibits an interface between the liquid and surrounding air [99]. This state is typically what is formed when sand castles are created by allowing the water to drain from fully saturated sand.

In the funicular regime, there exists a large variety of possible shapes for the interconnecting fluid entities [100]. However, most of the properties can simply be determined by regarding the fluid volumes of the funicular regime as interconnected structures that just consist of individual binary capillary bridges glued together at their outer perimeters [85]. As will be thoroughly discussed in section 6.1.1, single binary bridges in the pendular state can have any half-filling angle  $\beta < 30^\circ$ , while the interconnected bridge structures in the funicular state all should show, in good approximation,  $\beta \approx 30^\circ$  when they have merged at their outer perimeters [85, 101, 102]. This has consequences on the Laplace pressure in the fluid entities, which can be calculated from equation 2.38 for toroidal bridges with radii  $R_1$  and  $R_2$  as depicted in Fig. 2.7. With the toroidal approximation, the Laplace pressure as function of  $\beta$  and  $\theta$  is [85]

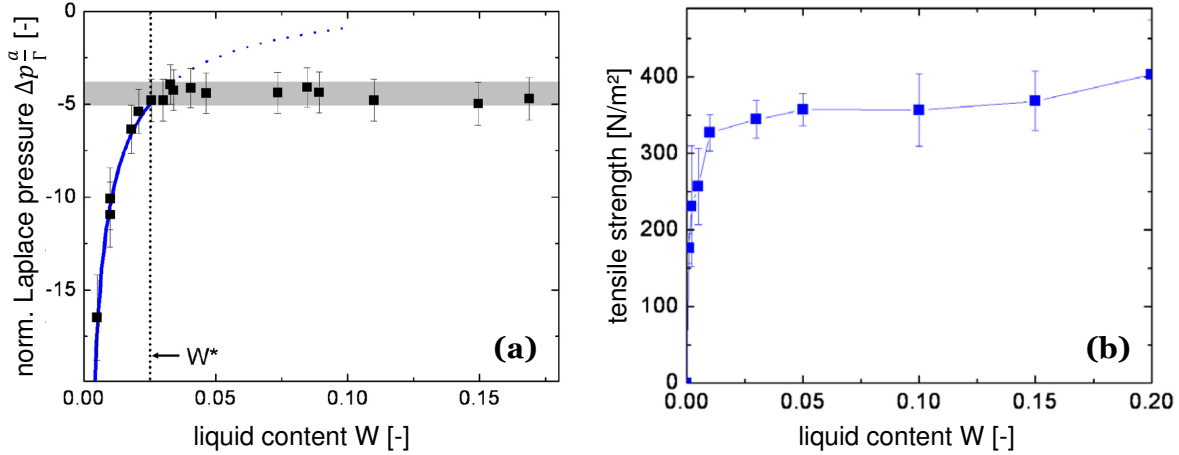
$$\Delta p(\beta, \theta) = \frac{\Gamma}{a} \left( \frac{1}{\sin \beta} + \frac{\cos(\theta + \beta)}{1 - \cos \beta} \right) \quad (2.52)$$

where  $|\Delta p|$  is monotonically decreasing with increasing  $\beta$  (increasing bridge volume) when  $\theta$  is fixed. Assuming  $\theta = 0^\circ$  and  $\beta = 30^\circ$ , this leads to

$$\Delta p(30^\circ, 0^\circ) \approx -4.46 \frac{\Gamma}{a}. \quad (2.53)$$

It is important to note, that the Laplace pressure does not depend directly on the volume of the bridge, but solely on its radii of curvature, which is the same for a single binary bridge with a  $30^\circ$  half-filling angle as for a funicular structure where many such bridges of  $30^\circ$  half-filling angle are glued together at their perimeter. Thus, the Laplace pressure in the funicular regime is expected to be independent of the amount of added fluid  $W$ , with

a value given by eq. 2.53. For the pendular state, where the volumes of individual bridges increase, i.e.  $\beta$  also increases for fluid amounts  $W_{cb} < W < W^*$ , a steady decrease in the magnitude of Laplace pressure is expected. Fig. 2.9a shows an experimental proof of both of these expectations, with data provided by Scheel et al., who measured the Laplace pressure over a broad range of  $W$  [97, 101].



**Figure 2.9:** Experimental determination of (a) Laplace pressure normalized by interfacial tension and particle radius and (b) tensile strength in wet granular materials as a function of the amount of added wetting liquid  $W$ . In both diagrams, the transition from pendular to funicular regime takes place at  $W^* \approx 0.026$ . The black points in (a) denote the experimental results, while the gray shaded area represents eq. 2.53 with an uncertainty of  $\theta = 0 - 10^\circ$  included and the blue line denotes eq. 2.52 for  $\theta = 0^\circ$ . The diagram (a) was reproduced from [97] ("Figure 4.8a" of the original text by M. Scheel, used under CC BY-NC-ND 3.0 / Axes relabeled), and diagram (b) from [100] ([hyperlink](#)), reproduced with permission of IOP Publishing in the format Thesis/Dissertation via Copyright Clearance Center.

The capillary force between the grains also depends on  $\beta$  and  $\Delta p$  (see eq. 2.44). Thus, the capillary force between individual grains should also be independent of  $W$  in the funicular regime. This is clearly shown from measurements of the tensile strength, which is the stress necessary to rupture a sample by external forces. Such sample rupture necessitates pulling apart the particles until elongational breakup of the capillary bridges occurs and, therefore, directly depends on the capillary force counteracting the rupturing forces. Fig. 2.9b shows an experimental determination of the tensile strength of a wet granular material as function of  $W$ . The independence of the tensile strength on  $W$  in the funicular regime ( $W > 0.026$ ), is readily apparent due to constant Laplace pressures and capillary forces.

An independence on the wetting, similar to that found for the tensile strength, may also be expected for the yield stress resisting a shearing force in wet granular materials. However, this is not completely true because of the high solid volume fractions. Due to the high packing, the densely packed sample is mechanically frustrated and the particles cannot easily move relative to each other during shear. This results in a combination of two forces counteracting the shear (as is comparable to the rheological response of colloidal suspensions in a glassy state at high volume fractions [38]). Thus, the total shear stress has a contribution  $\sigma_{cb}$  from the capillary force as well as from the interparticulate



solid-solid friction, represented by a stress  $\sigma_\mu$  [85]. The yield stress  $\sigma_y$  can be estimated as the sum of both contributions. Herminghaus proposed a calculation for the yield stress as function of solid and fluid volume fractions, coordination number, interfacial tension, contact angle, particle radius and friction coefficient [85]

$$\sigma_y = \sigma_{cb} + \sigma_\mu = \frac{\Gamma}{a} \phi_{\text{solid}} z \cos \theta \left( 4.37 P_r \sqrt{\frac{3W}{8\pi\phi_{\text{solid}}z}} + \frac{\mu}{2} \right), \quad (2.54)$$

where  $P_r$  is the probability that a capillary bridge will rupture when the sample experiences a shear deformation of  $\gamma = 1$ , which is typically close to unity. Estimations, with typical values for wet granular matter ( $\phi_{\text{solid}} = 0.6$ ,  $z = 6$ ,  $W = W^*$ ), show that the contributions of capillary force and friction to the yield stress are both in the same order of magnitude and, thus, of equal, non-negligible importance in such systems [85].

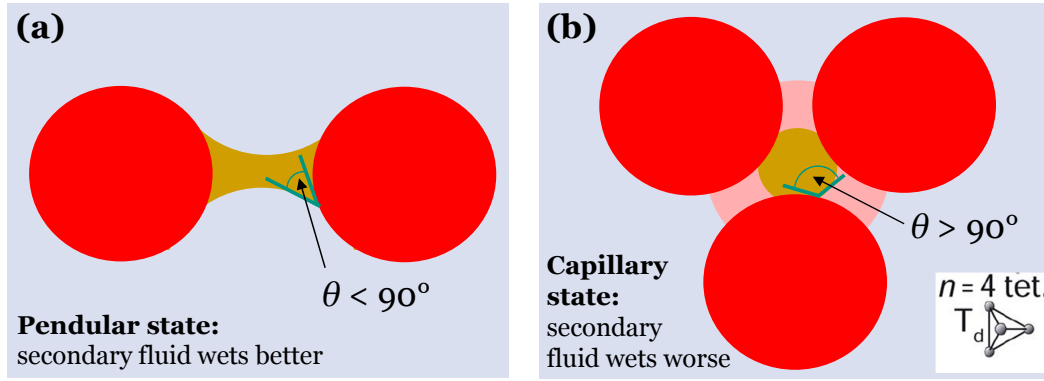
## 2.4 Capillary suspensions

Capillary suspensions are solid-liquid-liquid systems, which can appear in two different morphological occurrences called the pendular and capillary states [1]. Their localization in a solid-liquid-liquid ternary diagram was already introduced in the schematic diagram of Fig. 1.2, where they form the boundaries of this diagram at intermediate solid loadings. Similar ternary diagrams, which include the influence of the three-phase contact angle, have been researched by Velankar and coworkers and different ternary structures were additionally imaged by surface electron microscopy. Such a diagram for  $\theta = 0^\circ$  is found in reference [103], while reference [29] gives a ternary diagram for an unknown contact angle that is far away from  $0^\circ$  but smaller than  $90^\circ$ . Capillary suspensions are distinguished from other, well-known ternary systems (e.g. wet granular matter, Pickering emulsions [104, 105] and Bijels [106]) primarily by the relative amounts of secondary fluid and particles. The overall secondary fluid volume fraction  $\phi_{\text{sec}}$  is small compared to the volume fraction of dispersed solid particles  $\phi_{\text{solid}}$  in capillary suspensions and is much smaller than the fraction of bulk liquid [27].

### 2.4.1 Pendular and capillary state

Capillary suspensions can be formed when either the secondary phase wets better than the bulk phase, which is referred to as pendular state, or when it wets less well in the capillary state. In both cases, a percolating particle network arises, leading to a transition in rheological properties due to network formation [1]. Correspondingly, capillary suspensions can be regarded rheologically as attractive particle gels.

The basic building blocks of capillary suspension structures are sketched in Fig. 2.10. When the secondary fluid wets better than the bulk fluid, the three-phase contact angle  $\theta$  is smaller than  $90^\circ$ . For small bridge volumes, this enables a binary bridge with concave shape to form and therefore the pendular state as depicted in Fig. 2.10a. The bridge shape for contact angles larger than  $90^\circ$  would geometrically have to be convex, leading to a positive Laplace pressure and particle repulsion, especially at short particle distance [89]. No stable, symmetric binary bridges can be expected under these circumstances, but other stable micro-clustered particle-droplet arrangements, as exemplified



**Figure 2.10:** Schematic drawings of the basic building blocks for (a) pendular state and (b) capillary state structures. For reasons of visibility, particle surface distances are drawn unrealistically large. In the pendular state, two particles (red) are interconnected by a bridge of secondary fluid (dark yellow). In the capillary state, the easiest possible building block is a tetrahedron of four particles shielding a droplet of secondary fluid that is in the center between the particles. Also for reasons of visibility, the fourth particle only is indicated in pale color in the background. The inset in (b) shows a schematic sketch of a tetrahedron.

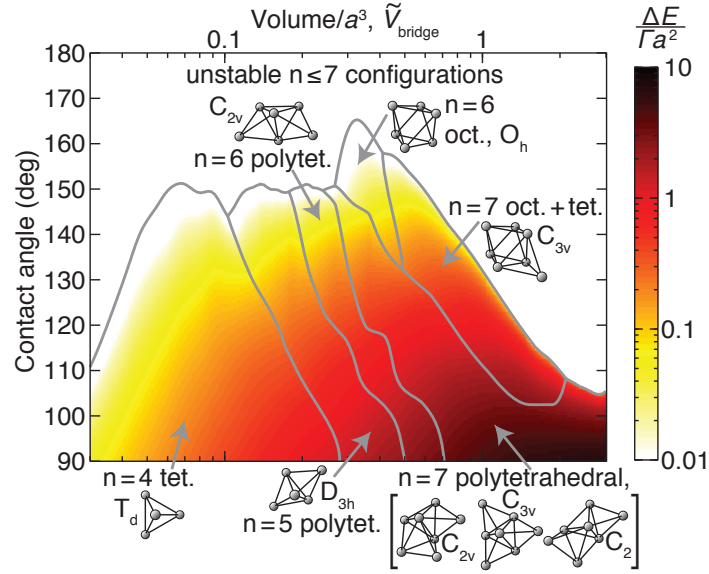
for the capillary state tetrahedron of Fig. 2.10b, may occur. Therefore, the transition between pendular and capillary state is expected at approximately  $90^\circ$ . For larger bridge volumes, it should take place at smaller contact angles due to the curvature of the particle surface [94].

In the capillary state, as was calculated numerically, small secondary phase droplets serve as a center for tetrahedral, octahedral, or other clusters with small numbers of particles surrounding the secondary fluid drop due to energetic reasons [8, 30]. The binary, bridged particles of the pendular state or the small clusters of the capillary state serve as generic building blocks for the formation of sample-spanning networks. The energetic favorabilities of different basic building blocks in the capillary state have been calculated as function of contact angle and normalized secondary fluid droplet volume by Koos et al. [8], as shown in Fig. 2.11. The tetrahedron presented in Fig. 2.10b is the easiest, but not the only possible micro-cluster configuration. With larger volumes of the central secondary fluid droplet, building blocks with larger particle numbers are energetically more favorable. The formation of capillary suspensions becomes impossible for contact angles  $\theta > 150 - 165^\circ$  [8]. Network percolation in the capillary state with increasing amounts of secondary phase content was calculated numerically by Fortini [30]. However, experimental proof and visualization of this structure had not yet been achieved prior to the present thesis.

It is important to note that the capillary state of a capillary suspension is obviously different in structure to the capillary state in wet granular matter mentioned in section 2.3.3. So, although both structures share a name, they must not be conflated. The pendular state is unproblematic on that score, as it is equally defined in both classes of materials.

In capillary suspensions, the pro-rata composition of the solid and two liquid phases is described by the solid volume fraction  $\phi_{\text{solid}}$ , defined as the ratio of the solid volume to the total sample volume, and by the secondary fluid volume fraction  $\phi_{\text{sec}}$  that is analogously defined as ratio of the secondary fluid volume to the total sample volume. Essentially,  $\phi_{\text{sec}}$  of capillary suspensions is identical to the property  $W$  of the previously described





**Figure 2.11:** Energetically favorable basic building blocks consisting of 4 – 7 particles for capillary suspensions in the capillary state, numerically calculated as function of the relative secondary fluid droplet volume and the contact angle. The figure is reproduced from [8] ([hyperlink](#)) with permission of The Royal Society of Chemistry.

wet granular materials (section 2.3.3). Alternatively, the amounts of bulk and secondary fluid can also be expressed by the saturation  $S$ , which is defined as the ratio of the better wetting fluid volume to the sum of both fluid volumes [7]

$$S = \frac{V_{\text{better wetting fluid}}}{V_{\text{bulk fluid}} + V_{\text{secondary fluid}}} \quad (2.55)$$

where the better wetting fluid is either the bulk or the secondary fluid. The saturation takes values in a range of  $0 < S \lesssim 0.1$  for the pendular state, where only a small amount of better wetting liquid is added. The saturation is  $0.9 \lesssim S < 1$  in the capillary state, where the less wetting liquid is the secondary fluid and the better wetting bulk represents the majority of the liquid volume.

### 2.4.2 A system between wet granular materials and colloidal gels

Capillary suspensions share some commonalities with other attractive colloidal particle gels, introduced in chapter 2.2.4, as well as with wet granular materials, detailed in chapter 2.3.3. All three of these systems are generally based on a percolating particle network stabilized by attractive interactions, while simultaneously each system is fundamentally distinct. Table 2.1 provides a comparison of their main features, where the most obvious difference is in the composition. Two-phase colloidal gels without secondary fluids typically have van der Waals forces as the dominant attractive interparticle forces, while capillary suspensions and wet granular matter have an additional third, liquid phase and thus share the capillary force as the dominant interaction. This allows many of the concepts and equations presented in the previous chapter 2.3 to also be applied to capillary suspensions. On the other hand, colloidal gels and capillary suspensions both have a liquid

**Table 2.1:** Comparison between basic properties of colloidal particle gels, capillary suspensions and wet granular materials.

	Colloidal network	Capillary suspension	Wet granular material
<b>Composition</b>	Solid–liquid	Solid–liquid–liquid	Solid–gas–liquid
<b>Main attractive force</b>	Van der Waals	Capillary	Capillary
<b>Bulk transmits force</b>	Yes	Yes	No
<b>Particle size</b>	$a < 1 \mu\text{m}$	$0.5 \mu\text{m} < a < 50 \mu\text{m}$	$a \gg 10 \mu\text{m}$
<b>Péclet number</b>	$\text{Pe}_{\text{gravity}} \ll 1$	$\text{Pe}_{\text{gravity}} > 1$	$\text{Pe}_{\text{gravity}} \gg 1$
<b>Solid volume fraction</b>	$\phi_{\text{solid}} < 0.15$	$0.1 < \phi_{\text{solid}} < 0.45$	$0.52 < \phi_{\text{solid}} < 0.64$
<b>Fractal structure</b>	Often	Not known yet	No ( $D = 3$ )

continuous phase, in contrast to air in wet granular matter. Therefore, the bulk can transmit viscous and hydrodynamic forces in colloidal gels and capillary suspensions, which is impossible via the gaseous phase of wet granular matter. Finally, the density difference between bulk and particles is reduced in capillary suspensions and colloidal gels compared to wet granular materials. Both of these features enable the preparation of colloidal and capillary suspensions at lower particle volume fractions. The high volume fraction in wet granular matter is attributed to the packing of dry granular piles and cannot be significantly reduced.

The possible range of solid volume fractions is also closely related to the typical particle size range. Wet granular matter usually contains particles  $> 50 \mu\text{m}$ , though the relevant physics have been shown in some elaborate experiments using liquid nitrogen as wetting liquid to be valid down to particle sizes of at least  $10 \mu\text{m}$  [85]. Regardless, the particle size in wet granular matter is large enough to ignore van der Waals force contributions. Colloidal particle gels, on the other hand, require these attractive van der Waals forces (or any other short-ranged attractive interactions) to form percolating networks and are therefore typically limited to very small particle sizes in the submicron range [38]. Particle sizes in capillary suspensions are typically in the range of  $1\text{--}10 \mu\text{m}$  [2], with only few exceptions having smaller (e.g. [19]) or larger (e.g. [21]) sizes, closing the gap between colloidal gels and wet granular matter.

In this intermediate size range, the movement of single particles is mainly governed by gravity, as captured by the Péclet number in equation 2.27, while their interactions still experience a small contribution from the van der Waals force. This, in combination with the aforementioned density difference and bulk forces, directly leads to the intermediate solid volume fraction range for capillary suspensions that lie between the high volume fractions  $\phi_{\text{solid}} > 0.52$  found in wet granular matter [97] and the very low volume fractions of colloidal gels, which are below 0.15, but often sparser than 0.05 (e.g. [38, 57, 107]). From a structural point of view, percolating particle networks in this low range usually exhibit a fractal structure, while fractal structures can no longer appear in the densely packed volume fractions of wet granular matter as is directly apparent from equation 2.30. Prior to this thesis, there was no knowledge on the fractal (or non-fractal) nature of capillary sus-

pensions. However, there is no obvious reason why such a fractal concept, or the concepts of capillary forces and pendular and funicular wetting regimes of wet granular matter, cannot be applied to evaluate the structure of capillary suspensions.

Finally, another implication of the reduced solid volume content of capillary suspensions in comparison with wet granular matter is expected from yield stress measurements. While wet granular materials are mechanically frustrated so that particles cannot relocate under shear without high interparticle friction, the capillary suspension networks are much more flexible as there is more void space for particles to move by each other. Therefore, the interparticle friction, which dominates the yield stress in wet granular matter as captured by equation 2.54, should be negligible compared to the capillary force contribution. Accordingly, the yield stress behavior of capillary suspensions is expected to be similar to the tensile strength behavior of wet granular matter, shown in Fig. 2.9b, which also is governed only by capillary forces and not by friction.

### 2.4.3 Mechanical features

As previously mentioned, the capillary force emerging from the presence of the secondary liquid between the particles in capillary suspensions is typically much higher than the van der Waals or other relevant interparticle forces [2]. This leads to an increased cohesion between particles compared to suspensions without added secondary fluid, resulting in marked changes in flow behavior and preventing particle sedimentation [22]. Key rheological properties of capillary suspensions are their shear-rate dependent viscosity  $\eta(\dot{\gamma})$ , their storage and loss moduli  $G'$  and  $G''$  as function of the strain amplitude  $\hat{\gamma}$  (stress amplitude  $\hat{\sigma}$ ), and their yield stress  $\sigma_y$ .

The viscosity of a capillary suspension is strongly shear-thinning, i.e. it decreases strongly with increasing shear rate until reaching a rate-independent viscosity value at high shear rates [7]. Comparing the capillary suspension to a two-phase suspension with same solid volume fraction, but without added secondary fluid, shows that both systems share the same high-shear viscosity value while the viscosity of the capillary suspensions is significantly higher (up to several decades) than that of the regular, two-phase suspension at low shear rates [6, 7, 16, 21]. The capillary forces strongly counteract shear forces, leading to the elevated viscosity at low shear rates. At sufficiently high shear rates, the shear forces are sufficiently strong to break the capillary bridges and the final viscosity plateau is reached when all bridges are broken. After this point, the capillary suspension behaves the same as the suspension without secondary fluid, since the effective, hydrodynamic volume fraction is the same as the true volume fraction.

For oscillatory experiments inside the linear-viscoelastic (LVE) region, both  $G'$  and  $G''$  of capillary suspensions are essentially constant over a very broad range of frequencies, or, at least, have only a very weak dependence on the frequency. At the same time,  $G'$  is always higher than  $G''$  [1, 6]. This behavior is a typical characteristic of particle gels in general [38]. When examining  $G'$  and  $G''$  as function of the stress or strain amplitude, the LVE region of capillary suspensions is markedly short (upper limit of the LVE region at  $\hat{\gamma} \approx 10^{-5} - 10^{-3}$ ), which is typical for gels with very strong attractive particle interactions [44]. Due to the dominance of  $G'$  over  $G''$ , the complex shear modulus  $|G^*|$  of capillary suspensions usually is very close to  $G'$  (see equation 2.11).

Capillary suspensions generally exhibit a yield stress caused by their strong attractive

particle interaction [1, 2, 6, 7]. As any stress, by definition, is represented by a force divided by an area, it is straightforward to express the stress in a single capillary bridge  $\sigma_{\text{bridge}}$  by means of the capillary force  $F_c$  and the squared particle radius  $a^2$  as a reference area, leading to

$$\sigma_{\text{bridge}} \propto \frac{|F_c|}{a^2}. \quad (2.56)$$

The yield stress of the whole sample is directly related to this bridge stress with an additional correction for the number of bridges  $N_{\text{bridge}}$  and particles  $N_{\text{particle}}$ . The particle number is directly proportional to the solid volume fraction via

$$\phi_{\text{solid}} = \frac{\frac{4}{3}\pi a^3 N_{\text{particle}}}{V_{\text{sample}}} \quad (2.57)$$

with the total sample volume  $V_{\text{sample}}$ . Accordingly, the yield stress of a capillary suspension can be universally written as

$$\sigma_y = f_1(\phi_{\text{solid}}, N_{\text{bridge}}) \frac{|F_c|}{a^2}. \quad (2.58)$$

Equation 2.45, including the modified geometric function of equation 2.46, can be used to calculate the capillary force. Inserting these into equation 2.58 leads to a yield stress equation, for equally-sized particles, given by [2, 90, 91, 94]

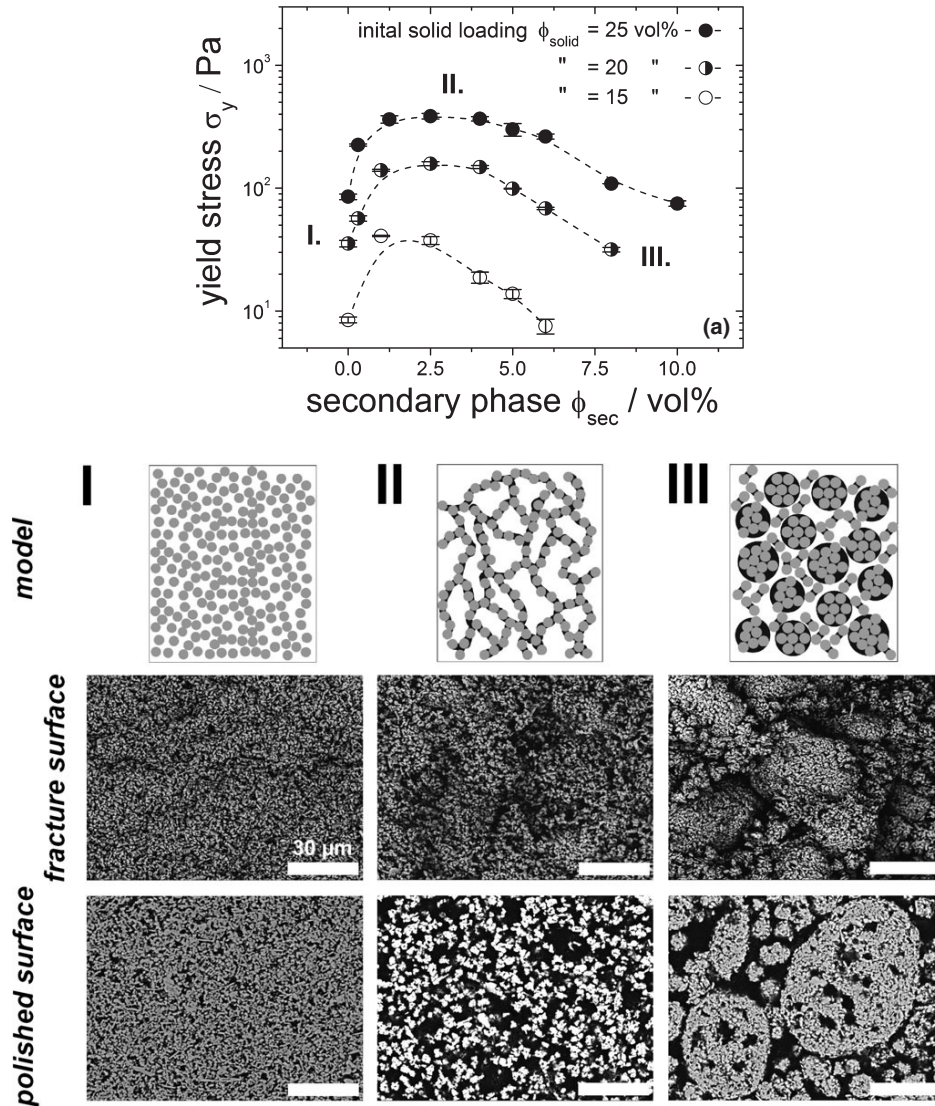
$$\sigma_y = f_1(\phi_{\text{solid}}, N_{\text{bridge}}) f_2(\tilde{V}_{\text{bridge}}, \tilde{s}) \frac{2\pi\Gamma \cos\theta}{a} \quad (2.59)$$

where  $f_2$  is the function given by equation 2.46 that takes the value of unity when the particle separation  $\tilde{s}$  is zero. This separation should be valid for a majority of capillary bridges in a sample at rest.

The secondary fluid volume fraction does not directly appear in the yield stress equation 2.59, but is very closely linked to both functions  $f_1$  and  $f_2$  as it is associated with the bridge number and individual bridge volumes by

$$\phi_{\text{sec}} = \frac{\sum_{i=1}^{N_{\text{bridge}}} V_{\text{bridge},i}}{V_{\text{sample}}} \quad (2.60)$$

with the index  $i$  denoting each individual bridge of the sample. Thus, the yield stress is also a function of the secondary fluid volume. Dittmann et al. have determined the yield stress of  $\text{Al}_2\text{O}_3$ -based capillary suspensions at different solid and secondary fluid volume fractions and imaged sintered surfaces (either fractured or polished) of some of their samples using surface electron microscopy (SEM) [10]. Fig. 2.12 shows the crucial result of this study. The yield stress first increases when the secondary fluid volume is increased, goes through a maximum and then decreases when the amount of secondary fluid is increased further. This behavior and the structures seen in the SEM images also resemble some of the structural features and transitions that have been investigated in wet granular matter, see Fig. 2.8. The increase in the yield stress at low secondary fluid volume fractions is hypothesized to correspond to the pendular state, while the maximum in the capillary suspension yield stress denotes funicular-like structures. The ensuing decrease in the yield stress appears due to the formation of spherical agglomerates. Experimental



**Figure 2.12:** Yield stress of ceramic precursor capillary suspensions as function of the solid and secondary fluid volume fractions (top) as well as schematic drawings (second row) and SEM images of the sintered body (third and fourth row) showing different structures, marked as “regime I, II and III” by the authors of this study. The figure is reproduced from *J. Dittmann and N. Willenbacher, Micro Structural Investigations and Mechanical Properties of Macro Porous Ceramic Materials from Capillary Suspensions, J. Am. Ceram. Soc. 97(12), 3787–3792, 2014* [10] ([hyperlink](#)), reprinted with permission from John Wiley and Sons.

studies by Heidlebaugh et al. [14] and Domenech and Velankar [6] have confirmed these trends for capillary suspensions of silica particles dispersed in a polymer blend. However, all of these works on capillary suspensions in the pendular state only have imaged the structure of sample surfaces after solidification. Thus, prior to this thesis an uncovering of non-solidified capillary suspension structures in situ was missing, as well as an analysis of the percolating particle network structure in 3D.

While equation 2.59 predicts the strength of capillary suspensions in the pendular state, the yield stress and its influencing parameters in the capillary state are uncertain.



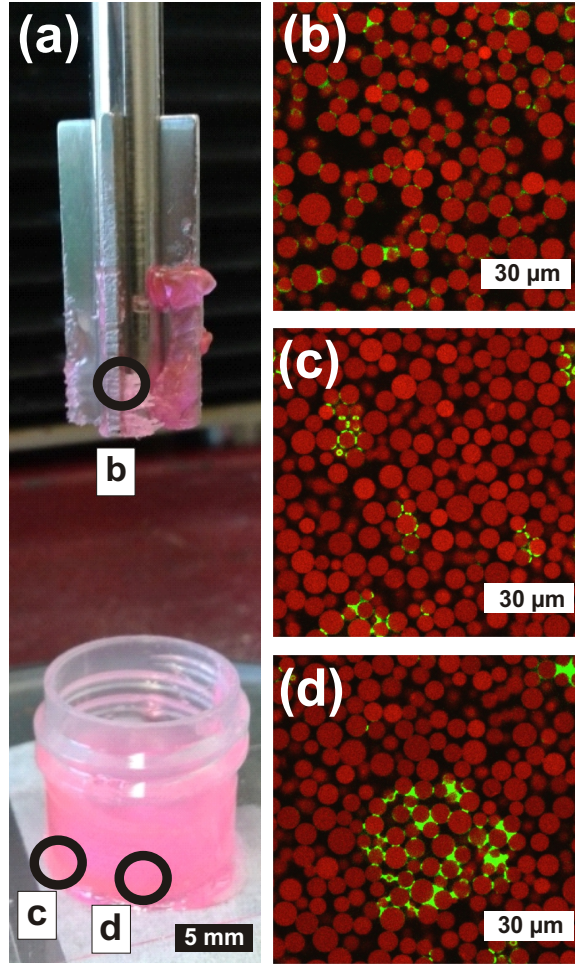
Simulations in the capillary state case indeed give some hints as to the contact angle dependence [8], see Fig. 2.11, but these are experimentally unproven. As the percolated network is not directly based on capillary forces between binary sphere contacts, but on interconnected energetically favored clusters of several particles, equations 2.45 and 2.59 cannot be used to predict the strength of such capillary state suspensions correctly, particularly since  $\cos\theta$  is negative for  $\theta > 90^\circ$ .

Equation 2.59 and Fig. 2.12 demonstrate a variety of tuning options for preparing capillary suspensions with a broad range of different yield stress values by varying either the particle size, solid volume fraction, contact angle, interfacial tension or the secondary fluid volume fraction [7]. However, with the latter, it is important to realize that  $\tilde{V}_{\text{bridge}}$  and  $N_{\text{bridge}}$  are not only related to the secondary fluid volume fraction  $\phi_{\text{sec}}$ , but also depend strongly on the sample preparation method [5]. Such a dependence on sample preparation conditions is true of capillary suspensions and other strong attractive particle gels that are not in thermodynamic equilibrium since the structure does not organize itself in a reproducible manner without the application of well-defined external forces and initial conditions [37]. During sample preparation, the secondary fluid has to be fragmented into separate droplets, their number and size depending on the preparation method. It is obvious from equation 2.60 that, at fixed  $\phi_{\text{sec}}$ , an increased number of bridges leads to a smaller mean bridge volume and vice versa. Using  $f_2 = 1$  in equation 2.59, resulting from the zero-distance assumption, the influence of the bridge volume onto the yield stress disappears. However, the bridge number in function  $f_1$  will surely influence the yield stress. Thus, measurements of the yield stress of a capillary suspension at given particle size, particle volume fraction, interfacial tension and contact angle should not only consider the secondary fluid volume fraction, but also the sample preparation.

## 2.5 Droplet breakup

When capillary suspensions are prepared, the secondary fluid has to be distributed into the sample and hence needs to breakup into small droplets that then either will form the individual binary bridges in the pendular state or the micro-cluster center points in the capillary state. The mechanisms of droplet breakup of one fluid in another are a well-examined topic, when particles are absent, in emulsification theory and technology. A basic understanding of these droplet breakup concepts also is of major importance for designing preparation protocols for capillary suspensions. Parts of this section were already published in the introduction of “Influence of mixing conditions on the rheological properties and structure of capillary suspensions” by Frank Bossler, Lydia Weyrauch, Robert Schmidt and Erin Koos, *Colloids and Surfaces A: Physicochemical and Engineering Aspects*, 518, 85–97, 2017 ([hyperlink](#)), copyright Elsevier, reproduced with permission from Elsevier [108].

In Fig. 2.13, a simple preliminary experiment where a capillary suspension was prepared using a vane geometry on a rheometer instead of a conventional stirrer is shown. In this experiment, different regions of the sample were exposed to different mixing intensities. As can be seen from the confocal images of Fig. 2.13b-d, a higher mixing intensity leads to a more homogeneous distribution of secondary fluid where many separate, small bridges between the solid particles are visible. Larger drop clusters are present in regions of lower mixing intensity where the secondary fluid was not well distributed. The general



**Figure 2.13:** Influence of mixing intensity on the distribution of secondary fluid. (a) Vane geometry (top) and stirred suspension of spherical particles and secondary fluid in bulk liquid (bottom). Three confocal microscopy images were taken at different positions of the sample as denoted by the black circles. (b) Region of highest mixing intensity at vane edge, (c) intermediate mixing intensity and (d) lowest mixing intensity directly below the vane. The particles are shown in red, the secondary fluid in green and the bulk liquid in black. Details on the used sample system and on confocal microscopy are given in chapters 3 and 4. Figure reproduced with permission from Elsevier [108].

importance of different mixing procedures for capillary suspension preparation was also recently shown by Domenech and Velankar [5].

Early droplet deformation and breakup theories were proposed by Taylor in the 1930s where droplet breakup in laminar flow was related to counteracting contributions of a droplet-deforming shear stress  $\sigma$  and the Laplace pressure  $\Delta p = 2\Gamma/a_{\text{drop}}$  [109, 110]. A droplet of size  $a_{\text{drop}}$  breaks as soon as a critical stress is exceeded. This is captured by the critical Capillary number  $\text{Ca}_{\text{crit}}$ , which denotes the relative contributions of critical droplet-deforming and shape-retaining stresses and is defined as

$$\text{Ca}_{\text{crit}} = \frac{\sigma_{\text{crit}} a_{\text{drop}}}{\Gamma} = \frac{\dot{\gamma}_{\text{crit}} \eta_b a_{\text{drop}}}{\Gamma} \quad (2.61)$$

where the shear stress in laminar flow is just the product of shear rate  $\dot{\gamma}$  and bulk liquid

viscosity  $\eta_b$ . At a given stress and interfacial tension,  $Ca_{\text{crit}}$  determines the smallest possible droplet size  $a_{\text{drop,crit}}$  that can be achieved. An extensive study on the critical capillary number under laminar flow conditions was performed by Grace [111], who also showed that  $Ca_{\text{crit}}$  is strongly dependent on the viscosity ratio  $\lambda = \eta_d/\eta_b$  relating the droplet viscosity  $\eta_d$  to the bulk viscosity. Under shear flow, the smallest droplets can be achieved for  $\lambda = 0.1 - 1$  as  $Ca_{\text{crit}}$  steadily increases for smaller viscosity ratios.  $Ca_{\text{crit}}$  increases even faster for ratios larger than unity and droplet breakup becomes impossible for  $\lambda > 3.5$  in laminar shear flow [111].

However, deviations from Grace's findings have to be considered when the flow field also contains elongational contributions [112], the volume fraction of the droplet phase is high [113, 114], the flow is confined [115], the flow field is not stationary [116], or one or both liquids are non-Newtonian [117]. Droplet breakup becomes further complicated in the additional presence of particles [118]. Additionally, the viscosity of the droplet has to be considered independently of  $\lambda$ , an effect that is captured in the Ohnesorge number  $Oh$ .  $Oh$  becomes much larger than zero for a relatively high droplet viscosity, which indicates an additional impairment in droplet breakup [119, 120].

For droplet breakup under turbulent flow conditions, which is mainly dominated by inertial forces, the concepts of Hinze are commonly used [121]. Here, the minimum possible droplet size is determined by a critical Weber number  $We_{\text{crit}}$ , which is defined similarly to the Capillary number of laminar flow breakup theory, but with a different droplet-deforming stress,

$$We_{\text{crit}} = \frac{\sigma a_{\text{drop,crit}}}{\Gamma} = \frac{\rho_b u^2 a_{\text{drop,crit}}}{\Gamma} \quad (2.62)$$

with  $\rho_b$  being the density of the bulk liquid and  $u$  the velocity scale inside the droplet, which also is a function of  $a_{\text{drop,crit}}$  [120–122]. Hinze showed that  $a_{\text{drop,crit}}$  is proportional to the power input per unit mass  $P_{\text{Watt,m}} = P_{\text{Watt}}/m$  (with the power  $P_{\text{Watt}}$  and the mass  $m$ ) for turbulent flow with  $Oh \ll 1$  with

$$a_{\text{drop,crit}} \propto \left(\frac{\rho_b}{\Gamma}\right)^{-0.6} P_{\text{Watt,m}}^{-0.4} \quad (2.63)$$

Therefore, a higher specific power input leads to smaller droplets. When droplet breakup in turbulent flow is performed with a stirrer, the power input depends on the stirrer power  $P_{\text{Watt}} = M\omega$  with the stirrer torque  $M$  and the angular speed  $\omega$ . Using  $P_{\text{Watt}} = E/\Delta t$ , where  $E$  is the energy input and  $\Delta t$  is the stirring time, the energy input of the stirrer can be calculated as [123]

$$E = M\omega\Delta t = M2\pi n\Delta t \quad (2.64)$$

where  $n$  is the rotational speed of the stirrer. Combining equations 2.63 and 2.64 predicts that an increased stirring speed  $n$  is expected to lead to smaller droplet sizes.

In general, a droplet has to be deformed longer than a critical deformation time  $t_{\text{def}}$  for a droplet breakup to occur, which can be related to deforming stress  $\sigma$ , Laplace pressure and droplet viscosity as [124]

$$t_{\text{def}} = \frac{\eta_d}{\sigma - \Delta p}. \quad (2.65)$$

Apart from rotating mechanical stirrers, several other types of devices are classically used for emulsification, amongst them being any types of more complex rotating geometries, high pressure homogenizers, membrane methods and ultrasonification [124]. To



capture the influence of energy input on the resulting emulsification result for each device, concepts of energy density may be used, where the energy density  $E_V = P_{\text{Watt},V} t_{\text{eff}} = E/V$  is the power input of the device per volume element  $P_{\text{Watt},V} = P_{\text{Watt}}/V$  multiplied with the time  $t_{\text{eff}}$  that the droplet spends in the zone of power input. This allows easy comparison between different devices. Similarly, the resulting droplet size can also be related to products of functions of  $P_{\text{Watt},V}$  and  $t_{\text{eff}}$ . Especially, a majority of technically relevant emulsification processes under turbulent flow conditions can be captured by [124]

$$a_{\text{drop,crit}} \propto P_{\text{Watt},V}^{-k_1} t_{\text{eff}}^{k_2} \eta_d^{k_3} \quad (2.66)$$

where the exact exponents  $k_1 = 0.25 - 0.4$ ,  $k_2 = -0.3$ ,  $k_3 = 0 - 0.75$  depend on the device used and sample dependent physical properties. The dependence on power input in this equation resembles the early findings of Hinze given in eq. 2.63, while eq. 2.66 also directly includes a relevant time scale. Thus, when droplets are allowed to remain longer in the emulsification zone, the droplet size will also decrease. However, the exponent  $k_2 = -0.3$  for the time dependence is not correct for long emulsification times  $t_{\text{eff}} > 1$  s. In this case, it has to be replaced by more exact functions, but will retain a negative sign.

The process of droplet breakup is counteracted by droplet coalescence. Especially in the absence of surfactants, as is true for most capillary suspensions, coalescence of droplets is unhindered and will occur as soon as two droplets come into contact with a very high coalescence probability,  $P_{\text{coa}}$ . This leads to larger droplets and, finally, a return to complete phase separation of both fluids. Stabilization of droplets against coalescence, e.g. by addition of surfactants, strongly reduces  $P_{\text{coa}}$ . Overall, the coalescence is captured by a coalescence rate  $\Omega_{\text{coa}} = P_{\text{coa}} f_{\text{coll}}$ , where  $f_{\text{coll}}$  denotes the frequency of droplet collisions [124]. In the simultaneous presence of particles, droplets will not only collide with each other, but also with particles and, depending on the wetting behavior comprised by the contact angle  $\theta$ , will stick to the particles as soon as they touch. In capillary suspensions droplet-particle collisions will appear much more frequently than droplet-droplet collisions as the volume fraction of particles is much larger than the volume fraction of secondary fluid. This should impede major droplet coalescence effects as most droplets will already be bound to particle surfaces before they contact another droplet.

If two droplets in a drop-particle pair collide, then they can, of course, coalesce while still being bound to the two particle surfaces. This should lead to a binary capillary bridge that binds the two particles together, assuming the new bridge is not directly ruptured again due to high particle collision impact forces. Such a binary capillary bridge can also form by the much more frequent collision between a droplet-particle pair and the surface of another particle. Such collisions would favor the formation of capillary suspensions with a narrow bridge size distribution. While experimentally unproven, these collisions are the most probable mechanisms underlying the structure formation during capillary suspension preparations under external stirring in cases where the surfaces of particles are not previously fully wetted by a thin layer of secondary fluid. In such fully wetted cases, theories for bridge formation can be found in the literature [85]. Capillary suspensions made with fully wetting droplets should have a broader distribution in bridge sizes due to the high probability of multiple coalescence events. A sample preparation method where particles are fully wetted by a secondary fluid film before mixing was performed by Hoffmann et al. [22] where water was used as the secondary fluid and hygroscopic particles were stored in a water-saturated atmosphere for 2–21 days prior to sample prepara-

tion. In all other cases up until now, sample preparations of capillary suspensions were performed by separately adding dry particles and secondary fluid into the bulk medium, as also is the case in this thesis.

## 3 Material Systems

Different particles and liquids have been used for preparing capillary suspensions in the experimental part of this thesis. Section 3.1 gives an overview over all types of capillary suspension compositions used, including descriptions of all raw particles and liquids involved. In section 3.2, chemical modification steps of silica particle surfaces are detailed, which had to be performed to obtain high-quality confocal images and also to vary the contact angle and porosity of these particles. Finally, section 3.3 presents the capillary suspension sample preparation methods.

### 3.1 Raw materials and capillary suspension compositions

Experiments were performed using six compositions of different ternary solid-liquid-liquid material systems. Each of them contains micron-sized particles as solid phase and two immiscible Newtonian fluids as bulk and secondary liquid phases. An overview of the general composition of these sample systems is given in Table 3.1, where the different compositions are termed C1 to C6. Each of these compositions is separately described in the following subsections.

**Table 3.1:** Composition and three-phase contact angles of the capillary suspension systems used.

Compo- sition	Solid phase	Bulk fluid (oil phase)	Secondary fluid (aqueous phase)	Contact angle $\theta$
C1	Silica beads (Kromasil)	Hexamoll DINCH/ dodecane mixture	Dyed aqueous glycerol	38-147° (tunable)
C2	Glass beads (NP3)	Hexamoll DINCH + 0.1 % Tween20	Water	$39 \pm 8^\circ$
C3	Hydrophobic $\text{CaCO}_3$ (Socal U1S1)	Hexamoll DINCH	Water	$156 \pm 5^\circ$
C4	Glass beads (NP3)	Silicone oil (AK100)	Aqueous glycerol	$49 \pm 7^\circ$
C5	$\alpha\text{-Al}_2\text{O}_3$	Paraffin oil	Sucrose solution	$41 \pm 4^\circ$
C6	$\text{CaCO}_3$	Paraffin oil	Sucrose solution	$51 \pm 9^\circ$

### 3.1.1 Basic physical characterization of particles and fluids

Particle densities  $\rho$  have been measured by gas pycnometry using a MultiVolume Pycnometer 1305 (Micromeritics Instrument Corporation, Norcross, USA) or were given by the particle supplier. Particle size distributions were obtained by low angle laser light scattering using a Helos H0309 device (Sympatec GmbH, Clausthal-Zellerfeld, Germany) following Fraunhofer diffraction theory. Therefor the particles were dispersed in ethanol or water and ultrasonication applied (with a Sympatec QUIXEL unit) directly prior to the size measurement to break any particle agglomerates. Surface electron microscopy (SEM) images of particles were taken with a Hitachi S-4500 microscope. BET surfaces of porous particles were determined with  $N_2$  gas adsorption (Autosorb-1, Quantachrome GmbH & Co. KG, Odelzhausen, Germany). Densities and mean particle radii of the particles used in compositions C1 to C6 are summarized in Table 3.2.

**Table 3.2:** Density and volumetric mean radius of particles used.

Particle name	Type	Density $\rho$ [g/mL]	Mean radius $a_{50,3}$ [ $\mu\text{m}$ ]	Part of composition
Kromasil 100-1.8-SIL	$\text{SiO}_2$	$1.95 \pm 0.08$	$0.95 \pm 0.03$	C1
Kromasil 100-3.5-SIL			$1.59 \pm 0.02$	
Kromasil 100-7-SIL			$3.21 \pm 0.03$	
NP3-P0	$\text{SiO}_2$	$2.46 \pm 0.01$	$1.78 \pm 0.02$	C2, C4
Socal U1S1	$\text{CaCO}_3$	$2.32 \pm 0.03$	$1.03 \pm 0.05$	C3
CT3000SG	$\alpha\text{-Al}_2\text{O}_3$	3.94	$0.32 \pm 0.01$	C5
CT1200SG			$0.70 \pm 0.01$	
CL3000SG			$1.94 \pm 0.02$	
CT19FG			$3.12 \pm 0.03$	
Ulmer Weiss XMF	$\text{CaCO}_3$	2.70	$1.60 \pm 0.02$	C6
Ulmer Weiss XM			$2.17 \pm 0.02$	

Pure fluid densities were provided by the suppliers. Glycerol/water mixture densities were taken from a water-glycerol mixture data sheet [125]. Hexamoll/dodecane mixture and sucrose solution densities were determined by pycnometry. Viscosities of all fluids were measured with steady shear experiments using a Searle geometry on the rotational rheometers described in section 4.1. All fluids are Newtonian. Fluid densities and viscosities are summarized in Table 3.3. The methods for determining interfacial tensions between two fluids (pendant drop) and three-phase contact angles  $\theta$  (sessile drop or direct confocal imaging) are described in detail in section 4.3. The determined contact angles for the six sample compositions are provided in Table 3.1.

### 3.1.2 Composition C1 – the confocal microscopy sample systems

Samples with composition of class C1 were used for the confocal microscopy experiments. This composition is based on “Kromasil” silica particles in an oil mixture as bulk with added aqueous glycerol as secondary fluid.

**Table 3.3:** Density and viscosity at 20 °C of oil based (top) and aqueous (bottom) fluids used.

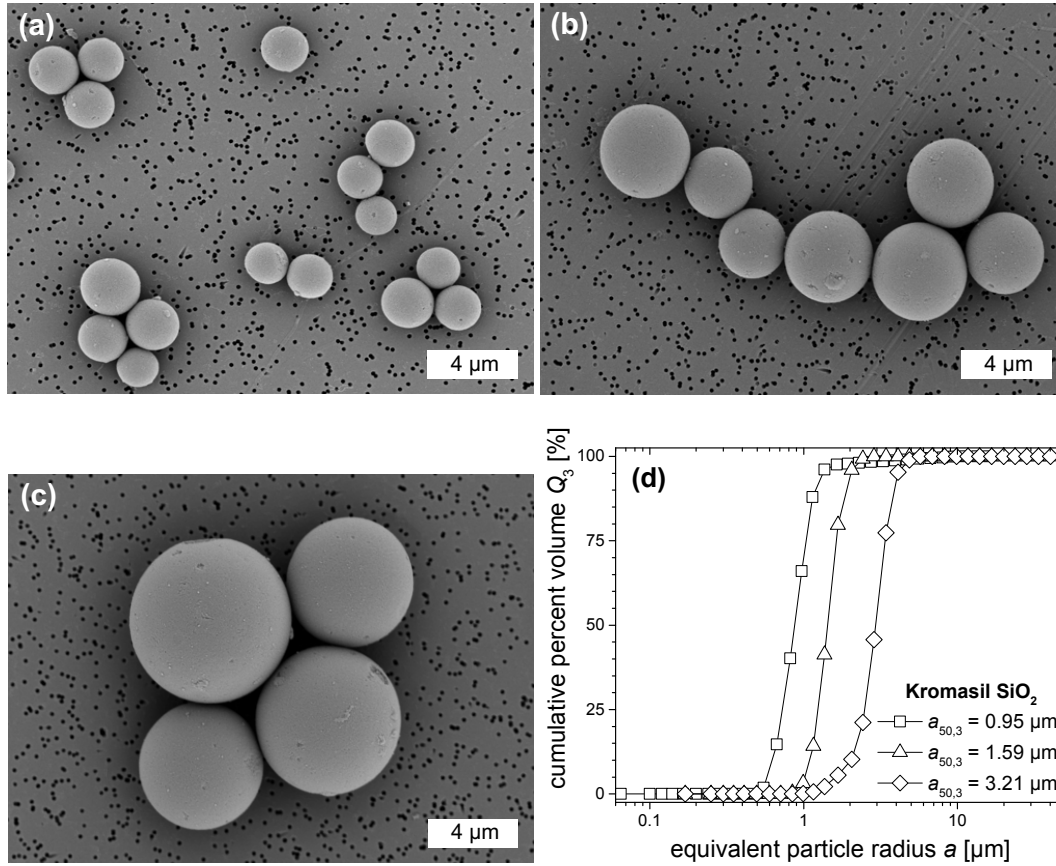
Fluid	Density $\rho$ [g/mL]	Viscosity $\eta$ [mPa s] at 20 °C	Part of composition
Hexamoll DINCH	0.95	46	C3
Hexamoll DINCH + 0.1 % Tween20	0.95	46	C2
Hexamoll/dodecane mixture 83.8vol%/16.2vol%	0.91	21	C1
AK100 Silicone oil	0.96	104	C4
Paraffin oil	0.85	29	C5, C6
Water	1.00	1	C2, C3
Glycerol/water mixture 84.6wt%/15.4wt%	1.22	104	C4
Dyed glycerol/water mixture 86.4wt%/13.6wt%	1.23	120	C1
Sucrose/water solution 50vol%/50vol%	1.28	80	C5, C6

### Kromasil particle characteristics

The used silica particles are Kromasil (Akzo Nobel, Bohus, Sweden; purchased from MZ-Analysentechnik GmbH, Mainz, Germany), which are nanoporous microspheres that are normally used as filling material for chromatography columns. As delivered, they have a pore volume of 0.9 mL/g, consisting of greater than 97 % open pores and mean pore size of 11 nm (values given by Akzo Nobel). The BET surface is  $295 \pm 2 \text{ m}^2/\text{g}$ . To be able to use these Kromasil particles for confocal microscopy, several chemical particle modifications had to be undertaken beforehand:

- Fluorescent dyeing of the particles with rhodamine B isothiocyanate
- Modification of the particle porosity
- Hydrophobization of the particle surface to adjust the three-phase contact angle over a range of 38-147°.

The dyeing modification was obligatory for all particles, while the other two were used to achieve a broad variation of experimental parameters without having to change the general composition C1. All these three chemical reaction methods are separately detailed in section 3.2. Three types of Kromasil silica with different mean particle radius  $a_{50,3}$  were used (Kromasil 100-1.8-SIL,  $a_{50,3} = 0.95 \text{ }\mu\text{m}$ ; Kromasil 100-3.5-SIL,  $a_{50,3} = 1.59 \text{ }\mu\text{m}$ ; Kromasil 100-7-SIL,  $a_{50,3} = 3.21 \text{ }\mu\text{m}$ ; all sizes determined after chemical modifications). SEM images and the particle size distributions of these are given in Fig. 3.1. The dyed particles maintain a spherical shape. Their measured solid density is  $1.95 \pm 0.08 \text{ g/mL}$ .



**Figure 3.1:** SEM images of Kromasil silica particles after the fluorescent dyeing reaction with (a) mean radius  $a_{50,3} = 0.95 \mu\text{m}$ , (b)  $a_{50,3} = 1.59 \mu\text{m}$  and (c)  $a_{50,3} = 3.21 \mu\text{m}$ . (d) Particle size distributions of all three of these particle types.

### Determination of the refractive index of the dyed Kromasil particles

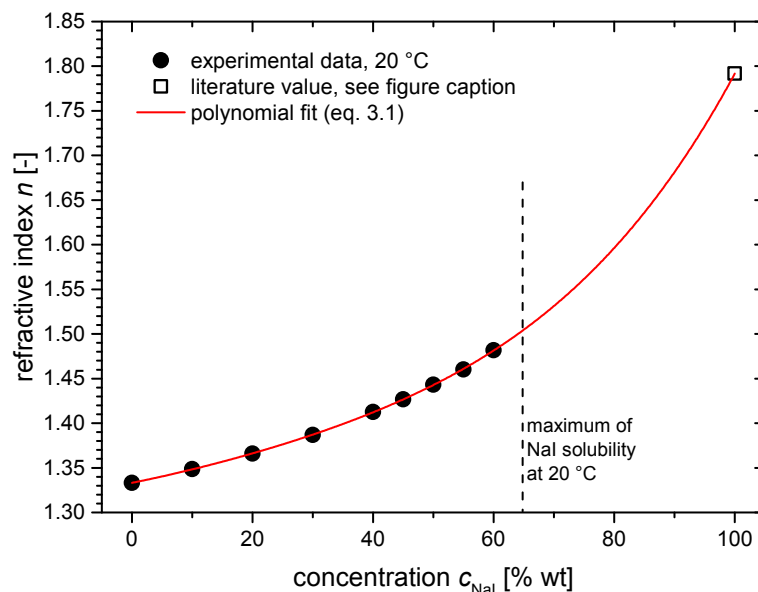
The particle refractive index was obtained with the help of sodium iodide (NaI) solutions. The dependence of aqueous solutions on the NaI concentration was determined by measuring a concentration series of NaI solutions between 0 wt % and 60 wt % NaI with an Abbe refractometer, as shown in Fig. 3.2, where the refractive index  $n$  was fit using the empirical relation

$$n = 1.333 + 1.340 \cdot 10^{-3} c_{\text{NaI}} + 1.750 \cdot 10^{-5} c_{\text{NaI}}^2 - 1.697 \cdot 10^{-7} c_{\text{NaI}}^3 + 3.189 \cdot 10^{-9} c_{\text{NaI}}^4 \quad (3.1)$$

with the NaI concentration  $c_{\text{NaI}}$  in wt %. This fit is shown as the red line in Fig. 3.2.

To obtain the Kromasil particle refractive index, ultrapure water was added dropwise under constant stirring to a 57 wt % NaI solution ( $n = 1.469$ ) with added Kromasil particles until the sample looked transparent. The amount of added water was determined by measuring the total increase in sample weight. The refractive index of the particles could be deduced by calculating the actual NaI concentration and then using equation 3.1 to determine the refractive index.

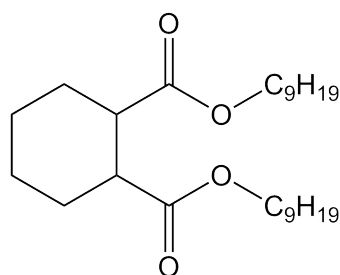
The refractive index of the Kromasil particles after the chemical modifications was  $n = 1.455 \pm 0.006$ .



**Figure 3.2:** Refractive index of NaI solutions as measured with an Abbe refractometer and polynomial fit to the data. The pure NaI value at  $c_{\text{NaI}} = 100$  wt % is a literature value [126] for a temperature of 293 K and a wavelength of 500 nm.

### Bulk and secondary fluid

The ratio of the components of the oil (bulk) as well as the aqueous (secondary) phase was chosen to fit the refractive index of the chemically modified silica particles. Index-matching is necessary to obtain high-quality confocal images. A mixture of 1,2-cyclohexane dicarboxylic acid diisononyl ester (i.e. a plasticizer with product name “Hexamoll DINCH”, BASF, Ludwigshafen, Germany, refractive index  $n = 1.463$ ) and n-dodecane (Alfa Aesar, Karlsruhe, Germany,  $n = 1.421$ ) was used as the oil phase. Fig. 3.3 shows the chemical structure of a Hexamoll molecule. The proper Hexamoll to dodecane volume ratio for index matching ( $n = 1.455$ ) was found to be 83.8/16.2. Both oil phase components are fully miscible as was confirmed by detecting no emulsion drops when the mixture is observed with bright field light microscopy. Additionally, no phase separation of the oil mixture was noted after six months in a closed vessel.



**Figure 3.3:** Chemical structure of 1,2-cyclohexane dicarboxylic acid diisononyl ester. The used “Hexamoll DINCH” is a mix of a multiplicity of isomers which only differ in the structure of the two nonyl groups ( $-\text{C}_9\text{H}_{19}$ ).

The aqueous phase consisted of a mixture of glycerol ( $n = 1.474$ , purity >99.5 %, Carl

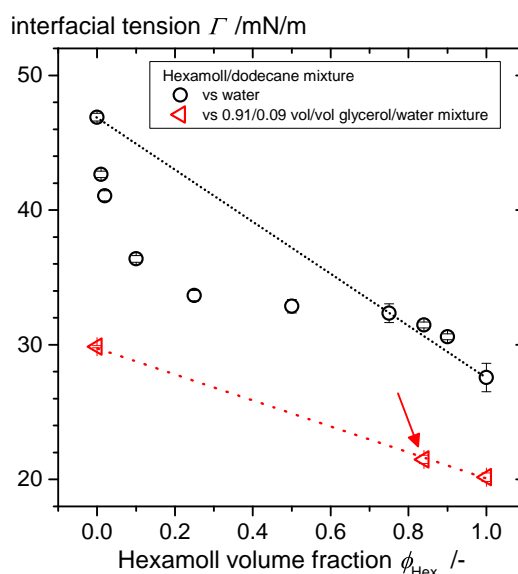


Roth, Karlsruhe, Germany) and ultrapure water ( $n = 1.333$ ) with a desired glycerol/water weight ratio of 86.4/13.6 to obtain the desired refractive index [125]. PromoFluor-488 Premium carboxylic acid (PromoKine, Heidelberg, Germany) was added as fluorescent dye to the aqueous phase. This dye is insoluble in the oil phase and does not adsorb to the particle surface. For preparing the aqueous phase, a stock solution of 6.25 mg of the dye in 1 g water was prepared to ensure a well controlled dye concentration. A second stock solution of 9.2 wt % water in 90.8 wt % glycerol was prepared. The aqueous phase then was obtained by mixing 5 vol % of the dye stock solution with 95 vol % of the second stock solution using a vortex stirrer.

### Interfacial properties of the liquid phases

The interfacial tension in system C1 was measured using the bulk oil mixture against a glycerol/water mixture with 0.91/0.09 volume ratio. The slight deviation in glycerol/water ratio compared to the secondary fluid of composition C1 here was necessary due to the pendant drop method requiring a mismatch in refractive index, which is obviously avoided in the actual system C1. The measured value is  $\Gamma = 21.5 \pm 0.3$  mN/m.

Hexamoll is immiscible with the aqueous glycerol, but tends to adsorb to the interface with the aqueous phase as it is a slightly polar ester and thus expected to be surface active against the polar secondary fluid (aqueous glycerol). To survey this surface activity interfacial tensions of Hexamoll/dodecane mixtures with varied volume ratio from 0 (pure dodecane) to 1 (pure Hexamoll) were measured against pure water and against the glycerol/water mixture with 0.91/0.09 volume ratio. The results are shown in Fig. 3.4. As water is more polar than glycerol, the surface activity of Hexamoll should be more pronounced against pure water than against glycerol/water mixtures. The dashed black line



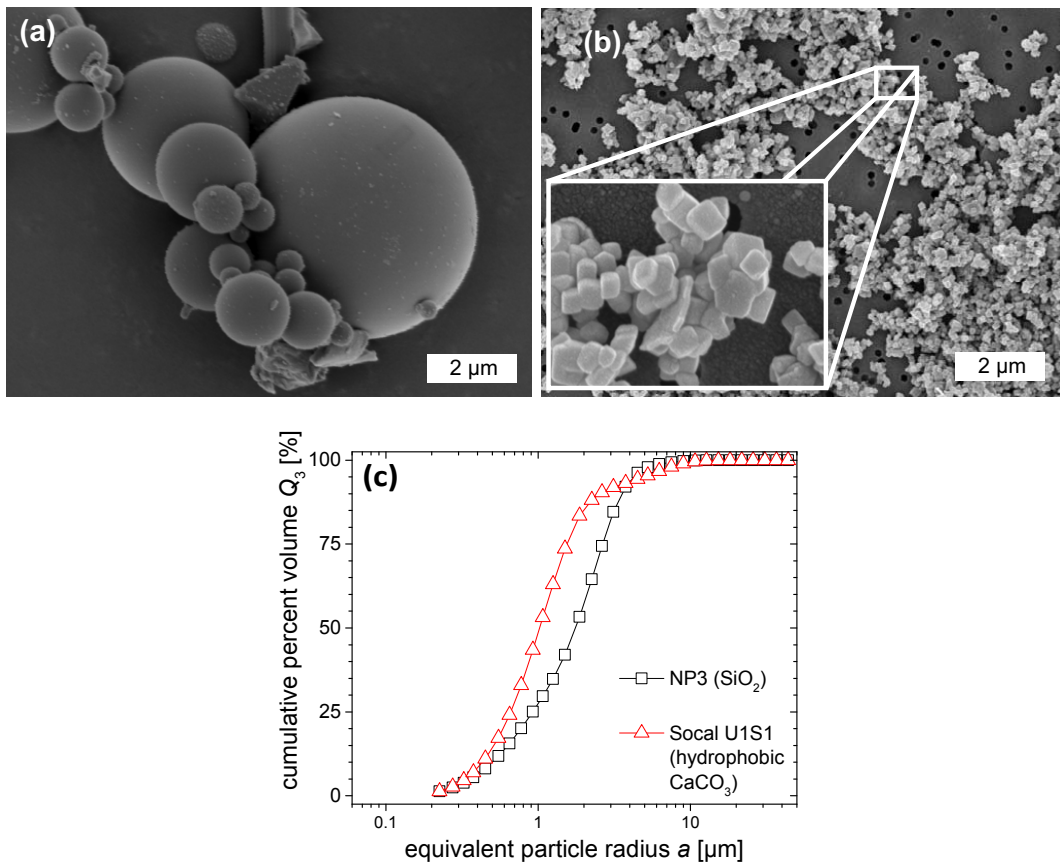
**Figure 3.4:** Interfacial tension of Hexamoll/dodecane mixtures with varied volume ratio against pure water (black circles) and against aqueous glycerol solutions (red triangles). The red arrow marks the fluid combination closest to the one used in all of the prepared capillary suspension samples of composition C1.



in the diagram identifies a theoretical linear dependence of the surface tension on the Hexamoll/dodecane ratio. While for low loadings of Hexamoll a strong reduction in the interfacial tension below this line is obvious, the measured values approach the linear dependence for Hexamoll loadings  $> 0.75$ . This data proves relevant surface activity of Hexamoll against water, as expected. However, this surface activity is irrelevant at high Hexamoll loadings as used in all of the C1 samples. The data shown as red triangles in Fig. 3.4 further corroborate the lack of a significant influence of surface activity near the ratios used for confocal experiments.

### 3.1.3 Compositions C2 and C3 – pendular and capillary state model system

Material composition C2 is a pendular state model system. This composition is based on “NP3” particles (OMicron NP3-P0, Sovitec, Fleurus, Belgium) which are hydrophilic non-porous mostly spherical glass beads with the presence of a small amount of non-spherical particles. A SEM image of these particles is shown in Fig. 3.5a and the particle size distribution included in Fig. 3.5c. Hexamoll DINCH (1,2-cyclohexane dicarboxylic acid diisononyl ester) is used as bulk fluid with 0.1 vol % of the nonionic surfactant Polysorbat 20 (Tween20, Carl Roth, Karlsruhe, Germany) added. The surfactant was necessary to avoid



**Figure 3.5:** SEM images of (a) NP3 silica beads and (b) Socal U1S1 hydrophobic CaCO<sub>3</sub>. (c) Particle size distributions of both of these particle types.

particle agglomeration that was otherwise too strong and would have made most C2 samples too inhomogeneous for an appropriate rheological characterization. The secondary fluid is ultrapure water. The contact angle measured with the pendant drop method is  $\theta = 39 \pm 8^\circ$ . The surfactant (same amount of 0.1 vol % in the oil phase) had also been used in the contact angle measurements. Addition of surfactants to capillary suspensions has been shown to increase the contact angle [7]. Due to relatively small droplet sizes in the capillary suspensions, the liquid-liquid interface per unit volume is probably much smaller in the pendant drop experiment than in the capillary suspension samples. Thus, the liquid-liquid interface in the contact angle measurement may possibly be more densely covered with surfactant, leading to a higher contact angle. Thus, while the contact angle in the capillary suspensions is possibly lower than the measured  $39^\circ$ , the samples of system C2 certainly can be classified as in the pendular state. Capillary suspensions based on glass beads have already been used as model pendular state systems in previous studies [5, 7].

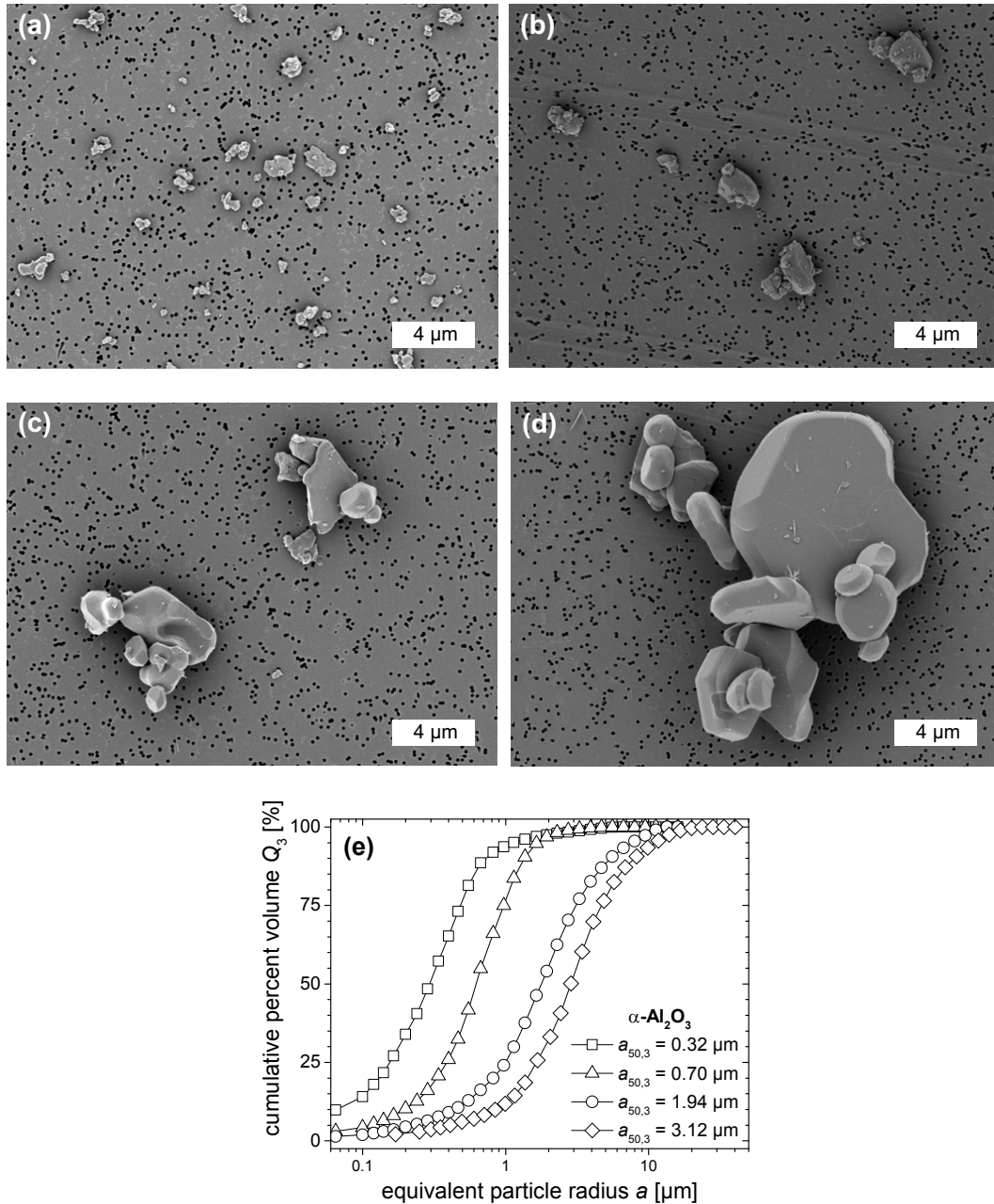
Material composition C3 is a capillary state model system ( $\theta = 156 \pm 5^\circ$ ), based on non-spherical hydrophobic calcium carbonate (product name “Socal U1S1”) manufactured by Solvay Advanced Functional Minerals (Salin-de-Giraud, France). The surface modification for rendering the  $\text{CaCO}_3$  hydrophobic was performed by the manufacturer. Like in system C2, the bulk and secondary fluid in system C3 also are Hexamoll DINCH (but without surfactant) and ultrapure water. While the primary Socal U1S1  $\text{CaCO}_3$  particles have an equivalent mean radius of only  $\approx 40$  nm, these primary particles form strong agglomerates that cannot be broken by mechanical stirring or even strong ultrasonication as applied for particle size measurement. Thus, the agglomerate size,  $a_{50,3} = 1.03 \pm 0.05 \mu\text{m}$ , and not the primary particle size represents the relevant particle length scale for structural investigations of capillary suspensions. The measured size distribution is also included in Fig. 3.5c. An SEM image with an inset showing the small primary particles is shown in Fig. 3.5b. Despite that issue of particle size, these particles have been used several times in previous studies as well-investigated model particles for capillary state suspensions [1, 127].

### 3.1.4 Composition C4 – a viscosity matched model system

Material composition C4 is based on the same NP3 glass beads used for composition C2. Silicone oil (AK100, Wacker Chemie AG, Burghausen, Germany,  $\eta(20^\circ\text{C}) = 104$  mPa s) and a mixture of glycerol (purity  $>99.5$  %, Carl Roth, Karlsruhe, Germany) with ultrapure water are used as the two immiscible Newtonian liquids. The glycerol/water weight ratio is 84.6/15.4 with a mixture viscosity of  $\eta(20^\circ\text{C}) = 104$  mPa s to match the viscosity of the oil phase. The contact angle ( $\theta_{\text{pendular}} = 49 \pm 7^\circ$ ) was measured using the oil phase as bulk fluid. Therefore, composition C4 is in the pendular state when aqueous glycerol is used as the secondary fluid (saturation  $0 < S \lesssim 0.1$ ). The contact angle of the silicone oil towards a pellet of compressed particles in aqueous glycerol also was measured using an inverted sessile drop method. In this case, the angle is  $\theta_{\text{capillary}} = 119 \pm 13^\circ$  and thus system C4 is expected to be in the capillary state when the aqueous glycerol is used as bulk ( $0.9 \lesssim S < 1$ ). As the viscosity ratio is  $\lambda = 1$ , the droplet breakup behavior in composition C4 and the resulting droplet size in particular is expected to be independent of which liquid is in the majority according to Grace theory [111].

### 3.1.5 Composition C5 – $\text{Al}_2\text{O}_3$ -based capillary suspensions

Material composition C5 is a pendular state system ( $\theta = 41 \pm 4^\circ$ ) that is utilized as precursor for ceramics production [9, 10]. Thus, this system is more application oriented than the model systems C1 to C4. The solid phase is aluminum oxide powder (hydrophilic  $\alpha$ - $\text{Al}_2\text{O}_3$ ) with four different average particle radii (CT3000SG,  $a_{50,3} = 0.32 \mu\text{m}$ ; CT1200SG,  $a_{50,3} = 0.70 \mu\text{m}$ ; CL3000SG,  $a_{50,3} = 1.94 \mu\text{m}$ , CT19FG,  $a_{50,3} = 3.12 \mu\text{m}$ ). All four particle types were obtained from Almatix GmbH (Ludwigshafen, Germany). Fig. 3.6 shows SEM

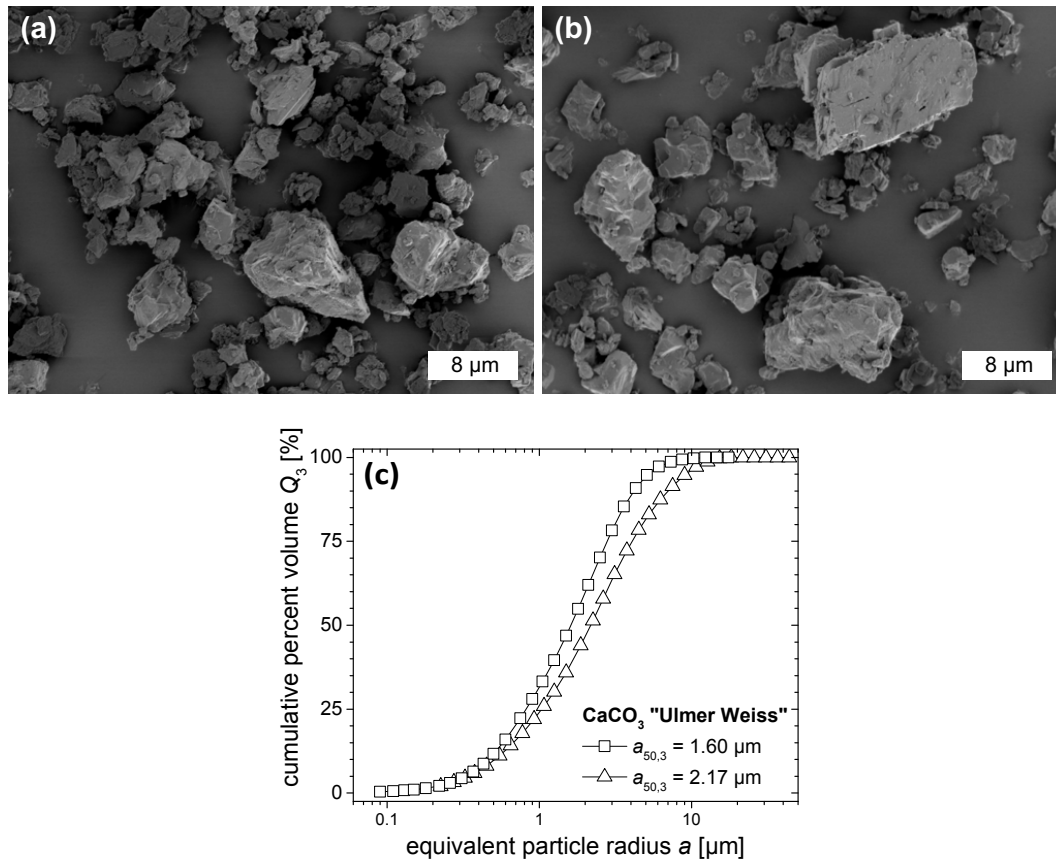


**Figure 3.6:** SEM images of (a) CT3000SG  $\text{Al}_2\text{O}_3$  particles, (b) CT1200SG  $\text{Al}_2\text{O}_3$  particles, (c) CL3000SG  $\text{Al}_2\text{O}_3$  particles, and (d) CT19FG  $\text{Al}_2\text{O}_3$  particles. (e) Particle size distributions of all four of these particle types.

images and the particle size distributions of the particles. The bulk fluid is paraffin oil (“Paraffinöl dünnflüssig”, Carl Roth, Karlsruhe, Germany), the secondary fluid a 50 vol % solution of D-(+)-sucrose (Carl Roth, Karlsruhe, Germany) in ultrapure water. The interfacial tension between bulk and secondary liquids is  $\Gamma = 41.2 \pm 0.7$  mN/m.

### 3.1.6 Composition C6 – $\text{CaCO}_3$ -based capillary suspensions

Material composition C6 is based on hydrophilic  $\text{CaCO}_3$  particles with two different size distributions and mean radii (“Ulmer Weiss XMF”,  $a_{50,3} = 1.60$   $\mu\text{m}$ ; “Ulmer Weiss XM”,  $a_{50,3} = 2.17$   $\mu\text{m}$ ). The particles were obtained from Eduard Merckle GmbH und Co. KG (Blaubeuren, Germany). SEM images and particle size distributions are shown in Fig. 3.7. As bulk and secondary fluid, exactly the same liquids (paraffin oil and 50 vol % sucrose solution) have been used as for composition C5. System C6 also is in the pendular state ( $\theta = 51 \pm 9^\circ$ ).



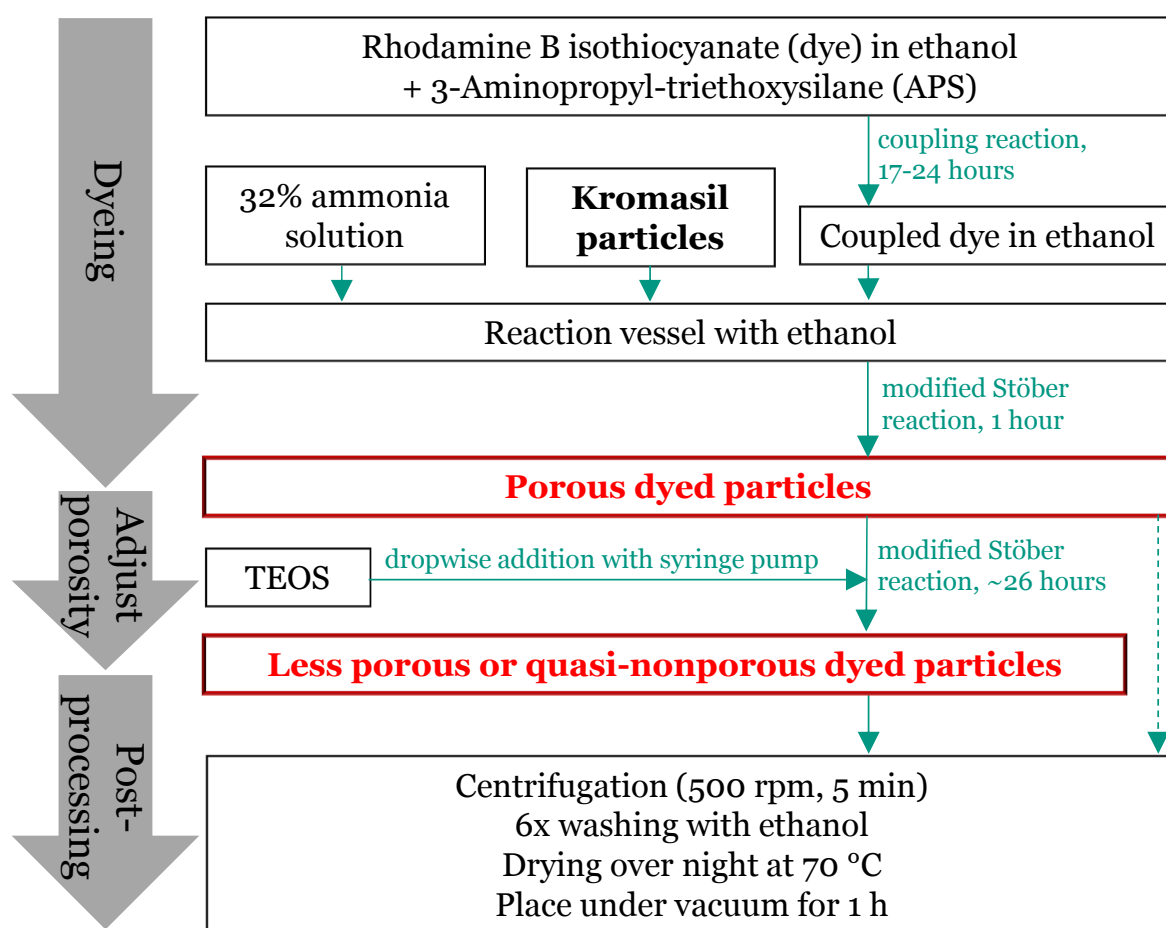
**Figure 3.7:** SEM images of (a) Ulmer Weiss XMF  $\text{CaCO}_3$  particles and (b) Ulmer Weiss XM  $\text{CaCO}_3$  particles. (c) Particle size distributions of both of these particle types.

## 3.2 Chemical modification of Kromasil silica particles

As mentioned in section 3.1.2, the Kromasil silica particles have to undergo a fluorescent dyeing reaction to be functional for confocal microscopy. An additional adjustment of the particle porosity and surface hydrophobicity was completed in most cases.

### 3.2.1 Particle dyeing and porosity modification

The silica spheres are highly porous as delivered. This porosity is utilized to fluorescently dye the interior of the particles. A modified Stöber synthesis [128] was used to covalently bond the dye to the particles [129, 130]. Wenzl et al. recently used a similar procedure to prepare Kromasil silica microspheres for their confocal study [131]. An overview over the reaction is provided in Fig. 3.8.



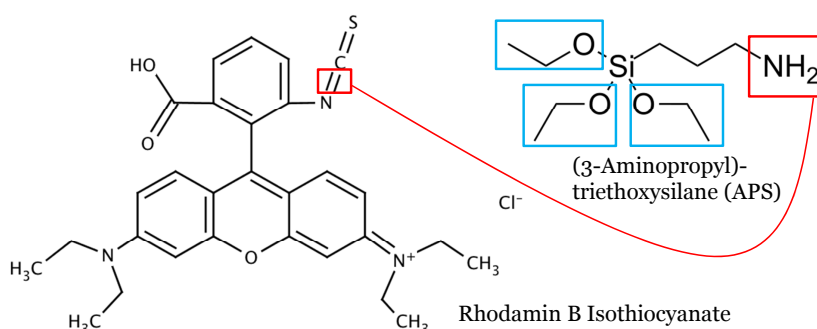
**Figure 3.8:** Overview over the fluorescent dyeing reaction scheme of Kromasil silica, the subsequent porosity adjusting reaction and the post-processing of the reaction(s).

#### Dye coupling

First, 8 mg of the fluorescent dye rhodamine B isothiocyanate (Sigma-Aldrich, Steinheim, Germany) and 8  $\mu\text{L}$  of (3-Aminopropyl)-triethoxysilane (APS, Merck, Darmstadt,



Germany) were covalently bonded using 10 mL of ethanol as a solvent. The free electron pair of the amin group of the APS (Fig. 3.9, right-hand side) attacks the C=N double bond of the thiocyanate group (Fig. 3.9, left-hand side) where a covalent single bond between



**Figure 3.9:** Rhodamine B isothiocyanate molecule (left) and APS molecule (right). The red groups are involved in the dye coupling reaction. The blue groups are involved in the modified Stöber reaction.

the nitrogen of the APS and the carbon of the thiocyanate group is formed, while one hydrogen shifts from the nitrogen of the APS to the nitrogen of the thiocyanate. Thus, this coupling reaction effectively results in rhodamine B dye molecules covalently bond to a triethoxysilyl group. This reaction took place under gentle stirring for 17–24 h with a magnetic stirrer.

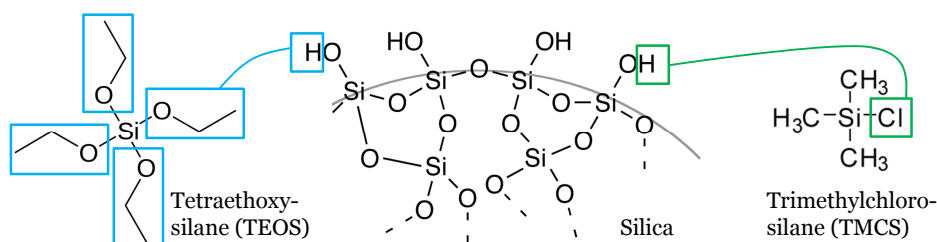
### Covalent binding of dye and Kromasil

In the reaction used, 110 mL ethanol (solvent in the reaction), 10 g Kromasil silica particles, 10 mL of 32 % ammonia solution (Carl Roth, Karlsruhe, Germany; catalyst in the reaction) and the previously prepared APS-coupled rhodamine B dye solution were assembled in a two-necked round-bottom flask attached to a KPG stirrer. The coupled rhodamine dye was covalently bonded to the silica particles while moderately stirring the vessel contents for 1 hour, after which the particle dyeing reaction is completed. Chemically, this is a modified Stöber reaction, where the coupled dye is bonded to the silica surface by a condensation reaction, see the blue marked ethoxy groups in Fig. 3.9, that react with the Kromasil silica surface. The pores of the Kromasil are large enough to enable this reaction to also take place inside of the particles. Thus, rhodamine B is covalently bonded not only to the outer Kromasil surface, but also to the interior, resulting in homogeneously dyed particles. If no porosity adjustment is desired, the reactions can be finished at this point (dashed green arrow in Fig. 3.8).

### Principle of the modified Stöber reaction

The original Stöber reaction was not completed with silica particles and dye, but only with tetraethoxysilane (TEOS) molecules (Fig. 3.10, left-hand side). Under the alkaline conditions provided by the ammonia solution, ethoxy groups ( $-\text{O}-\text{C}_2\text{H}_5$ ) of the TEOS are replaced by hydroxy groups ( $-\text{OH}$ ) via a hydrolysis reaction with water. Two hydrolyzed  $(\text{R})_3-\text{Si}-\text{OH}$  molecules or one  $(\text{R})_3-\text{Si}-\text{OH}$  with another  $(\text{R})_3-\text{Si}-\text{O}-\text{C}_2\text{H}_5$  molecule can then condensate, producing water or ethanol, to form  $(\text{R})_3-\text{Si}-\text{O}-\text{Si}-(\text{R})_3$  bonds. Thus,

starting from single TEOS molecules, large  $\text{SiO}_2$  structures can be built by polycondensation [128].



**Figure 3.10:** TEOS molecule (left), silica surface (middle) and TMCS molecule (right). The blue groups are involved in the original and modified Stöber reactions. The green groups are involved in the surface hydrophobization.

In the modified Stöber synthesis, the condensation reactions do not primarily occur between two TEOS molecules, but between a TEOS molecule and an existing silica surface (Fig. 3.10, middle). This is symbolized by the blue connection line in Fig. 3.10.

### Porosity adjustment

To adjust the porosity of the Kromasil, another modified Stöber reaction step was applied directly following the dyeing reaction. Tetraethoxysilane (TEOS, Merck, Darmstadt, Germany) was added dropwise into the reaction vessel using a syringe pump (neMESYS 290N, Cetoni GmbH, Korbussen, Germany) under constant stirring. The pump dosing rate was chosen as  $0.12 \mu\text{L/s}$ . Small dosing rates were necessary to avoid secondary nucleation (i.e. a “regular” Stöber reaction between TEOS molecules forming new silica particles) [132]. Depending on the total amount of added TEOS (10 mL in total were used for “nonporous” particles), the remaining porosity can be adjusted and minimized. Particles were classified as “nonporous” when a wetting secondary fluid did not migrate into the particle interior on the time scale needed to perform the confocal and rheological experiments ( $\approx 8$  hours after sample preparation), while these particles still had some remaining nanoporosity that cannot be easily avoided by Stöber reactions [133]. Anyway, a complete closing of the pores would be detrimental since this traps some solvent in the pores and, thus, induces a mismatch in refractive index inside of the particles. Indeed, most of the particles turned out to be “porous”, which means a rapid imbibition of either bulk or secondary fluid into the particles after sample preparation. These, nevertheless, had reduced porosities (BET surface  $\approx 200 \pm 50 \text{ m}^2/\text{g}$ ) compared to untreated Kromasil ( $295 \pm 2 \text{ m}^2/\text{g}$ ). Sadly, the reason for the bad predictability of the particle porosity is not known. The “porous” particles were typically used in experiments where the bulk fluid, rather than the secondary fluid, is adsorbed by the particles.

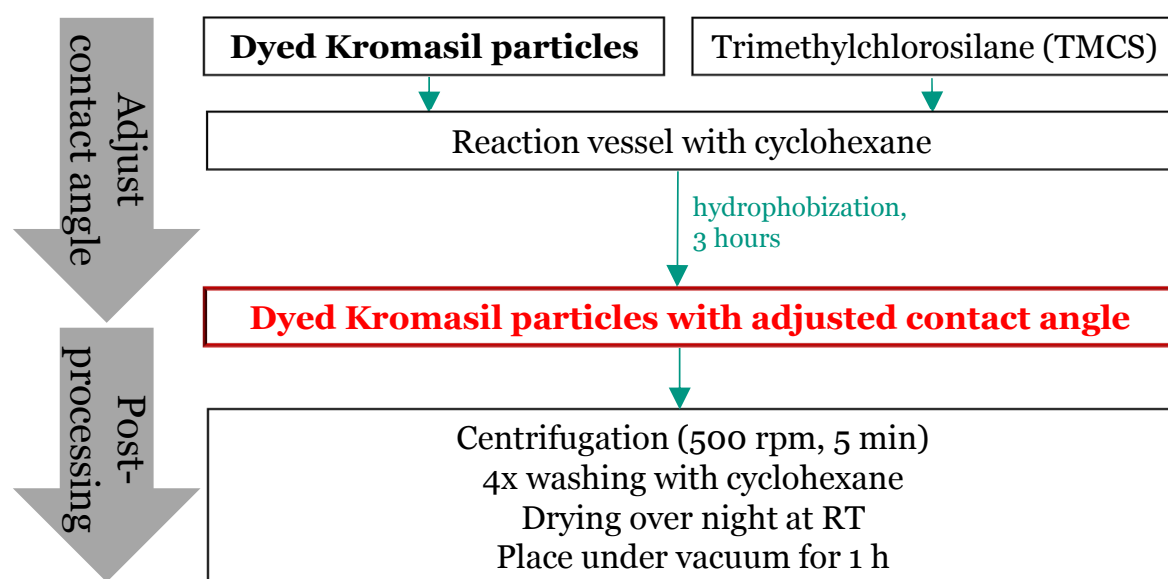
### End of the reaction – particle post-processing

The reactants were stirred for another 3 h after the last TEOS drop was added and then the reaction was ended by removal of the reactants. The vessel contents were centrifuged for 5–10 min at 500 rpm using a “Hettich Universal 320” centrifuge, the supernatant was discarded, and the particles were rinsed (re-dispersed) six times in ethanol to remove any

remaining reactants, where each rinsing step was again followed by 5–10 min centrifugation at 500 rpm. The low centrifuge speed is required to not break the particles. Finally, the particles were dried overnight at 70 °C and kept under vacuum for 1 h to remove any remaining ethanol.

### 3.2.2 Particle hydrophobization

To tailor the contact angle of the dyed Kromasil particles, the silica surface of the porous and nonporous particles were treated with trimethylchlorosilane (TMCS, Alfa Aesar, Karlsruhe, Germany). An overview on this hydrophobizing reaction is given in Fig. 3.11. When exposed to TMCS, the –OH groups on the silica surface are replaced by trimethyl-



**Figure 3.11:** Overview over the reaction protocol for hydrophobization of previously dyed Kromasil silica.

silyl groups ( $-\text{Si}-(\text{CH}_3)_3$ ), producing HCl, making the particle surface more hydrophobic [134], see the righthand side of Fig. 3.10. The number of replaced groups depends on the reaction time, the TMCS concentration and the reaction kinetics [135]. Degassing of the silica particles before the reaction can lead to more reproducible reaction kinetics [136], therefore the dyed particles were placed under vacuum for at least 1 h before being added to the reaction vessel. Different degrees of hydrophobicity, reflected by different resulting three-phase contact angles, were reached by choosing different amounts of TMCS between 5 and 200  $\mu\text{L}$  TMCS per gram silica as shown in Table 3.4. The contact angle as a function of TMCS concentration is not fully predictable as it can be batch dependent, resulting from previous differences in the reactions described in section 3.2.1. Particles with different TMCS-treated surface used in one series of experiments always originated from the same batch of dyed particles. However, surface heterogeneities cannot be excluded.

For the reaction, TMCS was first distributed in cyclohexane (Merck, Darmstadt, Germany) at room temperature after which the Kromasil silica particles were added. Following 3 h of constant shaking, the reaction was interrupted by centrifuging the par-



**Table 3.4:** Surface modified Kromasil silica particles prepared. The reaction time was 3 hours for all TMCS reactions. The contact angle  $\theta$  was measured as described in chapter 4.3. “Batch” denotes the batch of dyed particles used as starting material for the surface hydrophobization in the dedicated chapter of this thesis. The star (\*) marks three hydrophobization reactions where n-hexane was used as solvent instead of cyclohexane, which does not make a difference in regard to the final particle properties.

Batch [Chapter]	Particle size $a_{50,3}$ [ $\mu\text{m}$ ]	TMCS concentration [ $\mu\text{L}$ per gram particles]	Contact angle $\theta$ [ $^\circ$ ]
5 porous	3.21	30	$102 \pm 7$
6.1 nonporous	3.21	10	$40 \pm 6$
	3.21	20	$61 \pm 4$
	3.21	40	$94 \pm 5$
6.1 porous	3.21	0	$38 \pm 4$
	3.21	10	$67 \pm 14$ (*)
	3.21	26	$72 \pm 4$
	3.21	23	$90 \pm 5$ (*)
	3.21	35	$109 \pm 5$
	3.21	29	$115 \pm 4$ (*)
	3.21	41	$117 \pm 6$
	3.21	47	$133 \pm 4$
	3.21	200	$139 \pm 10$
	3.21	200	$147 \pm 7$
6.2 porous	3.21	30	$87 \pm 8$
	3.21	60	$115 \pm 8$
6.3 nonporous, small	0.95	15	$66 \pm 12$
6.3 nonporous, medium	1.59	12	$68 \pm 8$
6.3 nonporous, large	3.21	5	$61 \pm 5$

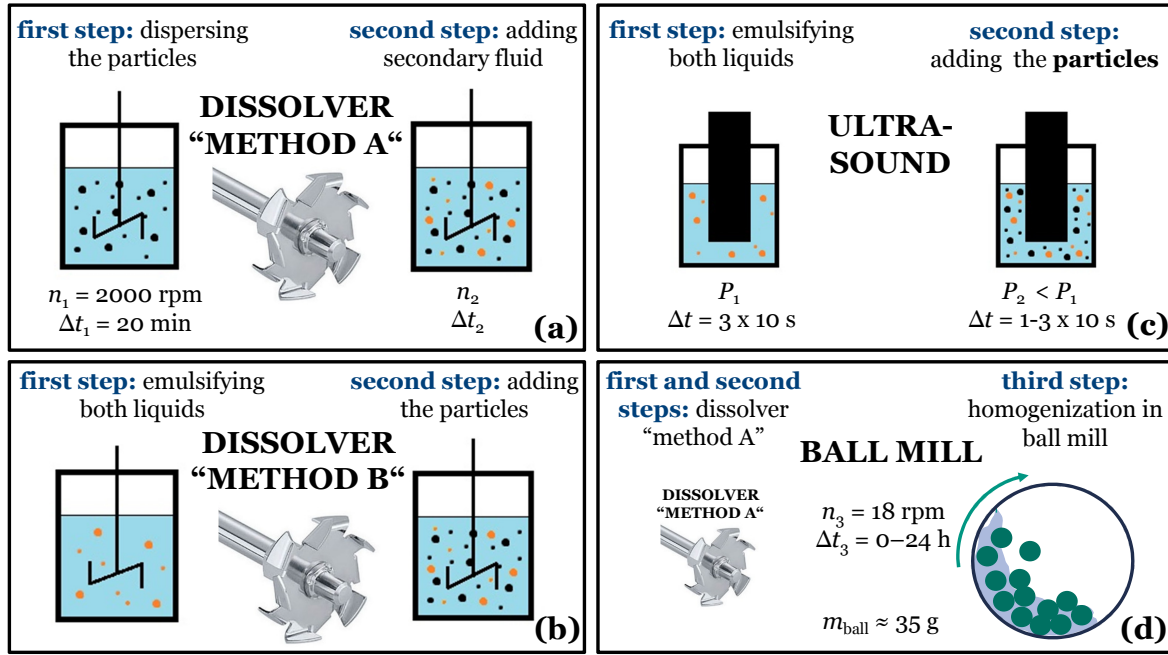
ticles, washing them four times in cyclohexane, drying them overnight at room temperature, and then degassing them for 1 h under vacuum.

### 3.3 Capillary suspension sample preparation

The influence of capillary suspension sample preparation on the resulting structure and rheology was one of the central research topics of this thesis. Accordingly, a variety of different preparation protocols was employed. Fig. 3.12 shows an overview over the four preparation protocols used.

#### 3.3.1 Preparation protocols for compositions C1 to C6

The choice of preparation protocol is closely linked to the different sample compositions summarized in Table 3.1. The pendular and capillary state model compositions C2 and C3



**Figure 3.12:** Four protocols used for capillary suspension sample preparation. (a) Turbulent stirring using a dissolver stirrer, (b) changed mixing order with the dissolver stirrer, (c) preparation with ultrasound and (d) with an additional homogenization step using a ball mill.

as well as the viscosity-matched composition C4 were prepared with the dissolver stirrer “method A” or “method B” depicted in Fig. 3.12a and b, respectively. The ultrasound method (Fig. 3.12c) was used for the confocal microscopy samples of composition C1 and the ball mill method (Fig. 3.12d) for the  $\text{Al}_2\text{O}_3$ - and  $\text{CaCO}_3$ -based compositions C5 and C6.

### Preparation of compositions C2, C3 and C4 – dissolver methods

Dissolver stirrers possess sharp edges (see the photograph of a dissolver included in Fig. 3.12a and b) and thus are well-suited for emulsification problems [123]. Therefore, due to the necessity to achieve a sufficient droplet breakup and distribution of secondary fluid, the dissolver stirrer “method A” is most commonly used for preparing capillary suspensions (e.g. [2, 17, 19, 21, 22]). It is a two-step method where the solid particles are first dispersed in the bulk fluid using a dissolver stirrer and then the secondary fluid is added and distributed in the sample using the same stirrer as before.

If not explicitly mentioned otherwise, for samples with composition C2 or C3, the particles and bulk fluid first were placed in a glass beaker (inner diameter of 38 mm) and stirred with a dissolver stirrer with a diameter of 25 mm at constant stirring speed  $n_1 = 2000 \text{ rpm}$  for a constant time interval  $\Delta t_1 = 20 \text{ min}$  to fully disperse the particles in the bulk fluid. The secondary fluid was then added and the sample was again stirred. The stirring speed  $n_2$  and time  $\Delta t_2$  were varied in this second step while the sample volumes as well as stirrer and beaker geometry were kept constant for all sample preparations. The total sample volume was always  $V_{\text{sample}} = 30 \text{ mL}$ .

The dissolver stirrer “method B” was also used for few experiments with compositions C2 and C3, where the mixing order is inverted. In this case corresponding stirring speeds

and times are directly explained in chapter 5.2.2 wherein these experiments are discussed.

For material composition C4, only the dissolver stirrer “method B” was used. Here, both fluids were first emulsified at 1250 rpm for 20 min. The particles were then added and stirred for another 2 min at 1250 rpm, followed by 1 min at 800 rpm. For composition C4 preparations, a dissolver stirrer with 36 mm diameter and a beaker with 46 mm diameter were used. All stirring speeds and times were kept constant, as well as sample volume  $V_{\text{sample}} = 55$  mL, while the ratio of secondary and bulk fluid volumes was varied.

#### **Preparation of compositions C5 and C6 – ball mill**

For material compositions C5 and C6, the samples were prepared with the method involving a ball mill (Fig. 3.12d). Here, samples were first prepared with dissolver “method A” with constant stirring parameters of  $n_1 = 1200$  rpm,  $\Delta t_1 = 10$  min,  $n_2 = 1000$  rpm,  $\Delta t_2 = 2$  min,  $V_{\text{sample}} = 100$  mL in a beaker with inner diameter of 65 mm and using a dissolver stirrer with 50 mm diameter. The resulting “preliminary” capillary suspension was then transferred into a custom-built ball mill [10–12]. The samples were then homogenized on the ball mill with a rotation speed of 18 rpm in a 100 mm diameter vessel using 19-21 balls (mass  $m = 34.5 \pm 1.3$  g each) with  $25 \pm 2$  mm diameter for different time intervals  $\Delta t_3 = 0 - 24$  h.

#### **Preparation of composition C1 – ultrasound**

The capillary suspensions of compositions C1 were prepared using ultrasonication (Fig. 3.12c). Emulsification with ultrasound occurs due to cavitation bubbles that appear during the depression phase of longitudinal acoustic pressure waves migrating through the sonicated sample. This leads to droplet breakup when the cavitation gas bubbles implode close to an interface between the two liquids [137]. Preparation volumes of C1 samples were limited by the small total amounts of available silica particles resulting from the different chemical modification steps detailed in section 3.2. This is the reason why ultrasound preparation was chosen instead of the more common dissolver or ball mill methods. As the energy input due to sonication only occurs very near to the ultrasonic horn, this method allows good droplet breakup in small volumes but also cannot be directly applied to large sample volumes. In this later case, the acoustic energy amplitude decays very quickly radially from the horn and the energy is transformed into heat due to viscous friction [137].

For sample preparation, an ultrasound sonifier (Digital Sonifier model 250, Branson Ultrasonics Corporation, Danbury, USA) with an ultrasonic horn of 12.5 mm diameter and a maximum available output power of 200 W was used. Total sample volumes were 0.85 mL per preparation. The bulk and secondary phases were placed together into a small vessel (18 mm inner diameter) and the fluids emulsified in a first step at an amplitude of 35 % for 30 s. For pure suspension preparations (no secondary fluid added), the same input (35 % for 30 s) was also applied to the pure bulk phase to ensure any temperature changes are roughly equivalent in each preparation. After this first step, the Kromasil silica particles were stirred in with a spatula. As there is no emulsifier for stabilization against coalescence in composition C1, care was taken to stir the particles in as quickly as possible. One to three more ultrasonic mixing steps were then rapidly applied to the sample (each 10 s at 10 % amplitude, stirring with a spatula between steps to enhance

sample homogeneity; number of steps was three if not explicitly mentioned otherwise). The measured overall sample temperature after the second sonication steps was approximately 40 to 50 °C, however the local temperature near the ultrasonic horn was probably higher.

### 3.3.2 Set and effective solid and secondary fluid volume fractions

Solid and secondary fluid volume fractions,  $\phi_{\text{solid}}$  and  $\phi_{\text{sec}}$ , are a direct result of the volumes (or masses) of the three components (particles, bulk fluid, secondary fluid) as set when preparing the samples. Composition C1 contains porous particles. Two different definitions of the volume fractions have to be considered in this case. The first of them is the set volume fraction determined by weighing in the components during sample preparation. This is given by

$$\phi_{\text{solid,set}} = \phi_{\text{solid}} = \frac{V_{\text{solid}}}{V_{\text{sample}}} = \frac{m_{\text{solid}}}{\rho_{\text{solid}} V_{\text{sample}}} \quad (3.2)$$

$$\phi_{\text{sec,set}} = \phi_{\text{sec}} = \frac{V_{\text{sec}}}{V_{\text{sample}}} \quad (3.3)$$

with the total solid mass  $m_{\text{solid}}$ , solid density  $\rho_{\text{solid}}$ , totally added solid and secondary fluid volumes  $V_{\text{solid}}$  and  $V_{\text{sec}}$  and total overall sample volume  $V_{\text{sample}}$ . For porous particles with porosity  $\epsilon = V_{\text{pore}}/(V_{\text{solid}} + V_{\text{pore}})$ , the pore volume  $V_{\text{pore}}$  is in the particles' interior that will, after sample preparation, be filled with secondary and/or bulk fluid, depending on the wetting behavior. Thus, the total secondary and bulk fluid volumes will partially be located inside of these pores ( $V_{\text{in}}$ ), and partially outside ( $V_{\text{out}}$ ) with  $V_{\text{sec}} = V_{\text{sec,in}} + V_{\text{sec,out}}$  and, analogously,  $V_{\text{bulk}} = V_{\text{bulk,in}} + V_{\text{bulk,out}}$ .

Sample rheology and microstructure are determined by an effective solid volume fraction  $\phi_{\text{solid,eff}}$  rather than by the set fraction  $\phi_{\text{solid,set}}$ , where the effective volume fraction incorporates the fluid-filled pore volume as effectively being part of the solid. The effective secondary fluid volume in these cases is only the fraction that is not inside of the pores. Therefore it is

$$\phi_{\text{solid,eff}} = \phi_{\text{solid,set}} + \frac{V_{\text{pore}}}{V_{\text{sample}}} = \frac{\frac{m_{\text{solid}}}{\rho_{\text{solid}}} + V_{\text{sec,in}} + V_{\text{bulk,in}}}{V_{\text{sample}}} \quad (3.4)$$

$$\phi_{\text{sec,eff}} = \frac{V_{\text{sec,out}}}{V_{\text{sample}}} \quad (3.5)$$

with the obvious relations  $\phi_{\text{solid,eff}} > \phi_{\text{solid,set}}$  and  $\phi_{\text{sec,eff}} \leq \phi_{\text{sec,set}}$ . As the porosity and thus pore volume of the particles in system C1 is not exactly known,  $\phi_{\text{solid,eff}}$  and  $\phi_{\text{sec,eff}}$  were directly determined by image analysis of confocal images as described in section 4.4. If not explicitly detailed otherwise,  $\phi_{\text{solid}}$  and  $\phi_{\text{sec}}$  in the remainder of this text always denote the set values defined by equations 3.2 and 3.3.

Compositions C2 to C6 contain nonporous particles. Thus,  $\phi_{\text{solid}}$  and  $\phi_{\text{sec}}$  are here unambiguously calculated from the set amounts of the components weighed into the sample, as equations 3.4 and 3.5 simplify to equations 3.2 and 3.3 when the pore volume is zero.

## 4 Experimental Techniques and Devices

This chapter gives an overview over the two main experimental techniques used for structural investigations of capillary suspensions – shear rheology and confocal microscopy. First, the devices and data acquisition protocols used for rheological measurements are described in section 4.1, based on the fundamentals already introduced in section 2.1. Then, basic principles of confocal microscopy as well as the used microscope and protocol for image acquisition are presented in section 4.2. Section 4.3 explains the realized contact angle measurement method, which also uses confocal microscopy. Finally, section 4.4 details the computational image evaluation methods to extract structural information from raw confocal images.

### 4.1 Rheological measurements

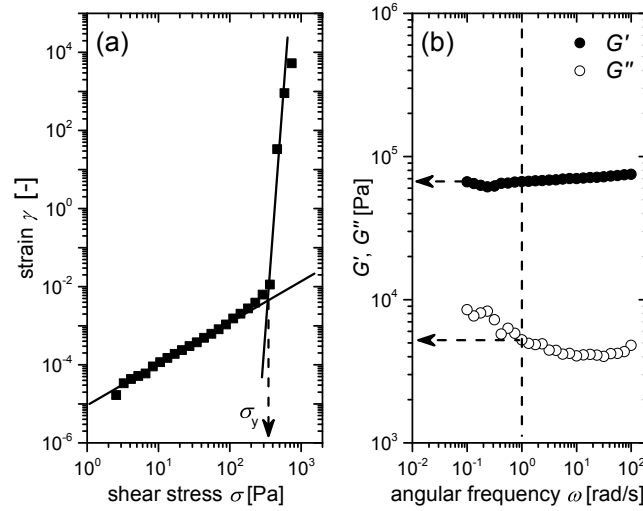
The confocal experiments of this thesis investigate capillary suspensions at rest. Accordingly, the focus of the rheological characterizations was on the strength of the sample structure at rest. In this context, the viscosity is only of minor interest and thus all rheological characterizations are solely based on oscillatory rheometry to obtain the shear moduli in the linear viscoelastic (LVE) region, and on yield stress measurements. Both methods are well-suited to characterize the strength of the structure at rest. All measurements have been performed with rotational rheometers using plate-plate and vane geometries as sketched in Fig. 2.2. As with the composition-specific sample preparation protocols (section 3.3.1), the devices and geometries used were chosen depending on the six material compositions presented in Table 3.1 to fulfill sample-specific requirements. For example, wall slip, which is known to be a common problem when measuring particle suspensions [138, 139], has to be avoided to obtain correct rheological data [140]. Wall slip was not observed in any of the oscillatory measurements performed. For yield stress measurements, techniques to avoid wall slip were employed for some of the different sample compositions as described below. All rheological measurements were conducted at 20 °C.

#### Compositions C2, C3 and C4: plate-plate geometry

For compositions C2, C3 and C4, all measurements (oscillatory rheology as well as yield stress measurements) were performed with the stress-controlled rheometer Physica MCR 501 (Anton Paar GmbH, Filderstadt, Germany) using a plate-plate geometry with 25 mm plate diameter and 1 mm gap width. The plates exhibit a small-scale roughness on the order of  $\approx 2 - 4 \mu\text{m}$ . No wall slip was observed for measurements of compositions C2 and C3 using these plates. In contrast, samples of composition C4 were prone to wall

slip on these plates. Therefore, silicon carbide sandpaper (P320C, roughness  $\approx 50 \mu\text{m}$ , Jean Wirtz, Düsseldorf, Germany) was attached to the plates before gap adjustment for all measurements of C4 samples.

Yield stress measurements were performed by increasing the shear stress from 0.1 Pa or 1 Pa to 1000 Pa or 5000 Pa stepwise with dwell time of 20 s per point. A plot of the measured strain vs applied shear stress shows a sharp transition from linear, elastic deformation at small stress (equal to a slope of 1 in the double-log plot) to a rapid deformation at large stress as soon as the sample flows, see Fig. 4.1a. The yield stress  $\sigma_y$  was evaluated



**Figure 4.1:** Determination of (a) yield stress  $\sigma_y$  and (b) storage and loss moduli  $G'$  and  $G''$  for all samples of material compositions C2, C3 and C4. The example data shown belongs to a sample of composition C3 with  $\phi_{\text{solid}} = 15\%$  and  $\phi_{\text{sec}} = 0.255\%$  prepared with a dissolver stirrer where the stirring speed and time in the second mixing step was set to  $n_2 = 2000$  rpm and  $\Delta t_2 = 5$  min. The yield stress is determined as the shear stress corresponding to the intersection point of two tangents fitted to the strain vs applied shear stress data.  $G'$  and  $G''$  are evaluated at a frequency  $\omega = 1$  rad/s at a previously determined strain amplitude in the LVE region. Figure reproduced with permission from Elsevier [108].

as the shear stress at the intersection of the tangent fit to the first deformation regime, and the tangent fit to the first three points of the second deformation regime [141]. This method has been previously used for yield stress measurements of capillary suspensions (e.g. [22, 142]).

Oscillatory shear strain amplitude sweep measurements were performed at a constant frequency of  $\omega = 1$  rad/s as well as 100 rad/s while increasing the strain amplitude  $\hat{\gamma}$  from 0.001 % to 100 %. In all cases, the upper limit of the LVE region, denoted by the critical strain amplitude  $\hat{\gamma}_{\text{crit}}$ , was found to be independent of the frequency and, for most C2, C3 and C4 samples, had a value between 0.01 % and 0.1 %, which was not further evaluated for these compositions. Frequency sweep measurements with  $\omega = 100 - 0.1$  rad/s were performed using a strain amplitude inside the LVE region. Single values of the storage modulus  $G'$  and loss modulus  $G''$  in the LVE region were evaluated at  $\omega = 1$  rad/s, as shown in Fig. 4.1b. The magnitude of the complex shear modulus  $|G^*|$  as well as  $\tan \delta$  can be calculated from these single  $G'$  and  $G''$  values using equations 2.11 and 2.15, respectively.



### Compositions C5 and C6: plate-plate and vane geometries

Rheological behavior of suspensions based on  $\text{Al}_2\text{O}_3$  particles (composition C5) and  $\text{CaCO}_3$  (composition C6) was determined using the stress-controlled rheometers Haake MARS II and Haake RheoStress RS150 (both from Thermo Fisher Scientific, Karlsruhe, Germany). Yield stress data obtained from these two rheometers have been tested to be fully comparable among each other.

The yield stress measurements were performed alternately on both rheometers with a vane geometry with four blades with dimensions  $R_{\text{blade}} = 5$  mm and  $h_{\text{blade}} = 22$  mm, see the sketch of Fig. 2.2d, and an appropriate cylinder cup (Z-20-DIN, with  $R_{\text{cup}} = 10.8$  mm). The shear stress was increased stepwise from 1 to 10,000 Pa. Each step was followed by a dwell time of 5 s. The steps were logarithmically distributed with 50 steps per decade. The yield stress was determined from stress vs strain curves using the same method previously described (Fig. 4.1a).

The storage modulus  $G'$  and loss modulus  $G''$  were determined on the MARS II rheometer equipped with a plate-plate geometry (plate diameter 35 mm, gap height 1 mm). The lower steel plate and upper titanium plate surfaces were sandblasted to prevent wall slip. Stress amplitude sweep measurements were performed at angular frequencies  $\omega = 1$  rad/s and  $\omega = 100$  rad/s. Stress controlled frequency sweep measurements were performed at a stress inside the linear viscoelastic region (sample dependent, between 10 Pa and 150 Pa) in a frequency range of 100 – 0.1 rad/s and show a frequency independent storage modulus of the suspensions in this range.

### Composition C1: small-sized plate-plate geometry

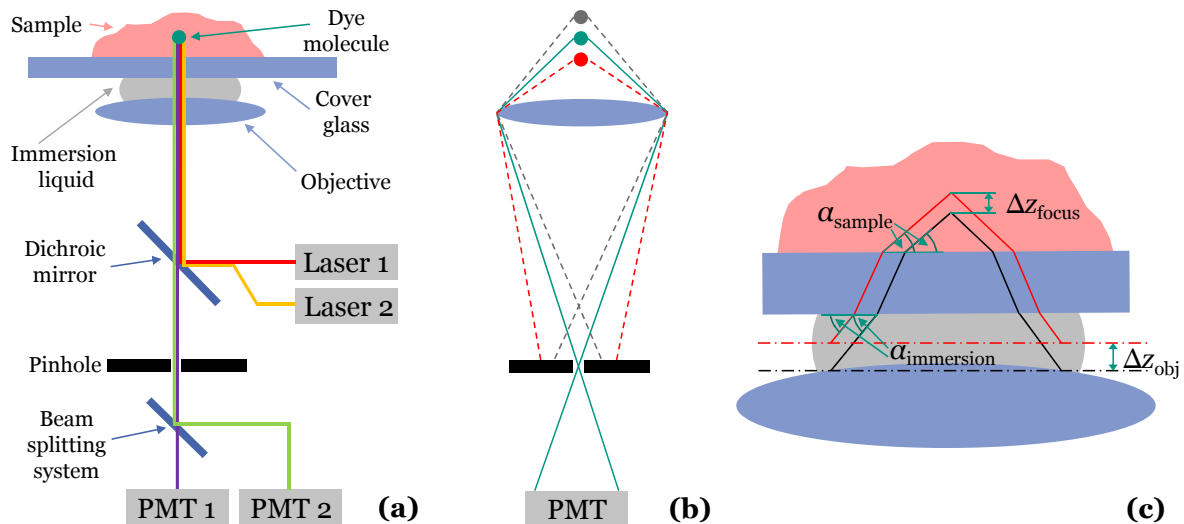
The rheological measurements of composition C1 were carried out with a stress-controlled Physica MCR 501 or Physica MCR 702 rheometer (both from Anton Paar GmbH, Filderstadt, Germany). Results presented in chapter 5 and 6.1 were completely obtained using the MCR 501 and in chapter 6.2 completely with the MCR 702. Due to the small available sample volumes a very small-sized plate-plate geometry with only 8 mm plate diameter and a gap width of 0.5 mm were used. As this small plate employed is smooth, only oscillatory measurements were conducted. Strain sweep measurements were completed at a constant angular frequency of  $\omega = 1$  rad/s or  $\omega = 10$  rad/s. Frequency sweep measurements were made in a frequency range of 100–0.1 rad/s at a previously determined strain amplitude within the linear viscoelastic domain. Some test experiments to measure the yield stress of C1 samples with this geometry failed due to wall slip. Additional use of sandpaper as for system C4 induced large errors on this very tiny geometry with the small gap and the vane geometry also could not be used due to the needed large sample volume not being available. Therefore, measurements on this sample were restricted to small amplitude oscillatory shear where slip was insignificant.

## 4.2 Confocal microscopy

### General principle

Confocal microscopy is commonly used for high-resolution 3D imaging of suspensions [31, 32]. A simplified sketch of a confocal microscope is shown in Fig. 4.2a. An aligned





**Figure 4.2:** (a) Simplified sketch of a confocal microscope setup with two lasers and two detectors. (b) Beam paths of in-focus (turquoise) and out-of-focus (red, black) emitted fluorescence signals through the objective and the pinhole. (c) Excitation beam paths through the immersion liquid, cover slip and sample for two different  $z$  positions of the objective with distance  $\Delta z_{\text{obj}}$ .

laser beam with specified wavelength (red line in Fig. 4.2a) is coupled into the system. The beam is bent by a dichroic mirror and passes through an objective, immersion medium and cover slip into the sample where it is focused. If there is a fluorescent dye molecule located at this focus position absorbing photons at the laser wavelength, the dye will be excited and then emit photons in a different, longer wavelength range. Emitted photons (purple line in Fig. 4.2a) propagate back through the objective and this longer wavelength emitted light passes through the dichroic mirror, further passes a pinhole and is detected by a photomultiplier tube (PMT) or other appropriate detection component. In case the microscope contains more than one laser, other excitatory beams will be coupled into the sample via the same route (yellow line) and may, dependent on the laser wavelength, be absorbed by a different fluorescence dye emitting in a different wavelength range. As these emitted photons (green line) pass back via the same route as the emitted photons depicted by the purple line, both emission signals covering different wavelength ranges have to be well-separated by a sufficient beam splitting system (e.g. low-pass filters or via a prism) and the separated signals then detected by two different PMTs. For obtaining 2D images, the sample is excited pointwise by moving the focus in lateral position via mirrors located in the beam pathway (not shown in the sketch) and the light intensities, pointwise detected by the PMTs, are computationally assembled into a single image per detector. The pointwise scan of the sample is expanded to third dimension by a vertical movement of the objective for 3D images.

Fig. 4.2b shows another, more appropriate, detail sketch of the emitted light paths of the in-focus and two inadvertent out-of-focus emitted signals through the objective and the pinhole. The pinhole is positioned exactly on the second focus point opposed to the objective (the “con-focal” point). Thus, light from an in-focus emitted signal passing the objective also passes the pinhole nearly completely, while out-of-focus emitted signals are mostly blocked as only insignificant portions of them pass the pinhole.

In reality, the excited focal “point” has some spatial extent, described by the point

spread function (PSF). The size of the PSF determines the accessible resolution of the microscope, which can be estimated as the full-width half-maximum diameter of the PSF, denoting the minimum distance that two neighboring points can still be distinguished as separate points (Abbe diffraction limit). It is [143]

$$d_x = d_y = \frac{0.37\lambda}{NA} \quad (4.1)$$

$$d_z = \frac{0.67\lambda}{n_{\text{sample}} - \sqrt{n_{\text{sample}}^2 - NA^2}} \quad (4.2)$$

with  $d_x$ ,  $d_y$  and  $d_z$  denoting the full-width half-maximum distances in  $x$ ,  $y$  and  $z$  directions, the numerical aperture  $NA$  of the objective, the wavelength  $\lambda$  of the light and the refractive index  $n_{\text{sample}}$  of the sample.

Additional errors can occur due to mismatched refractive indices. If there is a sample-inherent index mismatch, the excitatory and emitted light will be heavily scattered in all directions and the well-defined positions of the focal and confocal point and thus also the signal reaching the PMT has a lower signal to noise ratio impeding imaging of such an index-mismatched sample. If the sample itself is index-matched, but has a different refractive index than the immersion liquid ( $n_{\text{immersion}}$ ), the shift of the focal point in the sample  $\Delta z_{\text{focus}}$  will differ from the shift of the objective  $\Delta z_{\text{obj}}$  as the objective is moved during 3D image acquisition as sketched in Fig. 4.2c [144]. For  $\Delta z_{\text{focus}}/\Delta z_{\text{obj}} \neq 1$ , the apparent dimensions of the sample are therefore stretched or squeezed in  $z$  direction. The mismatch in focal shift can be sufficiently estimated using Snell's law as

$$\frac{\Delta z_{\text{focus}}}{\Delta z_{\text{obj}}} = \frac{\sin(90^\circ - \alpha_{\text{immersion}})}{\sin(90^\circ - \alpha_{\text{sample}})} = \frac{n_{\text{sample}}}{n_{\text{immersion}}} \quad (4.3)$$

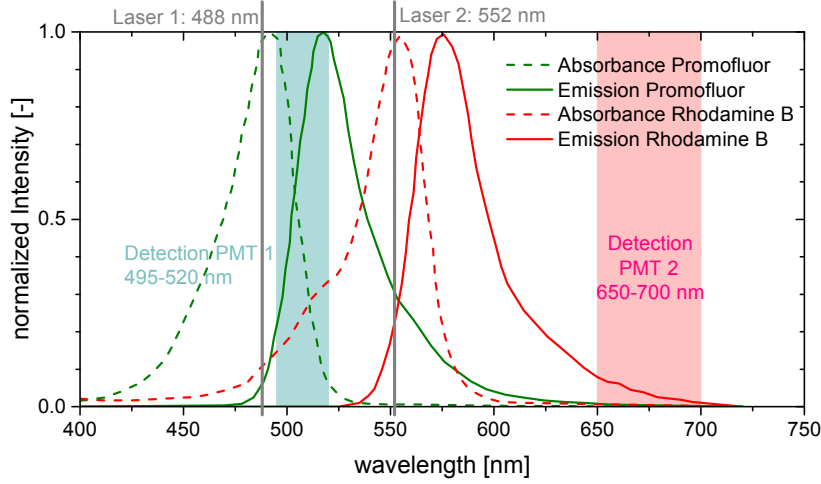
with the refractive angles  $90^\circ - \alpha_{\text{immersion}}$  and  $90^\circ - \alpha_{\text{sample}}$  (see Fig. 4.2c), as long as the difference between both indices is less than  $\approx 0.05$  [145]. The apparent size  $s_{\text{app}}$  of a detected object in  $z$  direction, including the extent  $d_z$  of the point spread function estimated via eq. 4.2, is

$$s_{\text{app}} = \frac{n_{\text{immersion}}}{n_{\text{sample}}} (s_{\text{true}} + d_z) \quad (4.4)$$

with the true object's  $z$  dimension  $s_{\text{true}}$  [146].

### Used device and parameters

Images were taken with a Leica TCS SP8 inverted confocal laser scanning microscope (Leica Microsystems, Mannheim, Germany). The microscope is equipped with two solid state lasers with wavelengths of 488 nm and 552 nm that have a maximum power of 20 mW. The PromoFluor-488 Premium carboxylic acid dye in the capillary suspensions secondary phase of material composition C1 is excited by the 488 nm laser and the rhodamine B groups bound to the particles are excited by the 552 nm laser, both of these wavelengths being close to the maximum of photon absorption of the respective dyes. Absorption and emission spectra of both dyes are shown in Fig. 4.3. The microscope is equipped with a spectral detector (Leica SP detector), which is a combination of a prism- and mirror-based beam-splitting system allowing the two detected wavelength ranges to



**Figure 4.3:** Absorption and emission spectra of Promofluor-488 Premium carboxylic acid (taken from [147]) and native rhodamine B (taken from [148]). The excitation wavelengths of the two lasers are shown as gray vertical lines, close to the absorption maxima of the dyes, and the detected emission wavelength ranges are shown by the green and red shaded regions.

be freely adjusted in order to minimize crosstalk between the emission signals and separate PMT detectors for both wavelength emission ranges. The secondary phase dye emission was detected in a wavelength range of 495–520 nm and the particles at 650–700 nm. Although only small portions of the dye emission spectra are incorporated in these ranges, especially for the rhodamine B, dye concentrations in the samples were large enough to still enable detections of very bright images (high signal to noise ratio) while only applying 0.5-2% of the maximum available laser input power.

A glycerol immersion objective with correction collar with a numerical aperture of 1.3 and 63x magnification (HC PL APO 63x/1.30 GLYC CORR CS2, Leica Microsystems, Mannheim, Germany) was used as this matches the sample refractive index of 1.455 best and, therefore, should lead to negligibly small optical distortions like spherical aberrations [149]. Additionally, due to the glycerol immersion liquid ( $n = 1.46$ ) placed between objective and cover glass, the discrepancy between the covered distance of the vertically moving objective and the focal point  $\Delta z_{\text{focus}} / \Delta z_{\text{obj}} = 0.9966$  (eq. 4.3) was negligible. Below a depth in the sample of  $\approx 150 \mu\text{m}$  it was lower than the error in  $z$  accuracy induced by the width of the PSF (eq. 4.4) and, therefore, was not corrected during subsequent image analysis. The diffraction limit (equations 4.1 and 4.2) using this objective is  $d_x = d_y \approx 148 \text{ nm}$  and  $d_z \approx 496 \text{ nm}$  based on an averaged wavelength from the excitations and emissions.

The sample was carefully deposited onto a microscope slide (170  $\mu\text{m}$  thickness) using a spatula. The slide was then placed on the inverted confocal microscope for 3D image acquisition. If not mentioned otherwise, image sizes of  $144.72 \times 144.72 \times 142.03 \mu\text{m}^3$  with  $1024 \times 1024 \times 300$  voxels were chosen for capillary suspension imaging, i.e. a voxel size of  $141 \times 141 \times 475 \text{ nm}$  in the order of the previously calculated resolution limit. The pinhole diameter was kept at 1 airy unit. Every voxel was excited 8 times ( $x$  direction line average using the bidirectional scanning mode) and the emitted signal averaged from these to reduce noise. Scanning speeds of 700 Hz were applied. These parameters led to an acquisition time of  $\approx 30 \text{ min}$  per image. As the samples are imaged at rest and, in the case of capillary suspensions, are stabilized against sedimentation, such slow imaging times are

sufficient while being beneficial to reduce noise and get a high resolution. If not otherwise mentioned, 8 images per sample were taken at different spatial positions. Microscopy images were always recorded at room temperature.

## 4.3 Contact angle and interfacial tension determination

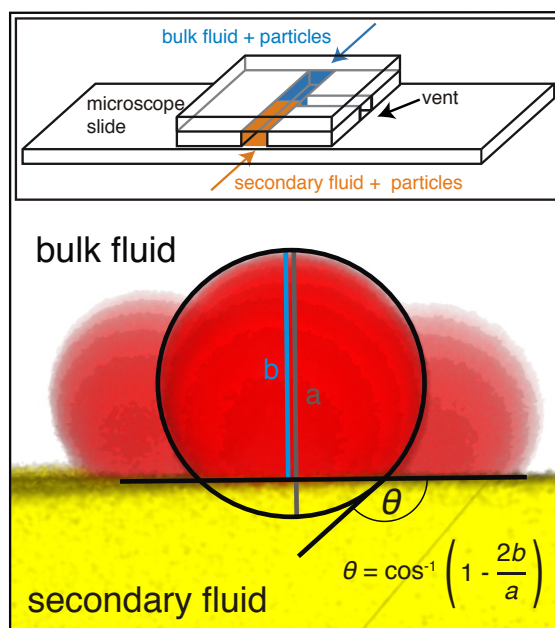
### Contact angle of composition C1

The contact angle  $\theta$  in samples with composition C1 was directly measured using confocal microscopy images. The method was published in “Structure of Particle Networks in Capillary Suspensions with Wetting and Nonwetting Fluids” by Frank Bossler and Erin Koos, *Langmuir*, 32(6), 1489–1501, 2016 ([hyperlink](#)), copyright ACS, reproduced with permission from ACS [150]. The dependence of the three-phase contact angle on the surface coverage of hydrophobic groups, and therefore on the TMCS concentration during the particle hydrophobization, is highly nonlinear [134]. This fact, together with the variable reaction kinetics, makes contact angle measurements of each surface treated C1 particle type necessary. A very small amount ( $\lesssim 0.5$  mg) of dyed particles was distributed in 10  $\mu\text{L}$  of oil phase as well as 10  $\mu\text{L}$  of the aqueous glycerol phase. These sparse dispersions were brought into contact in a custom-built microchannel on top of a microscope slide and were allowed to rest for at least 10 min to equilibrate. Some particles migrated to the fluid interface during this period. The slide with the sample was placed on top of the confocal microscope and 3D confocal pictures of individual particles sitting in the interface were taken. The 3D images were adjusted to show a 2D projection directly perpendicular to the interface (see Fig. 4.4 for an example image). The three-phase contact angle  $\theta$  was calculated directly via the geometry of a circular segment, due to the spherical particle shape. The contact angle is always defined as the angle the secondary phase makes with respect to the solid surface. The values determined have already been listed in Table 3.4.

The 3D images of single particles in the interface have been obtained with varying, much smaller voxel sizes than mentioned in section 4.2, below the resolution limit. In these cases the particles seemed somewhat elongated in  $z$  direction and also the exact position of the interface between both liquids was blurred due to a reduced number of photon emissions per voxel and, more crucial, an apparently increased dimension of objects as stated in eq. 4.4. Nevertheless, fits to the sphere and interface as shown in Fig. 4.4 were possible. However, due to this elongations in  $z$  direction, the error in the fits was smallest when the liquid-liquid interface during image acquisition was oriented parallel to the  $z$  axis of the microscope as the resolution in lateral direction is better than in vertical direction (eq. 4.1 vs eq. 4.2), whereas fits became more ambiguous for more tilted images. Contact angles were calculated as mean values from 8–14 images per particle type. A contact angle hysteresis could be observed in all cases, for some particles reaching up to  $\pm 15^\circ$ .

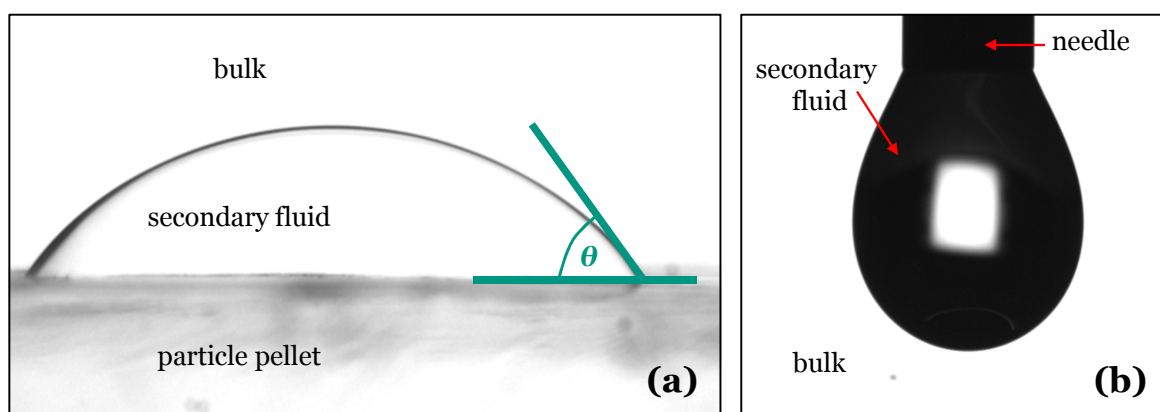
### Contact angle of composition C2 to C6

The confocal method of contact angle determination is only straightforward if the particles are perfectly spherical and particles as well as one of the two fluids are fluorescently dyed. Therefore it was not used for compositions C2 to C6. For all of these systems, the



**Figure 4.4:** Determination of the contact angle  $\theta$  for composition C1: The main figure shows an example 2D projection of a confocal 3D image of single particles (red) in the interface between bulk (uncolored) and secondary fluid (yellow). The circle and lines are added for better visualization of the geometry. The inset shows a schematic drawing of the custom built microchannel on the microscope slide. Figure reproduced with permission from ACS [150].

contact angle was determined with the sessile drop method using a high-resolution objective on a Stingray camera (Allied Vision, Stadroda, Germany) and evaluated via a numerical Young-Laplace fit to the imaged droplet contour [151] using a drop shape analysis software by Krüss GmbH (Hamburg, Germany). An example image is shown in Fig. 4.5a. Here,  $\theta$  was measured as the angle that an equilibrated secondary fluid droplet forms towards a pellet of compressed solid particles surrounded by the bulk fluid. To avoid air entrapment in any open pores, the pellet was completely soaked in the bulk fluid and degassed before the secondary fluid droplet was added [22]. For systems C5 and C6, po-



**Figure 4.5:** (a) Example image (composition C6) of a sessile drop experiment (b) Example image (secondary vs bulk liquid of composition C3) of a pendant drop experiment.

lished flat surfaces of  $\alpha\text{-Al}_2\text{O}_3$  or  $\text{CaCO}_3$ , respectively, were accessible, which were used instead of compressed particle pellets. While the contact angle measured on a polished flat surface might differ from the contact angle developing on a curved particle surface, the error in this case is expected to be lower as for the compressed pellets. As these pellets obtain a rough surface and liquid-filled pores, the sessile drop will surely show a different wetting here due to the effects described by Cassie-Baxter [75] and Wenzel [73] as already discussed in section 2.3.1. Therefore, the obtained contact angles in systems C2 to C6 should be used with caution as they can only provide rough estimates of the angle the bridges will form in the capillary suspension, while their general order of magnitude is expected to be correct. In any case, as for system C1, a large hysteresis in wetting is expected on the compressed pellets as well as on the particles [79], overshadowing most of these errors. The measured values have been already given in Table 3.1.

### Interfacial tensions

All interfacial tensions were determined with the pendant drop method using the same setup and software as used for the previously described sessile drop experiments. In this case, a droplet of the liquid with higher density, hanging from the orifice of a needle with well defined diameter of 1.65 mm, was placed into a cuvette filled with the lower-density liquid. An example image is shown in Fig. 4.5b. The equilibrated droplet shape was captured with the camera and the interfacial tension directly calculated from the fit. Both pendant drop and sessile drop experiments have been performed 10 times per sample at room temperature. Measured interfacial tension values can be found in the text of section 3.1.

## 4.4 Computational image evaluation

### General description

Image analysis of confocal 3D images was mainly completed using a self-written algorithm in IDL (Exelis VIS). As input, the IDL program requires confocal raw 3D image data, separated into its two detection channels, where every voxel is represented by an intensity value between 0 and 255. These two conjugate 3D images representing the particle and secondary fluid detection intensities are hereafter referred to as  $I_{\text{particles}}$  and  $I_{\text{secondary}}$ . Further, the image dimensions  $x_{\text{size}} = y_{\text{size}}, z_{\text{size}}$  and the expected mean particle radius  $a_{\text{exp}}$ , all of these in  $\mu\text{m}$ , are needed as input values. The image dimension in  $y$  is required to be identical to the dimension in  $x$  direction in the IDL algorithm. For all calculations,  $a_{\text{exp}}$  was allocated to the  $a_{50,3}$  radii given in Table. 3.2.

The program detects and localizes the particles (calculation of their total number, spatial sub-pixel position and individual size), calculates the effective volume fractions  $\phi_{\text{solid,eff}}$  and  $\phi_{\text{sec,eff}}$  (see section 3.3.2), the particle pair correlation function  $g(R/a)$ , the fractal dimension  $D$  of the particle network, and the histogram and mean value of the particle coordination number  $z$ . Localization of particle positions is based on modifications of the 3D particle tracking code of Weeks [152, 153], which is based on the widely-used 2D algorithm of Crocker and Grier [154]. Due to the size distribution and high volume fractions of particles in composition C1, more elaborate processing steps were necessary



for particle detection, similar to the procedures used by Wenzl et al. [131]. A pseudo-algorithm that summarizes the whole IDL calculation procedure is presented in Alg. 4.1 and is detailed stepwise in the next paragraphs.

### Image pre-processing

First, both 3D images are read in using the “readtiffstack.pro” function as provided by Weeks [155]. The number of voxels in all three spatial directions is extracted. In combination with the user-provided true image dimensions  $x_{\text{size}}$  and  $z_{\text{size}}$ , the  $\mu\text{m}$  dimensions  $x_v$  and  $z_v$  of a single voxel and its elongation factor in  $z$  direction,  $z_{\text{factor}} = z_v/x_v$ , are calculated (line 2 in Alg. 4.1). Then, the intensity loss in the particle image  $I_{\text{particles}}$  over  $z$  depth, resulting from slight mismatches in the sample’s refractive index, is adjusted (line 3). This is done by calculating the mean intensity of all of voxels of an intensity value  $\geq 10$  in the lowermost as well as the uppermost 20  $x$ - $y$  image slices, followed by a linear interpolation over the entire image to suitably raise intensities of every individual image slice to a level equivalent to the lowermost 20 slices. The adjusted image is binarized (line 4) using a threshold value optimized individually for every  $x$ - $y$  image slice by a moments-preserving thresholding method [156].

Afterward, the adjusted image  $I_{\text{adj}}$  is convolved with a mask (line 5), which is a necessary pre-detection step inherent to the algorithm of Crocker and Grier [154]. The original Weeks code (function “bpass3D.pro” [155]), with minor modifications, was used for each convolution step.  $I_{\text{adj}}$  is convolved with a Gaussian-like mask of size  $m$  mimicking the spherical particles, where in the 3D case  $m$  is a three-component vector incorporating the  $z_{\text{factor}}$  elongation. To account for the particle size distribution of the Kromasil silica (see Fig. 3.1d), four convolutions were executed with four different mask size vectors spanning the range of the particle size distribution. Here, the appropriate values for  $m$  were chosen based on the user-provided estimated mean particle radius  $a_{\text{exp}}$ . Voxel-wise, the maximum intensity value of the four different convolved images was chosen to obtain an optimized image. This multi-convolution method was originally developed by Wenzl et al. and is described in their publication and her PhD thesis in much more detail [36, 131].

### Particle detection

From the multiply convolved image  $I_{\text{conv}}$ , the particle positions were detected using the original Weeks algorithm (function “feature3D.pro” [155]). Applying only a single detection step to  $I_{\text{conv}}$  led to many erroneous detections, thus the feature3D function (line 11) was incorporated in a multi-step detection function “multfeature3D.pro” (lines 6–18 in Alg. 4.1). Similar to the previous convolution step, the detection was executed with five varied mask sizes, in decreasing order, spanning the whole range of the particle size distribution (line 9–11). After every step, the detected features positions were refined and the individual particle radii detected (line 12), again following a method introduced by Wenzl [36, 131]. First, nine vectors in differing spatial directions are drawn feature-wise through the pre-detected feature position in the binarized particle image  $I_{\text{bin}}$ . Then, 18 particle surface points (decay in the nine vectors from full to zero intensity) are determined. Miscalculated surface points due to neighboring particles are excluded and the remaining correct particle surface points fit to a sphere function (taken the  $z_{\text{factor}}$  elongation into account) using a Powell minimization algorithm. The four variables of the sphere fit contain



**Algorithm 4.1** IDL program for evaluating confocal 3D images of capillary suspensions

---

```

1: read in particle image ( $I_{\text{particles}}$ ) and secondary fluid image ( $I_{\text{secondary}}$ )
2: determine image and particle dimensions
3: adjust intensity of  $I_{\text{particles}} \rightarrow I_{\text{adj}}$ 
4: binarize  $I_{\text{adj}} \rightarrow I_{\text{bin}}$ 
5: multiple convolution of  $I_{\text{adj}}$ , "Wenzl method", leads to  $I_{\text{conv}}$ 

6: procedure MULTFEATURE3D( $I_{\text{conv}}, I_{\text{bin}}$ )
7:   set  $I_{\text{calc}} = I_{\text{bin}}$ 
8:   for  $i = 0$  to 2 do
9:     for  $j = a_{\text{max}}$  to  $a_{\text{min}}$  do
10:      get mask size  $m(j)$ 
11:      detect features in  $I_{\text{conv}}$  with Weeks algorithm and mask  $m(j)$ 
12:      detect the individual radius and center of every feature from image  $I_{\text{calc}}$ 
13:      remove misdetected features
14:      ignore double-detected features
15:    end for
16:    remove all correct detections from  $I_{\text{calc}}$ 
17:  end for
18: end procedure
19: remove misdetected features  $\rightarrow$  matrix  $\mathbf{P}$  containing all particle positions and radii

20: count number of particles in  $\mathbf{P}$ 
21: crop margins of  $I_{\text{particles}}$  using  $\mathbf{P}$ 
22: calculate mean particle radius  $a_{\text{mean,interim}}$  from  $\mathbf{P}$ 
23: calculate pair correlation function  $g$  from  $\mathbf{P}$  with  $a_{\text{mean,interim}}$ 
24: refine radii using first peak position of  $g$ 
25: recalculate all radii in  $\mathbf{P}$  and calculate corrected  $a_{\text{mean}}$ 

26: calculate  $\phi_{\text{solid,eff}}$  from  $\mathbf{P}$  using cropped margins
27: calculate  $D$  via 'N-vs-R' approach using  $\mathbf{P}$  with corrected  $a_{\text{mean}}$ 
28: recalculate  $g$  from  $\mathbf{P}$  with corrected  $a_{\text{mean}}$ 
29: calculate coordination number histogram and mean from  $\mathbf{P}$ 

30: check detection quality (overlay  $I_{\text{particles}}$  with  $\mathbf{P}$ ; check for sub-pixel bias and brightness of particles)
31: calculate particle size distribution, including  $a_{50,3}$  and polydispersity

32: overlay  $I_{\text{secondary}}$  with  $\mathbf{P}$ 
33: calculate  $\phi_{\text{sec,eff}}$ 

34: export data
35: save

```

---

the spatial position of the particle and its individual radius.

Afterward, the particles were checked for misdetections (line 13) by excluding particles that had a center position detected inside of another particle, particles that showed a significant overlap with other particles, and particles whose relative brightness compared to correct detected particles was very low. Additionally, particles that had been correctly detected in a previous step were also ignored in the subsequent detection steps (line 14). The correctly detected particles were added to a matrix  $\mathbf{P}$ .

This process of five detections with varied mask size was repeated two more times (line 8), on images where previously detected particles were removed from the binarized image, i.e. the intensity of the voxels occupied by their volume was set to zero in  $I_{\text{bin}}$  (line 16 in combination with line 7). This led to an improved refinement step (line 12) due to minimizing surface point misdetections evoked by adjacent particles, enabling correct detections of particles that had erroneously been rejected as misdetections in prior steps. After the final particle detection step was completed, the particle matrix  $\mathbf{P}$  was checked for misdetections once more (line 19).

### Radius refinement

The arithmetic mean particle radius  $a_{\text{mean,interim}}$  was directly calculated from the matrix  $\mathbf{P}$  (line 22 in Alg. 4.1). In the binarized images, the apparent particle surfaces are expected to slightly differ from the true surfaces. Thus, the detected radii have to be refined, which was done by means of the radial pair distribution function  $g(R/a)$ , which can be understood as the probability of finding a particle center at a radial distance  $R$  from another particle center. This function was determined following the recommended procedure from Weeks [157], first using  $a = a_{\text{mean,interim}}$  (line 23). One caveat mentioned by Weeks is the intersection of the spheres of radius  $R$  by artificial edges of the 3D image, impeding calculations of  $g$  for large values of  $R/a$ . This problem was solved by calculating the exact partial sphere volume located inside of the 3D image with closed-form volume equations. These rather lengthy equations are given in the appendix section 9.1.

For attractive capillary forces, the surface distance of two neighboring particles linked by a bridge is, a priori, expected to be zero (see chapter 2.3.2). Therefore, the first peak maximum of  $g(R/a)$  is expected to be at  $R/a = 2$ . The exact position of the first peak is determined from a six parameter Gauss fit to  $g(R/a)$  at  $1 < R/a < 3$  and its difference from  $R/a = 2$  calculated (line 24). This difference then is added to all radii of the particles in  $\mathbf{P}$  and the corrected arithmetic mean particle radius  $a_{\text{mean}}$  calculated (line 25). As particle sizes measured from light scattering (see section 3.1.1) were determined as volumetric mean  $a_{50,3}$  rather than arithmetic mean, the full particle size distributions as well as  $a_{50,3}$  are also computed (line 31).

### Determination of structural information

From the detected particles  $\mathbf{P}$ , various structural parameters of the particle network can be calculated. Apart from the trivial particle number  $N_{\text{total,img}}$  in the image (line 20 in Alg. 4.1), the calculation of the effective solid volume fraction  $\phi_{\text{solid,eff}}$  (line 26) is also straightforward, as each detected particle volume can be summed and divided by the volume of the 3D image. As particles cut at the margins of the image are not detected, the

image margin has to be cropped adequately (line 21) before this calculation to avoid an underestimation of  $\phi_{\text{solid,eff}}$ .

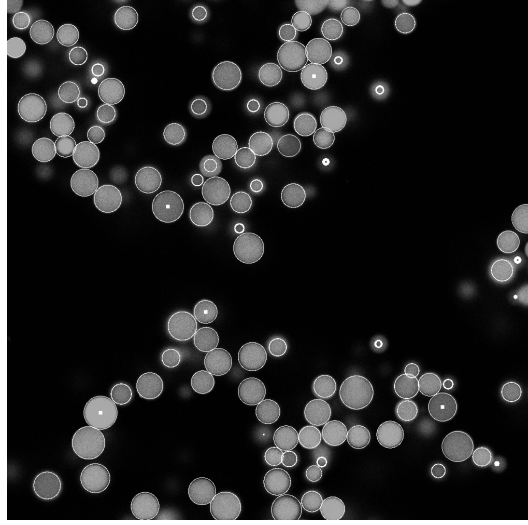
For all particles farther away than  $12 \cdot a_{\text{mean}}$  from all image margins, the number of surrounding particles  $N$  as function of the radial distance  $R/a_{\text{mean}}$  to the center of the actual reference particle was calculated. Usually, 350–550 reference particles per image fulfilled this margin distance condition. The fractal dimension  $D$  then was obtained by fitting a power law in the range  $2 < R/a_{\text{mean}} < 10$  to the determined particle numbers  $N$ , using the relation  $N(R/a) \propto (R/a)^D$ , see eq. 2.29 (line 27). The pair correlation function was also recalculated using the corrected radius (line 28).

Furthermore, a pairwise calculation of all particle surface distances was executed. All particle pairs exhibiting a surface distance smaller than a given threshold value are counted as particle contacts. The choice of an appropriate threshold is somewhat difficult. Taking the vertical resolution into account (eq. 4.2), a fixed value of  $0.85 \mu\text{m}$  has been chosen as a threshold for all calculations. This value is much larger than the expected zero surface distance, but is still less than twice the resolution limit. Therefore, it represents a compromise between erroneously assigning contacts to too many non-contacting particles and missing too many real contacts that suffer from misdetected surface positions. However, while the threshold value was optimized, the detected particle contacts should be treated cautiously due to this somewhat arbitrary choice. From the contact points, a histogram of contacts per particle as well as a mean contact number, i.e. the mean coordination number  $z$ , are calculated (line 29).

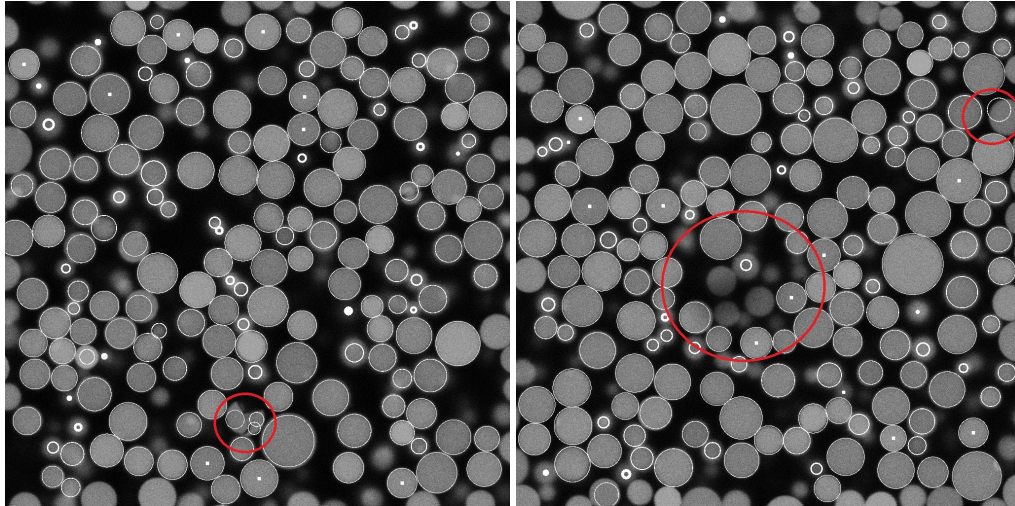
Finally, the secondary fluid image  $I_{\text{secondary}}$  is overlaid with the detected particles  $P$  (line 32), where every secondary fluid voxel lying inside of a particle is replaced by a zero intensity voxel to exclude secondary fluid volumes inside of any particle pores from further calculations. From this adjusted image, the effective secondary fluid volume fraction  $\phi_{\text{sec,eff}}$  is calculated by counting the number of voxels with intensity larger than a threshold value and dividing them by the total voxel number of the image (line 33). A fixed intensity value of 65 was chosen as threshold, as this showed more robust results than any “optimized” thresholding algorithms that provided mean bridge size dependent thresholds leading to a severe overestimation of  $\phi_{\text{sec,eff}}$  for samples with only few small capillary bridges.

### Detection accuracy and possible errors

To check the accuracy of the detections (line 30 in Alg. 4.1), the raw image  $I_{\text{particles}}$  can be overlaid with a representation of the surfaces and particle centers contained in  $P$ . Different 2D slices of such overlay images can be checked to get an optical impression of the detection accuracy. Fig. 4.6 gives an example detection containing particles from batch “6.2 porous” (see Table 3.4). Two additional example overlay images are shown in Fig. 4.7, where three problematic issues for the detection, namely overly dark particles, broken particles and errors at the edges of the image are depicted. While these problems could not be fully avoided, the chemical treatment of the particles and the sample preparation (sections 3.2 and 3.3.1) were adequate to only lead to very few broken particles on the order of  $\approx 1$  per 1000–3000 particles. Regions of many neighboring particles that are too dark, as shown in Fig. 4.7, can be attributed to either photobleaching of these particles during adjustments of the microscope before image acquisitions or to air bubbles in the sample leading to an unwanted local obstacle deteriorating the microstructure and



**Figure 4.6:** Example overlay image showing an  $x$ - $y$  image slice of a 3D confocal particle raw image overlayed with detected particle surfaces (white circles) and centers (white dots). For particles without a dot, the center lies in a different  $z$  slice of the image. The sample shown is from batch “6.2 porous”, with  $\theta = 87 \pm 8^\circ$ ,  $\phi_{\text{solid,set}} = 0.08$  and  $\phi_{\text{sec,set}}/\phi_{\text{solid,set}} = 0.08$ .



**Figure 4.7:** Two example overlay images that show three unwanted effects, denoted by the red circles: broken particles that are incorrectly detected, dark particles that are detected not at all and errors in particle detections at the image edge. Both images are from batch “6.1 porous”, with  $\theta = 109 \pm 5^\circ$ ,  $\phi_{\text{solid,set}} = 0.25$ .

inducing a mismatch in refractive index leading to an intensity loss propagating through all  $z$  slices lying deeper in the sample. However, such bubbles were thankfully easy to see. Thus, while such sloppy experimentation was avoided when producing the real data, an example image of such an unwanted effect in a not further evaluated image still is shown here as caveat.

Furthermore, histograms of the sub-pixel distribution of the  $x$ ,  $y$  and  $z$  center positions of all particles were plotted to exclude any sub-pixel bias [36, 158] as an additional check of detection quality.

## 5 Influence of Sample Preparation

Chapter 5 is mostly based on the publication “Influence of mixing conditions on the rheological properties and structure of capillary suspensions” by Frank Bossler, Lydia Weyrauch, Robert Schmidt and Erin Koos, *Colloids and Surfaces A: Physicochemical and Engineering Aspects*, 518, 85–97, 2017 ([hyperlink](#)), copyright Elsevier, reproduced with permission from Elsevier [108]. Everything apart from the newly added subsections 5.1.1 and 5.2.3 was part of the “results” section of this publication and is to a large extent reproduced here with relatively minor changes.

### 5.1 Turbulent mixing with a dissolver stirrer

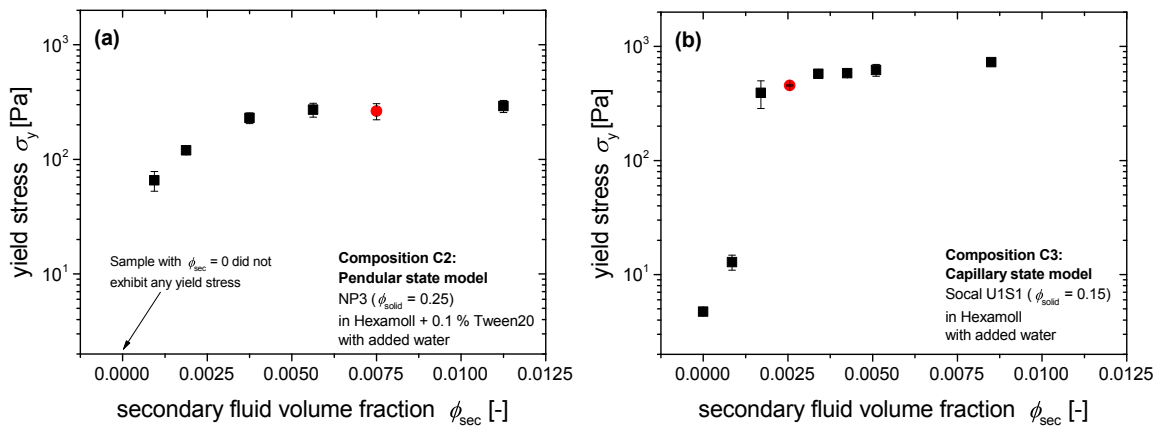
In many recent publications, capillary suspensions were prepared in a lab scale using a dissolver stirrer (e.g. [2, 17, 19, 21, 22]), where the secondary fluid was added to the suspension while stirring with a non-optimized stirring speed and mixing time. Thus, the series of experiments presented in chapter 5.1 evaluate the influence of different stirring speeds and times on the rheology and structure of capillary suspensions in both pendular and capillary states of sample compositions C2 and C3 (see Table 3.1), respectively.

#### 5.1.1 Choice of a pendular and capillary state reference sample

To evaluate the influence of the stirring speed and time during sample preparation on the rheology of the resulting capillary suspension samples, one reference sample for each the pendular state model system C2 and capillary state model system C3 were used. The yield stress was chosen as an appropriate reference for the different samples with varied secondary fluid volume fraction at a fixed solid fraction of  $\phi_{\text{solid}} = 0.25$  for C2 and  $\phi_{\text{solid}} = 0.15$  for C3 samples, as shown in Fig. 5.1. Sample preparation protocols followed the dissolver mixing “method A” (see section 3.3.1) where the stirring speeds and times were kept constant, with  $n_1 = 2000$  rpm,  $\Delta t_1 = 20$  min,  $n_2 = 2000$  rpm and  $\Delta t_2 = 20$  min. This choice of  $n_2$  and  $\Delta t_2$  is close to the upper limit of speeds and times examined in sections 5.1.2 and 5.1.3.

Starting from lower yield stress values (or in the case of C2, no yield stress value), the yield stress quickly increases with small amounts of added secondary fluid and, in both compositions, then enters a plateau value around  $\approx 200$ -300 Pa in the pendular state system and  $\approx 500$ -700 Pa in the capillary state system. The appearance of this plateau is a well-known characteristics of capillary suspensions and denotes a fully-established percolated particle network [10]. Based on the data shown in Fig. 5.1, the sample with  $\phi_{\text{sec}} = 0.0075$  for system C2 and  $\phi_{\text{sec}} = 0.00255$  for system C3 were selected as reference





**Figure 5.1:** Yield stress  $\sigma_y$  as a function of secondary fluid volume fraction  $\phi_{\text{sec}}$  for (a) pendular state model compositions C2 with  $\phi_{\text{solid}} = 0.25$  and (b) capillary state model compositions C3 with  $\phi_{\text{solid}} = 0.15$ . Both series of samples have been prepared with  $n_2 = 2000$  rpm and  $\Delta t_2 = 20$  min during the second mixing step. The two samples marked by the red circle symbol have been chosen as reference compositions for the following experiments.

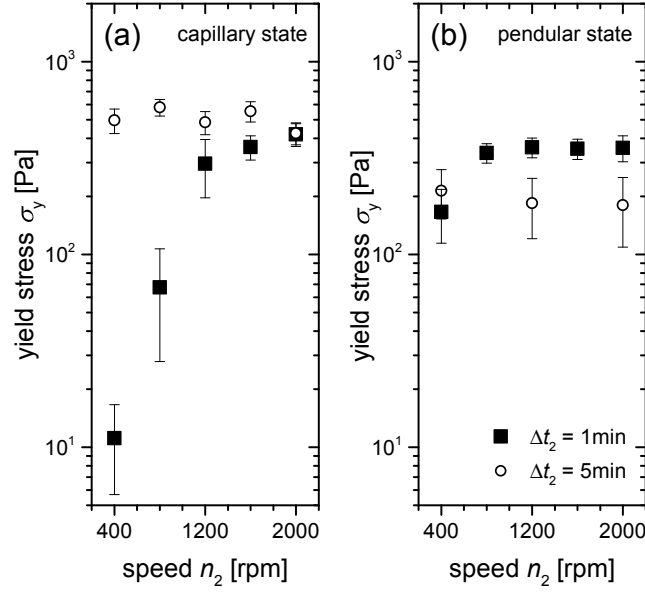
samples. Both of these compositions are in the yield stress plateau region, but still close to its starting point. Thus, a fully-established capillary suspension can be prepared for both sample suspensions with the “high” chosen values of  $n_2 = 2000$  rpm and  $\Delta t_2 = 20$  min. Deviations in the yield stress for this same compositions can thusly be directly accredited to the influence of the mixing itself.

### 5.1.2 Influence of stirring speed

The reference C2 and reference C3 sample compositions determined in the previous section have been used to evaluate the influence of stirring speed and time during sample preparation on the rheology of the resulting capillary suspension samples. The samples have been prepared with different stirring speeds  $n_2$  upon the addition of the secondary fluid into the homogenized suspensions of particles in oil. The yield stress of these compositions is shown in Fig. 5.2.

The capillary state system (Fig. 5.2a) shows a strong increase in yield stress from 11 Pa to 420 Pa with increasing stirring speed from 400 rpm to 2000 rpm for stirring times of 1 min. The standard deviation between measurements also decreases, indicating a more homogeneous structure when faster stirring speeds are used. A similar trend can be seen for the pendular system (Fig. 5.2b) prepared with 1 min stirring time, where the yield stress increases from 165 Pa to 360 Pa when the stirring speed is increased from 400 rpm to 1200 rpm. The influence of the stirring speed here is weaker in the pendular state than in the capillary state and the yield stress reaches a constant value for stirring speeds larger than 1200 rpm.

The increase in stirring speed is directly proportional to an increase in stirring energy input and power input as described by equation 2.64. Therefore, higher speeds should lead to an enhanced droplet breakup under turbulent flow conditions and a decrease in secondary fluid droplet size (equation 2.63). The same should be true under laminar flow conditions, where Grace theory applies (equation 2.61) and increased stirring speed di-

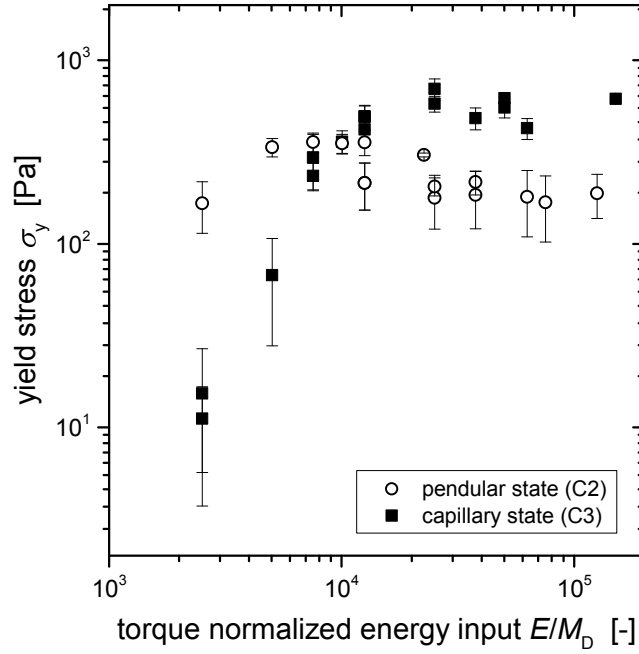


**Figure 5.2:** Dependence of the yield stress  $\sigma_y$  on the stirring speed  $n_2$  for the (a) capillary state model system C3 reference sample ( $\phi_{\text{solid}} = 0.15$  and  $\phi_{\text{sec}} = 0.00255$ ) and (b) pendular state model system C2 reference sample ( $\phi_{\text{solid}} = 0.25$  and  $\phi_{\text{sec}} = 0.0075$ ). Both systems were prepared with a stirring time of  $\Delta t_2 = 1$  min (filled squares) or 5 min (open circles). Figure reproduced with permission from Elsevier [108].

rectly translates into larger shear rates and thus smaller droplet sizes when the system approaches  $\text{Ca}_{\text{crit}}$ . The overall number of droplets increases when the droplet size is decreased. Thus, there is a larger number of droplets available to serve as center of the basic building blocks for the capillary state network. Moreover, simulations have identified that smaller (e.g. tetrahedral) blocks show an increase in strength when compared to their larger (e.g. octahedral) cousins [8]. This is manifested in the increased network strength as found in the yield stress data of Fig. 5.2. In the pendular state, the increased number of droplets also leads to a larger coordination number of bridges between particles raising the sample's overall attractive capillary force and therefore also the yield stress (equation 2.59).

There appears to be a maximum energy input where the yield stress does not increase any further. This can be observed from the plateau value of the yield stress ( $\sigma_y \approx 360$  Pa) for stirring speeds larger than 1200 rpm at 1 min stirring time in the pendular state sample (Fig. 5.2b). Such a plateau also occurs for the capillary state sample when a stirring time of 5 min is applied (Fig. 5.2a,  $\sigma_y \approx 500$  Pa). Under the applied mixing conditions in the capillary state model system, this plateau is reached, following equation 2.64, at  $E \approx 400\text{rpm} \cdot 5\text{min} \cdot 2\pi M_D = 2000\text{rpm} \cdot 1\text{min} \cdot 2\pi M_D \approx 12566 \cdot M_D$  as derived from a comparison of the yield stress values of the sample prepared at 400 rpm for 5 min and the sample prepared at 2000 rpm and 1 min. Both of these samples should have experienced this same energy input as the energy input is proportional to  $n_2 \cdot \Delta t_2$  (see equation 2.64), and indeed show very similar yield stress values. This influence of the energy input can be seen even better in Fig. 5.3 where the yield stress of compositions C2 and C3 prepared at different  $\Delta t_2$  and  $n_2$  are plotted as function of the energy input  $E$  normalized by the dissolver torque  $M_D$ . The data presented in Fig. 5.3 includes all the data from Fig. 5.2





**Figure 5.3:** Yield stress  $\sigma_y$  of different pendular state (C2, open circles) and capillary state (C3, filled squares) reference sample compositions as function of the dissolver torque normalized energy input  $E / M_D = 2\pi n_2 \Delta t_2$ . Figure reproduced with permission from Elsevier [108].

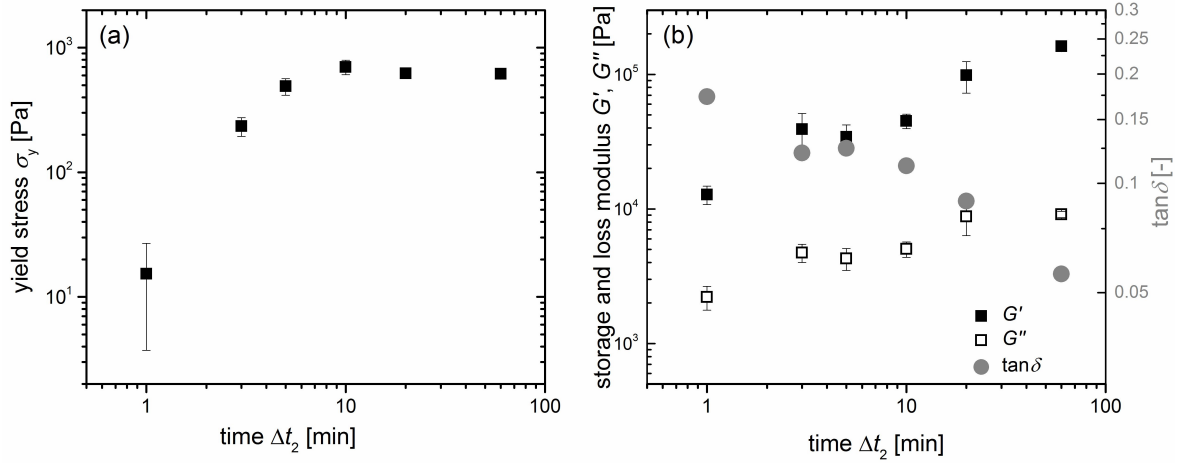
in a rescaled form, with some additional new points included. As both  $E$  and  $M_D$  are unknown, the abscissa  $E / M_D$  was calculated using equation 2.64 as  $E / M_D = 2\pi \cdot n_2 \cdot \Delta t_2$ .

The yield stress also seems not to depend on the speed for the pendular state system (Fig. 5.2b) after 5 min of stirring, but the average value ( $\sigma_y \approx 200$  Pa) is clearly smaller than for 1 min stirring time and these longer stirring times also show much larger errors between measurements. This behavior cannot be explained by the energy input alone as higher energy inputs should lead to smaller droplets contradicting this observed reduction in strength. To understand this effect, a closer look at the stirring time influence separately is necessary.

### 5.1.3 Influence of stirring time

For the capillary state sample system C3 with reference composition of  $\phi_{\text{solid}} = 0.15$  and  $\phi_{\text{sec}} = 0.00255$ , the yield stress values discussed in section 5.1.2 increased with stirring speed until they reached a plateau. This effect was explained by an enhanced droplet breakup with increasing stirring energy input. The same findings can also be reproduced when the energy input is increased by varying the stirring time  $\Delta t_2$  and keeping the speed constant as shown for  $n_2 = 400$  rpm in Fig. 5.4a.

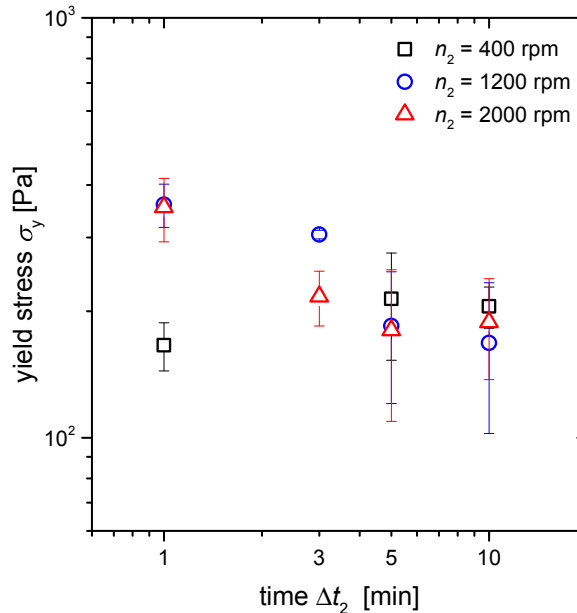
As expected, the yield stress increases when  $\Delta t_2$  is extended from 1 to 10 min and then enters a plateau region where no further increase is observed up to  $\Delta t_2 = 60$  min. The storage and loss moduli,  $G'$  and  $G''$  also increase with increasing stirring time and thus energy input (Fig. 5.4b). Interestingly, a plateau is not reached after 10 min, but both moduli continue to increase in the observed time range. This can additionally be seen in the decrease in  $\tan \delta = G'' / G'$ , denoting a steadily increasing ratio of the elastic over the



**Figure 5.4:** Dependence of the (a) yield stress  $\sigma_y$  as well as (b) storage modulus  $G'$ , loss modulus  $G''$  and  $\tan \delta$  on the stirring time for the capillary state model system C3 with reference composition of  $\phi_{\text{solid}} = 0.15$  and  $\phi_{\text{sec}} = 0.00255$ . The stirring speed of all samples was  $n_2 = 400$  rpm. The oscillatory data in (b) was obtained at a strain amplitude in the linear viscoelastic region with  $\omega = 1$  rad/s. Figure reproduced with permission from Elsevier [108].

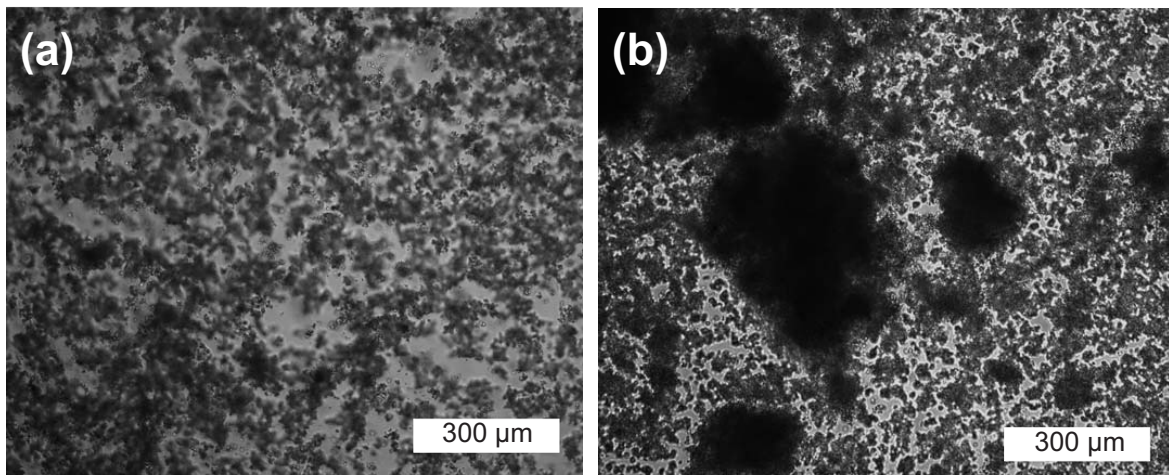
viscous properties of these capillary suspensions. Altogether, the capillary state strength always strengthens when the energy input during sample preparation is increased either by longer times or faster speed.

The same improvement in the network structure with increasing mixing time, as demonstrated for the capillary state sample, is not shown for the pendular state system C2 with reference composition of  $\phi_{\text{solid}} = 0.25$  and  $\phi_{\text{sec}} = 0.0075$  (Fig. 5.5). When the stirring



**Figure 5.5:** Dependence of the yield stress on the stirring time  $\Delta t_2$  for the pendular state model system C2 with reference composition of  $\phi_{\text{solid}} = 0.25$  and  $\phi_{\text{sec}} = 0.0075$  for stirring speeds of  $n_2 = 400$  rpm (black filled triangles), 1200 rpm (blue open triangles) and 2000 rpm (red half-filled triangles). Figure reproduced with permission from Elsevier [108].

time  $\Delta t_2$  is increased from 1 to 10 min, the yield stress only increases very slightly at an applied speed of 400 rpm, while it decreases for speeds of 1200 rpm and 2000 rpm. High stirring speeds only lead to strong networks at relatively low stirring times. The standard deviation between consecutive measurements increases for all samples at longer stirring times and the yield stress tends to have similar values ( $\approx 200$  Pa) independent of  $n_2$  then (at  $\Delta t_2 = 10$  min). The decrease in yield stress values appears at shorter times for 2000 rpm than for 1200 rpm implying that this trend is related to the total energy input. The large error bars indicate severe inhomogeneities in the sample structure. Indeed, large agglomerates were visible by eye with increasing stirring time, whereas the samples were homogeneous in the beginning and lacked such large structures. Light microscopy images of samples stirred at 2000 rpm for 1 min and 10 min are shown in Fig. 5.6. These



**Figure 5.6:** Bright field microscopy images of the pendular state model system C2 with reference composition of  $\phi_{\text{solid}} = 0.25$  and  $\phi_{\text{sec}} = 0.0075$ , prepared with stirring speed  $n_2 = 2000$  rpm and stirring times (a)  $\Delta t_2 = 1$  min and (b)  $\Delta t_2 = 10$  min. Figure reproduced with permission from Elsevier [108].

images were taken with an inverted bright field light microscope (Axio Observer D1, Carl Zeiss, Oberkochen, Germany) equipped with an objective having 10 $\times$  magnification and a numerical aperture of 0.25 (A-PLAN 10 $\times$  /0.25, Carl Zeiss). The large agglomerates present after 10 min are clearly visible, while only small clusters are present for the 1 min stirring time.

The droplet breakup enhancement due to increased energy input competes with the agglomeration kinetics, which increasingly dominates at longer mixing times. Such kinetics are well known from wet agglomeration processes where fluid is added to dry granular matter. However, the agglomeration occurs here at lower secondary liquid to solid fractions than is typical for wet granular materials [27, 159]. This may be due to the lower solid volume fraction allowing easier rearrangement of the particle network (through energy neutral rotations), causing dense agglomerates, which maximize the local coordination number, to form even without bridge coalescence, but this hypothesis cannot be proven here. In general, spherical agglomerates grow with increasing mixing time and these agglomerates become increasingly compact and difficult to break since the fluid in the agglomerate is completely interconnected [159]. With a lab-scale dissolver stirrer, these agglomerates are effectively irreversible since their destruction would require very

high shear rates that this type of stirrer cannot realize. It can be broken down much easier when the secondary fluid inside of an agglomerate is not completely interconnected, but merely is held together by many separate smaller fluid bridges [159]. To achieve such less densely packed agglomerates, the secondary fluid droplets must already be relatively small before agglomeration starts [160]. This agglomeration type is favored when shear rates are high and the droplet fluid viscosity is rather small [161].

In a capillary suspension, large agglomerates destabilize the structure in a manifold way. An agglomerate immobilizes large amounts of secondary fluid, which is no longer well-distributed over the sample and thus the overall number of pendular bridges decreases. The large agglomerates also behave like large particles that are affected by gravitational forces (increasing with particle size cubed) or inertia (increasing with particle size squared) to a much greater degree compared to the capillary force, which has a linear dependence on particle size (see equation 2.59) [85].

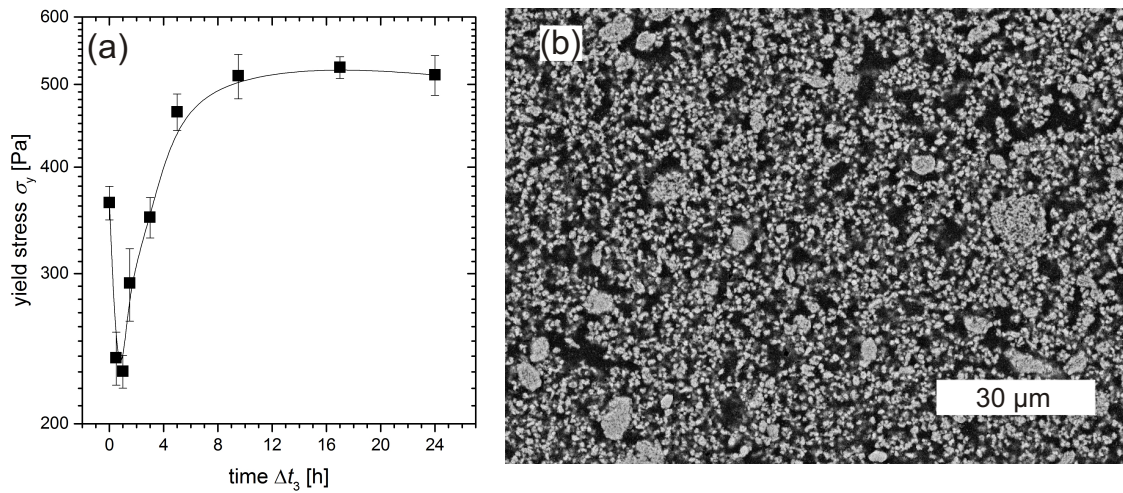
One necessary precondition to form compact agglomerates is that the added fluid must wet the particles. This is the case in the pendular state where the three-phase contact angle of the secondary fluid towards the particles is smaller  $90^\circ$ . In the capillary state, the secondary fluid wets the particles less well than the bulk fluid thereby preventing large-scale agglomeration due to the addition of the secondary fluid. This explains why these effects were not found for capillary state system C3 in Fig. 5.4. While the capillary state by itself is a clustered structure, these clusters are not directly stabilized by attractive capillary forces and negative Laplace pressure of the secondary fluid interspersing the cluster as is the case for the pendular state. Instead, stabilization is based on energetic favorability of small droplets being shielded by the solid particles [8]. This kind of stabilization is not strong enough to build up large, densely-packed spherical agglomerates that are able to resist strong stirring for long times. In fact, these capillary clusters resemble the partially porous agglomerates of Knight et al., which have the tendency to break rather easily [159].

## 5.2 Alternative sample preparation methods

Alternative sample preparation approaches are examined in section 5.2, where either an additional mixing step with a ball mill was applied after turbulent dissolver stirring, where the order of addition of the three sample components was changed or where ultrasonication was used for sample preparation.

### 5.2.1 Mixing on a ball mill

In recent studies, pendular state systems based on aluminum oxide or silica have been prepared by first applying the dissolver stirrer method, discussed in section 5.1, followed by homogenization of the sample structure on a ball mill for  $\Delta t_3 = 24$  h [10–12], see section 3.3.1. Experiments with one aluminum oxide sample of composition C5 with  $a_{50,3} = 0.32$   $\mu\text{m}$ ,  $\phi_{\text{solid}} = 0.15$  and  $\phi_{\text{sec}} = 0.018$ , have been reproduced while the homogenization time on the ball mill  $\Delta t_3$  was varied, as shown in Fig. 5.7. This sample composition is lying in the yield stress plateau region denoting a fully established particle network as will be seen later in chapter 6.3.1. Pendular state systems of composition C5 often show many agglomerates with sizes  $>100$   $\mu\text{m}$  (i.e. greater than 100 particle diameters for the actual



**Figure 5.7:** (a) Dependence of the yield stress on the ball mill processing time  $\Delta t_3$  for the  $\text{Al}_2\text{O}_3$ -based pendular state system C5 with  $\phi_{\text{solid}} = 0.15$  and  $\phi_{\text{sec}} = 0.018$ . The line only serves as guide for the eyes. (b) SEM image of the sintered ceramic from the same sample composition prepared with  $\Delta t_3 = 24$  h showing some of the residual aggregates. The mean radius of single particles is  $a_{50,3} = 0.32 \mu\text{m}$ . Figure reproduced with permission from Elsevier [108].

particle size) visible with the naked eye after the dissolver stirrer preparation ( $\Delta t_3 = 0$  h,  $\sigma_y = 360 \pm 20$  Pa). As discussed previously in section 5.1.3, pendular state systems are prone to agglomeration.

When the homogenization time is increased, the yield stress first decreases until a minimum value around  $\sigma_y = 230$  Pa at  $\Delta t_3 = 1$  h is reached. Then, the yield stress starts to increase until it reaches a plateau value around  $\sigma_y = 515$  Pa after  $\Delta t_3 = 9.5$  h. Further increases to the homogenization time, up to 24 h, do not have any impact on the yield stress. The yield stress decrease in the first hour on the ball mill can probably be attributed to a destabilization of the structure through increasing agglomeration. The increase in the yield stress for  $\Delta t_3 > 1$  h can be ascribed to the mechanical load in the ball mill, which is completely different than the turbulent shear flow mixing from the dissolver stirrer preparation. Shear forces in the ball mill are comparably small, while the impact on the sample of balls colliding with each other or the bottom of the vessel is more important. The momentum at impact is very high due to the balls weight, and can easily smash any large agglomerates residing around impact position. Thus, in contrast to the turbulent shear flow from the dissolver stirrer, a reduction in agglomerate size is possible with sufficient mixing times, due to these local impacts. At the same time the kinetics of building new agglomerates is greatly slowed down, as global mixing of the sample is heavily reduced in the ball mill compared with the dissolver stirrer. The quality of homogenization should depend on the mass of the balls and, to a lesser degree, on the rotational speed. With heavier balls, the momentum is higher and thus the probability to destroy any nearby agglomerate increases. It is, nevertheless, important to note that complete de-agglomeration does not occur. The yield plateau value does not indicate an absence of agglomerates, but more likely an equilibrium between agglomerate growth and disintegration. SEM images of a sintered aluminum oxide ceramic sample (for the sintering method see [10]) after 24 h of homogenization showed that flocs in a relatively narrow diameter range of 5-15  $\mu\text{m}$ , each containing a small number of particles ( $a_{50,3} = 0.32 \mu\text{m}$ ),

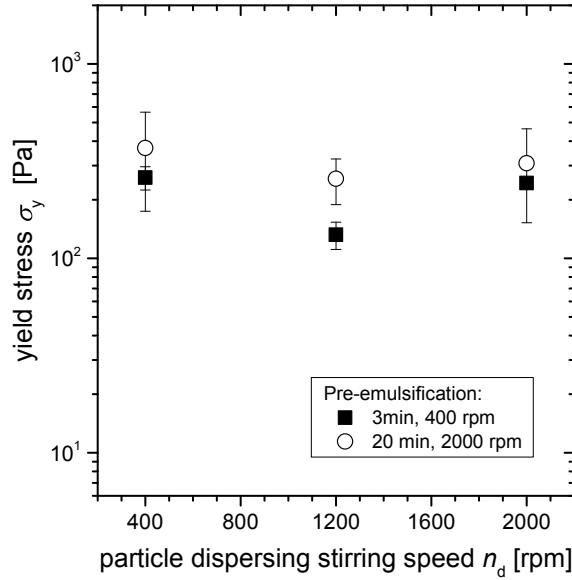


are still present (Fig. 5.7b). There are, however, none of the very large agglomerates as found in the pendular state system C2 in Fig. 5.5b with sizes greater than 100 particle diameters. The ball mill homogenization cannot completely avoid particle agglomeration as this is inherent to pendular state systems since the preferred wetting of the secondary fluid towards the particles ( $\theta$  less than  $90^\circ$ ), and especially since there are droplets involved whose size is larger than single particle diameter, which is always the case when the secondary fluid is added to the suspension of pre-dispersed particles in the bulk fluid. The use of the ball mill, nevertheless, leads to much more homogeneous structures and higher yield stress values than the turbulent flow stirring alone. Finally it should be noted, that neither in this study nor in earlier experiments [10] any crushing of the aluminum oxide particles in the ball mill was observed. However, such crushing of particles can appear for other sample systems, e.g. the glass based system C2. Thus, while the ball mill can be a very helpful mixing instrument to prepare relatively homogeneous capillary suspensions, it is not applicable with all types of solid particles.

### 5.2.2 Secondary fluid emulsification before particle addition

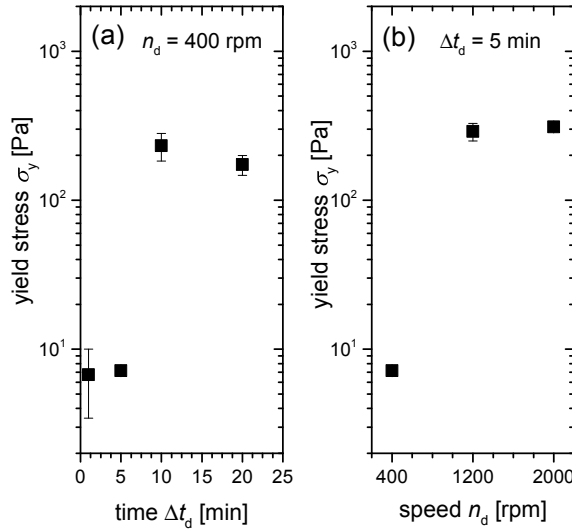
One possible option to thwart the growth of agglomerates during mixing in pendular state systems is to change the mixing order so that the secondary fluid is first stirred into the pure bulk liquid to produce an unstabilized (or weakly stabilized) emulsion. Only afterward are the particles added [5]. The goal of this mixing order, specified as dissolver “method B” in section 3.3.1, is to better control the secondary fluid droplet size. When the particles first come into contact with the secondary fluid, secondary fluid droplet size is ideally smaller than the particle size which is not the case for the conventional mixing order used in the preceding sections. This mixing order should avoid or at least reduce the buildup of compact agglomerates [6, 159].

The pendular state model system C2 with the reference composition of  $\phi_{\text{solid}} = 0.25$  and  $\phi_{\text{sec}} = 0.0075$  (see section 5.1.1) is shown in Fig. 5.8 where this changed mixing order was applied. The secondary fluid was first emulsified with low energy input (3 min at 400 rpm) or high energy input (20 min at 2000 rpm). The particles were then added and stirring continued for a dispersing time  $\Delta t_d = 3$  min with varied speeds  $n_d$ . Changes to the dispersing time after particle addition were avoided due to the complications described in section 5.1.3. The detrimental effects of particle agglomeration are expected for larger stirring times even in the case where the secondary fluid was pre-dispersed very well before [159]. The change in dispersing speed  $n_d$  was expected to influence the yield stress as seen in section 5.1.2. However, no significant trend of the yield stress with the speed  $n_d$  can be seen. As composition C2 contains some small amounts of surfactant, the emulsion of secondary fluid in the bulk liquid is stable enough to show very little coalescence in the short rest time between emulsification and particle addition. No further change in droplet size seems to appear following the addition of particles, leading to the observed absence of dispersing speed influence. Nevertheless, the samples that have been pre-emulsified with relatively low energy input for all dispersing speeds show a weaker yield stress than the samples pre-emulsified with the higher energy input. Therefore, the energy input during pre-emulsification determines the resulting structure with higher energy input leading to stronger samples due to smaller droplets. This result agrees with droplet breakup theory as discussed in section 5.1.2 and also with the findings of Domenech and Velankar [5].



**Figure 5.8:** Dependence of the yield stress on the stirring speed  $n_d$  for the pendular state model system C2 with  $\phi_{\text{solid}} = 0.25$  and  $\phi_{\text{sec}} = 0.0075$  when the particles are added to a pre-emulsified mixture of secondary and bulk fluid. Dispersing time after particle addition was 3 min for all samples shown. Energy input for pre-emulsification was relatively low ( $\Delta t = 3$  min,  $n = 400$  rpm, filled squares) or high ( $\Delta t = 20$  min,  $n = 2000$  rpm, open circles). Figure reproduced with permission from Elsevier [108].

Fig. 5.9 shows samples with the capillary state system C3 with reference composition of  $\phi_{\text{solid}} = 0.15$  and  $\phi_{\text{sec}} = 0.00255$  where the secondary fluid was first emulsified with rela-



**Figure 5.9:** Yield stress of the capillary state model system C3 with  $\phi_{\text{solid}} = 0.15$  and  $\phi_{\text{sec}} = 0.00255$  when the particles are added to a pre-emulsified mixture of secondary and bulk fluid. Stirring time and speed for pre-emulsification always were  $t = 20$  min and  $n = 2000$  rpm. (a) Variation of dispersing time  $\Delta t_d$  after particle addition at constant speed  $n_d = 400$  rpm. (b) Variation of dispersing speed  $n_d$  at constant time of  $\Delta t_d = 5$  min. Figure reproduced with permission from Elsevier [108].

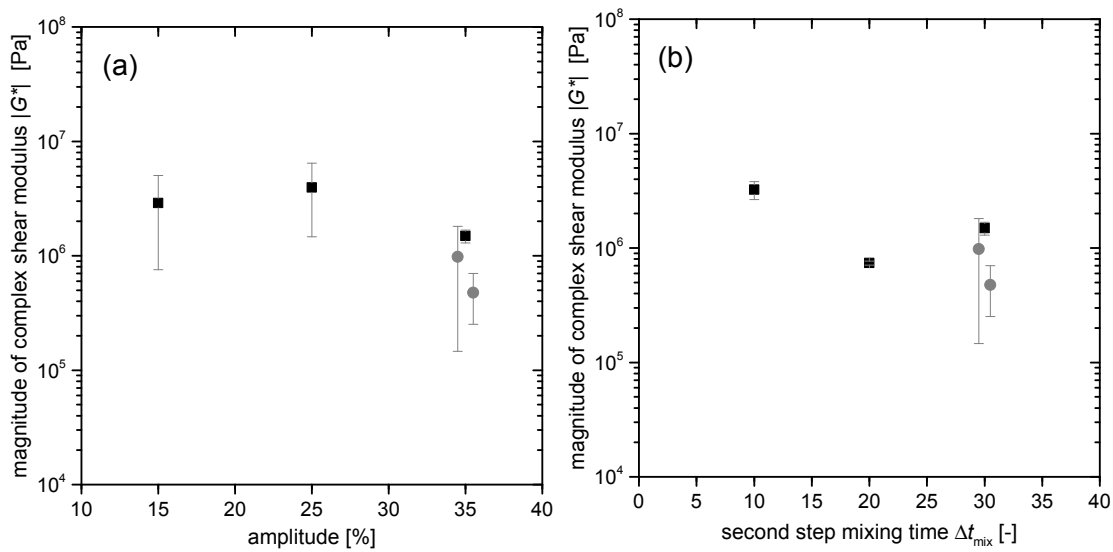


tively high energy input (20 min at 2000 rpm) before particle addition and further stirred with varied dispersing time or speed. Although a relatively high energy input (i.e. expected good droplet breakup) has been chosen for pre-emulsification, the yield stress depends strongly on the dispersing time as well as dispersing speed after particle addition, contrary to the behavior of composition C2 discussed before. Increased energy input after particle addition leads to stronger yield stress values, implying a further reduction in droplet size in this sample preparation step. The most probable explanation is not any difference between pendular and capillary state, but merely the fact that system C3 does not contain an emulsifier and thus the droplets of secondary fluid without stabilization tend to coalesce during and after the pre-emulsification step. The rate of coalescence directly competes with the droplet breakup and thus does not lead to comparatively small droplets of secondary fluid. The dependence of the yield stress on dispersing time and speed after particle addition then relies on identical breakup characteristics as already described in sections 5.1.2 and 5.1.3. Thus, a change in capillary suspension preparation order can be beneficial when the pre-emulsion is stabilized against droplet coalescence or the bulk fluid viscosity slows the kinetics adequately, while coalescence can annihilate this benefit otherwise.

### 5.2.3 Emulsification and mixing using ultrasound

For samples with composition C1, ultrasonication was used for sample preparation, see section 3.3.1. To obtain information on this preparation method, a series of experiments was performed on a C1 sample with particles of batch “5 porous” ( $\theta = 102^\circ$ , see Table 3.4), using  $\phi_{\text{solid, set}} = 0.25$  and  $\phi_{\text{sec, set}} = 0.0225$ . This is comparable to the porous particle compositions used later in chapter 6.1. As in the previous subsection, the ultrasonication method first emulsifies both fluids before the particles are subsequently added. Fig. 5.10a shows the complex shear modulus  $|G^*|$  of experiments where the amplitude in the emulsification step was varied. The number of mixing steps (one to three steps of 10 s duration each) was varied in Fig. 5.10b. Every data point shown in Fig. 5.10 contains three rheological measurements of a single prepared sample, while the gray circles denote repeated preparations of samples prepared by applying exactly the same conditions as for the directly neighboring black data point (offset slightly). The measurement error of most samples is very large, sometimes encompassing one decade in  $|G^*|$  values. Thus, no clear trends on the applied amplitude and particle mixing time can be deduced. There might be a decrease in  $|G^*|$  with increasing amplitude and with mixing time, but this remains speculative given the measurement errors. This becomes even more obvious when the differences between samples that were prepared using exactly the same conditions are examined. Additionally, the range of error shows a broad, unsystematic variation from fairly small to very large error bars.

One reason for the large deviations between experiments and the variation in error bars surely is the very local energy input of the ultrasonic horn into the sample and the difficulty to always place the horn at exactly the same position in the vessel containing the sample. An increased number of mixing steps (i.e. an increased mixing time in Fig. 5.10b should, in any case, be beneficial for sample homogeneity, although this is not seen in the data. Another factor is secondary fluid coalescence, which has already been shown to be problematic in the previous subsection. Thus, differences in time needed to stir



**Figure 5.10:** Complex shear modulus  $|G^*|$  of a sample with composition C1 with  $\phi_{\text{solid,set}} = 0.25$  and  $\phi_{\text{sec,set}} = 0.0225\%$  at a strain amplitude in the linear viscoelastic region with  $\omega = 1$  rad/s.  $|G^*|$  is shown as a function of (a) ultrasonication amplitude in the emulsification step during ultrasonic sample preparation and (b) mixing time after particle addition. The data shown as gray circles denote a second and third sample preparation applying exactly the same conditions as for the directly neighboring black data point. The slight shift of these points on the respective horizontal axis is only drawn to enable a visible discrimination of the error bars.

in the particles after the emulsification step might also lead to a different occurrence of coalescence effects taking place. However, ultrasonication produces very small droplets, so coalescence appears much slower than with the dissolver stirrer method as droplets settle much slower and thus are not coming into close contact that quickly. A major part of the error probably can be attributed to the necessity of using the small plate-plate-geometry with only 8 mm diameter for the rheological measurement in the C1 composed samples where larger geometries cannot be used due to the small sample volumes.

Overall, the capillary suspension preparation with ultrasound appears not to be the method of choice as long as any other options, like turbulent mechanical stirring or the use of a ball mill, are possible. However, it remains the only applicable option for very small sample volumes, while the bad reproducibility issues of this method clearly have to be kept in mind. Anyway, as will be seen later in sections 6.1 and 6.2, even with the large error spanning one decade in  $|G^*|$ , the method is still sufficient to obtain very unambiguous trends between different samples of composition C1. The same is true for the determination of structural data from confocal images as will be seen in sections 6.2 and 6.3. Due to the unclear influence of ultrasonication parameters, all C1 samples used in chapter 6 have been prepared with the same parameters of 35 % amplitude in the emulsification step and three mixing steps (i.e. 30 s mixing time) after particle addition.

### 5.3 Viscosity-matched model system

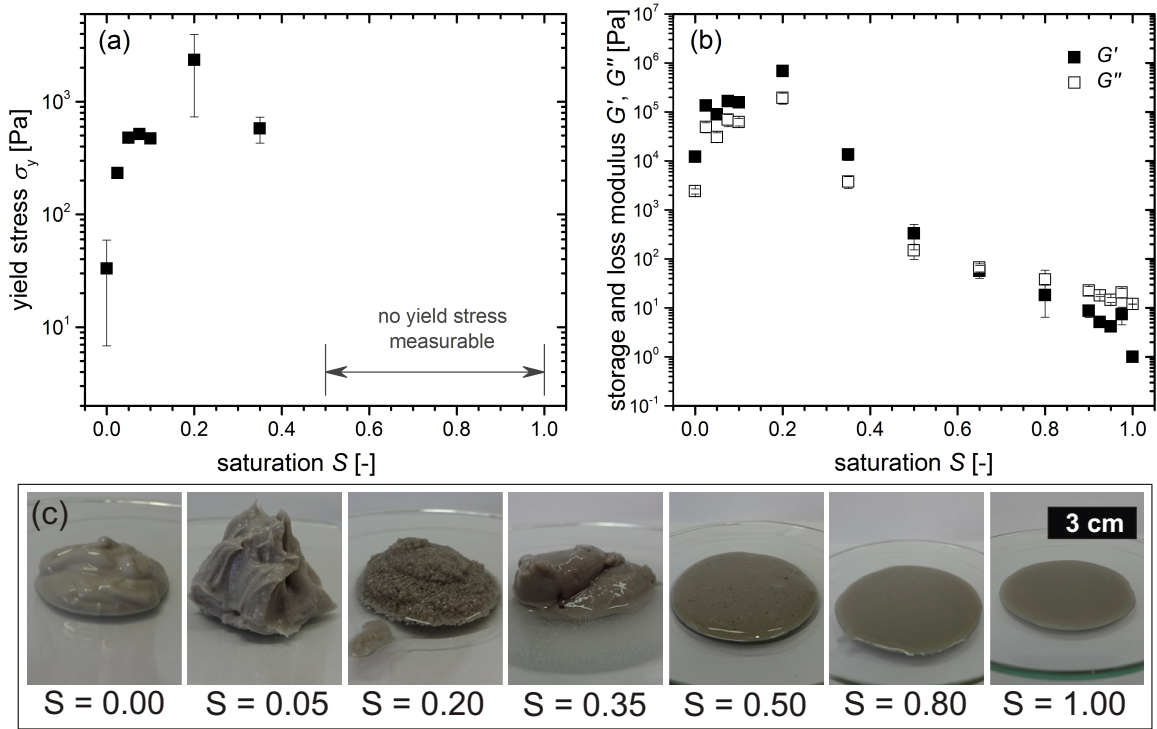
Theoretically, it should be possible to prepare both pendular and capillary state samples with a single sample composition by just modifying the ratio of the secondary and bulk

fluid. However, there has never been a sample system reported that was able to exhibit both states. One possible explanation for this contradiction may be the dependence of the droplet breakup on the viscosity ratio of the two fluids. This is expected to be particularly critical when the viscosity ratio of dispersed to continuous liquid phase is larger than 3.5 since droplet breakup under shear flow conditions is practically impossible [111]. For the pendular state sample system C2, the viscosity ratio of secondary to bulk fluid is  $\lambda = 0.019$ . The ratio would be  $\lambda = 1 / 0.019 \approx 52$  if the secondary fluid and bulk fluid were to be exchanged, a value much larger than the limit predicted by Grace [111]. In reality, droplet breakup in this range is possible to some extent as the applied mixing does not obey the necessary preconditions described by Grace theory, e.g. the presence of solid particles changes the breakup behavior [118] and the dissolver stirrer also does not provide a laminar shear flow. Nevertheless, droplet breakup should be much more difficult for  $\lambda = 52$  than for  $\lambda = 0.019$ . The influence of different  $\lambda$  ratios when exchanging the bulk and secondary fluid is avoided in material composition C4 (see section 3.1.4) as both fluids have the same viscosity. To also minimize any particle influence on the droplet breakup, both fluids were emulsified followed by particle addition as in section 5.2.2 for preparation of C4 samples.

A series of samples of composition C4 with varied saturation (i.e. varied ratio of the better wetting aqueous glycerol and worse wetting silicone oil) at constant solid volume fraction  $\phi_{\text{solid}} = 0.30$  was prepared. Despite the equal drop breakup behavior, this viscosity-matched system only leads to a stable pendular state suspension. A capillary state could not be prepared, as shown in Fig. 5.11. Thus, the viscosity ratio cannot be the only factor impeding the formation of a strong particle network in both states. Indeed, Hoffmann et al. also found that a change in viscosity ratio had effectively no direct influence on the strength of starch-based capillary suspensions [22]. However, direct comparisons to the current study is somewhat complicated since parts of the secondary fluid were absorbed by the starch granules in Hoffmann's experiments.

The absence of any capillary state structure can be seen directly from photographs of the sample texture (Fig. 5.11c) and is also obvious from the missing yield stress values (Fig. 5.11a) as well as in the oscillatory rheology data (Fig. 5.11b) where the elastic storage modulus  $G'$  is lower than the loss modulus  $G''$  at  $S \geq 0.65$ . The sample with very little preferentially wetting liquid at  $S = 0.05$  is clearly stronger than the sample at  $S = 0$  indicating the buildup of a pendular state structure. No such strengthening appears when adding a small amount of non-preferentially wetting liquid (changing  $S$  from 1 to 0.95) where the formation of a capillary state network should be expected. No yield stress is measurable for any of the samples with  $S \geq 0.5$ , which indicates that no particle percolation occurred. All of these higher saturation samples appear to be very viscous. This highly viscous behavior is substantiated by the  $G''$  modulus dominating over  $G'$  in the linear viscoelastic regime at  $\omega = 1$  rad/s for samples with  $S > 0.65$ . In the low and intermediate saturation range  $S < 0.5$ , all samples show a measurable yield stress and  $G'$  dominates over  $G''$  indicating that these samples all demonstrate a gel-like behavior originating from particulate networks.

From the sample photographs (Fig. 5.11c), one can see that the sample with  $S = 0.05$  is a pendular state network with a homogeneous structure. There is still a strong capillary attraction and a sample-spanning network for the  $S = 0.20$  sample, but it is no longer homogeneous. This sample has agglomeration with the large flocs reaching sizes of 1 mm.

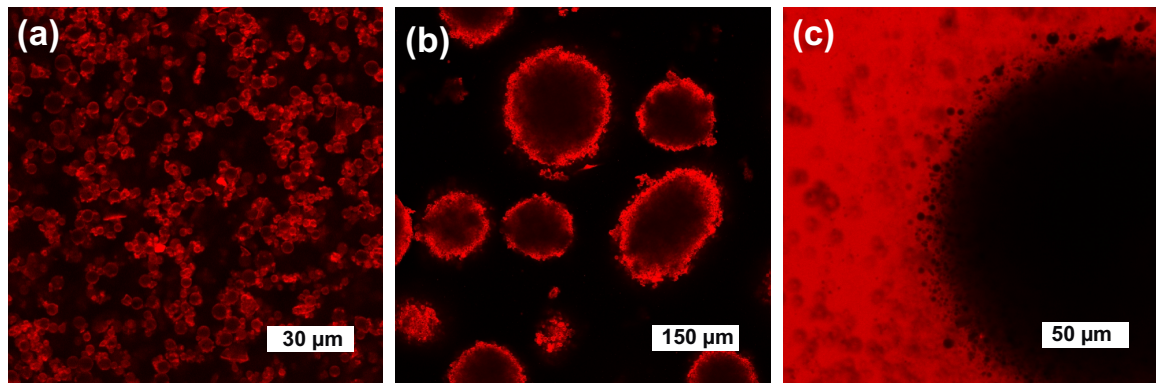


**Figure 5.11:** Variation in the (a) yield stress  $\sigma_y$ , and (b) storage  $G'$  and loss moduli  $G''$  as a function of saturation  $S$  for the viscosity-matched composition C4 with  $\phi_{\text{solid}} = 0.30$ . (c) Photographs illustrating different sample textures. The samples at  $S \geq 0.5$  did not have any measurable yield stress and clearly show a weakening of the structure in the photographs. Oscillatory measurements were made at a strain amplitude in the linear viscoelastic region with  $\omega = 1$  rad/s. Figure reproduced with permission from Elsevier [108].

At  $S = 0.35$ , all of the particles are incorporated into a single (or small number of) large agglomerate(s) and phase separation occurs such that the bulk (non-wetting) fluid is expelled from the tightly packed agglomerate. Due to these large structures, the rheological data measured at  $S = 0.20$  and  $S = 0.35$  should only be treated as rough estimations of the material strength since the continuum assumption may be violated even at the large gaps used. It is therefore unclear for these two samples if the internal agglomerate strength, the interaction between agglomerates, or slip in a depletion region next to the plate is measured using the rotation rheometry experiments.

To understand the structural changes as the ratio of the two liquids is varied, certain key structures are imaged in Fig. 5.12. For obtaining these images, a small amount of rhodamine B isothiocyanate has been dissolved in the aqueous glycerol prior to sample preparation. The three different ternary structures appearing for  $S = 0.05, 0.20$  and  $0.35$  can be directly compared to the three distinct open-pore morphologies recently discussed by Domenech et al., which were found in the same saturation ranges of particle-laden polymer blends (using polymer melts having viscosities of 8,000 and 13,000 mPa s) [162]. Domenech et al. found a pendular network (equivalent to the  $S = 0.05$  sample here), a network of large agglomerates (akin to the  $S = 0.20$  sample) and a bicontinuous structure in a saturation range in the order around  $S \approx 0.5$ . They predicted this bicontinuous structure to be inaccessible when the fluid viscosities are lower, as is the case here (both liquids

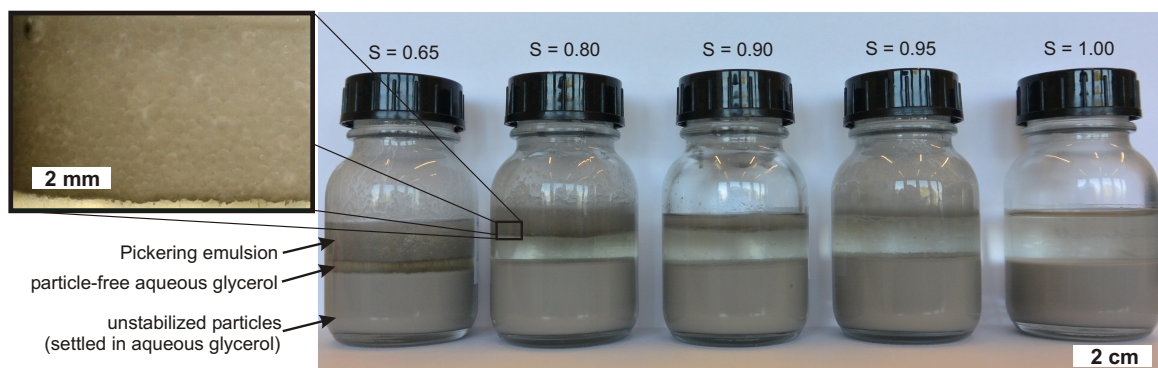




**Figure 5.12:** Confocal images of material composition C4 with  $\phi_{\text{solid}} = 0.30$  and (a)  $S = 0.05$ , (b)  $S = 0.20$  and (c)  $S = 0.95$ . The red color denotes the aqueous glycerol, while NP3 silica particles and silicone oil are undyed. The particles are nevertheless visible by their distinct spherical shape with particle diameter around  $3.5 \mu\text{m}$ . In (b), the dark regions inside of the agglomerates do not denote any lack of wetting liquid in the agglomerate but appear uncolored due to the refractive index mismatch between particles and fluids. In (c), the silica particles seem to extend into the bulk liquid because the image plane is not perpendicular to the oil droplet surface. Figure reproduced with permission from Elsevier [108].

with  $\eta = 104 \text{ mPa s}$ ), at which point they should collapse into a single, large agglomerate [162]. Their hypothesis seems to be borne out in the present system with  $S = 0.35$ , which could not be effectively imaged on the microscopic length scale.

After several days at rest, the samples with  $S > 0.5$  separated into three different layers, as shown in Fig. 5.13, further demonstrating the lack of a sample-spanning network. The bottom layer consists of unstabilized glass beads that are not in a capillary network and have settled due to gravity. A liquid layer of pure aqueous glycerol is in the middle. The top layer consists of distinct, particle coated Pickering droplets with a size of approximately



**Figure 5.13:** Photographs of the samples containing material composition C4 with  $\phi_{\text{solid}} = 0.30$  and (from left to right)  $S = 0.65$ ,  $S = 0.8$ ,  $S = 0.9$ ,  $S = 0.95$  and  $S = 1$ . These photographs were taken more than nine months after sample preparation. Three distinct layers are visible for the samples with added secondary fluid. The top layer contains Pickering-stabilized emulsion droplets as shown in the magnified inset. The middle layer contains pure aqueous glycerol and the bottom layer is formed by the unstabilized, settled particles. The sample with  $S = 1$  shows only two layers (aqueous glycerol over settled particles). Figure reproduced with permission from Elsevier [108].

0.1 mm to 1 mm. For saturation values decreasing from 0.99 to 0.5, this layer consisting of droplets of the lower density silicone oil becomes thicker. These droplets are exceedingly stable, even after storage times longer than nine months. This stability is achieved through the Pickering effect [104], where the interface between these droplets and the aqueous glycerol is covered by glass beads. One of these droplets is shown in the confocal image of Fig. 5.12c, where glass beads are visible surrounding the interface between the oil droplet (black) and the aqueous glycerol (red).

The appearance of Pickering emulsion droplets in the high saturation range can help to explain why a capillary state was not formed in this system. As the particles are added to the sample, they cover the interface between secondary fluid droplets and bulk liquid. Theoretically, the drops in a capillary state admixture should be smaller than the particles and form small clusters [8]. Although the viscosities of both fluids were matched, the droplets did not have the requisite small size even with the high shear rate dissolver stirrer before particle addition. The rapid adsorption of the particles to the droplet surface prevented particle-assisted drop breakup and even made such drop deformation and breakup more difficult. The Pickering droplets are stabilized against coalescence when their surfaces become covered with particles, but there is no attraction between Pickering emulsion droplets and there will not be any network percolation as the particles do not have any notable attractive interactions. In material composition C4, no strong attractive particle interactions in aqueous glycerol arises as is evident by the lack of a measurable yield stress or high storage modulus  $G'$  at  $S = 1$ . It is worth noting that this is in contrast to the capillary state system C3 based on hydrophobic  $\text{CaCO}_3$ , which already forms an attractive particle gel without any added secondary fluid, see the existing yield stress at  $\phi_{\text{sec}} = 0$  in Fig. 5.1b. This attractive van der Waals network is then reinforced when the capillary state is formed with the addition of a secondary fluid. For this case, the attractive particles seem to enhance the droplet breakup until sufficiently small droplet sizes are reached for the formation of a capillary state network. Therefore, it appears that the capillary state can be much more difficult to form than the pendular state, especially when the particles do not have any other attractive interactions even when the viscosities of both fluids are matched. The formation of a capillary state network directly competes with the production of Pickering emulsion droplets, which do not increase the sample strength due to the low packing fraction of these drops.

## 6 Microstructural Features and Transitions

This chapter summarizes the main results obtained from confocal microscopy of capillary suspensions of composition C1 and coupling these results to rheological data. From the equation for the yield stress of capillary suspensions, see section 2.4.3, the major properties influencing the sample strength are directly identified. The equation is repeated here, due to its importance in coupling structure and rheology:

$$\sigma_y = f_1(\phi_{\text{solid}}, N_{\text{bridge}}) f_2(\tilde{V}_{\text{bridge}}, \tilde{s}) \frac{2\pi\Gamma \cos\theta}{a}. \quad (6.1)$$

The main parameters influencing the yield stress are the solid volume fraction  $\phi_{\text{solid}}$ , the secondary fluid volume fraction  $\phi_{\text{sec}}$  which contributes to both the number  $N_{\text{bridge}}$  and particle size normalized volume  $\tilde{V}_{\text{bridge}}$  of bridges (see eq. 2.60), the normalized particle separation distance  $\tilde{s}$ , the interfacial tension  $\Gamma$ , the contact angle  $\theta$  and the particle size  $a$ . Most of these parameters will be examined in detail in the following sections.

First, the influence of wetting, comprised by the contact angle  $\theta$  is discussed in section 6.1 by using samples of composition C1 with various particle surface treatments. The data in this section are also used and thoroughly discussed as a proof of concept for the combinations of materials and methods employed. These include the confocal imaging of capillary suspensions by the method described in section 4.2, the chemical modifications of section 3.2, offering the possibility to produce pendular as well as capillary state samples depending on the surface treatment, the rather unconventional ultrasound preparation (see section 3.3.1) and the index matching and general composition of system C1 (section 3.1.2). Structural transitions between pendular and capillary state, but also between pendular and funicular state are discussed. These are based on confocal images and the detection of  $N_{\text{bridge}}$  and  $V_{\text{bridge}}$  from the images, which is transferred into a mapping of bridge sphericities. Also the influence of particle porosity is investigated confocally, which has major effects on the rheology via the effective secondary and solid volume fractions (i.e.  $\phi_{\text{solid}}$ ,  $N_{\text{bridge}}$  and  $\tilde{V}_{\text{bridge}}$  in eq. 6.1), see section 3.3.2. The secondary fluid volume fraction  $\phi_{\text{sec,eff}}$ , along with the contact angle and the porosity, also leads to a different structural transition behavior. The visualized structures are coupled to rheological measurements of the same samples.

As shown in section 6.1, confocal microscopy can be successfully applied to samples of composition C1. In section 6.2, the secondary fluid volume fraction  $\phi_{\text{sec}}$  of C1 samples with two different particle surface treatments is varied over a broad range. The sample preparation protocols examined in chapter 5.1 and 5.2 at constant  $\phi_{\text{sec}}$  influence the yield stress via the inversely proportional dependency of  $N_{\text{bridge}}$  and  $V_{\text{bridge}}$ , which in turn



depends on the droplet breakup during sample preparation. With this in mind, the sample preparation conditions, in contrast to chapter 5, are fixed in chapter 6, while  $N_{\text{bridge}}$  and  $\tilde{V}_{\text{bridge}}$  are varied in conjunction by the added amount of secondary fluid. Transitions from pure suspensions over pendular and funicular state into compact agglomerates are found here with increasing  $\phi_{\text{sec}}$ . Instead of detecting  $N_{\text{bridge}}$  and  $V_{\text{bridge}}$  as in section 6.1, the structures are investigated by determining the pair correlation function  $g(R/a)$ , fractal dimension  $D$  and coordination number  $z$  as function of  $\phi_{\text{sec}}$  using the algorithm presented in section 4.4. Again, the structural parameters are coupled to rheological measurements of the same samples.

Finally, section 6.3 deals with the influence of the solid volume fraction  $\phi_{\text{solid}}$  and the particle size  $a$ . The structure is characterized by the fractal dimension, which in addition to confocal image analysis is also deduced from different rheological models based on the scalings of the yield stress and oscillatory data on  $\phi_{\text{solid}}$ , as introduced for attractive colloidal particle networks in section 2.2.4. Therefore, this section also strives for a classification of capillary suspensions in the zone between colloidal gels and wet granular matter. A transition from less compact to more compact particle network structures with increasing particle sizes is found. A comparison between the model composition C1 and the more application-oriented capillary suspension compositions C5 and C6 is drawn and, as by-product of this set of experiments, a yield stress master curve for these compositions is obtained.

Altogether, microstructural effects of all parameters governing the yield stress equation 6.1 are investigated in chapter 6, with exception of the interfacial tension  $\Gamma$  and the particle separation  $\tilde{s}$  which was assumed to be  $\tilde{s} = 0$  in all cases. Impacts of this zero-distance assumption are discussed shortly in the outlook of chapter 7. Therefore, a broad overview on the micro- and macrostructural influence of capillary suspensions' core parameters is gained by the coupled optical and rheological characterizations presented here.

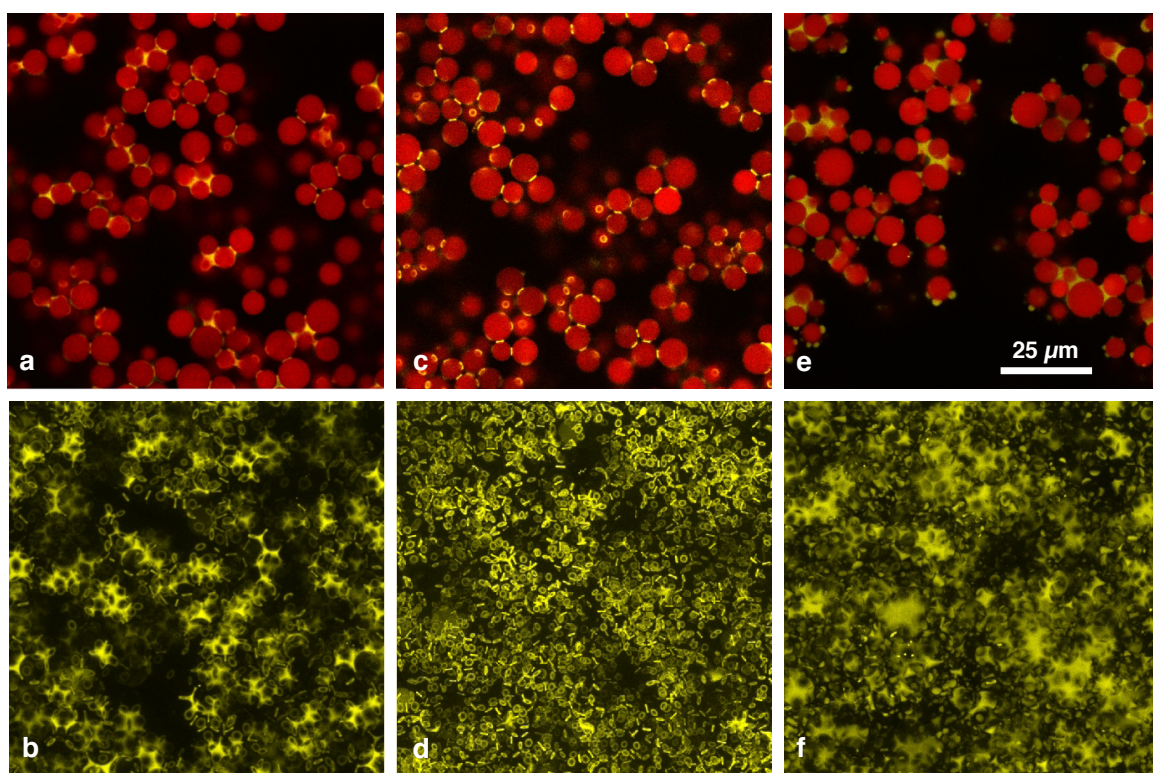
## 6.1 Variation of wetting and validation of methods

Section 6.1 is mostly based on the publication “Structure of Particle Networks in Capillary Suspensions with Wetting and Nonwetting Fluids” by Frank Bossler and Erin Koos, *Langmuir*, 32(6), 1489–1501, 2016 ([hyperlink](#)), copyright ACS, reproduced with permission from ACS [150]. It was part of the “Results and Discussion” section and the “Online Supplementary Information” of this publication and is, to a large extent, reproduced here with relatively minor changes. However, most parts of the methodical conclusion subsection 6.1.4 as well as Fig. 6.4 and 6.11 with respective accompanying discussions have not been part of the publication.

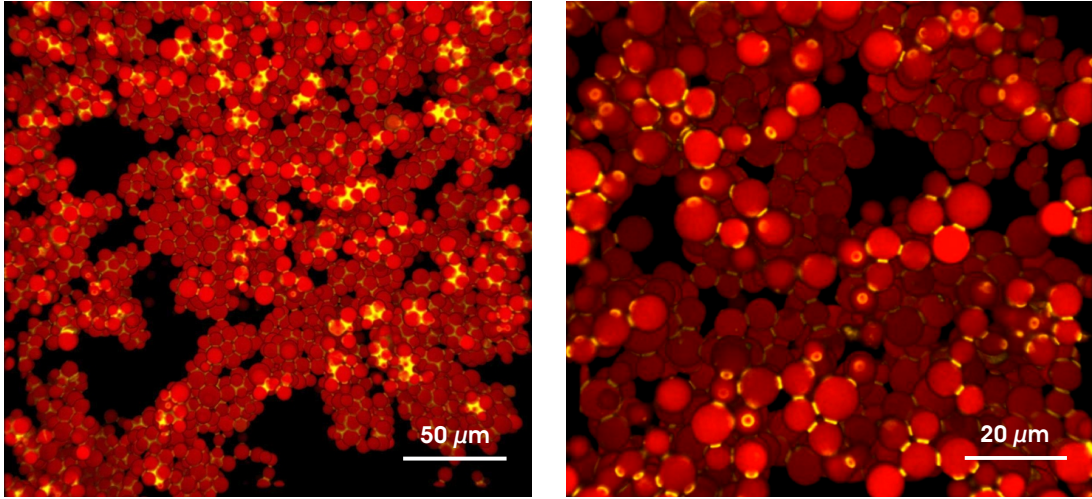
### 6.1.1 Structure of systems with nonporous particles

Three different treatments of nonporous silica particles with mean radius  $a_{50,3} = 3.21 \mu\text{m}$  have been used for producing capillary suspensions of composition C1 and investigate the influence of the contact angle on the microstructure, see Table 3.4, batch “6.1 nonporous”. The set solid and secondary volume fractions have been kept constant at  $\phi_{\text{solid,set}} = 0.25$  and  $\phi_{\text{sec,set}} = 0.0225$ . The three treatments of particles have three-phase

contact angles of  $40 \pm 6^\circ$ ,  $61 \pm 4^\circ$  and  $94 \pm 5^\circ$ . Confocal images of capillary suspensions prepared with these three particle types are shown in Fig. 6.1. Image sizes in this series of experiments were chosen smaller than the ones mentioned in section 4.2 which were applied for the more extensive studies of section 6.2 and 6.3. Here, a size of  $102 \times 102 \times 100 \mu\text{m}^3$  with  $1024 \times 1024 \times 300$  voxels was chosen. In the top row (Fig. 6.1a,c,e) a single  $x$ - $y$  slice of the three-dimensional image is shown. Both detection channels of the confocal microscope have been overlaid so that the position of the dyed particles (shown in red) and the dyed secondary fluid (shown in yellow) can be seen simultaneously. In the bottom row (Fig. 6.1b,d,f), only the detected secondary phase is depicted to further clarify the sample structure. These images of the secondary fluid are projections of the 3D image along the vertical  $z$  image axis, containing all of the secondary fluid detected in the corresponding 3D image, which allows the distribution and shape of the separate secondary phase droplets to be visualized. Three-dimensional images of capillary suspensions with nonporous particles have been reconstructed by overlaying all voxels of both detected channels using ImageJ, partially taken from images with a larger field of view. These are shown in Fig. 6.2. Additional videos that further clarify the 3D structure have been provided as supplementary information online, accompanying the original publication of this data [150, 163].

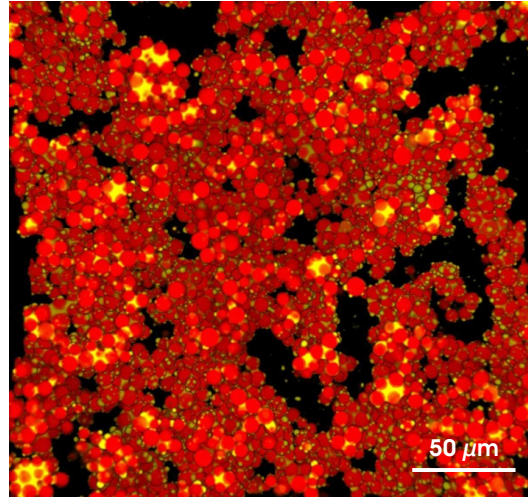


**Figure 6.1:** Confocal images of capillary suspensions with nonporous particles and contact angles of  $40^\circ$  (a,b),  $61^\circ$  (c,d) and  $94^\circ$  (e,f). The scale bar shown in (e) is valid for all six images. The top row shows example 2D slices with a size of  $102 \times 102 \mu\text{m}$ . The particles are shown in red, the secondary fluid in yellow, and black regions belong to the undyed bulk fluid. The bottom row images show projections of the detected secondary fluid from 3D image stacks, which have a depth of  $100 \mu\text{m}$  perpendicular to the image plane. Figure reproduced with permission from ACS [150].



(a) Funicular-like pendular state with three-phase contact angle  $\theta = 40^\circ$ .

(b) Pendular state (binary bridges) with  $\theta = 61^\circ$ .



(c) Capillary state with  $\theta = 94^\circ$ .

**Figure 6.2:** Three-dimensional reconstructions of confocal images of capillary suspensions. All samples consist of nonporous particles (red,  $\phi_{\text{solid}} = 0.25$ ) and added secondary fluid (yellow,  $\phi_{\text{sec}} = 0.0225$ ). The reconstruction was done with ImageJ. All voxels of both detection channels have been overlaid. The image size is  $246 \times 246 \times 40 \mu\text{m}$  in (a) and (c) and  $102 \times 102 \times 40 \mu\text{m}$  in (b).

### Binary toroidal bridges (pendular state) at $61^\circ$

For the sample with a contact angle of  $61^\circ$ , a network structure induced by single pendular bridges between the spherical silica particles is evident. There are neither any particle clusters visible nor large secondary phase droplets. The 2D projection of the spatially distributed secondary phase (Fig. 6.1d) shows that the structure indeed arises from binary bridges with a toroidal shape, which also gives a clear hint that the bridged particles have zero or close to zero separation. This further indicates that this structure is induced by strong attractive capillary forces. Network percolation can be seen in the 3D reconstructed image (Fig. 6.2b). This confocal image set is the first direct three-dimensional visualization of the pendular state in capillary suspensions. Previous images of capillary



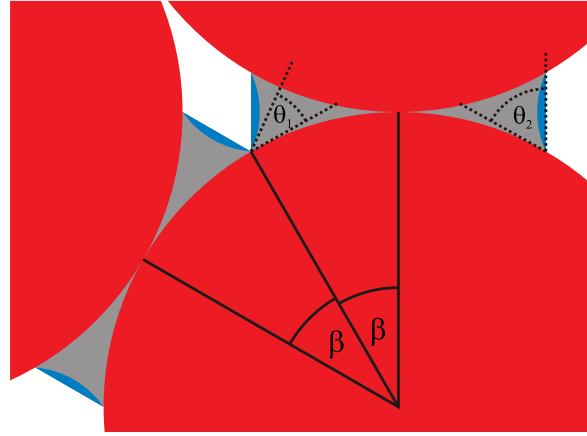
suspensions either illustrated some individual bridges between very few particles in diluted samples [1] or could only show capillary suspension sample surfaces by scanning electron microscopy after immobilizing the sample system, achieved by solidification of the secondary phase [5, 6] or sintering of the particles [10, 11], both of which can lead to structural changes in the sample. These studies were sufficient to deduce and verify the existence of the pendular state in capillary suspensions for contact angles smaller than  $90^\circ$ , but none of the studies could provide information on the network in the wet sample.

### **Funicular-like state at $40^\circ$ and the pendular-funicular transition**

There are many toroidal bridges visible in the  $40^\circ$  contact angle sample (Fig. 6.1a,b), which is expected for such a low contact angle. However, there are also numerous clustered structures where one larger secondary phase droplet binds three or more particles. This clustered structure is comparable to the funicular state described in wet granular matter [14, 91, 101, 102]. The funicular state, in general, is very similar to the pendular state as both appear for low contact angles and their main difference lies in the secondary phase volume. Funicular state clusters appear when the volume of neighboring pendular bridges becomes too large to prevent aggregation [102]. Adjacent bridges coalesce upon contact, leading first to particle trimers and later to larger agglomerated structures when the secondary phase volume is further increased.

The transition from the pendular to the funicular state normally occurs when the secondary phase volume fraction  $\phi_{\text{sec}}$  is increased [14, 27, 102], as already presented in section 2.3.3. There has to be another reason for this transition here, as the  $40^\circ$  and  $61^\circ$  samples both have  $\phi_{\text{sec}} = 0.0225$ . The contact angle influences the bridge shape and can, even for a constant volume, geometrically facilitate bridge coalescence. Heidlebaugh et al. proposed that the transition occurs when a third particle contacts an existing binary bridge [14]. A different criterion for the pendular-funicular transition was suggested by Flemmer [102], who stated that coalescence between two adjacent bridges leads to the funicular conformation. The critical volume  $V_{\text{bridge,crit}}$  of a secondary fluid bridge in this case is reached when the three-phase contact lines of two bridges touch.

The Flemmer criterion used for calculating the transition volume is visualized using the geometrical scheme depicted in Fig. 6.3. In a triangular configuration of equisized particles, the particle contact points have an angular distance of  $60^\circ$ . When there are capillary bridges at adjacent contact points (assuming both bridges have the same volume and shape), the base of each bridge can extend up to a half filling angle  $\beta < 60^\circ/2 = 30^\circ$ . As soon as this critical value of  $\beta$  is exceeded (e.g. by increasing the fluid volume per bridge), the neighboring bridges will touch and coalesce leading to a pendular-funicular transition [101]. The gray bridge in Fig. 6.3 has a half filling angle  $\beta = 30^\circ$  and a contact angle of  $\theta_1 \approx 40^\circ$ . Additional fluid volume (depicted in blue) is required to maintain  $\beta = 30^\circ$  when the contact angle is increased to  $\theta_2 \approx 60^\circ$ . Without this volume increase, a bridge with  $\theta_2 \approx 60^\circ$  would have a smaller half filling angle  $\beta < 30^\circ$  and thus would not transition to the funicular state. This simple geometrical argument is based on some tough assumptions, i.e. equisized particles and bridges, and the existence of triangular particle configurations. Nevertheless, this argument is very helpful in explaining why it is possible that binary bridges appear for a contact angle of  $61^\circ$  while the funicular-like clustered structure for a lower contact angle of  $40^\circ$  shows up even though the amount of secondary fluid is the same in both samples.

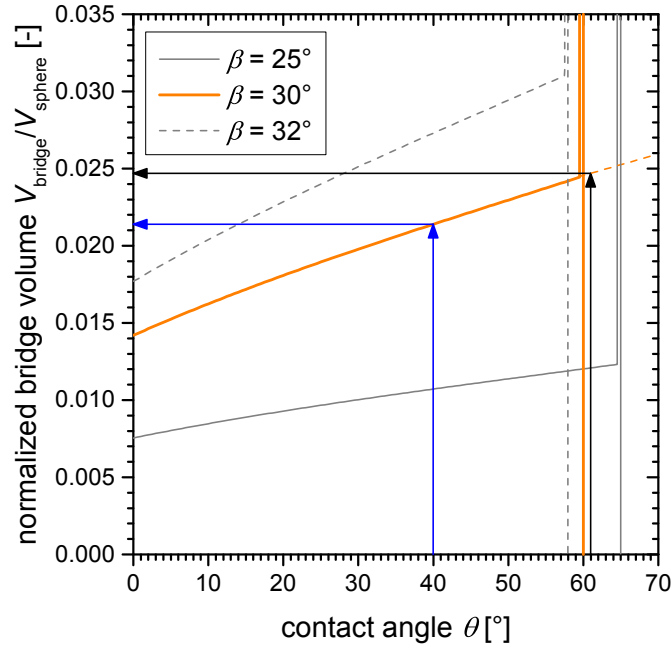


**Figure 6.3:** Schematic drawing of the contact angle dependent bridge volume. Three spherical particles (red) are in direct contact. The particles are connected by two identical binary bridges with half filling angles  $\beta$ . The bridge with contact angle  $\theta_1$  (gray) has a smaller volume compared to the bridge with contact angle  $\theta_2$  (gray + blue), while  $\theta_2 > \theta_1$ .

The set of equations from Megias-Alguacil et al. (eq. 2.48 to 2.51 in section 2.3.2), has been used to calculate the contact angle dependent volume  $V_{\text{bridge}}$  of capillary bridges with half filling angle  $\beta = 25^\circ, 30^\circ$  and  $32^\circ$  between particles with zero distance ( $s = 0$ ), normalized by the volume  $V_{\text{sphere}} = (4/3) \cdot \pi a_{50,3}^3$  of one particle [94]. The result of these calculations is shown in Fig. 6.4. The critical volume ratio using the Flemmer criterion can be read from the calculation with  $\beta = 30^\circ$  (orange curve) and is  $V_{\text{bridge,crit}}/V_{\text{sphere}} = 0.021 \pm 0.001$  for the contact angle of  $\theta = 40 \pm 6^\circ$  in the funicular-like sample system investigated here. As Megias-Alguacil et al. have established their equations only for concave bridge shapes, the upper limit of the equations is given by  $\theta = 90^\circ - \beta$ , as becomes obvious in the discontinuity appearing in all three curves in Fig. 6.4. Thus for  $\theta = 61 \pm 4^\circ$ , the critical volume was not directly calculated, but estimated from an extrapolation of the calculated curve beyond the discontinuity. This should be a valid approximation as the bridge volume at a fixed angle  $\beta = 30^\circ$  is expected to monotonically increase with  $\theta$  even when the sign of the bridge curvature changes. So,  $V_{\text{bridge,crit}}/V_{\text{sphere}} = 0.025 \pm 0.001$  is estimated in the pendular state system with  $\theta = 61 \pm 6^\circ$ . Thus, about 15 % less secondary fluid volume is expected to be necessary for the pendular-funicular transition in the  $40^\circ$  system than in the  $61^\circ$  system (assuming the coordination number  $z$  is the same in both cases). The actual secondary phase volume of  $\phi_{\text{sec}} = 0.0225$  seems to be larger than the necessary critical transition volume for the  $40^\circ$  sample, but less than this critical volume for the  $61^\circ$  sample. As the transition is dependent on the coordination number, this value cannot yet be fully explored here. However, coordination numbers of capillary suspensions are examined later in section 6.2.

### Capillary state at $94^\circ$

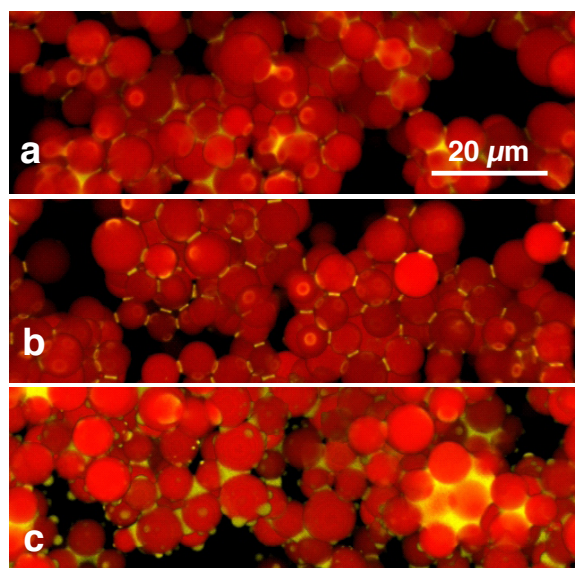
The network structure of the  $94^\circ$  sample (Fig. 6.1e,f) clearly differs from the  $61^\circ$  sample. The secondary fluid is mainly located between clusters consisting of three or more particles. Presumably, the secondary fluid induces small particle number clusters around these secondary phase droplets. The confocal image proves the existence of the capillary state for this sample. Its existence in real sample systems before only was inferred from simulations and rheological measurements [1, 8, 30]. There are still some binary bridges



**Figure 6.4:** Calculations of the bridge volume  $V_{\text{bridge}}$  normalized by the mean volume of a single particle  $V_{\text{sphere}}$  obtained with the set of equations from Megias-Alguacil et al. [94] for half filling angles  $\beta = 25^\circ$ ,  $30^\circ$  and  $32^\circ$  at a particle surface distance  $s = 0$ . The critical volumes are obtained from the curve for  $\beta = 30^\circ$  following the Flemmer coalescence criterion. The blue and black arrows denote the two confocal imaged samples discussed. The upper limit of the equations  $\theta = 90^\circ - \beta$  appears as a discontinuity. In general, bridge volumes with larger contact angles should also be computable (but with other equations). The dashed orange line suggests an extrapolation beyond the discontinuity.

visible, which are in principle not expected for  $\theta > 90^\circ$ , but as the mean contact angle of  $94^\circ$  is not too far above the expected transition value of  $90^\circ$  from pendular to capillary state, this could be caused by inhomogeneous particle surface reactions during particle modification, with some less hydrophobic particles still exhibiting contact angles smaller than  $90^\circ$ . Recently, possible standard deviations of  $19.3^\circ$  in the three-phase contact angle distribution of interfacially adsorbed chemically homogeneous spherical particles were experimentally found by Snoeyink et al., which highly supports this hypothesis [79]. Also, contact angle hystereses had been observed during the contact angle measurements here. Less ambiguous capillary state structure will additionally be shown later in sections 6.1.2 and 6.1.4.

Fig. 6.5 shows some magnified details of the reconstructed 3D images already presented in Fig. 6.2. In the capillary state sample (Fig. 6.5c) there are many separate droplets of secondary fluid that interact with only single particles with some particles even showing several such droplets. These singly-connected droplets may be caused by the rupture of clusters during the vigorous mixing required to form these capillary suspensions. They do not contribute to the sample-spanning network and, therefore, have no influence on the material strength. In the pendular state samples (Fig. 6.5a,b), no such singly-connected droplets are visible and the entire secondary fluid volume contributes to the particle network structure.



**Figure 6.5:** Detailed view showing parts of the reconstructed 3D network structure of capillary suspensions with nonporous particles with a contact angle of 40° (a), 61° (b) and 94° (c). The scale bar is valid for all three images. Figure reproduced with permission from ACS [150].

### Structural differences – secondary fluid droplet shape and distribution

The qualitative differences between the three samples which can be seen in the confocal images of Fig. 6.1, 6.2 and 6.5 can also be quantified. The volume and surface of each of the secondary fluid droplets detected by the 495-520 nm channel of the confocal microscope has been determined using the “3D object counter” plug-in in ImageJ [164, 165]. The confocal images of the secondary fluid were binarized with missing voxels inside the droplets filled prior to calculations of the surface area and volume.

The threshold used for binarization has some influence on the results. If the threshold is chosen to be too low, noise in the images is incorrectly detected as small droplets and some separated adjacent droplets can be mistakenly detected as forming a single large connected droplet. Noise near single droplets can also result in the volume and surface area of these droplets being overestimated. If the threshold chosen is too high, the droplet volumes are underestimated and the surface area overestimated. Single droplets can also be computationally split into several separated small droplets (e.g. a dimer split into two pendular bridges or a single pendular bridge split into several parts). None of these effects can be completely avoided by choosing any single threshold value, but the effects can be minimized. The same intermediate threshold value of 30 related to an intensity value range of 0 to 255 has been used for all samples to ensure comparability of results. The detection of larger droplets seems to be quite accurate for the chosen threshold value: errors in droplet connectedness were minimized and the droplet smoothness maximized (minimizing the surface area). Nevertheless, there remain small droplets visible in the data. While a portion of these droplets may be linked to the wetting of asperities, especially for smaller contact angles, many more – especially the smallest of these droplets – should be attributed as misdetections mainly caused by the partitioning of larger bridges. Therefore, any droplets smaller than  $0.1 \mu\text{m}^3$  were eliminated (close to the smallest resolution of the microscope which is  $\approx 0.01 \mu\text{m}^3$  based on eq. 4.1 and 4.2). The number of

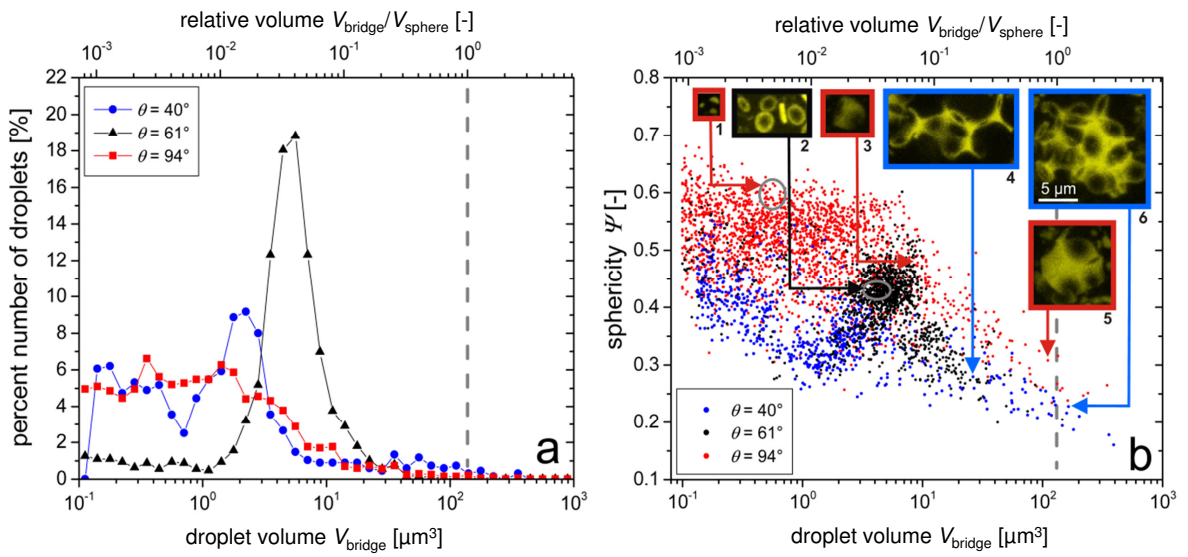


detected droplets was greater than 600 for all of the samples.

A histogram of the droplet numbers, evaluated from the determined droplet volume data, is shown in Fig. 6.6a. The Wadell sphericity  $\Psi$ , which is defined as

$$\Psi = \frac{\pi^{1/3} (6V_{\text{bridge}})^{2/3}}{A_{\text{bridge}}} \quad (6.2)$$

with  $V_{\text{bridge}}$  and  $A_{\text{bridge}}$  representing the volume and surface area of the droplet, respectively, was calculated for each droplet. A perfectly spherical droplet has a sphericity  $\Psi = 1$ , while non-spherical droplets have values less than unity. The calculated sphericity, as a function of droplet volume, for each secondary fluid droplet in all three samples is shown in Fig. 6.6b.



**Figure 6.6:** Droplet number percent distribution (a) and Wadell sphericity  $\Psi$  (b) of the individual secondary fluid droplets with  $40^\circ$  (blue),  $61^\circ$  (black) and  $94^\circ$  (red). Both parameters are shown as function of the droplet volume (bottom axis of abscissae) and as a function of the droplet to particle volume ratio  $V_{\text{bridge}}/V_{\text{sphere}}$  (upper axis of abscissae). The dashed gray lines denote the mean volume of a single solid particle. The insets (1–6) in (b) show projections of example droplets from the 3D confocal images with volumes and sphericities as marked. Gray circles denote the regions containing all of the separate droplets of insets 1 and 2. The scale bar in inset 6 is valid for all of the droplet images. Figure reproduced with permission from ACS [150].

The data in Fig. 6.6b reveal three distinct populations between the pendular ( $61^\circ$ ), funicular ( $40^\circ$ ) and capillary state ( $94^\circ$ ) samples. The pendular state sample shows a narrow range of drop volumes between  $2\text{--}10 \mu\text{m}^3$  with sphericities in the range of  $0.35\text{--}0.50$ . This narrow distribution in volumes is seen even better in the volume histogram (Fig. 6.6a) with a very pronounced peak with few larger or smaller droplets. A total of 77 % of the total number of drops, representing 64 % of the total secondary fluid volume, falls within this range of  $2\text{--}10 \mu\text{m}^3$ . When compared to the mean volume  $V_{\text{sphere}}$  of the solid silica particles, most of the secondary fluid droplet volumes in the pendular state are around 2–5 % of the particle volume. This is in agreement with the maximum size ratio for binary bridge coalescence calculated by the Flemmer criterion before. In Fig. 6.6b, inset 2 shows some of these binary bridges that fall into this volume and sphericity peak.

For both the funicular and capillary state samples, the volume distributions are much wider. The capillary state sample ( $94^\circ$ ) shows the most spherical droplets over the entire volume range. The large number of smaller droplets with  $V_{\text{bridge}} < 2 \mu\text{m}^3$  ( $V_{\text{bridge}}/V_{\text{sphere}} < 0.015$ ) and sphericities of approximately 0.5–0.6 can be identified as the singly-connected droplets. In this sample, about  $25 \pm 10$  % of the droplets in the volume range below approximately  $0.5 \mu\text{m}^3$ , however, have to be considered misdetections from binarization, as determined by comparing 300 of these detections to the original 3D confocal image. Three correctly detected droplets are shown in inset 1 of Fig. 6.6b. While these singly-connected droplets account for 70 % of the total number and 12 % of the total secondary fluid volume, they cannot contribute to the network strength. The  $94^\circ$  capillary state sample also exhibits a population of larger bridging droplets, two examples of which are given in the inset 3 and 5. The sphericity strongly decreases with increasing droplet size, due to the increase in droplet surface as the droplets fill the narrow voids between particles as particle clusters are built.

The funicular state sample ( $40^\circ$ ) also shows such large droplets, but their sphericity is even lower than in the capillary state sample, as such large droplets (inset images 4 and 6) are even less compact than their capillary state counterparts (inset image 5). Even though particle clusters are visible in both the capillary and funicular samples, the difference in the sphericity is most likely due to the different clustering mechanisms. Large particle clusters with single large droplets in the capillary state are energetically not very favorable, compared to particle clustering by multiple, non-interconnected small droplets and additionally such larger droplets would not form close-packed particle clusters [8]. Large funicular state clusters on the other hand are expected to consist of one or only few interconnected droplets being able to reach extensive sizes with still a compact particle configuration due to the attractive capillary force from the negative Laplace pressure [166]. A similar preferred tendency to form dense funicular-like clusters compared to non-stable capillary state clusters has already been found and discussed in chapter 5.1.3 when the influence of mixing time on the sample preparation was examined and the capillary state samples did not show any relevant large agglomerate buildup, while the pendular state samples (which with the onset of agglomeration indeed also should be rather called funicular) clearly did (Fig. 5.6b).

Further proof for the capillary force induced interaction for the  $40^\circ$  sample can be found in Fig. 6.6a in the clear peak at  $2 \mu\text{m}^3$ , implying that a large number of binary bridges also exists in this sample. Their slightly smaller volume compared to the pendular state bridges of the  $61^\circ$  sample can be explained by the pendular-funicular transition at lower volumes for this lower contact angle. A closer look at 230 droplets below  $0.5 \mu\text{m}^3$  revealed that in this volume range only  $35 \pm 10$  % were correct detections, mostly denoting small wetted regions of particle surface asperities. The other  $65 \pm 10$  % are mostly – apart from a small amount of noise – incorrectly detected pendular bridges that have been separated into two or more smaller volumes due to the image binarization. In this funicular sample, the correctly detected binary bridges account for 42 % of the total number of droplets, but only 15 % of the total secondary liquid volume. Larger clusters with a size greater than  $10 \mu\text{m}^3$  ( $V_{\text{bridge}}/V_{\text{sphere}} > 0.07$ ) account for 83 % of the liquid volume in the funicular sample.

The funicular sample with  $40^\circ$  contact angle seemingly resembles the  $94^\circ$  capillary state sample when only viewing the confocal images, e.g. Fig. 6.1a and e, but the data of

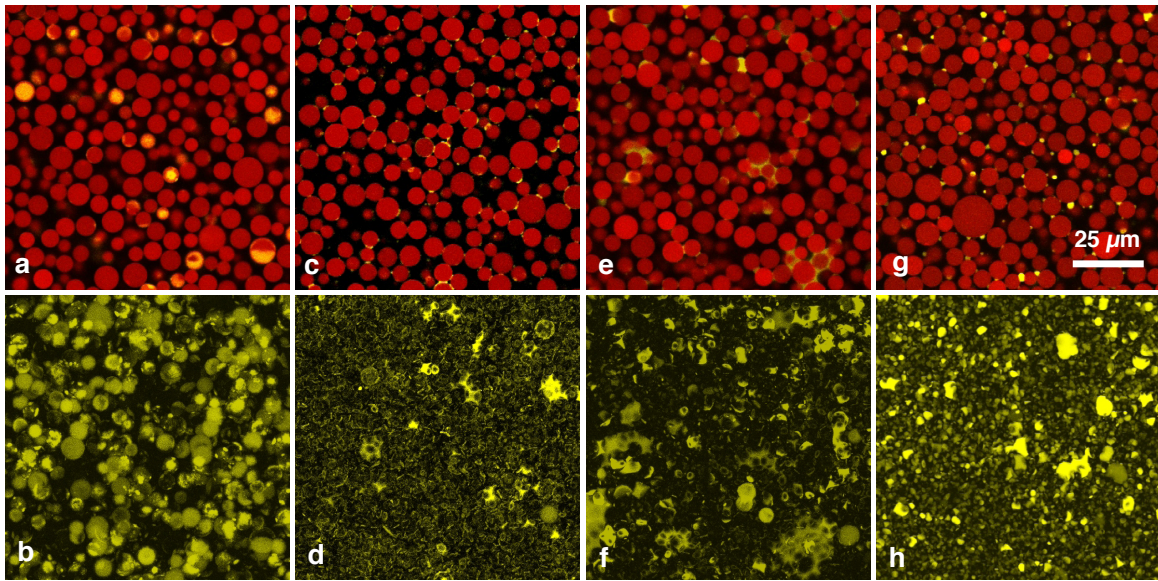
Fig. 6.6 proves that this is misleading. Clustering through bridge coalescence in the 40° sample actually leads to droplets whose interface towards the bulk fluid still have a concave curvature. The Laplace pressure inside of such a droplet is negative so these droplets still exhibit attractive capillary forces between the adjacent particles. This is not the case for the droplets in the capillary state seen at 94°, due to their convex interface towards the bulk phase, leading to positive Laplace pressures. This leads to a loss of symmetry for small clusters, as shown in inset 3 in Fig. 6.6b, or to a less compact particle arrangement around larger droplets (inset 5 in Fig. 6.6b). Both of these effects lead to higher droplet sphericities compared with the funicular state and hint at key physical differences between these two states. In reality, the 40° funicular sample more resembles the 61° pendular state sample. Scheel et al. [101] showed for low contact angles, that the interacting attractive forces between three particles are nearly equivalent, regardless of if there are three separate bridges or if there is only one central single concave droplet binding the three particles together. This finding also is valid for larger funicular clusters. That is, the force on each particle of the cluster is independent of the number of particles in the cluster [91, 101]. This implies that a plateau in strength is reached as soon as the binary bridge pendular state transitions to the funicular state, a conclusion also supported by previous experiments that investigated the tensile strength of wet granular matter [100] or the yield stress of capillary suspensions [6, 10]. This plateau in strength will also be one of the key features of capillary suspensions investigated in chapters 6.2 and 6.3.

### 6.1.2 Structure of systems with porous particles

The use of porous particles can lead to pronounced changes on the observed behavior of capillary suspensions. For evaluating structural differences between porous and non-porous particles, samples of composition C1 were also prepared from a batch of porous particles with mean size  $a_{50,3} = 3.21 \mu\text{m}$  and ten different degrees of surface hydrophobicity, see “batch 6.1 porous” in Table 3.4. BET surface measurements of this batch showed a reduction from  $295 \text{ m}^2/\text{g}$  to  $249 \text{ m}^2/\text{g}$ . Therefore, although the porosity of the dyed particles has decreased compared to untreated silica, it remains very high. The formulation of samples was kept the same as for the nonporous ones of section 6.1.1, i.e.  $\phi_{\text{solid,set}} = 0.25$  and  $\phi_{\text{sec,set}} = 0.0225$ . However, the effective solid volume fraction  $\phi_{\text{solid,eff}}$  is significantly higher than 0.25 for the porous particles with  $V_{\text{pore}} \gg 0$  and was measured by imaging to be  $\phi_{\text{solid,eff}} = 0.55 \pm 0.02$ . As the untreated silica particles as delivered by the supplier have a porosity of around  $\epsilon = 65 \%$  and the BET surface only decreased from  $295 \text{ m}^2/\text{g}$  to  $249 \text{ m}^2/\text{g}$  during the dyeing, it is reasonable to assume a porosity greater than 50 % for the dyed porous particles. The determined effective volume fraction  $\phi_{\text{solid,eff}} = 0.55 \pm 0.02$  indicates an average particle porosity of  $\epsilon = 55 \pm 3 \%$  for the treated particles, which is in good agreement with the BET surface reduction. A consequence of this high porosity is, that the whole secondary fluid volume fraction could easily be fully incorporated into the particle pores. Thus  $\phi_{\text{sec,eff}}$  is expected to be highly dependent on the wetting behavior of bulk and secondary fluid.

### Confocal images of capillary suspensions with porous particles

Fig. 6.7 shows confocal images of four of the samples prepared with porous particles having apparent contact angles of  $72 \pm 4^\circ$ ,  $115 \pm 4^\circ$ ,  $133 \pm 4^\circ$  and  $147 \pm 7^\circ$ . The considerable



**Figure 6.7:** Confocal images of capillary suspensions with porous particles and contact angles of 72° (a,b), 115° (c,d), 133° (e,f) and 147° (g,h). The scale bar shown in (g) is valid for all eight images. The top row shows example 2D slices with a size of 102x102  $\mu\text{m}$ . The particles are shown in red, the secondary fluid in yellow, and black regions belong to the undyed bulk fluid. The bottom row images show projections of the detected secondary fluid from 3D image stacks, which have a depth of 100  $\mu\text{m}$  perpendicular to the image plane. Figure reproduced with permission from ACS [150].

increase in  $\phi_{\text{solid,eff}}$  is obvious when comparing these images to the nonporous system of Fig. 6.1. For particles with 72°, no sample spanning network is obtained. The added secondary phase is completely absorbed into the particle pores as can be deduced from the overlay image (Fig. 6.7a). The corresponding projection of the secondary phase (Fig. 6.7b) further confirms these findings. The imbibition of the secondary fluid into the pores is determined by different parameters, the main one being the Laplace pressure which depends on the pore size and the contact angle of the wetting fluid towards the pore walls. Lower contact angles lead to faster absorption [167]. Therefore, the secondary phase will preferentially intrude into the pores as long as it is better wetting than the bulk phase.

For apparent three-phase contact angles higher than 90°, the bulk phase imbibition is favored while the secondary phase stays at the particle surface. Accordingly, a pendular state particle network is achieved for an apparent contact angle of 115° (Fig. 6.7c,d). The toroidal bridges are clearly visible and resemble the 61° nonporous sample described in the previous section. Most bridges are binary, thus the added secondary fluid volume at that contact angle is below the value that would cause the pendular-funicular transition which, taken the fairly increased effective solid volume fraction into account, is not surprising. At 147° (Fig. 6.7g,h) the capillary state is obtained. The droplets, which serve as cluster center, appear more convex than the ones reported for the 94° nonporous sample in the last subsection. The transition from pendular to capillary state using porous particles seems to be at a value around 133° (Fig. 6.7e,f), which is surprising since it is expected to occur at 90° or slightly below in both porous and nonporous systems. The particle porosity obviously has a strong influence on the contact angle dependence of capillary suspensions structure formation, shifting the transition between pendular and capillary configuration to apparently higher values.



### Discussion on the shifted transitions

At contact angles less than  $90^\circ$ , the secondary fluid is absorbed into the particle pores where it should no longer be available for interparticulate bridging. This would suggest a transition from non-bridged particles at  $\theta < 90^\circ$  to a capillary state system for  $\theta > 90^\circ$ . Therefore, the pendular state should not be accessible for a porous particle system without saturating the pores. This is clearly not the case, as the  $115^\circ$  samples clearly show a pendular state structure with concave binary bridges. For a sample system with different fluids but using the same silica particles with a slightly different treatment, Wenzl observed a similar behavior in wet granular media [36]. Wenzl reported that the three-phase contact angle measured for particles sitting on the surface of a large emulsion droplet of the secondary phase gave a value of  $\approx 130^\circ$ , whereas the exact same sample system showed a three-phase contact angle of only  $\approx 90^\circ$  when the secondary phase droplet volume was much smaller than the particle volume and each droplet only bridged two particles [36]. This discrepancy of  $\approx 40^\circ$  in the contact angle likely occurred due to particle surface roughness. This roughness can lead to a pronounced contact angle hysteresis [72, 73, 76], particularly in combination with three-phase contact line pinning [78].

In this work, the contact angle values were determined at flat liquid-liquid interfaces (see section 4.3), so the real contact angle in the pendular bridged conformation visible in Fig. 6.7c,d may be expected to actually have a much lower value than the measured  $115^\circ$ . A closer look on bridge shapes of porous systems in this contact angle range will be given in the outlook, chapter 7.2, where an additional factor aiding the buildup of binary-bridged structures at high contact angles, namely asymmetric bridge shapes, will become apparent. The actual contact angle for each individual bridge sadly cannot be measured accurately due to the inadequate resolution of the images. Nevertheless, the bridge shape in Fig. 6.7c,d seems to be concave rather than convex implying that it actually is less than  $90^\circ$  (see also Fig. 6.8a below). If, as in Wenzl's work, a discrepancy of  $40^\circ$  exists here, the real contact angle would be around  $75^\circ$  and the pendular state would indeed be expected. If the observed value marking the transition between the pendular and capillary state ( $\theta = 133^\circ$ ) is also reduced by  $40^\circ$ , a much more reasonable value nearby to  $90^\circ$  ( $\theta = 93^\circ$ ) is calculated. While this contact angle discrepancy clearly depends on the use of porous particles, the exact cause nevertheless remains unclear. It also remains unclear whether the measured contact angles in this set of experiments are equilibrium contact angles or systematically higher angles measured inside the possible value range given by the hysteresis.

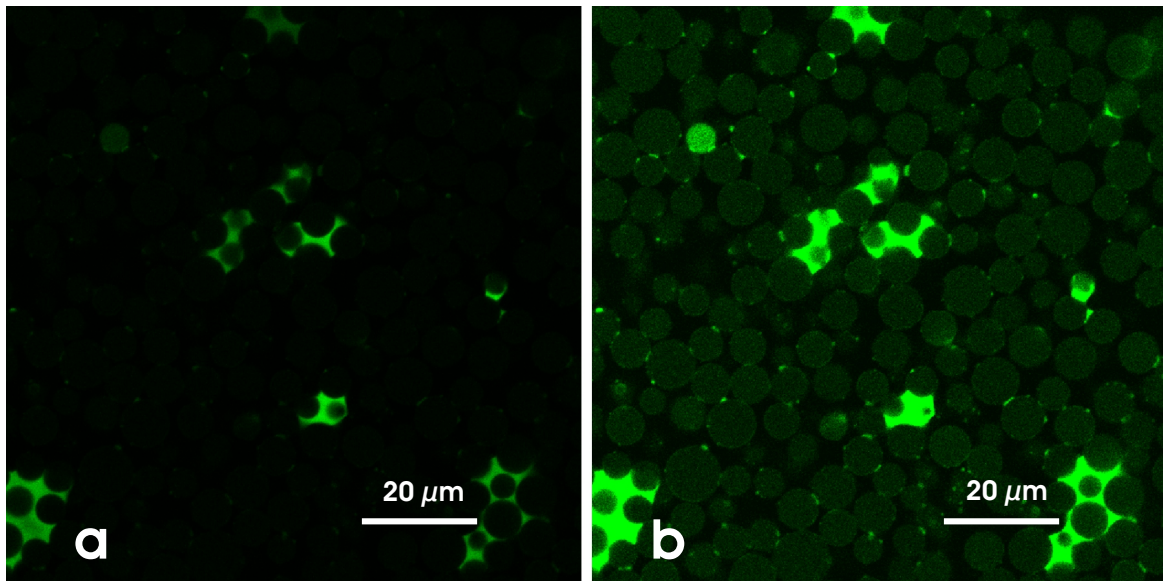
The differences in surface roughness are not the only factor that can influence the contact angle hysteresis. Chemical surface heterogeneities are also likely due to the variations in reaction kinetics during particle preparation. Some particles might be more hydrophobic than others, leading to an overall contact angle distribution in the sample, or there also could be chemical inhomogeneity on each particle surface. In the latter case, the heterogeneous surface wetting is described by the Cassie-Baxter model, which predicts an intermediate contact angle with hysteresis [74, 75]. In the porous sample system, the surface heterogeneity is further intensified if the oil phase fills the pores at  $\theta > 90^\circ$ . The secondary phase must then form a partial interface with the oil phase at the pore apertures, leading to even more heterogeneous wetting. If these pores are partially filled with a single phase and the porous particle then migrates to the interface between both fluids – as in the contact angle measurement – this might lead to a different contact an-

gle if re-wetting inside the pores is hindered compared to pores that are wet by both fluid phases simultaneously as is the case when these experimental samples are prepared.

### Difficulties in imaging microdroplets and microbridges

For samples made with porous particles where the contact angle is below  $90^\circ$ , Fig. 6.7a,b indicates the secondary fluid to be fully imbibed into the particle pores. However, microdroplets may be expected to be located in asperities on the surface of the silica particles. While the same also is true for samples with higher contact angle, in these cases the microdroplets are not expected to be of any structural relevance compared with the large secondary fluid droplets.

In the contact region of two adjacent particles, surface wetting microdroplets touching both particles would develop a negative curvature in the interparticle gap and thus experience a negative Laplace pressure forcing them to form small sized, but nevertheless attractive, microbridges [85, 92]. Such microbridges and microdroplets are very difficult to detect confocally due to their expected size below the microscope resolution limit and the possible broad size distribution of secondary fluid droplets, see Fig. 6.6. Large droplets are detected correctly if the laser intensity or detector gain of the confocal microscope is relatively low, but the smallest droplets are invisible or confounded with noise due to their low absolute dye content. An example of such detection problems is shown in Fig. 6.8. If the laser intensity or detector gain is increased, the small droplets



**Figure 6.8:** Effect of the laser intensity on the detected secondary phase signal for a sample with porous particles ( $\phi_{\text{solid,set}} = 0.25$ ,  $\phi_{\text{sec,set}} = 0.0225$ ,  $\theta \approx 115^\circ$ ). To better illustrate the problem, insufficient mixing conditions were used for this sample preparation and a stable capillary suspension does not form. The images show a 2D image of the secondary phase, excited by the 488 nm laser. (a) 0.2 mW laser intensity where separate sharp-edged droplets of secondary phase are visible. (b) 1.2 mW laser intensity. Tiny microbridges are visible, which cannot be seen in the 0.2 mW image, but the large droplets outshine the image and their contour becomes poorly defined. Crosstalk from the rhodamine B dye also begins to materialize.



can become visible – see the tiny bridges in Fig. 6.8b – but the large droplets saturate neighboring voxels in the image. The contour of these larger droplets then cannot be detected correctly.

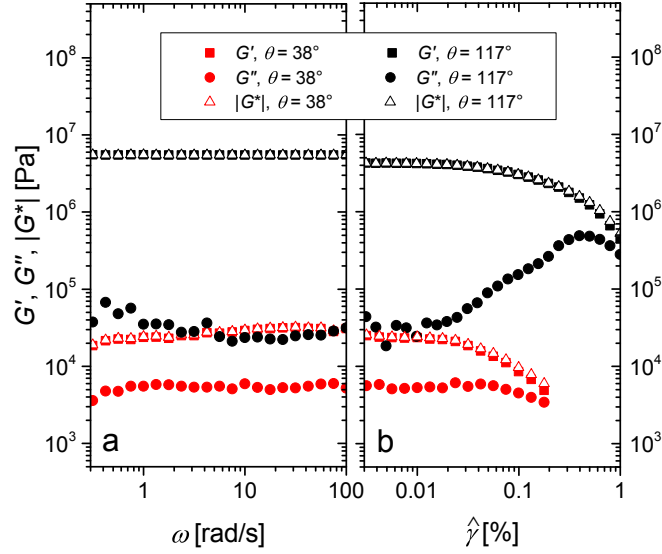
The example 2D images of Figure 6.8 only show the detected secondary phase channel. The sample shown consists of porous particles ( $\phi_{\text{solid,set}} = 0.25$ ) with a secondary phase content of  $\phi_{\text{sec,set}} = 0.0225$  and a contact angle of  $\theta \approx 115^\circ$ . Insufficient mixing conditions have been chosen here for sample preparation as the difficulties in imaging these microbridges then can be easier visualized in a single image. First, the secondary phase and bulk fluid were emulsified by ultrasound. Then, the particles were stirred into the non-stabilized emulsion with a magnetic stirrer, a process that does not lead to the formation of a stable homogeneous capillary suspension. The first image (Fig. 6.8a) was taken while applying a laser intensity of 0.2 mW, an intensity that was also used for all of the figures previously shown in sections 6.1.1 and 6.1.2. None of the small bridges between the particles are visible here, only some separate large droplets. The small bridges become visible when the intensity is increased to 1.2 mW. Such images, however, are problematic for the computational analysis described in section 4.4 which will be applied for the structural analyses in chapter 6.2, due to the oversaturation present particularly for particles surrounded by droplets. Additionally there is a signal detected inside of the particles. While this could be due to very small secondary phase droplets inside of the particles, this effect can in Fig. 6.8b more likely be assigned to crosstalk from the rhodamine B dye as the contact angle is greater than  $90^\circ$  and crosstalk was also observed when the laser intensity was increased for suspensions without any secondary fluid.

### 6.1.3 Coupling structure and rheology

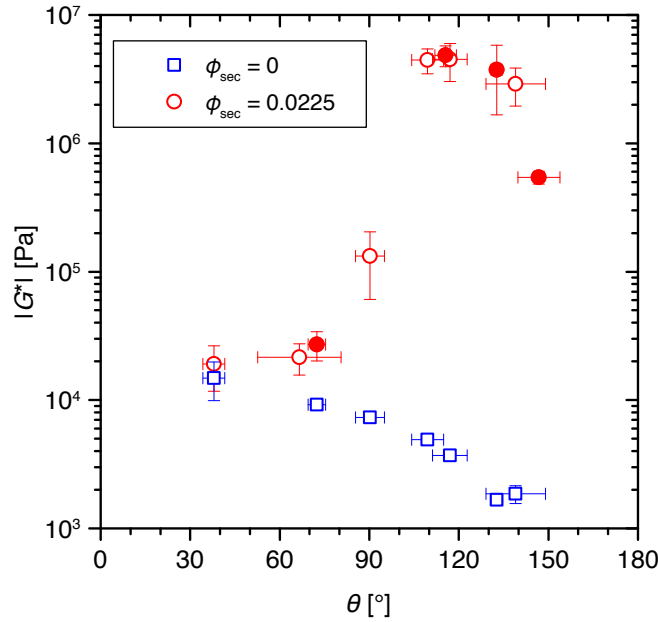
To couple the observed structural changes seen in the confocal images to the samples flow behavior, rheological measurements were made, using the porous particle system presented in the previous section. Fig. 6.9 shows strain sweep as well as frequency sweep experimental data for two systems with  $\phi_{\text{sec,set}} = 0.0225$  and particles with contact angles of  $38^\circ$  and  $117^\circ$ . In both systems,  $G'$  is nearly frequency independent and much higher than  $G''$ , which is typical for a strongly gelled sample. All ten samples with porous particles from batch “6.1 porous” having different contact angles were examined. The two samples shown in Fig. 6.9 had the maximum and minimum  $|G^*|$  values of these samples with all of the other intermediate samples also having a frequency independent complex shear modulus. If we are to assume a power law dependence of the shear modulus on the frequency,  $|G^*| \propto \omega^m$ , the exponent  $m$  is smaller than 0.08 in all cases. Therefore, the magnitude of the complex shear modulus  $|G^*| = \sqrt{G'^2 + G''^2}$  in the linear viscoelastic regime, which here is approximately equal to  $G'$ , can be considered as a single value and the magnitude of the complex shear modulus at  $10 \text{ rad} \cdot \text{s}^{-1}$  and strain amplitude of 0.01 % is considered as a function of only the contact angle in the following data.

#### Contact angle dependence of the complex shear modulus for porous particles

The magnitude of the shear moduli for different capillary suspensions with  $\phi_{\text{sec,set}} = 0.0225$  and different contact angles are shown in Fig. 6.10. Additionally some samples have been prepared with the same particles and same sample preparation proto-



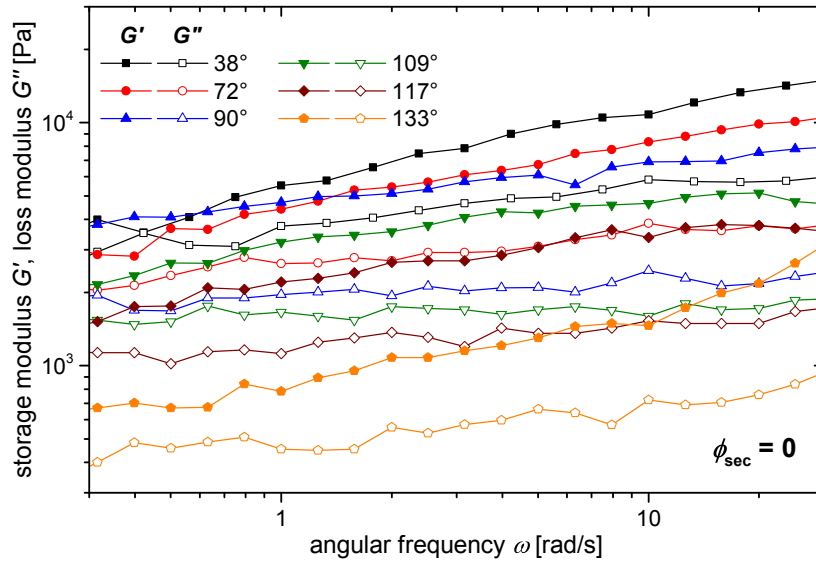
**Figure 6.9:** The storage modulus  $G'$ , loss modulus  $G''$ , and the magnitude of the shear modulus  $|G^*|$  as a function of (a) the oscillation angular frequency  $\omega$  and (b) strain amplitude  $\hat{\gamma}$  for two capillary suspension samples using porous particles with a contact angle of  $38^\circ$  (red symbols) and  $117^\circ$  (black symbols). The effective solid dispersed phase content was  $\phi_{\text{solid,eff}} = 0.55 \pm 0.02$  and the secondary fluid content  $\phi_{\text{sec,set}} = 0.0225$  for both samples. Figure reproduced with permission from ACS [150].



**Figure 6.10:** Dependence of the complex shear modulus magnitude  $|G^*|$  (at  $10 \text{ rad}\cdot\text{s}^{-1}$  and  $\hat{\gamma} = 0.01 \%$ ) on the three-phase contact angle  $\theta$  for capillary suspensions using porous particles, at  $\phi_{\text{sec}} = 0.0225$  (red circles) and  $\phi_{\text{sec}} = 0$  (blue rectangles). Data points with corresponding confocal images shown in Fig. 6.7 are denoted using filled symbols. The effective solid dispersed phase content was  $\phi_{\text{solid,eff}} = 0.55 \pm 0.02$  for all of the samples. Pure suspensions data points ( $\phi_{\text{sec}} = 0$ ) are shown as a function of the three-phase contact angle corresponding to the same surface treatment. Figure reproduced with permission from ACS [150].

col without added secondary fluid ( $\phi_{\text{sec}} = 0$ ). The samples with added secondary phase show a very slight increase in  $|G^*|$  between  $38^\circ$  and  $72^\circ$  from  $1.9 \times 10^4$  Pa to  $2.7 \times 10^4$  Pa. Above  $90^\circ$ , the complex shear modulus increases by more than two decades to  $4.6 \times 10^6$  Pa, where it remains nearly constant for contact angles between  $109^\circ$  and  $133^\circ$ . At contact angles above  $133^\circ$ ,  $|G^*|$  decreases again – dropping by one decade to  $5.4 \times 10^5$  Pa at  $147^\circ$ . It is obvious that this strong non-monotonic dependence of the modulus on the contact angle, and especially the large increase at  $90^\circ$ , for these capillary suspension samples (red circles) arises due to the addition of the small amounts of secondary fluid when compared to the pure suspension values (blue rectangles). The secondary fluid clearly leads to an increased network stability even though the samples already form gels without added secondary fluid.

When compared to the capillary suspension samples, the shear moduli in the pure suspensions ( $\phi_{\text{sec}} = 0$ ) exhibit a stronger frequency dependence with exponent  $m$  between 0.16 and 0.27. The frequency dependent storage and loss modulus for these samples are shown in Fig. 6.11, where their steeper slope is apparent. The dependence is



**Figure 6.11:** The storage modulus  $G'$  and loss modulus  $G''$  as a function of the angular frequency  $\omega$  at a strain amplitude  $\hat{\gamma} = 0.01$  % for six suspensions without added secondary fluid ( $\phi_{\text{sec}} = 0$ ) using porous particles with respective contact angle (in the three-phase C1 compositions) of  $38^\circ$  (black symbols),  $72^\circ$  (red),  $90^\circ$  (blue),  $109^\circ$  (green),  $117^\circ$  (brown) and  $133^\circ$  (orange). The effective solid dispersed phase content was  $\phi_{\text{solid,eff}} = 0.55 \pm 0.02$ .

nevertheless small enough that only single  $|G^*|$  values obtained at  $10 \text{ rad} \cdot \text{s}^{-1}$  and  $0.01$  % were included in Fig. 6.10. Furthermore, it is important to note that  $G'$  is larger than  $G''$  over the entire frequency range in all cases, so all the samples without added secondary fluid may also be characterized as a gel at this high solid volume fraction.

For the suspensions without secondary fluid prepared from particles with identical surface treatments as their corresponding capillary suspension, the complex shear modulus obtained at  $10 \text{ rad/s}$  decreases monotonically with increasing contact angle. The complex shear modulus decreases by nearly one decade from  $1.5 \times 10^4$  Pa for the hydrophilic particles ( $38^\circ$  contact angle) to  $1.9 \times 10^3$  Pa for the sample with a contact angle of  $139^\circ$ . This reduction hints to weakening particle attractions. Similar behavior has been demonstrated previously for other silica dispersions [168, 169].

### Explaining the shear modulus dependence using confocal images

The dependence of the shear modulus on contact angle in the capillary suspensions can be explained by comparing the rheological data to the confocal images as discussed in the previous section. The four samples imaged in Fig. 6.7 are highlighted using filled circles in Fig. 6.10. For the  $72^\circ$  sample, the complex shear modulus is only slightly higher than the corresponding value for the sample without secondary fluid. In the images, all of the fluid visible is inside of the particle pores where it cannot form capillary bridges and therefore does not lead to a significant increase in network strength. As there is some increase in  $|G^*|$  compared to the pure suspension as the contact angle approaches  $90^\circ$ , it is likely that the secondary fluid is not entirely located inside the pores. Tiny microdroplets of fluid are expected to adhere to small asperities on the particle surfaces where they form very small bridges upon contact with a second particle [92]. These bridges are able to transmit capillary forces, which are stronger than van der Waals interactions. However, the magnitude of the transmitted force is low compared to full particle bridging [92]. As discussed at the end of section 6.1.2, these microdroplets and microbridges cannot be seen in these confocal images with the imaging conditions applied.

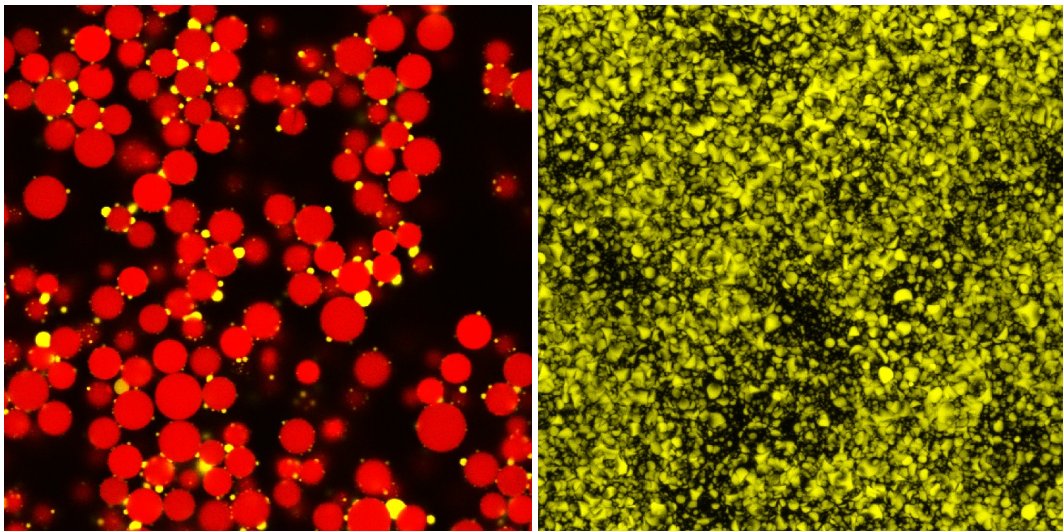
The absorption of the secondary phase into the particle pores decreases and slows as the contact angle increases, which leads to more fluid available on the particle surface to form bridges, i.e. an increase in  $\phi_{\text{sec,eff}}$ , corresponding to the drastic increase in  $|G^*|$  near  $90^\circ$ . While it is possible that additional changes in the van der Waals or electrostatic interaction contribute to the increase in  $|G^*|$ , there is no increase in the corresponding samples without secondary fluid implying that these possible contributions are absent or very minor. Above  $90^\circ$ , the secondary phase is no longer preferentially wetting and absorption of this fluid into the pores ceases, i.e.  $\phi_{\text{sec,eff}} = \phi_{\text{sec,set}}$  may be assumed. All of the secondary phase then is outside of the particle pores for the  $115^\circ$  sample where it bridges the particles. The corresponding  $|G^*|$  value at this angle is maximal and has a value that is about three decades higher than for the suspension without added secondary fluid. This is very clear proof of the strong adhesion force induced by capillary bridges in the pendular state. The reduction in  $|G^*|$  at very high contact angles can be attributed to the weakening of the bridges and the transition from the pendular to the capillary state. The sample with a contact angle of  $147^\circ$  shows particle aggregation by capillary state clusters and the corresponding rheological data also shows a decrease from the maximum value. The capillary state admixture is weaker on an absolute scale than the pendular state, but is nevertheless much stronger than the suspensions without any secondary fluid.

There remains some ambiguity on the extent of the reduction in strength for the capillary suspension ( $\phi_{\text{sec}} = 0.0225$ ) between  $133^\circ$  and  $147^\circ$  when the decrease in the pure suspensions complex shear modulus is taken into account. It is possible that this trend arises partly due to the same changes occurring in the pure suspension, but this is unlikely to be the case. First, the dominant attractive interaction mechanism is different between these two systems as evidenced by the change from concave bridges to convex clusters. Second, the drop in strength for the capillary suspensions between  $133^\circ$  and  $147^\circ$  of nearly one decade is more pronounced than the drop in the pure suspension. In fact, since the van der Waals force is much smaller than the capillary force, changes to the van der Waals force can only account for a drop in the magnitude of the shear modulus by a few percent. Therefore, the cause of this downturn must be due to a change in the capillary force that

is closely related to the transition from the pendular to capillary state as is observed in the confocal images.

#### 6.1.4 A short contemplation on the confocal method and composition C1

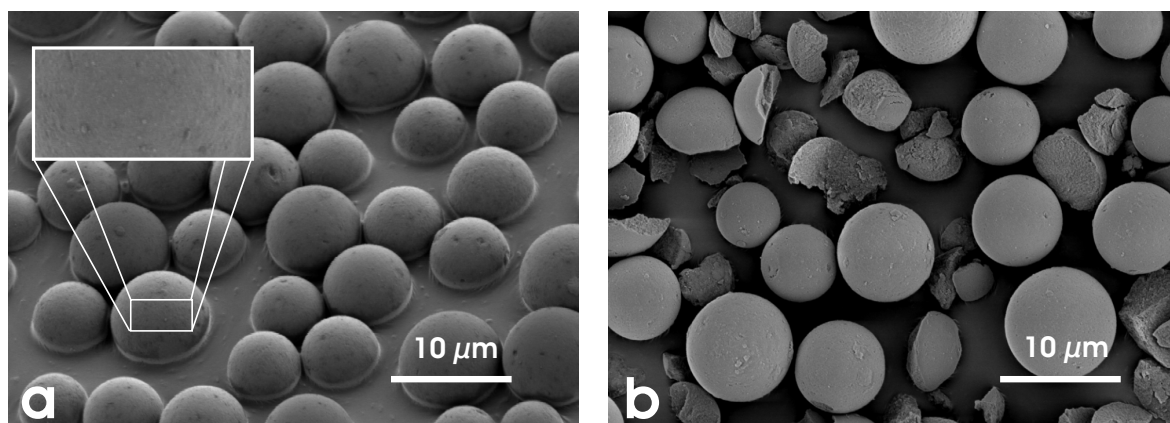
Before proceeding to section 6.2, a short intermediate review on using composition C1 for confocal imaging shall be given here. First of all, composition C1 has proven to be imageable in sufficient resolution in 2D and especially in 3D in section 6.1. The signal is not lost even deep into the samples, which is proof of the successful index matching, and not modified by the chemical particle treatments used to adjust the contact angle and porosity. Thus, composition C1 offers a broad tuneability of parameters without severely hindering imaging quality. Additionally, the confocal images show that the rhodamine B isothiocyanate dye is fully bound to the particles and does not migrate into the bulk or secondary liquid. The dye dissolved in the secondary liquid also does not diffuse into the bulk liquid. Thus, using composition C1 with various chemical particle treatments enables in-situ imaging of the exact spatial distribution of both particles and secondary liquid, which were not previously possible for any other capillary suspensions. Accordingly, the confocal images presented in section 6.1 were the first unambiguous experimental proof for the existence of the capillary state, while also providing much improved images of pendular state systems. In Fig. 6.1, 6.2, 6.5 and 6.7, the capillary state may still seem ambiguous to one not acquainted with viewing such images of capillary suspensions very often. Hence, an additional example image of a capillary state sample containing nonporous particles is shown in Fig. 6.12, where the convexly shaped droplets clustering the particles are clearer. This sample still showed a yield stress, although it has a rather high contact angle of  $130^\circ$ .



**Figure 6.12:** Capillary state sample of composition C1, originating from batch “6.3 nonporous, large”, with  $\phi_{\text{solid,set}} = 0.15$  and  $\phi_{\text{sec,set}} = 0.018$ , where the surface was accidentally rendered too hydrophobic ( $\theta \approx 130^\circ$ ) so these particles were not used in other experiments. 2D image ( $145 \times 145 \mu\text{m}^2$ ) showing both detection channels (left) and 3D projection ( $145 \times 145 \times 142 \mu\text{m}^3$ ) of secondary fluid channel (right).



Despite these many advantages and possibilities provided by composition C1, the sample preparation with ultrasound may be seen as a drawback. In section 5.2.3, this sample preparation method led to quite large errors in rheometric measurements due to the small sample sizes. As ultrasonication, accordingly, is not the preferred method, a more classical mechanical stirring preparation, using a small magnetic stirrer, was tried. This sadly failed to provide good enough droplet breakup (see the example in Fig. 6.8) and additionally led to particle breakage. Similar particle breakage was observed when the particles were treated too harshly during the chemical surface modifications. Thus, e.g., replacing the KPG stirrer used during the modified Stöber reactions by an easier to handle magnetic stirrer in a tightly closed vessel failed. Additionally, applying centrifugation speeds greater than 1000 rpm during the particle washing steps also broke the particles. The higher the particle porosity is, the more prone are the particles to fracture. Therefore, while composition C1 is superior to any other capillary suspensions for imaging issues, it is much more difficult to handle during sample preparation. Such issues can, at least, be minimized with careful experimentation. SEM images are shown in Fig. 6.13 where such broken particles due to careless handling can be seen. Broken particles are unusable for confocal image analysis, as already depicted in Fig. 4.7.



**Figure 6.13:** Scanning electron microscopy images of Kromasil particles ( $a_{50,3} = 3.21 \mu\text{m}$ ) after the dyeing reaction. (a) Spherical particles obtained after the reactions as described in section 3.2.1. The inset gives a magnified view of the particle surface. (b) Particle fracture due to too rapid centrifugation at 2000 rpm. Such fracture can also occur when magnetic stirrers are used.

While the ultrasound preparation method was shown in chapter 5 to be less favorable for obtaining rheological data, the confocal images prove that the ultrasound preparation leads to excellent secondary fluid droplet breakup and an acceptable structural homogeneity in the images. No large agglomerates around poorly distributed or large, coalesced secondary fluid entities were observed in any of the confocal images in this section. So, the ultrasound method is at least superior to the other mixing methods in agglomerate prevention, especially for the pendular state. This, together with the clear benefit of making in-situ, 3D imaging available, makes the ultrasound-prepared samples of composition C1 suitable and very valuable for more profound structural analyses, as long as the sample preparation difficulties are kept in mind. Such analyses will be the core of the following section 6.2. The data shown therein were not part of any publication up to now.



## 6.2 Variation of secondary fluid volume fraction

The structural investigations discussed in section 6.2 have been performed using capillary suspensions of composition C1 containing porous particles from the batch “6.2 porous” with two different surface treatments ( $\theta = 87 \pm 8^\circ$  and  $\theta = 115 \pm 8^\circ$ , see Table 3.4). In total, 19 samples where the composition was varied by using different set secondary to solid volume ratios  $\phi_{\text{sec,set}}/\phi_{\text{solid,set}}$  between 0 and 1.54 were prepared. All compositions are summarized in Table 6.1. In section 6.1, the dependence of the complex shear modulus on the contact angle was determined for capillary suspensions based on porous particles with  $\phi_{\text{solid,set}} = 0.25$ , which led to elevated effective solid volume fractions around 0.55. For the samples of Table 6.1, the aim was to obtain lower effective solid volume fractions on the order of  $\phi_{\text{solid,set}} \approx 0.15 - 0.25$ , which are more characteristic of capillary suspensions. Thus, the set particle volume fraction was reduced and fixed at  $\phi_{\text{solid,set}} = 0.08$ . The resulting effective volume fractions, also included into Table 6.1, will be discussed below. Due to the fixed value of  $\phi_{\text{solid,set}}$ , the experiments are designed as a variation of the secondary fluid volume fraction for two different contact angles using porous particles and also include one additional sample of a 50/50 mixture of both particle types.

**Table 6.1:** Overview on the 19 samples of composition C1 prepared from porous particles of batch “6.2 porous” having  $\theta = 87 \pm 8^\circ$  and  $\theta = 115 \pm 8^\circ$ . The amount of secondary fluid in relation to the solid volume fraction was varied, while the set particle volume fraction was fixed at  $\phi_{\text{solid,set}} = 0.08$ . The effective volume fractions were measured using an average from 8 confocal images.

Contact angle	$\phi_{\text{sec,set}}/\phi_{\text{solid,set}}$	$\phi_{\text{solid,eff}}$	$\phi_{\text{sec,eff}}/\phi_{\text{solid,eff}}$
$\theta = 87 \pm 8^\circ$	0.00	$0.469 \pm 0.011$	0.000
	0.04	$0.201 \pm 0.028$	$0.002 \pm 0.001$
	0.08	$0.166 \pm 0.014$	$0.010 \pm 0.002$
	0.16	$0.193 \pm 0.014$	$0.024 \pm 0.007$
	0.20	$0.164 \pm 0.045$	$0.036 \pm 0.018$
	0.30	$0.205 \pm 0.028$	$0.101 \pm 0.033$
	0.50	$0.176 \pm 0.018$	$0.180 \pm 0.036$
	1.00	$0.167 \pm 0.015$	$0.413 \pm 0.085$
	1.54	$0.504 \pm 0.076$	$0.845 \pm 0.202$
$\theta = 115 \pm 8^\circ$	0.00	$0.275 \pm 0.021$	0.000
	0.04	$0.192 \pm 0.019$	$0.002 \pm 0.001$
	0.08	$0.183 \pm 0.012$	$0.024 \pm 0.007$
	0.16	$0.243 \pm 0.018$	$0.056 \pm 0.010$
	0.20	$0.220 \pm 0.013$	$0.086 \pm 0.011$
	0.30	$0.203 \pm 0.049$	$0.171 \pm 0.079$
	0.50	$0.221 \pm 0.046$	$0.179 \pm 0.076$
	1.00	$0.163 \pm 0.040$	$0.481 \pm 0.249$
	1.54	$0.510 \pm 0.106$	$0.716 \pm 0.282$
50/50 wt % mixture	0.20	$0.176 \pm 0.024$	$0.074 \pm 0.021$

### 6.2.1 Confocal images and basic sample properties

#### Contact angle hysteresis

In Table 6.2, the contact angle values determined from 10 individual particles per type are shown and are used to calculate the mean angles  $\theta = 87 \pm 8^\circ$  and  $\theta = 115 \pm 8^\circ$ . The samples seem to contain particles showing contact angles that span a range of roughly  $20^\circ$  for both particle types. A possible hypothesis to explain this finding is that the individually measured angles denote meta-stable states found at local minima of the Gibbs energy in the contact angle hysteresis [72]. The particles were immersed in either of the pure fluids prior to the contact angle measurements and, therefore, entered the liquid-liquid interface from both sides. When permeating from the bulk phase, the contact angle of the secondary fluid towards the particle surface is advancing as the particle is wet by the secondary fluid. Alternatively, a de-wetting of to the secondary fluid has to occur when the particle enters the interface from the secondary fluid side, denoting the receding contact angle. This might also explain why the individually measured contact angle values for both particle types do not appear to be a Gaussian distribution around the mean angles ( $\theta_{\text{mean}} = 87 \pm 8^\circ$  and  $\theta_{\text{mean}} = 115 \pm 8^\circ$ , respectively), but are instead arranged in two distinguishable populations of particles with lower and higher angles. This could be the difference between advancing and receding angles caused by contact line pinning on the rough particle surface. Another possibility is the difference between Wenzel and Cassie-Baxter wetting if the pores are fully or only partially saturated with liquid before the particles enter the interface. Chemical inhomogeneities of the particle surface, resulting from the different treatments detailed in section 3.2, also represent a possible reason for the broad range of angles found here.

**Table 6.2:** Individual values of 10 contact angle measurements for the particle type with mean angles  $\theta = 87 \pm 8^\circ$  (left) and mean angles  $\theta = 115 \pm 8^\circ$  (right).

$\theta_{\text{mean}} = 87 \pm 8^\circ$	$\theta_{\text{mean}} = 115 \pm 8^\circ$
75.0°	105.3°
79.6°	105.5°
80.4°	107.5°
81.2°	109.7°
84.6°	110.2°
91.4°	116.6°
92.5°	122.0°
93.6°	123.1°
94.6°	123.2°
95.7°	125.0°

In general, the equilibrium angle, if there is one, is not easily determined as it does not have to be the mean between the advancing and receding angles [78]. The Wenzel angle  $\theta_{\text{Wenzel}}$  or the Cassie-Baxter angle  $\theta_{\text{CB}}$ , as introduced in section 2.3.1, should denote the most stable equilibrium angles for these particles. However, without information on the previous dynamics for each particle (which is not constrained during mixing) or knowledge about the particle surface on a length scale that is below the resolution of

the microscope, one cannot make any more specific claims about the particle wetting, or calculate  $\theta_{\text{Wenzel}}$  or  $\theta_{\text{CB}}$ . Thus, the mean contact angle is chosen as an approximate measure of the wetting.

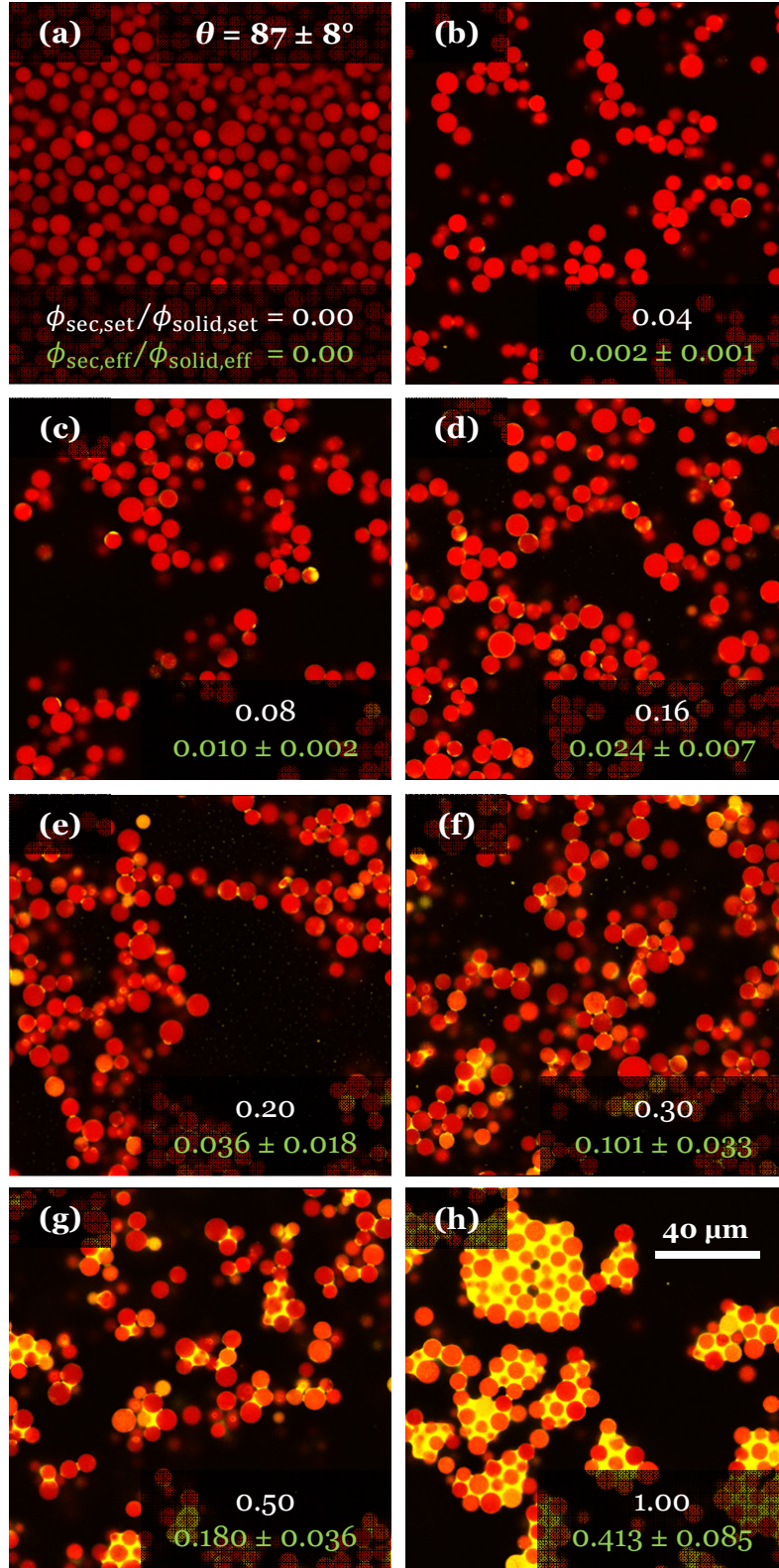
### Confocal microscopy images

Confocal 3D images of the samples, summarized in Table 6.1, were taken at eight different positions each, using the microscopy parameters and image sizes as described in section 4.2. 2D images of a representative  $x$ - $y$  plane of one of these 3D images per sample are shown in Fig. 6.14 and 6.15 containing an overlay of both the particle (red) and secondary fluid (yellow) signals. Fig. 6.14 shows the samples with  $\theta = 87 \pm 8^\circ$  and Fig. 6.15 for  $\theta = 115 \pm 8^\circ$ , each with a set volume ratio from 0.00 to 1.00. The effective volume ratios, written in green text at the bottom of each confocal image, are also included and will be discussed later.

The  $87^\circ$  sample without added secondary fluid (Fig. 6.14a) does not show a percolating particle network, but rather a bed of sedimented particles. With  $\phi_{\text{sec,set}}/\phi_{\text{solid,set}} = 0.04$  (Fig. 6.14b) there are no capillary bridges visible, but the structure shows particle percolation and the sample is clearly stabilized against sedimentation in contrast to the sample without secondary fluid. Therefore, the presence of small capillary bridges leading to an attractive particle network can be assumed, where the bridges are just too small to be imaged, as already discussed in section 6.1.2. From  $\phi_{\text{sec,set}}/\phi_{\text{solid,set}} = 0.04$  to 0.20 (Fig. 6.14b–e), the amount of secondary fluid increases. Part of this secondary liquid is immersed in the particle pores and part of it forms binary inter-particulate bridges in a pendular state conformation, which increase in size with the added amount of secondary fluid. At  $\phi_{\text{sec,set}}/\phi_{\text{solid,set}} = 0.30$  (Fig. 6.14f), the sample underwent a transition to the funicular state as seen by the coalesced capillary bridges. With further secondary liquid, the funicular droplets turn into small ( $\phi_{\text{sec,set}}/\phi_{\text{solid,set}} = 0.50$ , Fig. 6.14g) and finally large ( $\phi_{\text{sec,set}}/\phi_{\text{solid,set}} = 1.00$ , Fig. 6.14h) agglomerates, where the particle network percolation is no longer directly visible, but the large voids of bulk fluid between the particle agglomerates clearly prove a stabilization against sedimentation.

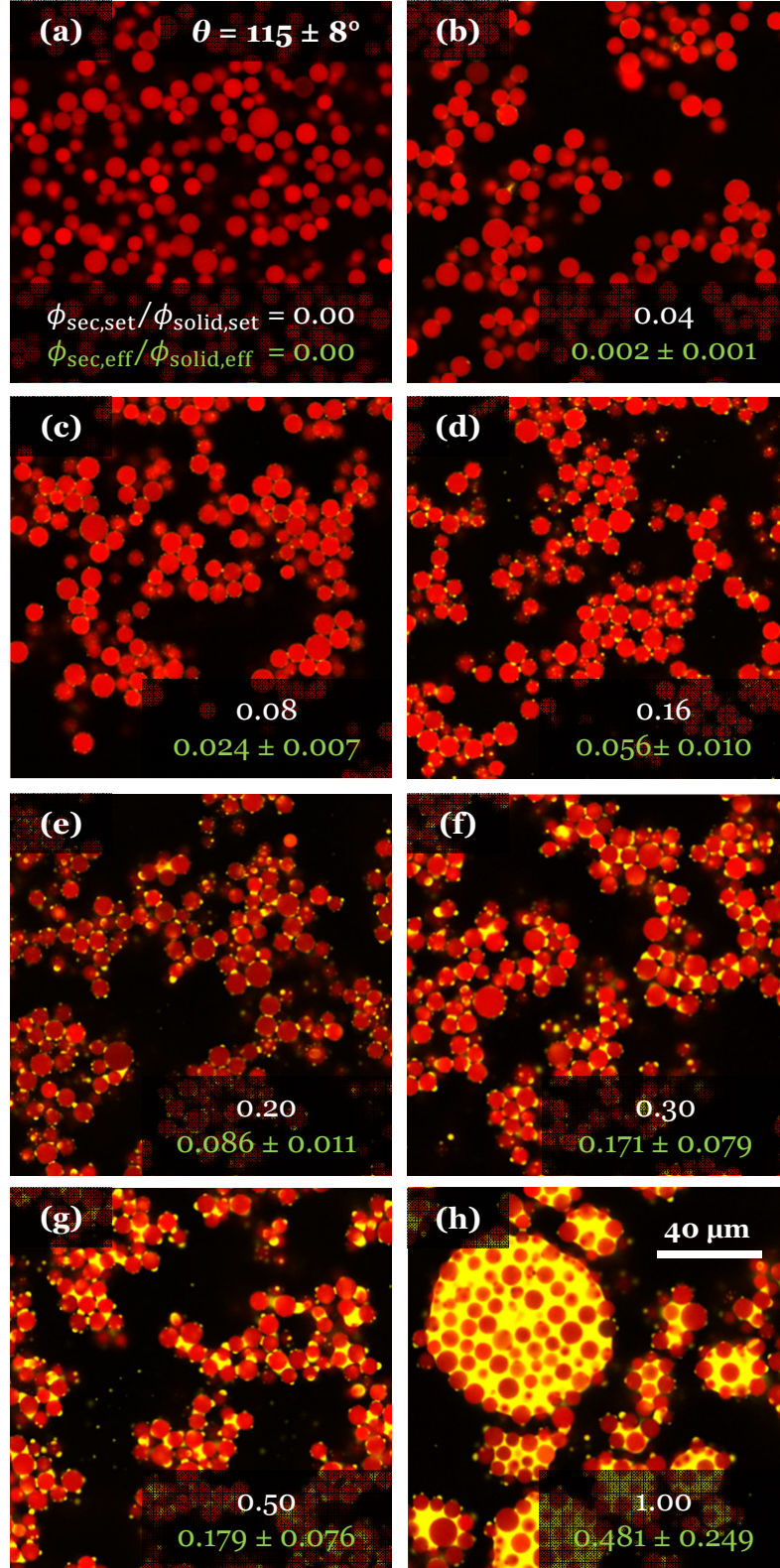
When further increasing the secondary fluid volume to  $\phi_{\text{sec,set}}/\phi_{\text{solid,set}} = 1.54$  the agglomerates grow much larger. This is shown in Fig. 6.16 for the  $87^\circ$  sample, where the sample with  $\phi_{\text{sec,set}}/\phi_{\text{solid,set}} = 1.54$  shows a complete phase separation. Fig. 6.16a shows one of the homogeneous samples for comparison. All particles in the phase-separated sample are aggregated into a few very large clusters that extend several millimeters in size, surrounded by the pure bulk fluid. The confocal image of the interior of the large aggregates shows that the aggregate mostly consists of densely packed particles in single, large secondary fluid drops with only a few small volumes of bulk liquid locked in the aggregate. Due to the phase separation, this sample cannot be characterized by shear rheology. Microscopy, applied only to the clusters themselves, is clearly not representative for the overall composition. Therefore, the range of experimentally accessible secondary to solid volume ratios is constrained by this agglomeration. Similar problems have already been discussed for the samples with saturations of  $S = 0.2$  and  $0.35$  in Fig. 5.11 and 5.12.

The  $115^\circ$  samples, at a first glance, show similar transitions as the  $87^\circ$  ones, but also differ in some important ways. First, for the sample without added secondary fluid (Fig. 6.15a) the sample neither shows a fully established sediment of particles nor a clear percolating particle network. Thus, the particle interactions themselves in pure bulk phase

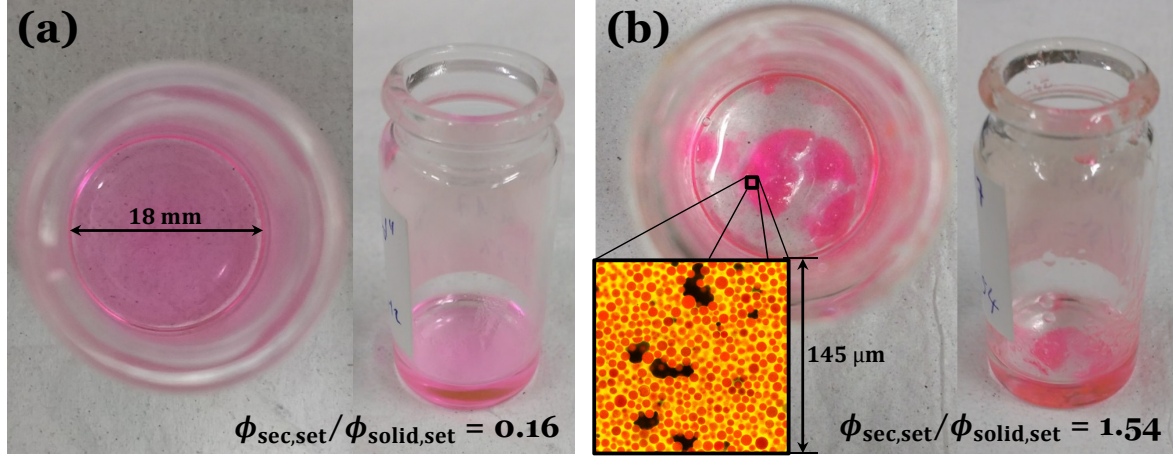


**Figure 6.14:** Confocal 2D images of samples of composition C1 containing porous particles with contact angle  $\theta = 87 \pm 8^\circ$ , mean radius  $a_{50,3} = 3.21 \mu\text{m}$  and varied amounts of secondary fluid. The set solid volume fraction was fixed at  $\phi_{\text{solid,set}} = 0.08$ . The set ratio of secondary to solid volume fractions is increased from  $\phi_{\text{sec,set}}/\phi_{\text{solid,set}} = 0.00$  in (a) to  $\phi_{\text{sec,set}}/\phi_{\text{solid,set}} = 1.00$  in (h) as included in white text color in the eight individual images. The corresponding determined effective ratios  $\phi_{\text{sec,eff}}/\phi_{\text{solid,eff}}$  are included in green text color. The scale bar in (h) is valid for all images.





**Figure 6.15:** Confocal 2D images of samples of composition C1 containing porous particles with contact angle  $\theta = 115 \pm 8^\circ$ , mean radius  $a_{50,3} = 3.21 \mu\text{m}$  and varied amounts of secondary fluid. The set solid volume fraction was fixed at  $\phi_{\text{solid,set}} = 0.08$ . The set ratio of secondary to solid volume fractions is increased from  $\phi_{\text{sec,set}}/\phi_{\text{solid,set}} = 0.00$  in (a) to  $\phi_{\text{sec,set}}/\phi_{\text{solid,set}} = 1.00$  in (h) as included in white text color in the eight individual images. The corresponding determined effective ratios  $\phi_{\text{sec,eff}}/\phi_{\text{solid,eff}}$  are included in green text color. The scale bar in (h) is valid for all images.



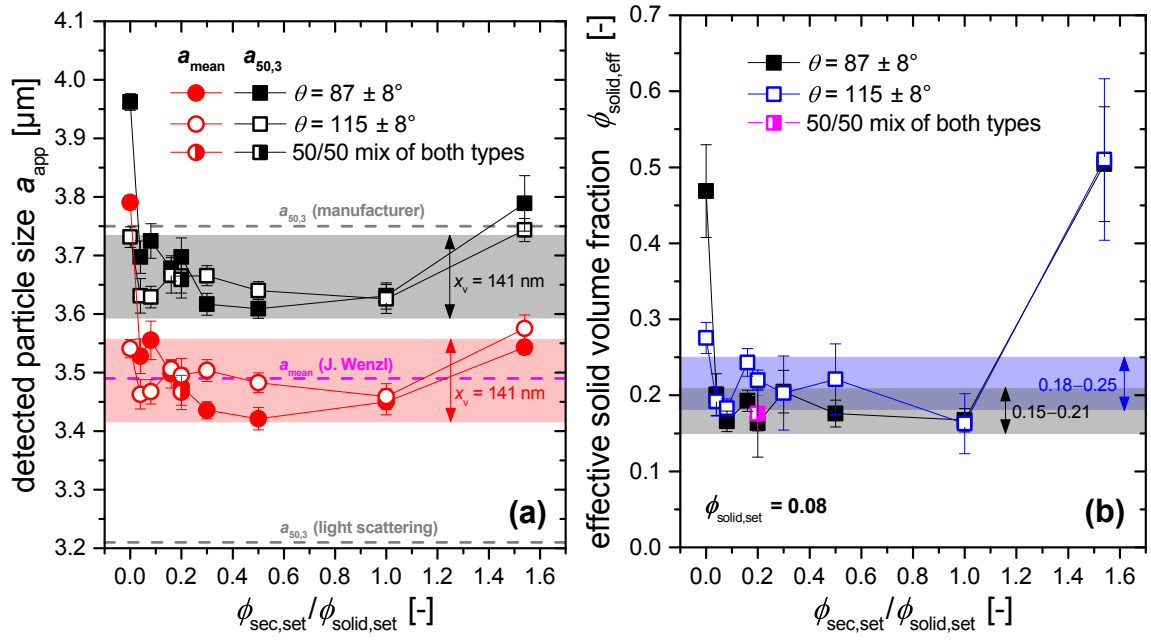
**Figure 6.16:** Top and side view photographs of samples of composition C1 with  $\theta = 87 \pm 8^\circ$ ,  $\phi_{\text{solid,set}} = 0.08$  and set volume ratios of (a)  $\phi_{\text{sec,set}}/\phi_{\text{solid,set}} = 0.16$  and (b)  $\phi_{\text{sec,set}}/\phi_{\text{solid,set}} = 1.54$ . The inset in (b) shows a confocal 2D image of the large agglomerates present in this sample. The very same phase separation was found in the sample with  $\theta = 115 \pm 8^\circ$  and  $\phi_{\text{sec,set}}/\phi_{\text{solid,set}} = 1.54$ .

environment have to be different than for  $87^\circ$ , independent of any capillary force. When the secondary fluid is added, the formation of a percolating particle network is obvious (Fig. 6.15b-g), but there also appear capillary-state-like clusters of particles around small droplets and also many singly-connected droplets residing on the surface of only one particle in addition to binary bridges. Additionally, no clear pendular-funicular transition can be observed. Instead, the transitions are more gradual and mostly just show an increasing size of bridges and droplets with increasing secondary fluid volume. The binary bridges often also seem to show an asymmetric rather than a toroidal shape, as will also be shortly discussed later in the outlook, chapter 7. Therefore, it is difficult to clearly ascribe these samples to either a pendular or capillary state structure, as they show structural peculiarities of both simultaneously. For  $\phi_{\text{sec,set}}/\phi_{\text{solid,set}} = 1.00$  (Fig. 6.15h), large agglomerates appear. These agglomerates seem to be more spherical and a little bit less tightly packed than for the  $87^\circ$  sample, which may indicate only weak attractive particle interactions inside of the agglomerates allowing the liquid-liquid interface to relax. However, such qualitative structural details lack the unambiguity of computational, quantitative analysis. Moreover, there is no obvious reason why the particles prefer to protrude into the secondary fluid at these high volume ratios while the samples with intermediate secondary fluid content, at least partially, show capillary state properties and the contact angle is well beyond  $90^\circ$ . However, a similar odd wetting behavior was also found for the  $115^\circ$  sample of section 6.1.2 (Fig. 6.7c,d) that should, though at a different  $\phi_{\text{solid,eff}}$ , be comparable to the pendular-state-resembling composition shown in Fig. 6.15c. Finally, for  $\phi_{\text{sec,set}}/\phi_{\text{solid,set}} = 1.54$  the same phase separation due to millimeter-sized agglomerates, as observed with the  $87^\circ$  particles (Fig. 6.16b), also occurs for the  $115^\circ$  sample.

### Particle size

In Fig. 6.17a, the arithmetic and volumetric mean particle radii,  $a_{\text{mean}}$  and  $a_{50,3}$  of all samples of Table 6.1 are shown as function of the set secondary to solid volume ratio. The radii shown in this diagram have been calculated from the confocal images as described





**Figure 6.17:** (a) Apparent detected particle sizes  $a_{mean}$  and  $a_{50,3}$ , and (b) effective solid volume fractions  $\phi_{solid,eff}$  as function of the ratio  $\phi_{sec,set}/\phi_{solid,set}$ . The data was obtained by computational evaluation of confocal 3D images of samples containing porous particles having  $\theta = 87 \pm 8^\circ$  or  $115 \pm 8^\circ$  as well as a 50/50 mixture of both of these particle types (as summarized in Table 6.1). The gray and red shaded areas in (a) demonstrate the dimension  $x_v$  of a single voxel of the confocal 3D images in  $x$  and  $y$  directions. The three dashed lines in (a) denote Kromasil particle sizes measured with other methods, as detailed in the text. The gray and blue shaded areas in (b) approximate the effective solid volume fraction regime of the  $87 \pm 8^\circ$  and  $115 \pm 8^\circ$  samples, respectively, when the samples not representing classical capillary suspension microstructures are excluded (i.e.  $\phi_{sec,set}/\phi_{solid,set} \neq 0.00, 1.00$  and  $1.54$ ).

in section 4.4. Physically, there should not be any systematic difference in particle sizes between samples. However, a larger calculated average radius is observed in the samples with  $\phi_{sec,set}/\phi_{solid,set} = 0.00$  and  $1.54$ , especially for the sample with  $\theta = 87^\circ$ . This has to be treated as an artifact of the detection algorithm rather than a real size dependence. The radii were obtained after a refinement step that shifted the first peak of the pair correlation function to  $R/a_{mean} = 2$  as discussed in the methods section. The assumption of zero particle surface distance has been used here, which should be valid for capillary suspensions. However, the samples with  $\phi_{sec,set}/\phi_{solid,set} = 0.00$  and  $1.54$  are not capillary suspensions, as is obvious from the confocal images of Fig. 6.14, 6.15 and 6.16. The larger particle sizes detected for these samples are artifacts due to a nonzero particle distance in these samples, which erroneously is added to the particle size. This artifact in particle size detection may then be used as a qualitative measure of particle attraction. The smaller the apparent detected radii, the more appropriate also is the zero distance assumption and thus also the stronger the particle attraction should be.

For the intermediate samples,  $\phi_{sec,set}/\phi_{solid,set} = 0.04$  to  $1.00$ , all detected radii lie in a similar range of  $a_{50,3} = 3.66 \pm 0.08 \mu\text{m}$  (or  $a_{mean} = 3.48 \pm 0.08 \mu\text{m}$ , respectively). Trends may be discussed in this region, e.g. the samples with  $87^\circ$  go through a minimum in detected radii, while the  $115^\circ$  ones show more constant values. However, one has to be cautious

to not over-interpret such trends as the differences between detected radii are in a size range smaller than the extent of a single image voxel in  $x$  direction, i.e. the detected size differences are already below the resolution limit of the microscope.

The detected radii in the range of  $a_{50,3} = 3.66 \pm 0.08 \mu\text{m}$  are roughly 14% larger than radii detected from the light scattering measurements ( $a_{50,3} = 3.21 \pm 0.03 \mu\text{m}$  in Fig. 3.1d). However, the manufacturer, Akzo Nobel, also determined the particle size before delivery as  $a_{50,3} = 3.75 \mu\text{m}$  by an electric sensing zone method. The radii determined from confocal image analysis agree well with this value. Agreement is also found with the detection of Wenzl, who determined arithmetic mean sizes  $a_{\text{mean}} = 3.49 \pm 0.44 \mu\text{m}$  for dyed Kromasil silica from her confocal images [36].

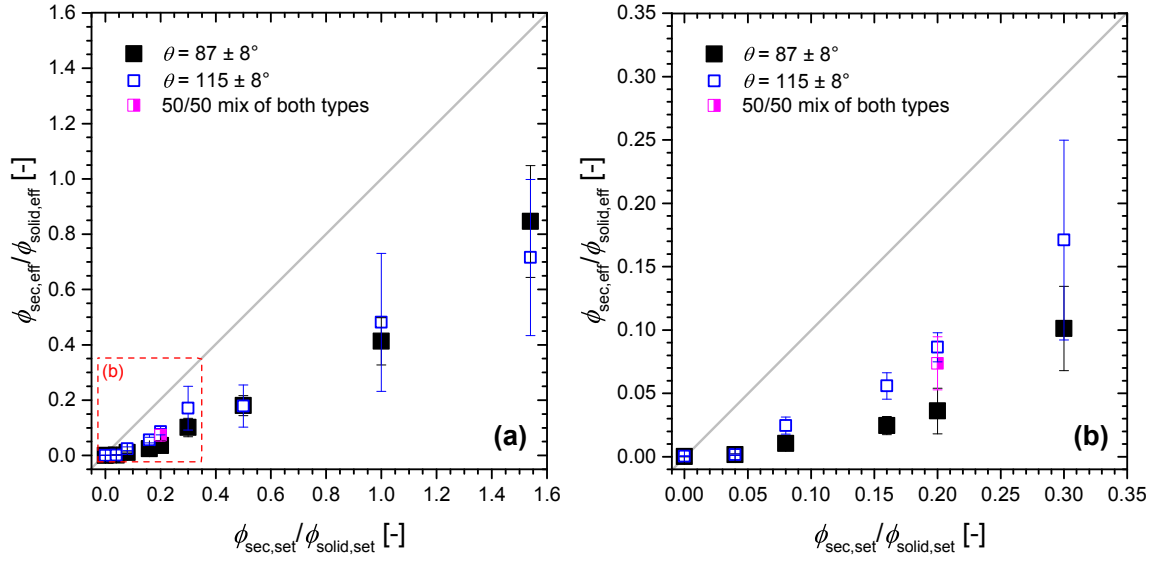
### Effective volume fractions of particles and secondary fluid

Fig. 6.17b shows the detected effective solid volume fractions  $\phi_{\text{solid,eff}}$  as a function of the set volume ratio  $\phi_{\text{sec,set}}/\phi_{\text{solid,set}}$ . This is directly related to the total number of particles detected in each image  $N_{\text{total,img}}$  from which  $\phi_{\text{solid,eff}}$  has been calculated (see the diagram of  $N_{\text{total,img}}$  as function of the set volume ratio in the appendix, Fig. 9.1).

Between  $\phi_{\text{sec,set}}/\phi_{\text{solid,set}} = 0.04$  and  $0.50$  no systematic trends in  $\phi_{\text{solid,eff}}$  can be observed. The effective volume fraction is in the range  $\phi_{\text{solid,eff}} = 0.15 - 0.21$  for the  $87^\circ$  samples, while it is slightly higher for the  $115^\circ$  samples ( $\phi_{\text{solid,eff}} = 0.18 - 0.25$ ). The data shows that the aim of preparing capillary suspensions with representative solid volume fractions of roughly  $0.15 - 0.25$  is acceptably reached. The slight difference in effective solid volume fractions between the  $87^\circ$  and  $115^\circ$  samples cannot be attributed to the particle porosity, which was the same for both particle types. Therefore, the  $115^\circ$  samples showing the higher volume fractions seem to tend to an increased compaction close to the bottom of the sample (at least in the imaged  $\approx 150 \mu\text{m}$  wide layer closest to the microscope slide) compared to the  $87^\circ$  samples. This may be a sign for a weaker sample strength. A characterization of the sample strength is given by rheological data, which will be the topic of the next subsection.

Again, the samples with  $\phi_{\text{sec,set}}/\phi_{\text{solid,set}} = 0.00$  and  $1.54$  have to be discussed separately. They show a much higher effective  $\phi_{\text{solid,eff}}$  as the other samples, reflecting the sedimentation of particles (see confocal image Fig. 6.14a) or the imaged agglomerate interior (inset in Fig. 6.16b), respectively. However, the sediment and agglomerates show  $\phi_{\text{solid,eff}}$  in the range of only  $\approx 0.5$ , still far away from random close packing. The sample for  $\theta = 115^\circ$  without secondary fluid even shows  $\phi_{\text{solid,eff}} = 0.28 \pm 0.02$ , which is much smaller than random close packing, but larger than for the capillary suspensions. In combination with the relatively low detected radius value in Fig. 6.17a and the optical impression of Fig. 6.15a, this hints at stabilizing attractive interactions that are large enough to form a particle network but likely weaker than for capillary suspensions as a compaction of the particle network due to gravity is not fully eliminated.

The effective volume ratios  $\phi_{\text{sec,eff}}/\phi_{\text{solid,eff}}$ , which had already been included in Table 6.1 and in the confocal images of Fig. 6.14 and 6.15, are plotted against the set volume ratios  $\phi_{\text{sec,set}}/\phi_{\text{solid,set}}$  in Fig. 6.18. It is obvious that, as expected, all effective ratios are lower than the set ratios. Before agglomeration begins to set in, i.e. for  $\phi_{\text{sec,set}}/\phi_{\text{solid,set}} < 0.5$ , the  $115^\circ$  samples always show a significantly higher effective ratio than the  $87^\circ$  samples at the same set ratio. This is very clear for  $\phi_{\text{sec,set}}/\phi_{\text{solid,set}} = 0.04$ , where there is nearly no effective secondary fluid detected. For  $\phi_{\text{sec,set}}/\phi_{\text{solid,set}} = 0.08 - 0.20$ , the  $115^\circ$  samples show

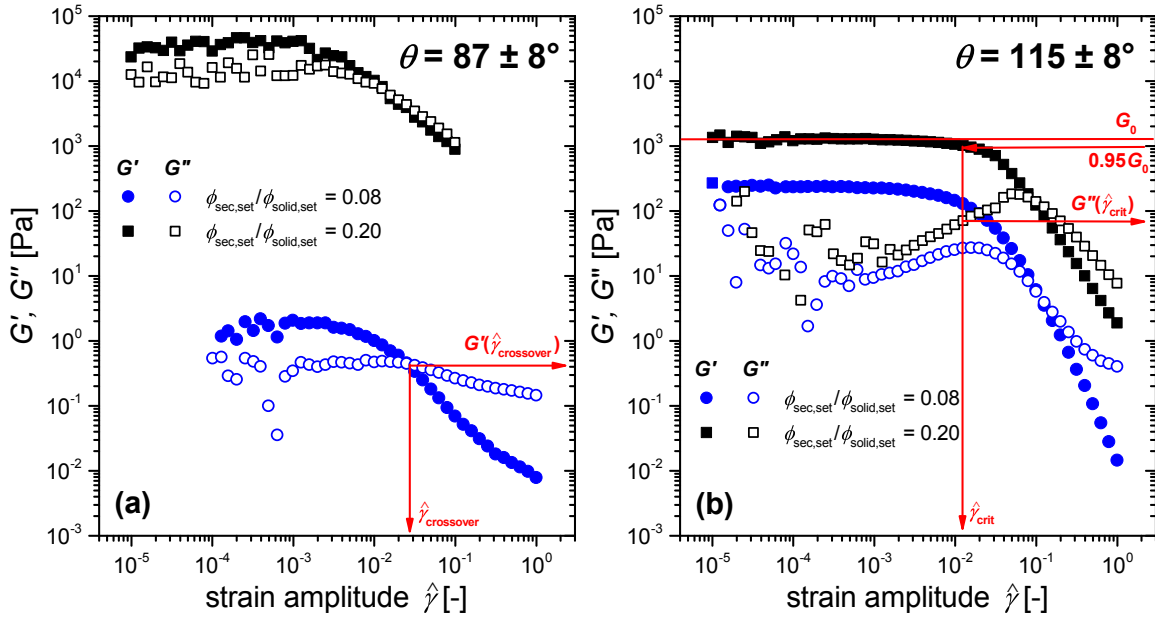


**Figure 6.18:** (a) The effective volume ratios  $\phi_{\text{sec,eff}}/\phi_{\text{solid,eff}}$  of all samples summarized in Table 6.1 as determined from confocal images as a function of the set volume ratio  $\phi_{\text{sec,set}}/\phi_{\text{solid,set}}$ . The gray line denotes the idealized nonporous limiting case where  $\phi_{\text{sec,eff}}/\phi_{\text{solid,eff}} = \phi_{\text{sec,set}}/\phi_{\text{solid,set}}$ . (b) Magnified excerpt, for reasons of enhanced visibility, of the very same data denoted by the red box in (a).

effective ratios that are  $2.4 (\pm 0.1)$  times higher than for the  $87^\circ$  sample. This difference is explained by the reduced absorption of secondary fluid into the particle pores with increasing contact angle as has been discussed in detail in section 6.1.2. The relative differences between  $87^\circ$  and  $115^\circ$  samples become smaller for samples with further increased set volume ratios and any differences are obscured by the large error bars for the agglomerated samples. For the agglomerated samples, the detected solid volume fraction becomes strongly dependent on the position of the confocal image as continuum assumptions are no longer valid.

### 6.2.2 Oscillatory rheometry

In Fig. 6.10 (section 6.1.3), the dependence of the complex shear modulus on the contact angle was determined for capillary suspensions based on porous particles with  $\phi_{\text{solid,set}} = 0.25$  and  $\phi_{\text{sec,set}} = 0.0225$ , i.e.  $\phi_{\text{sec,set}}/\phi_{\text{solid,set}} = 0.09$ . Based on this diagram, a capillary suspension sample with porous particles and  $\theta = 87^\circ$  would be expected to show an elastic modulus roughly two decades lower in magnitude than a sample with porous particles and  $\theta = 115^\circ$ . This should also be expected for samples with the lower effective solid volume fractions around  $\phi_{\text{solid,eff}} = 0.20 \pm 0.05$  discussed in this section compared with Fig. 6.10 that contains data for  $\phi_{\text{solid,eff}} = 0.55$ . Fig. 6.19 shows strain amplitude sweep measurements of  $G'$  and  $G''$  with this reduced solid volume fraction for the  $87^\circ$  and  $115^\circ$  samples with  $\phi_{\text{sec,set}}/\phi_{\text{solid,set}} = 0.08$ , very close to the value of 0.09 used in Fig. 6.10, as well as with  $\phi_{\text{sec,set}}/\phi_{\text{solid,set}} = 0.20$ . Indeed, the plateau modulus  $G_0$  for the sample with  $\phi_{\text{sec,set}}/\phi_{\text{solid,set}} = 0.08$  also shows a difference of magnitude of roughly two decades ( $\approx 1.5$  Pa for the  $87^\circ$  sample vs  $\approx 250$  Pa for  $115^\circ$ ) here. However, the order is reversed for

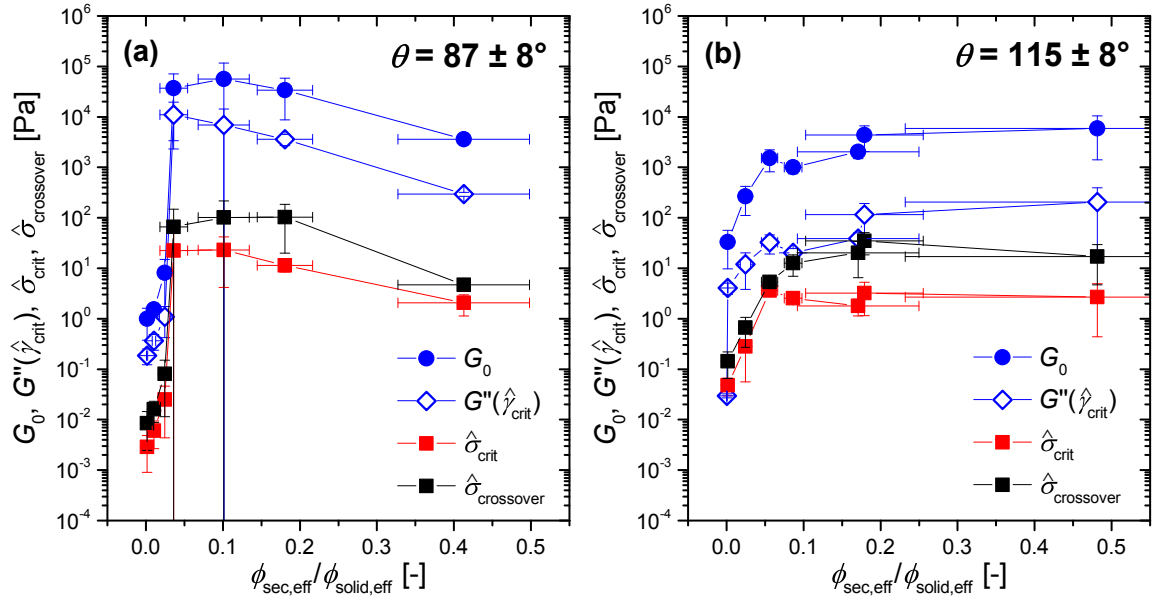


**Figure 6.19:**  $G'$  and  $G''$  as function of the strain amplitude at a frequency of  $\omega = 1$  rad/s. The example data shows samples with  $\phi_{\text{sec,set}}/\phi_{\text{solid,set}} = 0.08$  and  $\phi_{\text{sec,set}}/\phi_{\text{solid,set}} = 0.20$  for particles with (a)  $\theta = 87 \pm 8^\circ$  and (b)  $\theta = 115 \pm 8^\circ$ . The red lines and arrows describe the determination of the plateau modulus  $G_0$ , the critical strain amplitude  $\dot{\gamma}_{\text{crit}}$ , the loss modulus  $G''(\dot{\gamma}_{\text{crit}})$  at the end of the LVE region, the storage modulus  $G'(\dot{\gamma}_{\text{crossover}})$  at the crossover of  $G'$  and  $G''$ , and the strain amplitude  $\dot{\gamma}_{\text{crossover}}$ .

$\phi_{\text{sec,set}}/\phi_{\text{solid,set}} = 0.20$ . The  $87^\circ$  sample shows a plateau modulus that is more than one decade higher than in the  $115^\circ$  sample ( $\approx 40,000$  Pa for the  $87^\circ$  sample vs  $\approx 1,200$  Pa for  $115^\circ$ ). Thus, the assumption that the  $87^\circ$  particles generally produce weaker capillary suspension than for  $115^\circ$  is not generally true. The dependence of the moduli and critical strain amplitudes on the secondary fluid content are explored below.

### Characteristic stresses

The sample strength, which strongly depends on the amount of added secondary fluid, is displayed in Fig. 6.20, where key parameters determined from strain amplitude sweep measurements of all 19 samples are displayed as function of the effective volume ratios. The same data, but as function of the set volume ratios, is shown in the appendix, Fig. 9.2. The plateau modulus  $G_0$  and the loss modulus at the end of the LVE region,  $G''(\dot{\gamma}_{\text{crit}})$ , are chosen as representative values of  $G'$  and  $G''$ . The determination of these values is shown in Fig. 6.19. Additionally, the shear stress amplitude values  $\hat{\sigma}_{\text{crit}}$  and  $\hat{\sigma}_{\text{crossover}}$  at the end of the LVE region and at the crossover of  $G'$  and  $G''$  are shown, which are calculated from the shear moduli and strain amplitudes at the respective positions of the amplitude sweeps. Both of these stress values can be understood as possible representation of an apparent yield stress [41], but are expected to differ from the apparent yield stress determined using the method described in section 4.1. Therefore,  $\hat{\sigma}_{\text{crit}}$  and  $\hat{\sigma}_{\text{crossover}}$  from Fig. 6.20 probably cannot be directly correlated to the yield stress data presented in chapters 5 and 6.3. However, relative yield stress discussions are feasible.



**Figure 6.20:** Plateau modulus  $G_0$ , loss modulus  $G''(\dot{\gamma}_{\text{crit}})$  at the end of the LVE region, stress amplitude  $\hat{\sigma}_{\text{crit}}$  at the end of the LVE region and crossover stress amplitude  $\hat{\sigma}_{\text{crossover}}$  as function of the effective secondary fluid to solid volume ratio  $\phi_{\text{sec,eff}}/\phi_{\text{solid,eff}}$  for the samples with particles having (a)  $\theta = 87 \pm 8^\circ$  and (b)  $\theta = 115 \pm 8^\circ$ . The frequency was fixed at  $\omega = 1$  rad/s.

For the viscous sample with  $\phi_{\text{sec}}/\phi_{\text{solid}} = 0$ ,  $G''$  was larger than  $G'$ , which was too low to be measurable and hence is missing in Fig. 6.20 and Fig. 9.2. All other samples with  $\phi_{\text{sec}}/\phi_{\text{solid}} > 0$  show  $G_0 > G''(\dot{\gamma}_{\text{crit}})$ , as typical for a particle gel. At first, with increasing amounts of secondary fluid,  $G_0$  increases. It enters a plateau in the  $115^\circ$  sample while it goes through a maximum around  $\phi_{\text{sec,eff}}/\phi_{\text{solid,eff}} \approx 0.04 - 0.20$  in the  $87^\circ$  sample. The apparent yield stress values are more than two decades lower than  $G_0$ , but follow the very same trends.

The details of yield stress dependence on secondary fluid content have already been thoroughly investigated by Dittmann et al. [10] (see Fig. 2.12) and by Domenech et al. [6], and the trend found here for the  $87^\circ$  sample is a general characteristic of pendular state capillary suspensions [28]. Domenech and Velankar have also shown that  $G_0$  follows similar trends as the yield stress and is roughly 2-3 decades larger for sample systems with contact angles close to zero [103], which agrees well with the findings of Fig. 6.20, despite the contact angles being much higher. The increase in  $G_0$  and apparent yield stress with small amounts of added secondary fluid appears due to the buildup of capillary bridges. The maximum value is attributed to the transition to a funicular network structure, as discussed previously in section 6.1 [101, 150]. The ensuing decrease seen in the strength of the  $87^\circ$  sample occurs due to the formation of larger dense agglomerates, which lead to a weakening of the network structure [10]. This weakening in the structure due to agglomeration was also seen in chapter 5 for insufficient mixing conditions. The confocal image of Fig. 6.15h unambiguously shows that agglomeration has appeared at  $\phi_{\text{sec,eff}}/\phi_{\text{solid,eff}} = 0.481 \pm 0.249$  in the  $115^\circ$  sample, so there is no obvious reason why the yield stress and plateau modulus do not show a decrease in the respective data point of Fig. 6.20b. This expected decrease is found for the respective agglomerated sample

in the 87° data. Most likely, the appearance of the large agglomerates led to a violation of the continuum assumption for rheological measurements undertaken in a very small gap of 0.5 mm. Therefore, further rheological discussions will be limited to the samples with  $\phi_{\text{sec,eff}}/\phi_{\text{solid,eff}} < 0.2$  (i.e.  $\phi_{\text{sec,set}}/\phi_{\text{solid,set}} \leq 0.5$ ), representing capillary suspension structures without serious agglomeration.

The plateau modulus and yield stress values first increase comparatively slow in the 87° samples with set volume ratio in the range  $\phi_{\text{sec,set}}/\phi_{\text{solid,set}} = 0.04$  to 0.16 (Fig. 9.2a) due to the imbibition of secondary fluid into the particle pores, which explains why the elastic modulus in the sample with  $\phi_{\text{sec,set}}/\phi_{\text{solid,set}} = 0.08$  for 87° was about two decades below that of the respective 115° sample in Fig. 6.19. However, this turns into a very steep increase when plotted against the effective ratios in Fig. 6.20a. This steep increase denotes the buildup of the pendular state, with the transition to the plateau, i.e. to funicular structures, at an effective ratio of  $\phi_{\text{sec,eff}}/\phi_{\text{solid,eff}} \geq 0.036 \pm 0.018$  ( $\phi_{\text{sec,set}}/\phi_{\text{solid,set}} \geq 0.20$ ). This is consistent with the confocal images of Fig. 6.14. The transition to the plateau region also can be compared to the critical transition volume ratio  $V_{\text{bridge,crit}}/V_{\text{sphere}} = 0.025 \pm 0.001$  calculated for the pendular-funicular transition of a  $\theta = 61^\circ$  sample in section 6.1.1. While a correct transition volume ratio cannot be calculated for  $\theta = 87^\circ$  with the set of equations used in section 6.1.1, it might be expected to be roughly on the order of  $V_{\text{bridge,crit}}/V_{\text{sphere}} = 0.03$  when extrapolating the curves of Fig. 6.4. This is in acceptable agreement with  $\phi_{\text{sec,eff}}/\phi_{\text{solid,eff}} \geq 0.036 \pm 0.018$ . Agglomeration starts towards the end of the plateau region in Fig. 6.20a. The confocal images showing first some small agglomerates at  $\phi_{\text{sec,eff}}/\phi_{\text{solid,eff}} \geq 0.180 \pm 0.036$  in Fig. 6.14g agree with the equivalent decrease in the characteristic stress values seen in Fig. 6.20a.

The 115° sample set (Fig. 6.20b) does not show such a sharp increase in the characteristic stress properties for low volume ratios. The smooth transition to the plateau appears at higher volume ratios around  $\phi_{\text{sec,eff}}/\phi_{\text{solid,eff}} = 0.05 - 0.20$ . Any argumentation based on funicular transitions, as in section 6.1.1, has to be rejected for such a contact angle larger than 90°. The origins of the rheological fingerprint in the 115° sample cannot be fully resolved here, apart from the obvious sample strengthening with increasing secondary fluid volume, which agrees well with the optical impression of the confocal images in Fig. 6.15. The buildup of a particle network, followed by a transition to higher order clusters as simulated by Koos et al. [8] may be hypothesized, but cannot be proven unambiguously at this point as the confocal images of the 115° samples neither illustrate a clear capillary nor pendular state.

It is also worth examining why the rheological stress properties of Fig. 6.20 are mostly larger in the 87° than in the 115° samples. Explanations based on the capillary force equations of section 2.3.2, including the yield stress equation 6.1, are not appropriate for discussing samples resembling the capillary state, as these equations are not valid for large contact angles where the bridges are convex, asymmetric, connect more than two particles, or exhibit all of these properties. As the existence of the capillary state can be traced back to an energetically favorability of particles surrounding small convex droplets [30], the strength should also be related to a characteristic energetic property on the particle scale. The energy necessary to detach a spherical particle with radius  $a$  from an interface between two liquids with interfacial tension  $\Gamma$  is given by [170]

$$E_{\text{detach}} = \pi a^2 \Gamma (1 - |\cos \theta|)^2 \quad (6.3)$$



which can be related to the stress required to detach the particle [14]

$$\sigma_{\text{detach}} = \frac{2\Gamma}{a} \cos^2\left(\frac{\theta}{2}\right). \quad (6.4)$$

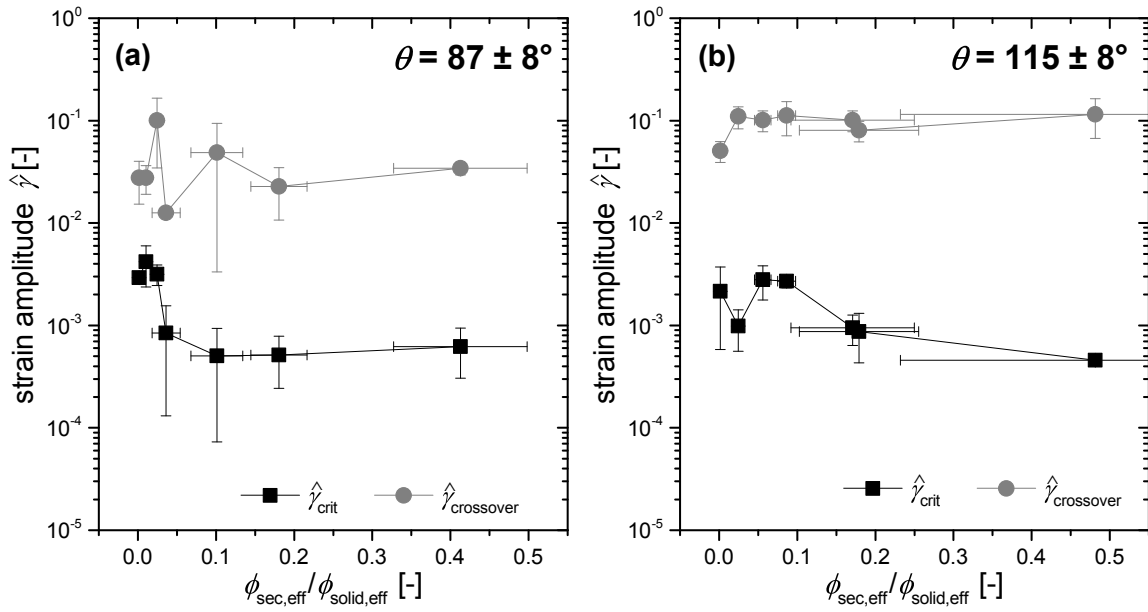
Based on this equation, the detachment stress of sample composition C1 (calculated with  $a = 3.21 \mu\text{m}$ ,  $\Gamma = 21.5 \text{ mN/m}$ ) is 7050 Pa for  $\theta = 87^\circ$ , while it is roughly reduced by half to 3870 Pa for  $\theta = 115^\circ$ . Therefore, it is easier to detach the particles from the secondary fluid entities in the  $115^\circ$  sample, which can explain their lower strength. Retrospectively, the same argument may also explain the decrease in  $G_0$  found in Fig. 6.10 for the  $147^\circ$  capillary state sample.

The lower strength of the  $115^\circ$  samples, along with their weaker inter-particulate attractions, may also be analyzed considering to the particle size detection artifacts discussed in Fig. 6.17a. The curves of detected effective radii, as function of the secondary to solid volume ratio, are roughly anti-correlated with the stress curves from oscillatory rheometry, i.e. stronger stress corresponds to smaller detected radii, as is attributed to a closer particle separation distance. Accordingly, the  $115^\circ$  samples showing effective particle radii, which are detected larger than for the  $87^\circ$  samples in the intermediate secondary fluid volume range ( $\phi_{\text{sec,set}}/\phi_{\text{solid,set}} \approx 0.2 - 1$ ), might also be related to their overall lower stresses.

The scatter in effective solid volume fractions shown in Fig. 6.17b can be used to explain scatter in the rheological measurements in Fig. 6.20 as the rheological properties always have a strong dependence on the solid volume fraction. A rough estimation using  $G_0$  on the  $115^\circ$  samples shows the extent of this effect. Assuming that the solid volume fraction dependence of the elastic modulus  $G'$  can be described by a Krieger-Dougherty equation with  $\phi_{\text{max}} = 0.57$  as proposed by Mahaut et al. [171], the quotient between a sample with  $\phi_{\text{solid,eff}} = 0.18$  and  $0.25$  would only be  $G_0(\phi = 0.25)/G_0(\phi = 0.18) = 1.33$ . Assuming, instead, a more realistic power law dependence of  $G_0 \propto \phi_{\text{solid,eff}}^4$  (as will be roughly found later in chapter 6.3.2), this quotient increases to  $G_0(\phi = 0.25)/G_0(\phi = 0.18) = 3.72$ . While this only denotes a relative difference, it nevertheless is very close to the range of most standard deviations between measurements as provided in Fig. 6.20.

### Characteristic strain amplitudes

In addition to the characteristic stress values, the equivalent strain amplitudes at the end of the LVE region and at the crossover,  $\hat{\gamma}_{\text{crit}}$  and  $\hat{\gamma}_{\text{crossover}}$ , are shown in Fig. 6.21. The values were determined as shown in Fig. 6.19 and are plotted as function of the effective volume fraction ratio. In contrast to the characteristic stress values of Fig. 6.20, the strain amplitudes only weakly depend on the amount of added secondary fluid. For the  $87^\circ$  samples, the critical strain  $\hat{\gamma}_{\text{crit}}$  at the end of the LVE region decreases roughly one decade from the already low values of  $\approx 0.4\%$  without added secondary fluid to  $\approx 0.06\%$ . Low values of this strain, associated with yielding of the sample, are typical for strong attractive particle gels [38]. This can be understood as the breakage of a particle bond by separating two particles and therefore  $\hat{\gamma}_{\text{crit}}$  is closely related to the microstructure. The steepest decrease in  $\hat{\gamma}_{\text{crit}}$  for the  $87^\circ$  sample corresponds to the buildup of pendular bridges as was shown by the stress values of Fig. 6.20. The critical strain amplitude remains constant for higher secondary fluid contents.



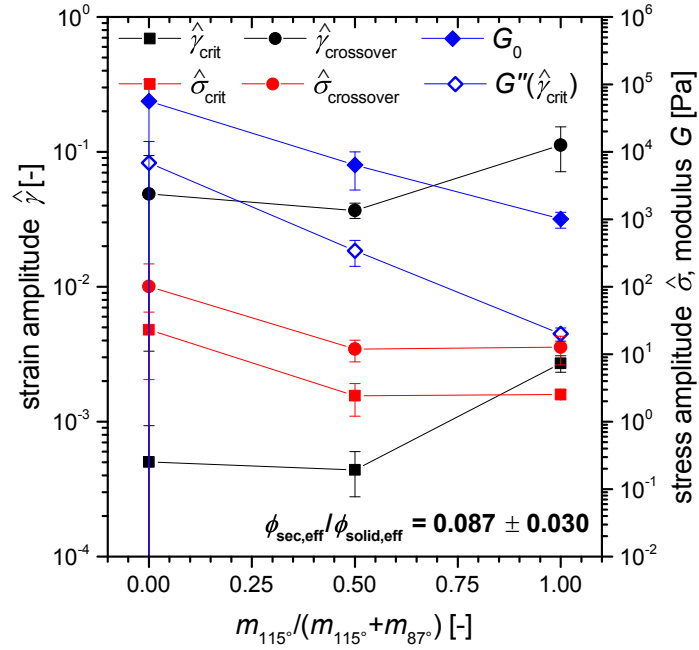
**Figure 6.21:** Strain amplitudes  $\hat{\gamma}_{\text{crit}}$  at the end of the LVE region and  $\hat{\gamma}_{\text{crossover}}$  at the intersection of  $G'$  and  $G''$  as function of the effective secondary fluid to solid volume ratio  $\phi_{\text{sec,eff}}/\phi_{\text{solid,eff}}$  for the samples with particles having (a)  $\theta = 87 \pm 8^\circ$  and (b)  $\theta = 115 \pm 8^\circ$ . The frequency was fixed at  $\omega = 1$  rad/s.

A similar behavior of the critical strain amplitude was also found by Domenech and Velankar for silica particles in an immiscible polymer blend with a three-phase contact angle close to zero [103]. Their samples also showed pendular and funicular states followed by agglomeration. In their study, the critical amplitude at the end of the LVE region drops slightly in the range  $\phi_{\text{sec}}/\phi_{\text{solid}} \approx 0 - 0.2$  and then remains constant for  $\phi_{\text{sec}}/\phi_{\text{solid}} \approx 0.2 - 1$ .

For the  $115^\circ$  sample, an overall decrease in  $\hat{\gamma}_{\text{crit}}$  with increasing secondary fluid volume is found, but the trend is more scattered than for the  $87^\circ$  sample. The decrease in the  $115^\circ$  sample is less abrupt than for  $87^\circ$ , which also resembles the smoother stress transitions of the  $115^\circ$  samples. The crossover strain amplitudes  $\hat{\gamma}_{\text{crossover}}$  do not show any significant trend for either the  $87^\circ$  nor  $115^\circ$  samples and, with respect to the error bars, should be considered as independent of the secondary fluid content.

### Mixture of particles

Finally, the characteristic rheological properties of the sample containing a 50/50 mixture of  $87^\circ$  and  $115^\circ$  particles ( $\phi_{\text{sec,eff}}/\phi_{\text{solid,eff}} = 0.074 \pm 0.021$ ) are shown in Fig. 6.22, where the mixture is compared to the two samples containing only  $87^\circ$  or  $115^\circ$  particles with effective volume ratios closest to the mixture sample, i.e.  $\phi_{\text{sec,eff}}/\phi_{\text{solid,eff}} = 0.101 \pm 0.033$  for  $87^\circ$  and  $\phi_{\text{sec,eff}}/\phi_{\text{solid,eff}} = 0.086 \pm 0.011$  for  $115^\circ$ , respectively. The elastic and loss moduli of the mixture are found to lie nicely in the middle between the values of the two pure samples. However, for the other properties either the  $115^\circ$  or the  $87^\circ$  particles seem to dominate the rheology of the particle mixture sample. Additionally, a direct comparison is somewhat problematic as  $\phi_{\text{sec,eff}}/\phi_{\text{solid,eff}}$  is slightly different for all three samples which obscures any trends.



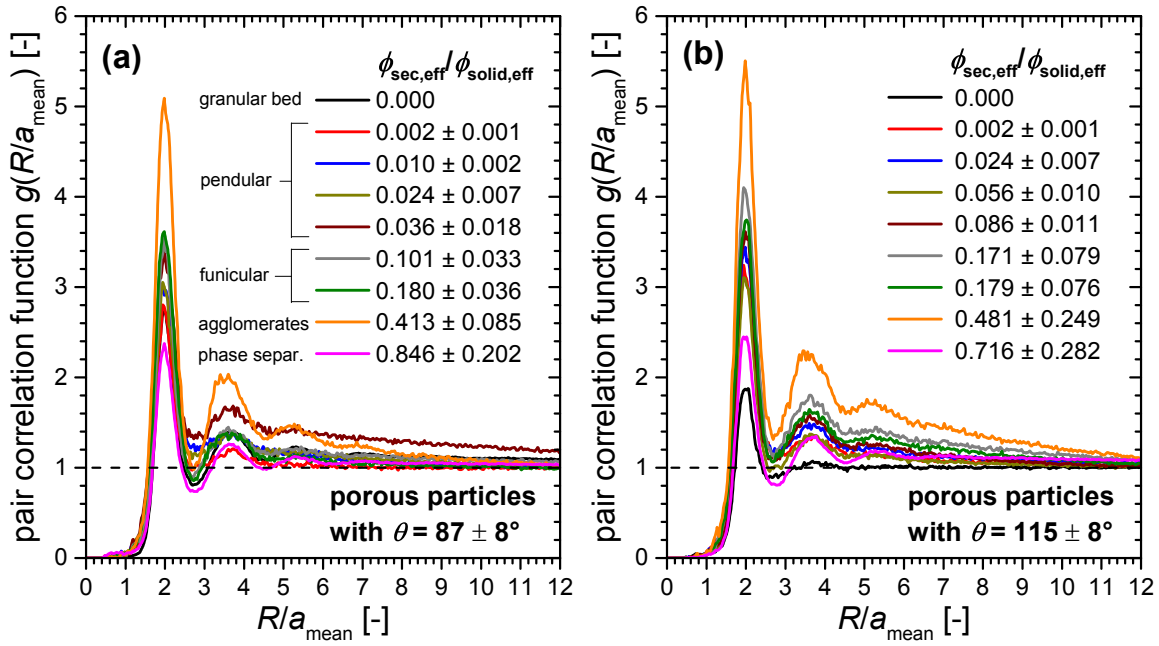
**Figure 6.22:** Rheological parameters determined from strain amplitude measurements at mean volume ratio  $\phi_{\text{sec,eff}}/\phi_{\text{solid,eff}} = 0.087 \pm 0.030$  with varied composition of particle types as expressed by the mass fraction of particles having  $115 \pm 8^\circ$  in relation to the total mass of added particles in the sample. A mass fraction of 0 denotes the sample only containing particles with  $87 \pm 8^\circ$ , mass fraction of 1 only particles with  $115 \pm 8^\circ$  and mass fraction of 0.5 a 50/50 mixture of both particle types.

### 6.2.3 Computational structure evaluations

#### Pair correlation functions

The structure of the samples of Table 6.1 is first characterized by the radial pair correlation functions. These are shown in Fig. 6.23a for the samples with  $\theta = 87^\circ$  and Fig. 6.23b for  $\theta = 115^\circ$ . The radial coordinate  $R$  is normalized by the arithmetic mean particle size  $a_{\text{mean}}$ , which was directly determined from the pair correlation functions themselves by fitting their first peak to the position  $R/a_{\text{mean}} = 2$ , see lines 22-25 and 28 of algorithm 4.1 in section 4.4. The functions of Fig. 6.23 are the  $g(R/a_{\text{mean}})$  calculations with the already refined radii of Fig. 6.17a. The data here are shown without error bars to allow discrimination of the curves by eye. The same data with error bars included is provided in the appendix, Fig. 9.3 ( $\theta = 87^\circ$ ) and Fig. 9.4 ( $\theta = 115^\circ$ ). The data for the 50/50 mixture of both particle types is also given in the appendix, Fig. 9.5, where individual pair correlation functions from the eight images of this sample are additionally included to illustrate an example of the order of magnitude of discrepancy between single images. The presence of these errors, while not shown in Fig. 6.23, has to be kept in mind when discussing the pair correlation functions.

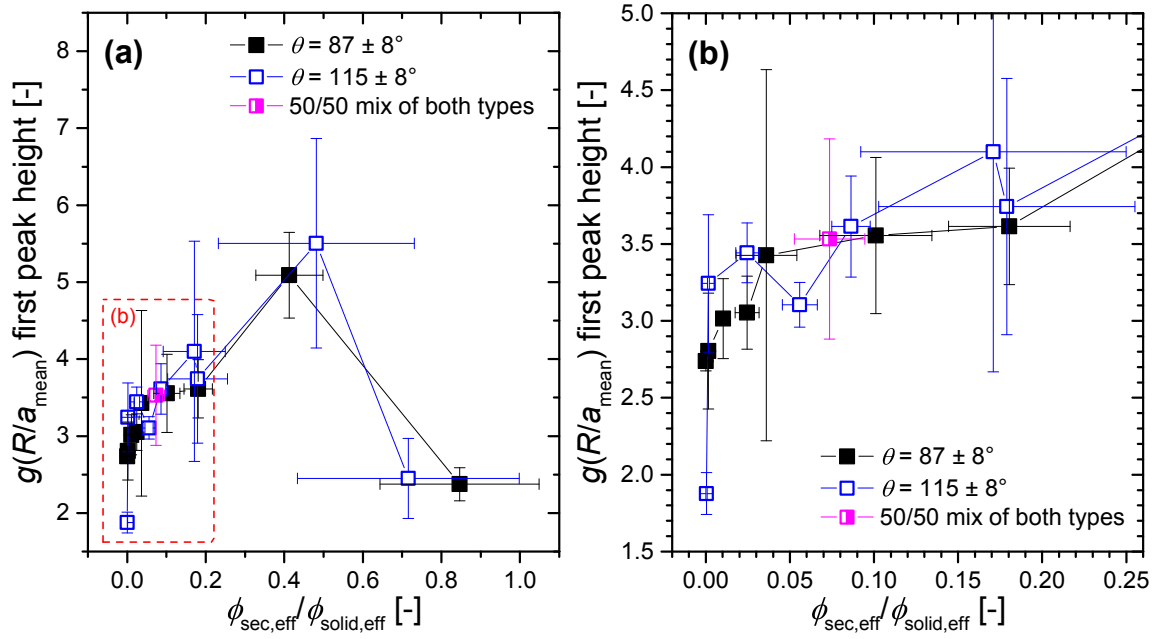
Fig. 6.23 shows that the pair correlation functions change with increasing the secondary to solid volume ratio. While their general shape is preserved, i.e. distinct first peak at  $R/a = 2$ , smaller second peak at  $R/a \approx 3.5 - 4$ , minimum between both peaks, asymptotic decrease towards  $g(R/a) = 1$  for large  $R/a$ , all of these properties change in height and



**Figure 6.23:** Pair correlation functions  $g(R/a_{\text{mean}})$  for  $R/a_{\text{mean}} \leq 12$  of C1 samples with varied effective secondary fluid to solid volume ratio with particles showing (a)  $87 \pm 8^\circ$  and (b)  $115 \pm 8^\circ$ . For reasons of better visibility, the data is shown without error bars. The same diagrams with included error bars are given in the appendix section 9.2. The radial coordinate  $R$  is normalized by the calculated mean radius  $a_{\text{mean}}$  of each individual sample as shown in Fig. 6.17a.

exact shape with the amount of added secondary fluid. Concerning the second peak, it is quite obvious, even within the large error, that this peak is distinctly higher for the agglomerated structures with  $\phi_{\text{sec,eff}}/\phi_{\text{solid,eff}} = 0.413$  and  $0.481$  for  $\theta = 87^\circ$  and  $115^\circ$ , respectively, than for any other structures. Additionally, these agglomerated samples exhibit a pronounced third peak that does not, or only less clear, show up in the other samples. This is an indication of the particles having a higher degree of order in the agglomerates than e.g. in the granular beds where the third peak is quasi-absent. However, concerning the capillary suspension samples that may be of more interest than any agglomerates, all curves are too close to each other for  $R/a > 3$  to make unambiguous statements on any differences in the shape and position of the second (and further) peaks and its antecedent minimum. The first peak of the functions seems to be the most pronounced feature of the diagrams and, thus, should be fewest affected by the large errors. Accordingly, the first peak height is displayed as a function of the effective secondary to solid volume ratio in Fig. 6.24.

For perfectly monodisperse particles, the first peak of attractive percolated particle networks should be a Dirac delta function, while the peak should be completely absent for perfectly dispersed non-contacting particles [172]. For attractive particles with a size distribution, the Dirac function is replaced by a peak that shows an increasing width (and decreasing height) with increasing broadness of the distribution [173]. As  $g(R/a)$  is computed as a discrete instead of a continuous function, the peak height also depends on the bin width  $\Delta(R/a)$  of discretization. All data of Fig. 6.23 (and thus also Fig. 6.24) contains particles with identical real size distributions and was calculated with constant bin width



**Figure 6.24:** (a) Height of the first peak of the pair correlation functions  $g(R/a_{\text{mean}})$  determined at  $R/a_{\text{mean}} = 2$  as a function of the effective volume ratio  $\phi_{\text{sec,eff}}/\phi_{\text{solid,eff}}$  for all samples summarized in Table 6.1. (b) Magnified excerpt, for reasons of enhanced visibility, of the very same data denoted by the red box in (a).

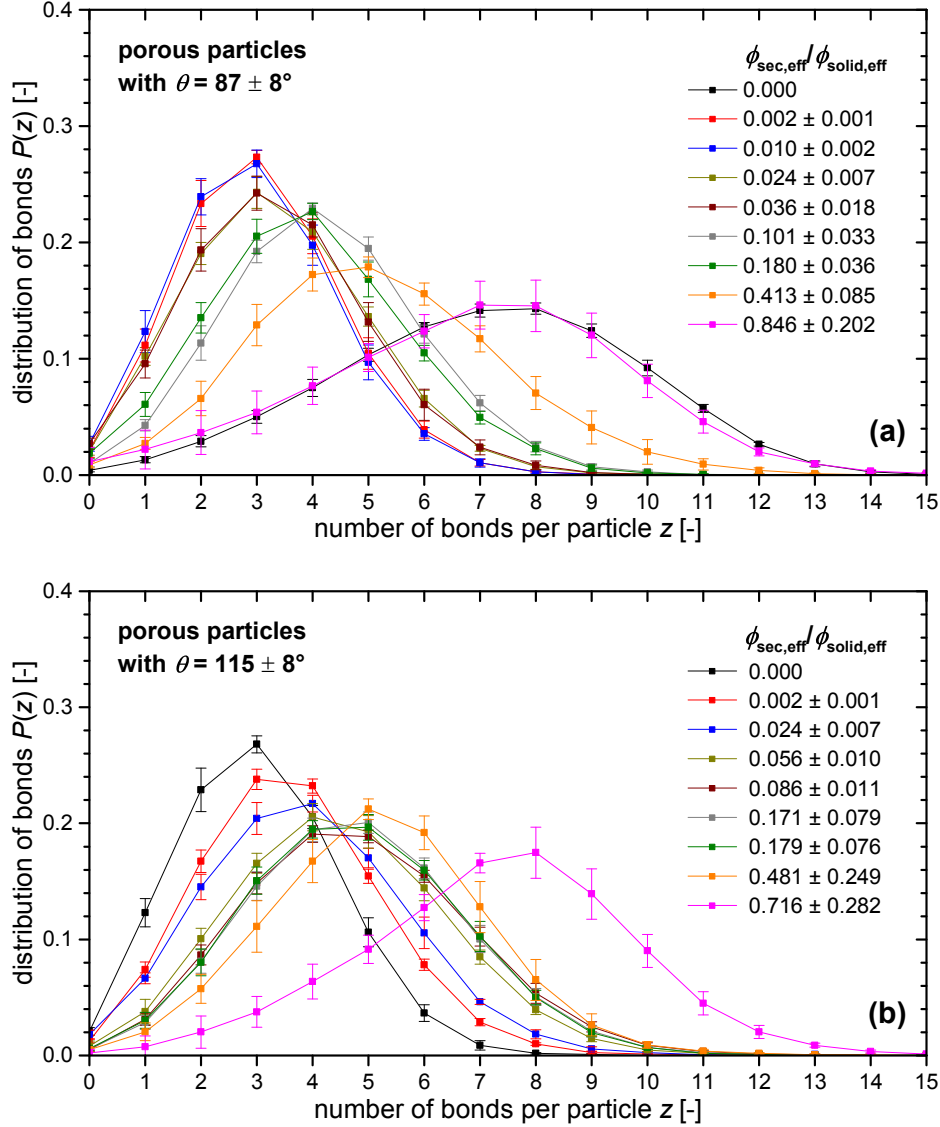
$\Delta(R/a) = 0.04 \cdot R/a$ . Hence, qualitative comparisons of peak heights between the samples can be executed.

For both contact angles, the peak height increases with increasing  $\phi_{\text{sec,eff}}/\phi_{\text{solid,eff}}$  from 0 to  $\approx 0.5$  with only the very last data point ( $\phi_{\text{sec,eff}}/\phi_{\text{solid,eff}} \approx 0.7 - 0.9$ ) dropping to lower values. In the latter case, the calculations were performed on images of the interiors of the very large agglomerates, as shown in Fig. 6.16. This agglomerate interior, with the quasi-absence of bulk liquid, can be regarded as a two-phase suspension of particles in one liquid. The relatively small peak height hints at a relatively homogeneous distribution of particles in the agglomerate interior. The same low peak value is true for the two samples without added secondary fluid as they are also two-phase suspensions. The increase in peak height with addition of secondary fluid then may be attributed to the attractive interaction between the particles induced by the capillary forces, which increases the probability of finding particles in direct contact. With increasing amount of secondary fluid, the number of adjacent particles (the coordination number), and thus the peak height, continues to increase.

Basically, also the fractal dimension  $D$  of the particle network can be determined from pair correlation functions by differences in the asymptotic convergence towards  $g(R/a) = 1$  for large  $R/a$  [52]. However, the error between single measurements for each sample in the diagrams of Fig. 6.23 was too large to extract reliable and physically meaningful values of  $D$ . Therefore, these were not further evaluated with this method.

### Coordination number

Instead of trying to deduce the number of particle contacts from the peak height of the pair correlation function, it is more straightforward to count this coordination number  $z$  directly. A plot of the histogram of coordination numbers is shown in Fig. 6.25a for the samples with  $\theta = 87^\circ$  and Fig. 6.25b for  $\theta = 115^\circ$ . The histogram for the sample contain-

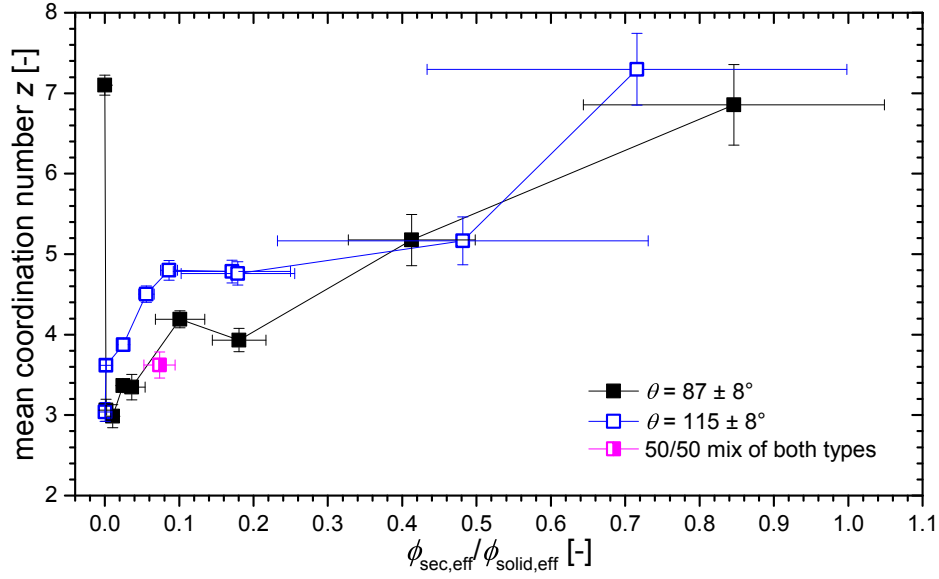


**Figure 6.25:** Probability histograms  $P$  of the coordination number  $z$  (contacts per particle) of porous C1 samples with varied secondary fluid to solid volume ratio with particles having (a)  $87 \pm 8^\circ$  and (b)  $115 \pm 8^\circ$ . Every particle pair with a surface distance  $< 0.85 \mu\text{m}$  was counted as a contact.

ning a 50/50 mixture of both particles (which will not be discussed here) can be found in the appendix, Fig. 9.6. The mean coordination numbers, directly evaluated from these histograms, are plotted as a function of the effective volume ratio in Fig. 6.26.

For  $87^\circ$ , the sample without secondary fluid ( $\phi_{\text{sec,eff}}/\phi_{\text{solid,eff}} = 0$ ) has settled to form a granular bed of silica particles, as was seen in the respective confocal image, Fig. 6.14a. This results in a very broad distribution of coordination numbers, with a relatively high





**Figure 6.26:** Mean coordination number  $z$  as a function of the effective volume ratio  $\phi_{\text{sec,eff}}/\phi_{\text{solid,eff}}$  for all samples summarized in Table 6.1. The data was directly obtained from the histograms of Fig. 6.25 and Fig. 9.6.

mean coordination number  $z = 7.1 \pm 0.1$ . For monodisperse particles, the maximum possible coordination number is  $z = 12$  for hexagonal closest packing of spheres. Larger individual coordination numbers are possible with broad particle size distributions when a large particle is surrounded by more than 12 particles of smaller size. This is seen in the small portion of particles with  $z > 12$  in Fig. 6.25 for the Kromasil silica particles that show a broad particle size distribution (Fig. 3.1d).

With only small additions of secondary fluid ( $\phi_{\text{sec,eff}}/\phi_{\text{solid,eff}} = 0.002 \pm 0.001$  and  $0.010 \pm 0.002$ ), the  $87^\circ$  sample is in the pendular state. The initial increase in the rheological stress properties (Fig. 6.20a) and the visible structural change in the confocal images (Fig. 6.14b,c) are also directly seen in the coordination numbers. The histograms become much narrower and the mean value shifts to much smaller numbers of  $z \approx 3.0 \pm 0.2$ . With increasing the secondary fluid volumes, the sample transition to funicular structures is accompanied by a broadening of the coordination number histograms with increasing mean values up to  $z = 4.2 \pm 0.1$  at  $\phi_{\text{sec,eff}}/\phi_{\text{solid,eff}} = 0.101 \pm 0.033$ . This increase in coordination numbers in the range of  $\phi_{\text{sec,eff}}/\phi_{\text{solid,eff}} = 0.002 \pm 0.001$  to  $0.101 \pm 0.033$  also is in agreement with the increase in first peak height of the pair correlation function seen for the same samples in Fig. 6.24. An increasing number of attractive contacts per particle lead to an increased sample strength and, thus, it is not surprising that the increase in coordination number also correlates well with the increase in sample strength seen from the rheological data in Fig. 6.20a.

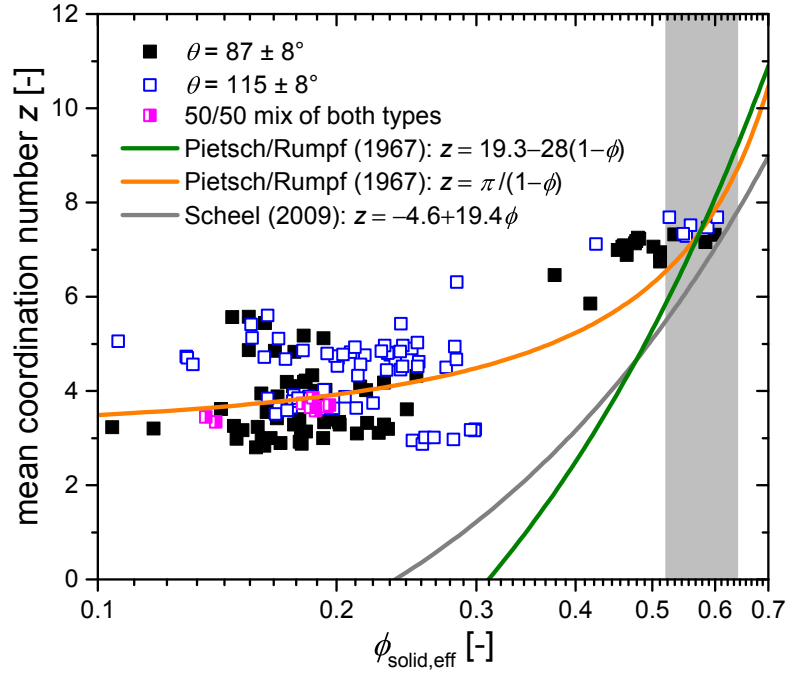
Upon further increases in the amount of secondary fluid to  $\phi_{\text{sec,eff}}/\phi_{\text{solid,eff}} = 0.180 \pm 0.036$ , a slight decrease in strength in the rheological data occurs as the sample begins to cluster. This decrease also is well reproduced in a slight decrease of the mean coordination number to  $z = 3.9 \pm 0.1$  at  $\phi_{\text{sec,eff}}/\phi_{\text{solid,eff}} = 0.180 \pm 0.036$  while the clusters are still very small (see Fig. 6.14g). Upon increasing the cluster size for even larger amounts of secondary fluid, the coordination number decouples from the sample strength. As soon as particles are completely immersed in the interior of clusters, these intra-cluster particles

will not greatly contribute in transferring stress through the sample. On the other hand, these intra-cluster particles are closely surrounded by many adjacent particles and thus show a very large coordination number. Therefore, with increasing cluster sizes, the coordination number histograms broaden and the mean coordination number increases significantly, but the sample strength simultaneously decreases. In the extreme case, where the whole sample has phase separated ( $\phi_{\text{sec,eff}}/\phi_{\text{solid,eff}} = 0.846 \pm 0.202$ ) and the confocal images only showed the interior of one very large cluster (Fig. 6.16), the coordination number histogram shows the same very broad shape as for the granular bed without secondary fluid. This also agrees with the small pair correlation function peak heights of these samples.

For the 115° sample, a similar relationship between the sample strength and the coordination number can be drawn. In the range where the structure represents capillary suspensions,  $\phi_{\text{sec,eff}}/\phi_{\text{solid,eff}} = 0.002 \pm 0.001$  to  $0.179 \pm 0.076$ , the mean coordination number increases from  $z = 3.6 \pm 0.1$  to  $4.8 \pm 0.1$ . This agrees well with the increase in the characteristic stress values of Fig. 6.20b in the same range. Especially, the increase in mean coordination number, very similar to the increase in the characteristic stress, gradually becomes less steep until finally becoming a plateau. The absence of any decrease in strength of the 115° sample seen in the rheological data also is reproduced by the absence of a decrease in coordination number. This is in contrast to the 87° sample where the decrease in strength was accomplished by a decrease in  $z$ .

The mean coordination numbers of the capillary suspension samples are higher for the 115° particles than the 87°. If the sample strength would be solely related to the coordination number, the rheological stress properties of Fig. 6.20 should also be larger in the 115° than in the 87° samples. This obviously is not true. Therefore, the result of capillary-state-like suspensions being weaker than pendular and funicular state ones cannot be attributed to the coordination number, which, in contrast to the previously calculated detachment energies, does not take the secondary fluid properties into account. In pendular and especially funicular structures, a capillary bridge is expected to be located at most of the contact points. In the capillary state, on the other hand, many direct particle contacts are instead “dry” contacts as the secondary fluid is not located directly at the contact points. The coordination number, thus, should only influence the strength of the system as long as the capillary force can act at the contact points [174]. At “dry” contacts, apart from omnipresent van der Waals forces, friction forces may also contribute to sample strength, but this friction is not a precondition to form stable particle networks [174]. Particularly, van der Waals and friction forces also contribute to the sample strength for the “wet” contacts formed by capillary bridges, where a stronger capillary force leads to a larger friction force [85].

The coordination number also is expected to depend on the solid volume fraction of the samples, as a larger number of particles in a more densely crowded sample will obviously lead to more contact points until close packing is reached. Taking the slightly higher effective solid volume fractions of the 115° samples into account (see Fig. 6.17b), may explain why the mean coordination numbers of these samples are higher than for 87°. The dependence of  $z$  on the solid volume fraction is checked in Fig. 6.27 where the mean coordination numbers from each confocal image are plotted against their individually detected effective solid volume fraction, irrespective of their secondary to solid volume ratio. In general, the expected increase in  $z$  with increasing  $\phi_{\text{solid,eff}}$  is found in the data, but the data points show a very broad distribution of  $z$  values at the same  $\phi_{\text{solid,eff}}$ . This



**Figure 6.27:** Mapping of determined mean coordination number  $z$  against effective solid volume fraction  $\phi_{\text{solid,eff}}$  for all individual samples summarized in Table 6.1 (eight samples per set composition, 19 compositions in total). Also included are three empirical equations as outlined in the figure legend [88, 97]. These have been fit by the respective authors to different wet granular matter data only in the denoted gray region with  $\phi_{\text{solid}} > 0.52$ .

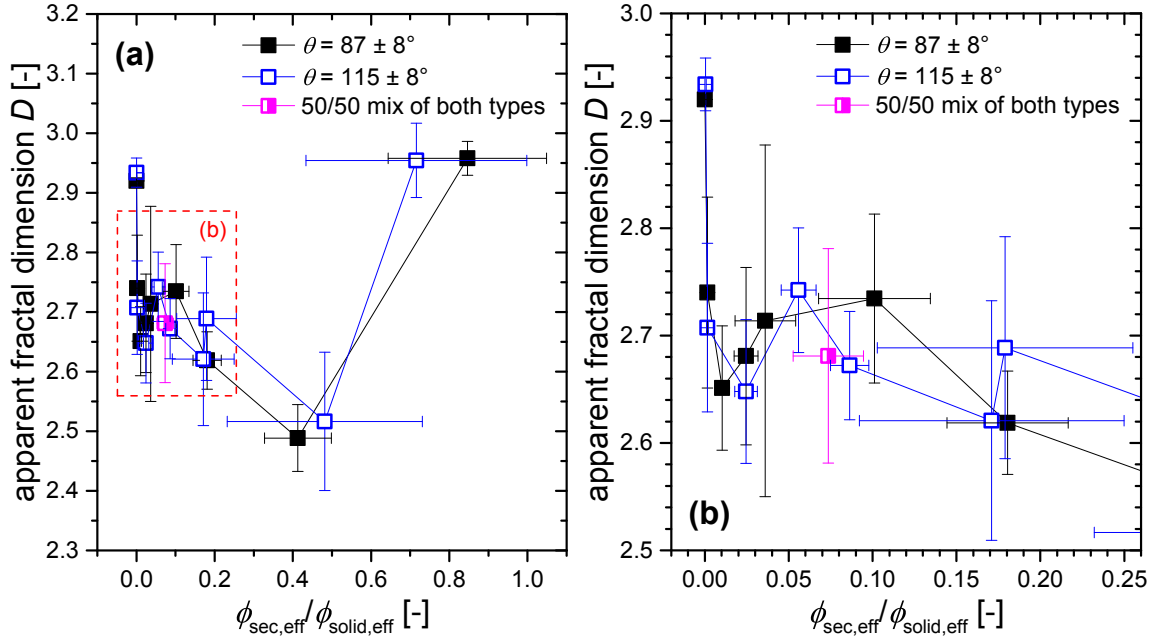
absence of a nice master curve for the data points shows that the solid volume fraction is not the only factor influencing the coordination number of the examined samples. This is further proof that the amount of secondary fluid indeed influences the coordination number of the samples, making the trends of Fig. 6.26 less ambiguous.

There do not seem to exist any constitutive model equations that yet relate the coordination number to the solid volume fraction in the solid volume fraction regime of typical capillary suspensions. Coordination numbers have been only modeled for two-phase suspensions without capillary bridges, which cannot be applied here. There do exist some empiric equations for wet granular matter systems with high solid volume fractions  $\phi_{\text{solid}} > 0.52$ , but they lack any underlying physical underpinnings. Three of these empiric equations, originating from Scheel [85, 97] and from Pietsch and Rumpf [88], are included in Fig. 6.27. The fit  $z = \pi / (1 - \phi_{\text{solid,eff}})$  seems to be appropriate for the intermediate solid volume fractions here, but this has to be seen as a coincidence rather than as a real fit due to its purely empiric nature. Therefore, the influence of the solid volume fraction on the coordination number in capillary suspensions cannot be fully elucidated here, but offers an interesting challenge for future research.

### Fractal dimensions – a first approach and its challenges

In addition to the coordination number, the fractal dimension  $D$  offers the possibility to capture the microstructure of the particle network. Fractal dimensions were determined from the radial power law dependence of the number of particles around a reference par-

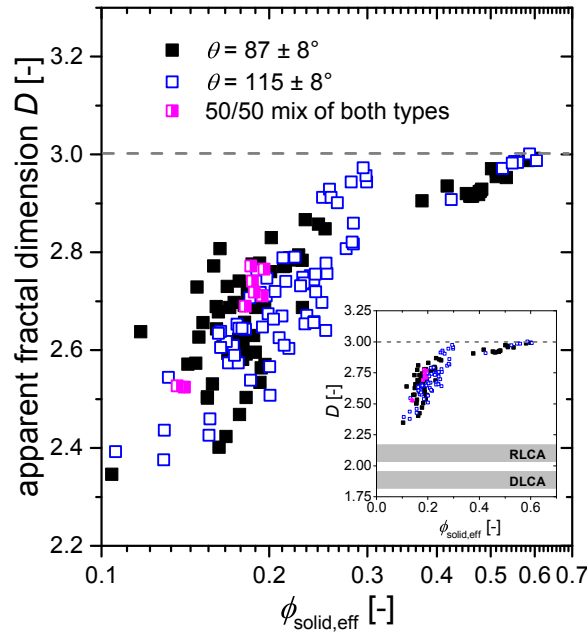
title, see equation 2.29 and line 27 in Alg. 4.1 (section 4.4). The results for all samples of Table 6.1 are summarized in Fig. 6.28.



**Figure 6.28:** (a) Apparent fractal dimension  $D$  as a function of the effective volume ratio  $\phi_{\text{sec,eff}}/\phi_{\text{solid,eff}}$  for all samples summarized in Table 6.1.  $D$  was determined from the power law dependency of particle number counts  $N$  on the radial distance  $R/a_{\text{mean}}$  as described by equation 2.29. (b) Magnified excerpt, for reasons of enhanced visibility, of the very same data denoted by the red box in (a).

The fractal dimensions calculated from the more homogeneous confocal 3D images (i.e. granular bed at  $\phi_{\text{sec,eff}}/\phi_{\text{solid,eff}} = 0$  and compact interior of a large aggregate at  $\phi_{\text{sec,eff}}/\phi_{\text{solid,eff}} > 0.6$ ) are very close to the value of  $D = 3$ , which is expected for homogeneously distributed particles at sufficiently high solid volume fraction. The capillary suspension samples in the range  $\phi_{\text{sec,eff}}/\phi_{\text{solid,eff}} \approx 0.002 - 0.2$  show lower dimensions in the range  $2.6 \pm 0.1 < D < 2.75 \pm 0.1$ . However, the errors are too large to deduce any trend between the different secondary fluid volume fractions or contact angles in this range. Accordingly, it is not possible to neatly link the calculated fractal dimensions to any of the rheological properties here. Calculations of more exact  $D$  values from the 3D confocal images of capillary suspensions is hindered by sample-inherent local microstructural inhomogeneities. This will be extensively detailed later in chapter 6.3.4.

The calculated fractal dimensions are significantly higher than the typical values of colloidal particle gels ( $D = 1.85 \pm 0.1$  for DLCA or  $D = 2.1 \pm 0.1$  for RLCA [51]). One of the main reasons for this result is the elevated volume fraction of capillary suspensions compared to diffusivity self-assembled colloidal gels where  $\phi_{\text{solid}} \ll 0.1$  is typically found. As with the coordination numbers before, the individual apparent fractal dimensions of all samples are plotted against their individual effective solid volume fraction in Fig. 6.29. The data also scatter over a broad range of possible dimensionality values at the same effective solid volume fraction, showing that  $D$  also does not solely depend on the solid, but also on the secondary fluid volume fraction with a very high probability, as was also found



**Figure 6.29:** Mapping of determined apparent fractal dimension  $D$  against effective solid volume fraction  $\phi_{\text{solid,eff}}$  of all individual samples summarized in Table 6.1 (eight samples per set composition, 19 compositions in total). The horizontal dashed gray line denotes the physical upper limit  $D = 3$ . The inset shows the same data as linear instead of a semi-logarithmic plot, where the gray shaded areas denote typical ranges of dimensions for DLCA and RLCA models.

for the coordination number. Overall, however, an increasing trend of  $D$  with increasing solid volume fraction is found, increasingly converging towards the physical upper limit of  $D = 3$ , which is reached upon close packing, but may also be reached before if a non-close-packed sample shows an overall homogeneous distribution of particles. The clear trend of increasing  $D$  with increasing  $\phi_{\text{solid}}$  is shown in Fig. 6.29. This trend is expected and has been calculated numerically by different authors [54, 175, 176], where the DLCA and RLCA model values ( $D \approx 1.85$  or  $2.1$ , respectively) are shown to be only valid for  $\phi_{\text{solid}}$  approaching zero [175]. This has not been shown as a general trend experimentally, but measured fractal dimension values are higher than expected values for DLCA or RLCA when the solid volume fraction is in an elevated range (e.g. [55, 177, 178]). Extrapolating the data shown in Fig. 6.29 towards  $\phi_{\text{solid}} = 0$ , might approach the model DLCA and RLCA values. However, this cannot be proven here.

Overall, the detection of the fractal dimension seems to not be very straightforward up until this point. Therefore, the next section 6.3 tries to tackle the issue of determining fractal dimensions of capillary suspensions with different approaches, based on rheological data of different sample compositions. This, in combination with systematic variations of particle sizes and solid volume fractions, enables a return to the confocal approach of fractal dimension determination, which will then become easier to understand. This will be the main topic of the next section.

### 6.3 Variation of solid volume fraction and particle size

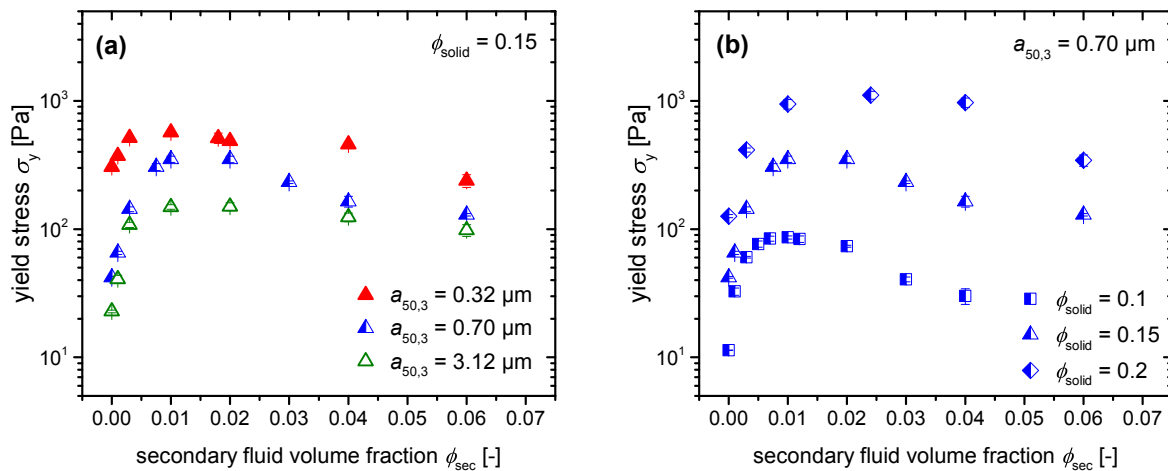
Chapter 6.3 is based on the publication “Fractal approaches to characterize the structure of capillary suspensions using rheology and confocal microscopy” by Frank Bossler, Jo-

hannes Maurath, Katrin Dyhr, Norbert Willenbacher and Erin Koos, Journal of Rheology, 62(1), 183-196, 2018 ([hyperlink](#)), copyright SOR, reproduced with permission from SOR [46]. Everything was part of either the “Results and Discussion” section or “Online Supplementary Information” of this publication and is to a large extent reproduced here with relatively minor changes, apart from the newly prepared extended master curve of Figure 6.40 and its accompanying section which was not part of the publication.

This chapter first takes a closer look at the well-known characteristic stress dependence of pendular state systems as function of the secondary fluid content [6, 10, 28], which has also been found for capillary suspensions of composition C1 with  $\theta = 87^\circ$  in the previous section (Fig. 6.20a). The influence of the solid volume fraction and particle size on such stress curves is investigated based on yield stress data of capillary suspensions of composition C5 ( $\text{Al}_2\text{O}_3$ -based system) and C6 ( $\text{CaCO}_3$ -based system), see Table 3.1. A yield stress master curve is found. Detailed investigations on the yield stress data, as well as on oscillatory rheometry data, are then used to determine fractal dimensions of capillary suspensions with the help of the rheological models presented in the theory section 2.2.4. After having gained knowledge on structural peculiarities of capillary suspensions by these rheological approaches, the confocal fractal dimension approach on composition C1 used at the end of chapter 6.2.3 is re-assessed. The results of this approach are somewhat unsatisfactory. We will understand the underlying reasons at the end of chapter 6.3. Moreover, the influence of the particle size on fractal dimensions is elucidated.

### 6.3.1 Yield stress master curve for $\text{Al}_2\text{O}_3$ -based system

The yield stress  $\sigma_y$  of various samples of the  $\text{Al}_2\text{O}_3$  system (composition C5) was measured using a vane geometry and the method as described in section 4.1, with variations of the mean particle size  $a_{50,3}$ , secondary fluid volume fraction  $\phi_{\text{sec}}$  and particle volume fraction  $\phi_{\text{solid}}$  (both of the latter ones in contrast to section 6.2 being unequivocally defined, as the used particles are nonporous). Fig. 6.30a shows  $\sigma_y$  as function of  $\phi_{\text{sec}}$  with different



**Figure 6.30:** Yield stress  $\sigma_y$  as function of secondary fluid volume fraction  $\phi_{\text{sec}}$  for  $\text{Al}_2\text{O}_3$ -based capillary suspensions of composition C5 at (a) three different particle sizes  $a_{50,3}$  with constant solid volume fraction  $\phi_{\text{solid}} = 0.15$  and (b) three different  $\phi_{\text{solid}}$  with constant particle size  $a_{50,3} = 0.70 \mu\text{m}$ . Figure reproduced with permission from SOR [46].

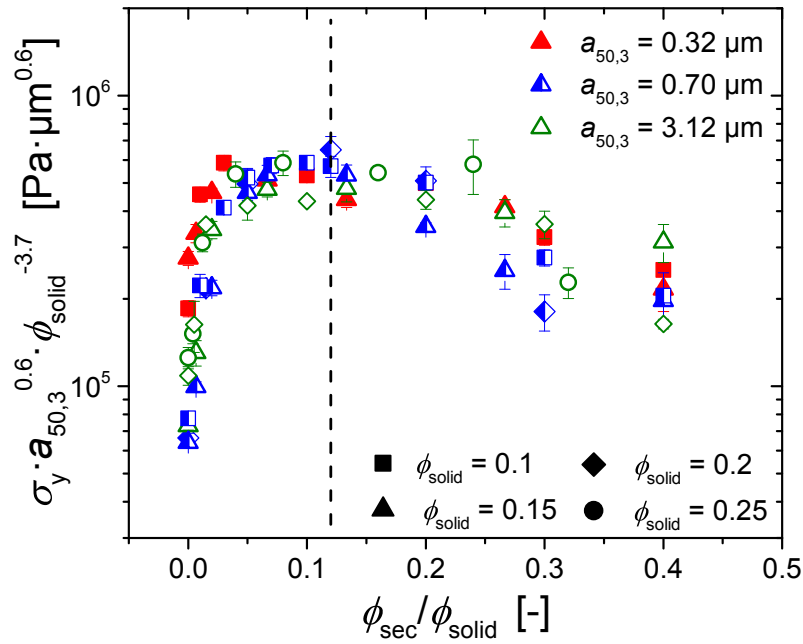


sizes  $a_{50,3}$  at a constant solid volume fraction  $\phi_{\text{solid}} = 0.15$ , while Fig. 6.30b shows  $\sigma_y$  as function of  $\phi_{\text{sec}}$  with varied  $\phi_{\text{solid}}$  at a constant particle size  $a_{50,3} = 0.70 \mu\text{m}$ . In all cases, the yield stress increases strongly at first with small amounts of added secondary fluid due to the buildup of capillary bridges in the pendular state, then goes through a maximum, and finally  $\sigma_y$  decreases again when  $\phi_{\text{sec}}$  is further increased. This is the same general dependence of a characteristic sample stress on secondary fluid content that already has been found for the  $87^\circ$  porous silica samples of composition C1 in section 6.2.2. Also this dependence already is well known from the investigations by Dittmann et al. on the same  $\text{Al}_2\text{O}_3$  sample system, see Fig. 2.12 [10].

The position of the maximum yield stress is shifted to higher secondary fluid volumes with increasing solid volume fraction (Fig. 6.30b), but is independent of particle size (Fig. 6.30a). This maximum value is attributed to a funicular network structure, i.e. merged capillary bridges [101, 150], as has also been demonstrated by the confocal images of composition C1 in Fig. 6.14e–g. The ensuing decrease occurs due to the formation of the larger dense agglomerates, which lead to a weakening of the network structure [6, 10], see also Fig. 6.14g,h.

In Fig. 6.31, the same data as in Fig. 6.30 is shown, with inclusion of additional data taken at  $\phi_{\text{solid}} = 0.10$  for  $a_{50,3} = 0.32 \mu\text{m}$  as well as  $\phi_{\text{solid}} = 0.20$  and  $0.25$  for  $a_{50,3} = 3.12 \mu\text{m}$ . This data has been rescaled so that all data collapse onto a single master curve that can be used to predict an approximate yield stress for any combination of particle size, secondary fluid and solid volume fraction. While this curve is a very helpful tool for directed product design based on such capillary suspensions, it is the details of the rescaling that are of fundamental scientific interest.

The rescaling on the abscissa, where  $\phi_{\text{sec}}$  is replaced by  $\phi_{\text{sec}}/\phi_{\text{solid}}$ , is quite easy to understand since all of the structural transitions, from pure suspension to pendular state



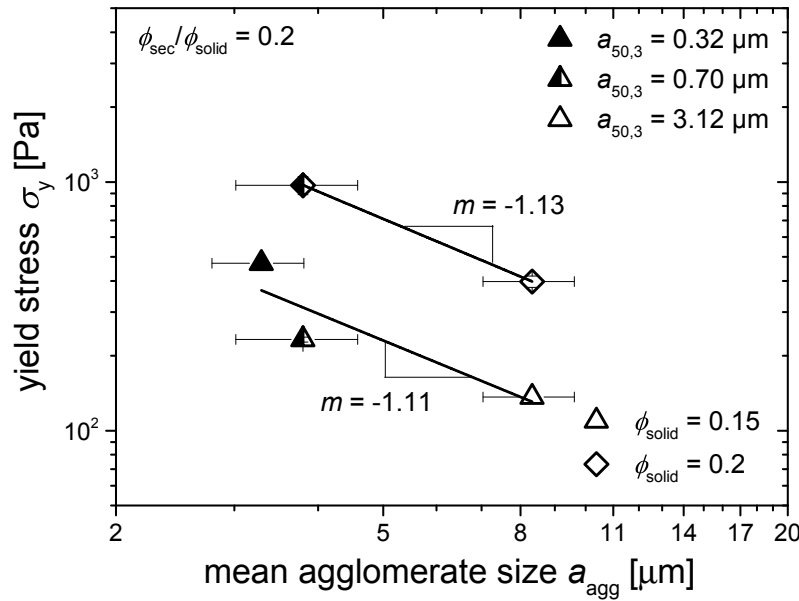
**Figure 6.31:** Yield stress master curve for  $\text{Al}_2\text{O}_3$ -based capillary suspensions. Different symbol shapes denote each solid volume fraction and symbol fillings and color denote each particle size. The dashed line designates the position of the yield stress maximum at  $\phi_{\text{sec}}/\phi_{\text{solid}} = 0.12$ . Figure reproduced with permission from SOR [46].

to funicular state and finally to spherical agglomeration, depend on the relative amount of the secondary fluid droplets, characterized by droplet size and number, to the amount of particles. This ratio is captured by the relative volume fractions with the addition of the average number of bridges per particle. Increasing, e.g., the particle volume fraction while keeping the secondary fluid volume fraction unchanged would either, at fixed droplet volumes, lead to a reduced number density of pendular bridges per particle contacts or, retaining the bridge number density, to a reduced volume of the bridges, and thus a different network structure or mechanical strength. Indeed, a mixed contribution of both effects is likely to appear. Accordingly,  $\phi_{\text{sec}}/\phi_{\text{solid}}$  has already been used as relevant property involved in structural transitions of capillary suspensions in other studies [6, 20, 28, 142]. Especially, it also has been naturally used for the whole study of chapter 6.2 presented before.

The transition from the yield stress increase to the maximum plateau value at  $\phi_{\text{sec}}/\phi_{\text{solid}} \approx 0.02\text{--}0.04$  in Fig. 6.31 agrees well with the ratio of single bridge to particle volumes  $V_{\text{bridge,crit}}/V_{\text{sphere}} = 0.021\text{--}0.025$  where the pendular-to-funicular transition was calculated for glass bead based capillary suspensions with contact angles in the range of  $\theta = 40\text{--}61^\circ$  in section 6.1.1 (see Fig. 6.4). Similarly, for wet granular materials with  $\phi_{\text{solid}} \approx 0.57$  the upper limit of the pendular regime has been found by Scheel et al. at  $\phi_{\text{sec}} \approx 0.025$ , denoting this transition to take place at  $\phi_{\text{sec}}/\phi_{\text{solid}} \approx 0.04$  [101].

The rescaling on the ordinate axis of Fig. 6.31 made by dividing the yield stress by  $\phi_{\text{solid}}^{3.7}$  and  $a_{50,3}^{-0.6}$  is more complex to interpret. Using the yield stress equation 6.1 as a guide, the dependence on  $N_{\text{bridge}}$  and  $\tilde{V}_{\text{bridge}}$  is via the normalized secondary fluid ratio  $\phi_{\text{sec}}/\phi_{\text{solid}}$  on the abscissa and  $\Gamma$  and  $\theta$  are constant for all samples. Therefore,  $\sigma_y$  can be rescaled by the only two remaining variables  $\phi_{\text{solid}}$  and  $a_{50,3}$  (assuming  $\tilde{s} = 0$ ). From eq. 6.1,  $\sigma_y$  should then be a function of  $a_{50,3}^{-1}$  instead of  $a_{50,3}^{-0.6}$  and the solid volume scaling is comprised in the unknown term  $f(\phi_{\text{solid}})$ . Recently,  $f(\phi_{\text{solid}}) = \phi_{\text{solid}}^2$  from sparse suspensions was proposed by Koos [2], but this obviously cannot hold. A dependence of  $\phi_{\text{solid}}^{3.3}$  has been found by Domenech et al. for a capillary suspension system with a much lower  $\theta$  [6], which corroborates the dependence of  $\phi_{\text{solid}}^{3.7}$  found here.

While the theoretical size dependence of  $a_{50,3}^{-1}$  already has been verified for capillary suspensions using glass beads [7], the deviation here might be explained by the presence of particle aggregates. Their presence, even after 24 h of mixing in the ball mill as applied to the  $\text{Al}_2\text{O}_3$ -based capillary suspensions, has been shown in Fig. 5.7. It may be assumed that these aggregates rather than the individual particles form a percolated aggregate network similar to what was proposed towards the end of section 2.2.4. These aggregates should then form a network backbone and the yield stress is related to this network backbone rupturing. The size of the aggregates varies based on the relative droplet volume, so the exponent cannot be easily predicted and the value of  $-0.6$  here was empirically determined. While the  $\text{Al}_2\text{O}_3$ -based capillary suspension cannot be directly imaged confocally due to a mismatched refractive index, SEM images of sintered ceramics produced from these capillary suspensions can be taken [10]. Some of the samples were sintered using gentle sintering conditions and the aggregate sizes  $a_{\text{agg}}$  estimated from SEM images of the sintered structures using the image analysis software “Visiometrics iPS”. The estimated sizes are shown in Fig. 6.32. The aggregate sizes determined using this method can only be seen as very rough estimates, as the microstructure is certainly changed by the sintering process, and they also show a very broad size distribution. Despite these short-



**Figure 6.32:** Yield stress of  $\text{Al}_2\text{O}_3$ -based capillary suspensions as function of the mean agglomerate size  $a_{\text{agg}}$  with different single particle sizes (denoted by different symbol fillings) and solid volume fractions (denoted by symbol shapes) at fixed ratio of  $\phi_{\text{sec}}/\phi_{\text{solid}} = 0.2$ .

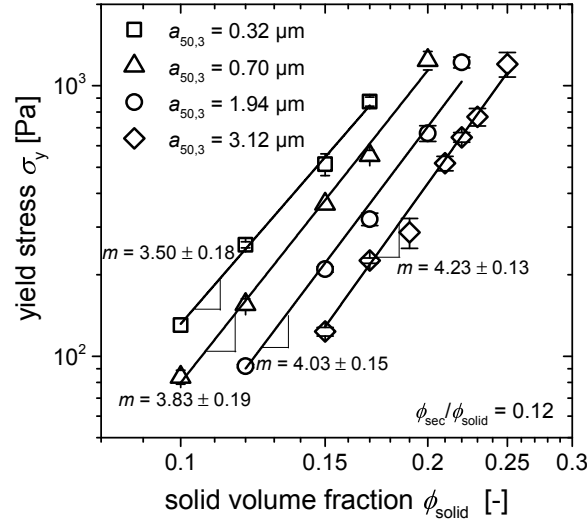
comings, Fig. 6.32 shows that the scaling exponent is probably closer to the expected value of  $-1$  if the mean particle size of single particles is replaced by the mean aggregate size. However, other explanations for the deviation from the  $a^{-1}$  scaling are also possible, e.g. a different polydispersity in particle size distributions or deviations from ideal spherical particle shape as seen in Fig. 3.6.

### 6.3.2 Fractal dimension from rheological scaling laws

#### Yield stress scaling – model from Piau et al.

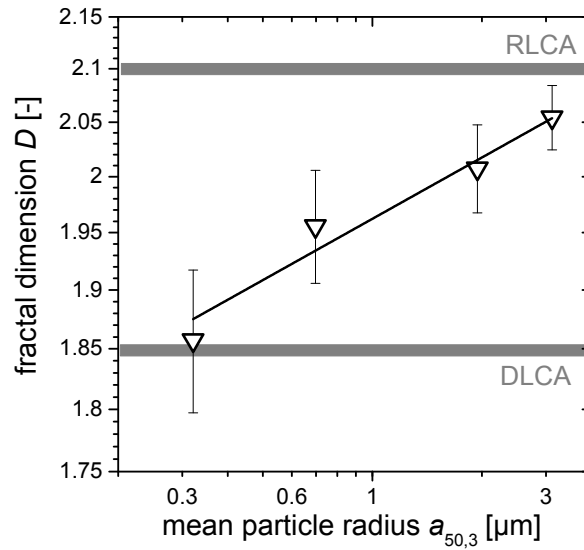
For capillary suspension based product design, the maximum achievable yield stress value is often of salient interest. As can be seen in Fig. 6.31, this maximum appears in the  $\text{Al}_2\text{O}_3$  system around a fixed sample composition ratio of  $\phi_{\text{sec}}/\phi_{\text{solid}} = 0.12$ . Fig. 6.33 shows the yield stress at this fixed ratio as a function of the solid volume fraction for all four particle sizes. While each particle size clearly shows a power law scaling, a closer look reveals that the scaling exponent of 3.7 used for the master curve is only an inaccurate averaged value. The actual exponents  $m$  increase with increasing particle sizes from  $m = 3.50 \pm 0.18$  at  $a_{50,3} = 0.32 \mu\text{m}$  to  $m = 4.23 \pm 0.13$  at  $a_{50,3} = 3.12 \mu\text{m}$ .

In Fig. 6.34, the model from Piau et al. (eq. 2.32) is applied to these scaling exponents to calculate the fractal dimensions  $D$  as function of the particle size [58]. The model predicts fractal dimensions increasing from  $D = 1.86 \pm 0.06$  at  $a_{50,3} = 0.32 \mu\text{m}$  to  $D = 2.05 \pm 0.03$  at  $a_{50,3} = 3.12 \mu\text{m}$ . These values all lie between the values of 1.85 and 2.10 reported for the DLCA and RLCA aggregation kinetic models [51]. However, one should hesitate when directly applying the DLCA and RLCA models from purely Brownian particle motion to capillary suspensions that are prepared using strong mixing (i.e. external flow fields determine particle motion) and are also influenced by gravity. In literature, hydrodynamic



**Figure 6.33:** Yield stress  $\sigma_y$  of  $\text{Al}_2\text{O}_3$ -based capillary suspensions as function of the solid volume fraction  $\phi_{\text{solid}}$  at a fixed ratio of  $\phi_{\text{sec}}/\phi_{\text{solid}} = 0.12$  for the four different mean particle radii. Figure reproduced with permission from SOR [46].

forces [107, 179] and gravity [180–182] both have been shown to lead to rearrangements of clusters with more compact geometries with higher  $D$  compared to purely diffusive aggregates, and a loss of fractality in some cases. This would imply that we should observe higher fractal dimensions  $D > 2.1$  that do not lie in the range between DLCA and RLCA values. As mentioned in the end of the theory section 2.2.4, however, the Piau model is expected to predict the dimension of a network's backbone instead of the internal dimension of the basic aggregates, which may explain the calculated fractal dimensions in Fig. 6.34 in this range. External forces mainly influence the internal structure of the aggregates



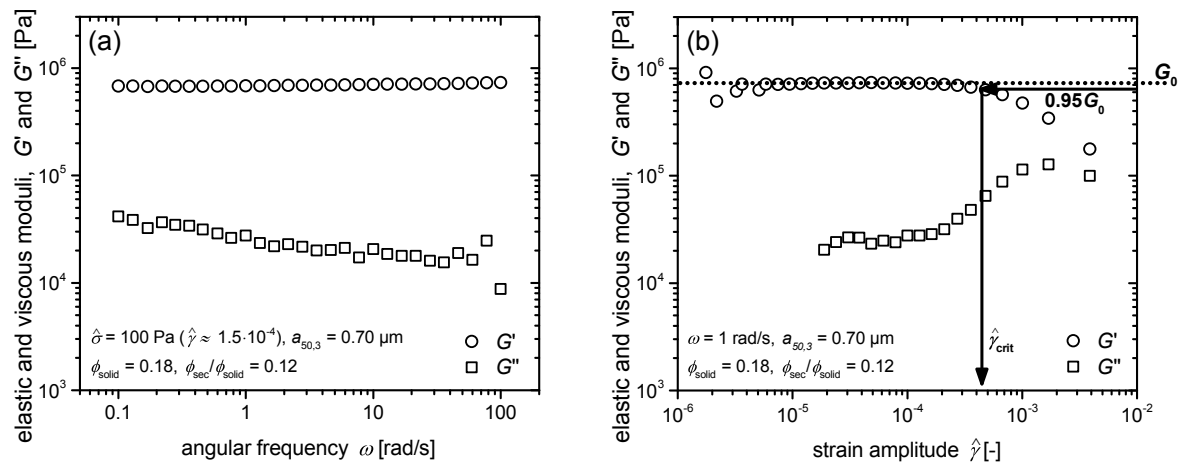
**Figure 6.34:** Fractal dimension  $D$  as function of the particle size calculated with the Piau yield stress scaling model. The gray horizontal lines denote expected fractal dimension values for DLCA and RLCA aggregation. Figure reproduced with permission from SOR [46].

and should have less influence on the percolating backbone as this only obtains its final configuration once the rapid external mixing has ceased. This backbone by itself is relatively sparse compared to the interior of the aggregate, even if there is an interconnected structure. Thus, the backbone dimensionality shown in Fig. 6.34 should be lower than the internal aggregate dimensionality, as fractal dimensions are linked to the relative number density of particles (eq. 2.29) [54, 175, 177]. An experimental representation of elevated values of  $D$  with higher solid volume fractions, i.e. a higher relative number density, has been shown for the confocal system of composition C1 in Fig. 6.29.

By considering the dependence of our observed dimensionalities on particle size in terms of aggregation, the sticking probability for approaching particles decreases with larger particle sizes. A hypothesis to explain this finding can be drawn when the attractive capillary force  $F_c$  is compared to other forces acting on the colliding particles. While  $F_c$  is a linear function of particle size  $F_c \propto a_{50,3}$  (eq. 2.45), the inertial force  $F_i$  and hydrodynamic force  $F_h$  scale as  $F_i \propto a_{50,3}^3$  and  $F_h \propto a_{50,3}^2$ , respectively [85]. Thus, with increasing particle size, the ratio of the capillary to inertial and hydrodynamic forces becomes weaker, which leads to a reduced sticking probability and thus to more compact agglomerate structures. The ratio of capillary to the other relevant forces decreases with increasing particle size independent of the mode of aggregation. Therefore, the increase in the fractal dimension for capillary suspensions with increasing particle size, seen in Fig. 6.34, is also expected even in the present case where the aggregation is not governed by diffusion. Further corroboration for this increase is given by yield stress data obtained with samples of composition C6, based on  $\text{CaCO}_3$  particles, which is shown in section 6.3.3 below.

### Oscillatory rheology – model from Wu and Morbidelli

It is also possible to determine the fractal dimension applying the model of Wu and Morbidelli (eq. 2.33 to 2.35) to data from oscillatory shear rheometry [59]. Fig. 6.35 shows an ex-



**Figure 6.35:** Elastic and viscous shear moduli  $G'$  and  $G''$  as a function of (a) angular frequency  $\omega$  at a stress (and strain) amplitude inside the linear viscoelastic region and (b) strain amplitude at a frequency  $\omega = 1$  rad/s. The elastic modulus  $G'$  is shown as open circles and the viscous modulus  $G''$  as open squares. The dotted line in (b) denotes the elastic plateau modulus  $G_0$  while the arrows illustrate the determination of the critical strain amplitude  $\hat{\gamma}_{\text{crit}}$ . Example data of an  $\text{Al}_2\text{O}_3$ -based capillary suspension with  $a_{50,3} = 0.70 \mu\text{m}$ ,  $\phi_{\text{solid}} = 0.18$  and  $\phi_{\text{sec}}/\phi_{\text{solid}} = 0.12$ . Figure reproduced with permission from SOR [46].

ample measurement of the moduli as a function of frequency as well as strain amplitude for an  $\text{Al}_2\text{O}_3$ -based capillary suspension at  $\phi_{\text{sec}}/\phi_{\text{solid}} = 0.12$ . All samples, independent of  $\phi_{\text{solid}}$  and  $a_{50,3}$ , showed a frequency independent elastic modulus  $G'$  at strain amplitudes within the linear viscoelastic region for the frequency range tested (Fig. 6.35a). Therefore, the frequency independent plateau modulus  $G_0$  can be identified directly using an amplitude sweep as shown in Fig. 6.35b, i.e. the same procedure that also has been used for obtaining the data of Fig. 6.20 from strain amplitude sweeps as in Fig. 6.19. In addition to  $G_0$ , a critical strain amplitude  $\hat{\gamma}_{\text{crit}}$  denoting the limit of linear viscoelastic response was determined following Shih et al. where  $\hat{\gamma}_{\text{crit}}$  is defined using the 95 % criterion [57]. The critical amplitude showed no dependence on frequency  $\omega$  at which the amplitude sweep was measured. The plateau modulus  $G_0$  and the amplitude  $\hat{\gamma}_{\text{crit}}$  are shown in Fig. 6.36a and Fig. 6.36b, respectively, as function of  $\phi_{\text{solid}}$  for the four different particle sizes.  $G_0$  can, with good agreement, be fitted by a power law with exponent  $m_G$  in the range of  $3.46 \pm 0.26$  to  $4.27 \pm 0.34$ , but no trend with particle size is observed. The  $\hat{\gamma}_{\text{crit}}$  data is more scattered, but still is fit using simple power law, as often done in literature [57, 59, 183]. The exponents increase with increasing particle size from  $m_\gamma = 1.11 \pm 0.20$  at  $a_{50,3} = 0.32 \mu\text{m}$  to  $m_\gamma = 4.28 \pm 1.05$  at  $a_{50,3} = 3.12 \mu\text{m}$ .

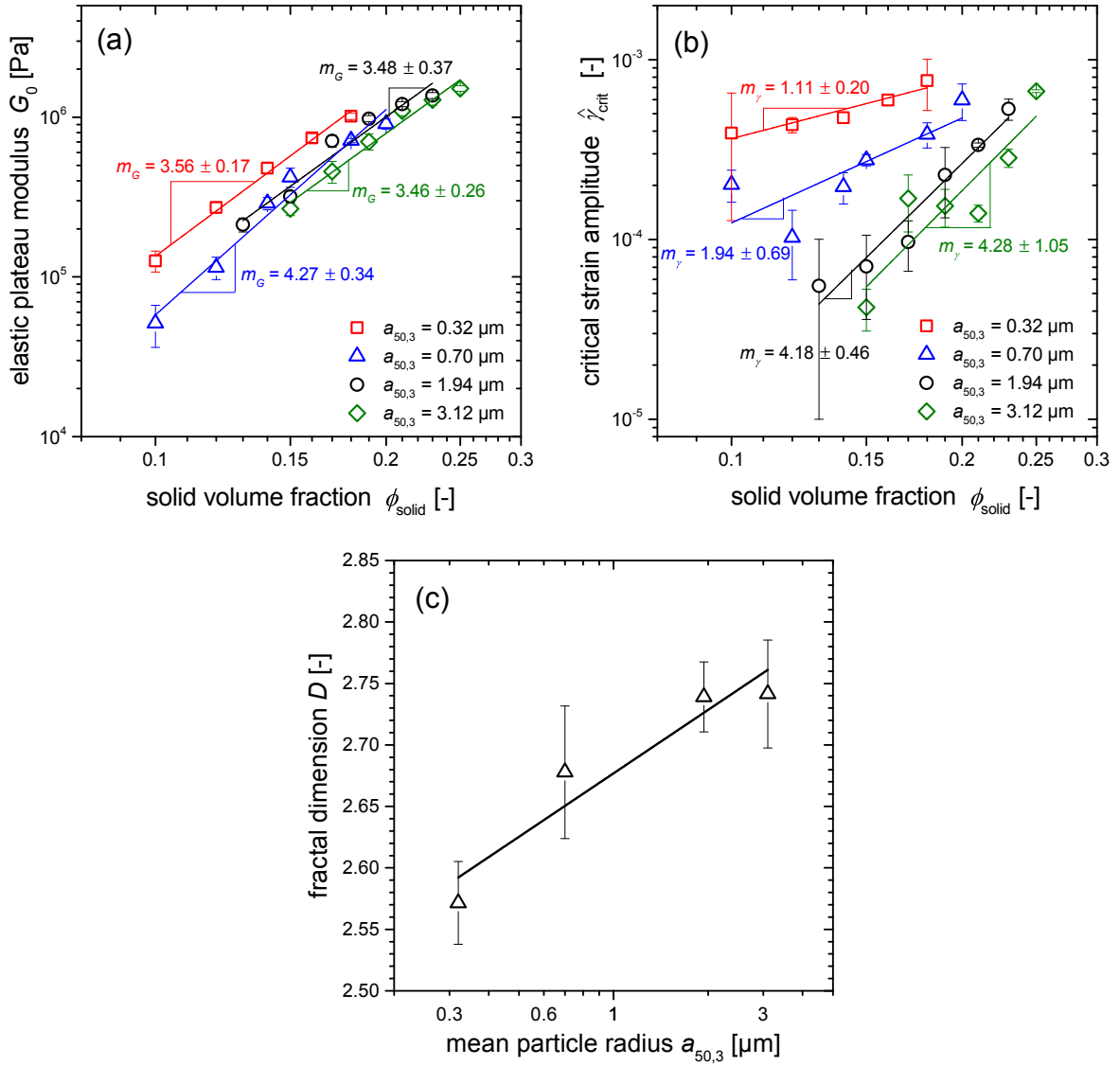
The fractal dimension  $D$  calculated from  $m_G$  and  $m_\gamma$  using the model of Wu and Morbidelli [59] (eq. 2.35) are shown in Fig. 6.36c for all four particle sizes. In contrast to the fractal dimensions calculated with the Piau model from the yield stress scalings (Fig. 6.34), these dimensions are expected to represent the internal floc structure (inside the flocs of size  $\xi$  in the model figure 2.5) and not the network backbone. The values are significantly higher than the RLCA value of  $D = 2.1$ , which due to the elevated solid volume fraction and strong external forces during sample preparation is expected. Although these dimensions differ from the ones calculated from the yield stress (Fig. 6.34), the trend of an increasing  $D$  with particle size is reproduced. Here, the dimension ranges from  $D = 2.57 \pm 0.03$  at  $a_{50,3} = 0.32 \mu\text{m}$  to  $D = 2.74 \pm 0.04$  at  $a_{50,3} = 3.12 \mu\text{m}$ .

Finally, it is worth noting some peculiarities in the scaling of  $G_0$  and  $\hat{\gamma}_{\text{crit}}$  with particle size. First, the dependence of the plateau modulus scaling exponents, seen in Fig. 6.36a, is not directly expected. While  $G_0$  is known to often be independent of particle size for a uniform gel structure [44] this is not obvious for the heterogeneous gels investigated here. The internal floc packing geometry should depend on the particle size, especially when the agglomerating tendencies of a single particle, which was discussed at the end of section 6.3.1 and is shown in Fig. 6.32, are kept in mind. Thus, since the fractal dimension is expected to increase, we might expect the  $G_0$  scaling exponents to also increase with particle size. This trend is clearly shown in the scaling exponents for the critical strain (Fig. 6.36b) and for the yield stress (Fig. 6.33). The model from Wu and Morbidelli can help to clarify this issue. The values of  $m_G$  and  $m_\gamma$ , obtained from Fig. 6.36a and 6.36b, can be used to estimate not only  $D$ , but also  $\beta_{\text{Wu}}$  by combining eq. 2.33 and eq. 2.34,

$$\beta_{\text{Wu}} = \frac{2m_G}{m_G + m_\gamma}. \quad (6.5)$$

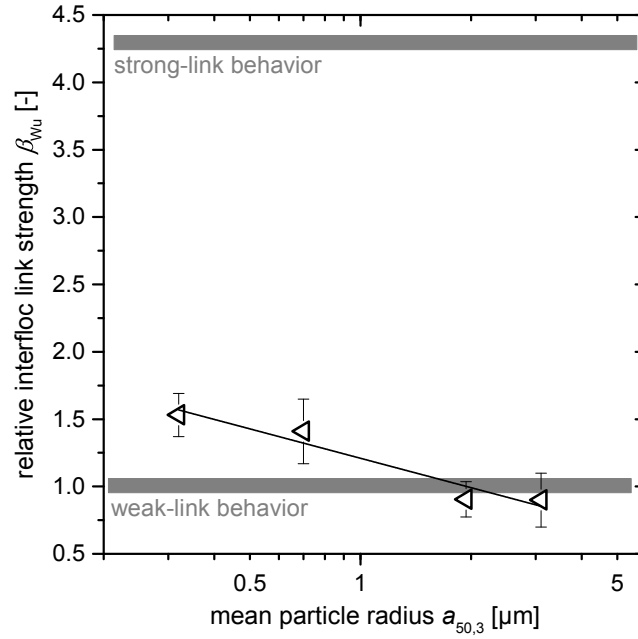
This parameter  $\beta_{\text{Wu}}$  denotes the relative strength of inter- and intra-floc connections in the network and decreases from  $\beta_{\text{Wu}} \approx 1.5 \pm 0.2$  at  $a_{50,3} = 0.32 \mu\text{m}$  to  $\beta_{\text{Wu}} \approx 0.9 \pm 0.2$  at  $a_{50,3} = 3.12 \mu\text{m}$ . Fig. 6.37 shows the  $\beta_{\text{Wu}}$  values for the  $\text{Al}_2\text{O}_3$ -based capillary suspensions for the four different particle radii  $a_{50,3}$  presented in Fig. 6.36. The limiting cases for





**Figure 6.36:** (a) Elastic plateau modulus  $G_0$  and (b) critical strain amplitude  $\hat{\gamma}_{crit}$  of  $\text{Al}_2\text{O}_3$ -based capillary suspensions as function of the solid volume fraction  $\phi_{solid}$  at a fixed ratio of  $\phi_{sec}/\phi_{solid} = 0.12$ . (c) Fractal dimensions  $D$  as function of the mean particle size calculated from the data shown in (a) and (b) using the model of Wu and Morbidelli. Figure reproduced with permission from SOR [46].

$\beta_{Wu}$  are the pure weak-link behavior (inter-floc links are much weaker than the intra-floc links), corresponding to  $\beta_{Wu} = 1$ , and strong-link behavior (inter-floc links are stronger than the intra-floc ones), where  $\beta_{Wu} \approx 4.3$ . These limits were first proposed in the original model of Shih et al. [57] with the intermediate values assigned only later by Wu and Morbidelli [59]. Therefore, the comparably low  $\beta_{Wu}$  values here show that the capillary suspension samples are primarily dominated by weak inter-floc links in all cases, but that these still become relatively weaker with increasing particle size, reaching the limit of pure weak-link behavior. The local change in packing inside of the flocs with increasing particle size (i.e. the increase in  $D$ ) does not correspond to an increase in the plateau modulus



**Figure 6.37:** Relative inter- to intra-floc link strength as captured by the  $\beta_{Wu}$  parameter of the model from Wu and Morbidelli [59]. This parameter is shown as function of the particle size  $a_{50,3}$  for  $\text{Al}_2\text{O}_3$ -based capillary suspensions. The linear fit is only a guide to the eye. The gray horizontal areas denote the limiting weak-link and strong-link behavior originally proposed by Shih et al. [57].

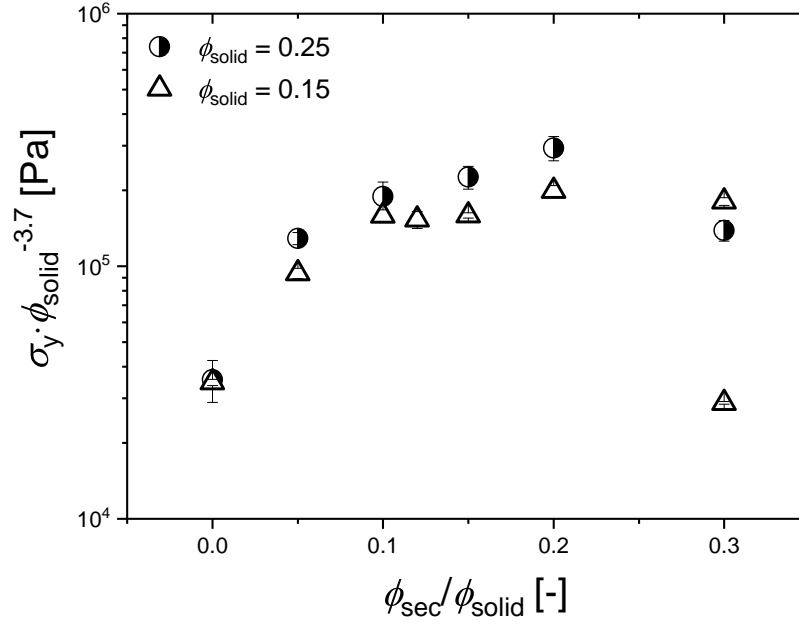
since the strengthening inside of the flocs is counteracted by a weakening of the inter-floc bonds. The critical strain amplitude, however, is more sensitive to the weakening of inter-floc bonds, which causes the observed dependence of the corresponding scaling exponents  $m_\gamma$  on particle size, as seen in Fig. 6.36b.

### 6.3.3 $\text{CaCO}_3$ -based system – further extending the master curve

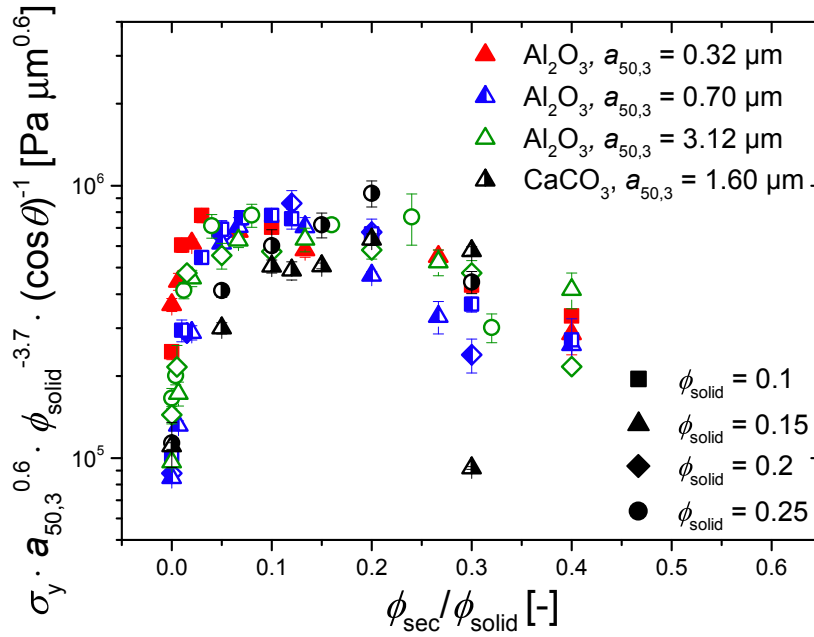
The yield stress measurements used for  $\text{Al}_2\text{O}_3$ -based capillary suspensions described in sections 6.3.1 and 6.3.2 partially were repeated with samples of composition C6, using  $\text{CaCO}_3$  particles with two different sizes  $a_{50,3}$  in the same bulk liquid (paraffin oil) and secondary fluid (sucrose solution) as taken for the  $\text{Al}_2\text{O}_3$  system.

#### Applying the $\text{Al}_2\text{O}_3$ master curve to $\text{CaCO}_3$ systems

For the  $\text{Al}_2\text{O}_3$  system, a master curve with a scaling of  $\sigma_y \propto \phi_{\text{solid}}^{3.7}$  was found as described in section 6.3.1. In a first set of data, this scaling was also tested with the  $\text{CaCO}_3$  system, using particles with  $a_{50,3} = 1.60 \mu\text{m}$  at two solid volume concentrations  $\phi_{\text{solid}} = 0.15$  and  $\phi_{\text{solid}} = 0.25$  and with different  $\phi_{\text{sec}}/\phi_{\text{solid}}$  ratios. As shown in Fig. 6.38, the scaling with an exponent of 3.7 leads, within error, to a quite reasonable agreement between the two data sets with  $\phi_{\text{solid}} = 0.15$  and  $\phi_{\text{solid}} = 0.25$ . Thus, the master curve scaling disposed for the  $\text{Al}_2\text{O}_3$  system can also be used for the  $\text{CaCO}_3$  system. This can be seen even better when both systems are plotted in one single diagram as shown in Fig. 6.39. When interpreting the  $\text{Al}_2\text{O}_3$  master curve in section 6.3.1, one basic condition was that the contact angle



**Figure 6.38:** Rescaled yield stress of  $\text{CaCO}_3$ -based capillary suspensions of composition C6 as function of  $\phi_{\text{sec}}/\phi_{\text{solid}}$ , using particles with  $a_{50,3} = 1.60 \mu\text{m}$  at two solid volume concentrations  $\phi_{\text{solid}} = 0.15$  and  $\phi_{\text{solid}} = 0.25$ . The yield stress is rescaled by the same function  $\sigma_y \propto \phi^{3.7}$  as used for the  $\text{Al}_2\text{O}_3$  shown in Fig. 6.33.



**Figure 6.39:** Yield stress master curve containing capillary suspensions based on  $\text{Al}_2\text{O}_3$  with three different particle sizes ( $a_{50,3} = 0.32 \mu\text{m}$  (red symbols),  $a_{50,3} = 0.70 \mu\text{m}$  (blue symbols) and  $a_{50,3} = 3.12 \mu\text{m}$  (green symbols)) and based on  $\text{CaCO}_3$  ( $a_{50,3} = 1.60 \mu\text{m}$ , black symbols). The different solid volume fractions are denoted by the different symbol shapes. The yield stress is rescaled by the same functions  $\sigma_y \propto \phi_{\text{solid}}^{3.7}$  and  $\sigma_y \propto a^{-0.6}$  as used for the  $\text{Al}_2\text{O}_3$  shown in the main text. Additionally, the contact angle  $\theta$  is included in the scaling, assuming  $\sigma_y \propto \cos\theta$  based on equation 6.1.

$\theta$  and interfacial tension  $\Gamma$  was unchanged in all samples tested. For the  $\text{CaCO}_3$  system, the same bulk and secondary fluids have been used so that  $\Gamma$  is still unchanged, but the three-phase contact angle is different. This angle is  $\theta = 41 \pm 4^\circ$  for the  $\text{Al}_2\text{O}_3$  system and  $\theta = 51 \pm 9^\circ$  in the  $\text{CaCO}_3$  system, as measured with a sessile drop method. This difference is incorporated into the master curve by additionally dividing the yield stress by  $\cos\theta$ , as predicted by equation 6.1 for pendular state systems. In Fig. 6.39, the rescaled yield stress values agree very well in the ordinate axis, but the position of the maximum yield stress value on the abscissa is shifted to a higher  $\phi_{\text{sec}}/\phi_{\text{solid}}$  ratio for the  $\text{CaCO}_3$  system. This shift can be partially explained by the difference in the contact angle since the transition from pendular structures (increasing yield stress) to funicular structures (maximum or plateau value of the yield stress) appears at smaller  $\phi_{\text{sec}}/\phi_{\text{solid}}$  ratios for smaller contact angles, see the discussion of Fig. 6.4. Other effects can also have an influence on the position of the maximum yield stress values, e.g. the particle shape, which cannot be easily quantified here [142].

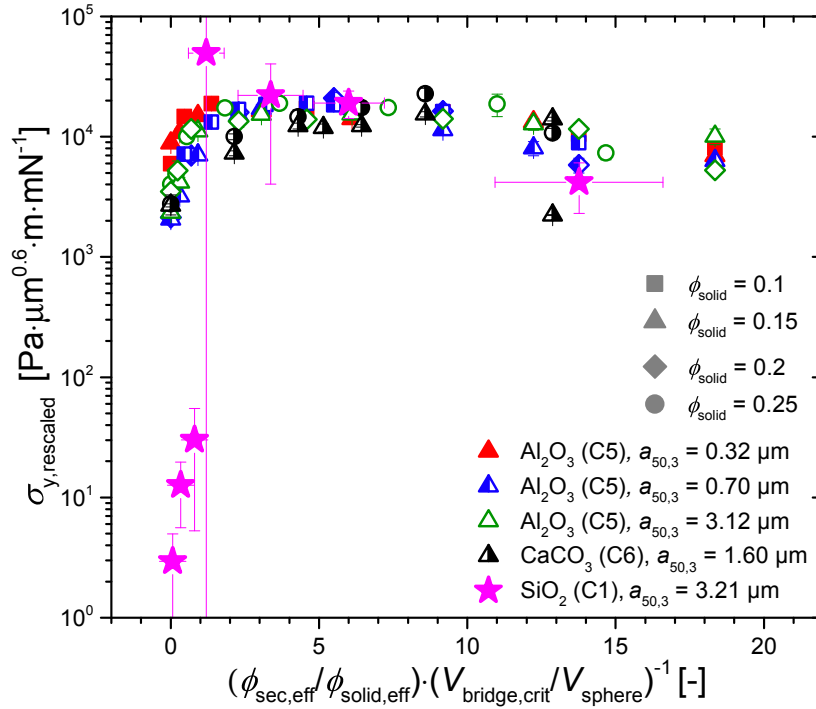
### Further extending the master curve – compositions C1, C5 and C6

Including the contact angle into the master curve by just dividing the yield stress by  $\cos\theta$ , Fig. 6.39, worked quite well. Accordingly, one might be tempted to also include the interfacial tension  $\Gamma$  to assess an even broader parameter range. Based on the yield stress equation 6.1 and the previously obtained scaling relations, a rescaled stress,  $\sigma_{y,\text{rescaled}}$  is proposed,

$$\sigma_{y,\text{rescaled}} \equiv \sigma_y \cdot \frac{a^{0.6}}{\phi_{\text{solid}}^{3.7} \cos(\theta) \Gamma} \quad [ = f_1(N_{\text{bridge}}) f_2(\tilde{V}_{\text{bridge}}, \tilde{s}) ] \quad (6.6)$$

which then only excludes functions of particle separation and the amount of secondary fluid as well as sample preparation dependent properties. Another improvement for the master curve by appropriately modifying the abscissa to account for the pendular-funicular transition, obtained in section 6.1.1, should be possible. The position of the pendular-funicular transition (i.e. the onset of the yield stress plateau) should coincide when the secondary to solid volume fraction is divided by the critical volume ratio of this transition,  $V_{\text{bridge,crit}}/V_{\text{sphere}}$ , for samples with different contact angles. The critical volume ratio can be determined from the volume calculations of Megias-Alguacil et al. [94] with the Flemmer coalescence criterion [102] of  $\beta = 30^\circ$  in Fig. 6.4.

Figure 6.40 shows the result of such an extended yield stress scaling that includes the interfacial tension on the ordinate and the critical coalescence volume on the abscissa axis. The extended scaling allows the yield stress data of composition C1 to be included into the diagram. The four data sets from composition C5 and C6 included in this extended scaling shown in Fig. 6.40 are recalculated from the previous master curve of Fig. 6.39. The new data points using composition C1 (magenta stars) are based on the critical stress data at the end of the LVE region,  $\hat{\sigma}_{\text{crit}}$ , of the system containing porous particles with  $87^\circ$  that were presented in Fig. 6.20a. The effective instead of the set secondary to solid volume fraction ratio was used to rescale on the abscissa for the composition C1 data points. The critical coalescence volume ratio was estimated as  $V_{\text{bridge,crit}}/V_{\text{sphere}} = 0.03$  using the extrapolation from data shown in Fig. 6.4. The detected mean effective solid volume fractions of the respective samples were used to rescale the ordinate axis. The



**Figure 6.40:** Extended yield stress master curve containing capillary suspensions made from:  $\text{Al}_2\text{O}_3$  with three different particle sizes ( $a_{50,3} = 0.32 \mu\text{m}$  (red symbols),  $a_{50,3} = 0.70 \mu\text{m}$  (blue symbols) and  $a_{50,3} = 3.12 \mu\text{m}$  (green symbols));  $\text{CaCO}_3$  ( $a_{50,3} = 1.60 \mu\text{m}$ , black symbols); and porous  $\text{SiO}_2$  ( $a_{50,3} = 3.21 \mu\text{m}$ , magenta symbols). The different solid volume fractions are denoted by the different symbol shapes. For the porous  $\text{SiO}_2$ , the solid volume fraction was detected from individual confocal images in section 6.2.1. The yield stress is rescaled as was given by equation 6.6. For the porous  $\text{SiO}_2$ , the critical stress at the end of the LVE region (Fig. 6.20) was used in lieu of the yield stress values.

scaling of  $a^{-0.6}$ , included in eq. 6.6, was also applied to system C1, although it has been assigned to the presence of clusters that obscure the scaling of the primary particles. While for the better dispersed system C1 the original scaling of eq. 6.1, i.e.  $a^{-1}$ , might be equally appropriate [7], the difference between both particle size scalings here should only be of minor importance.

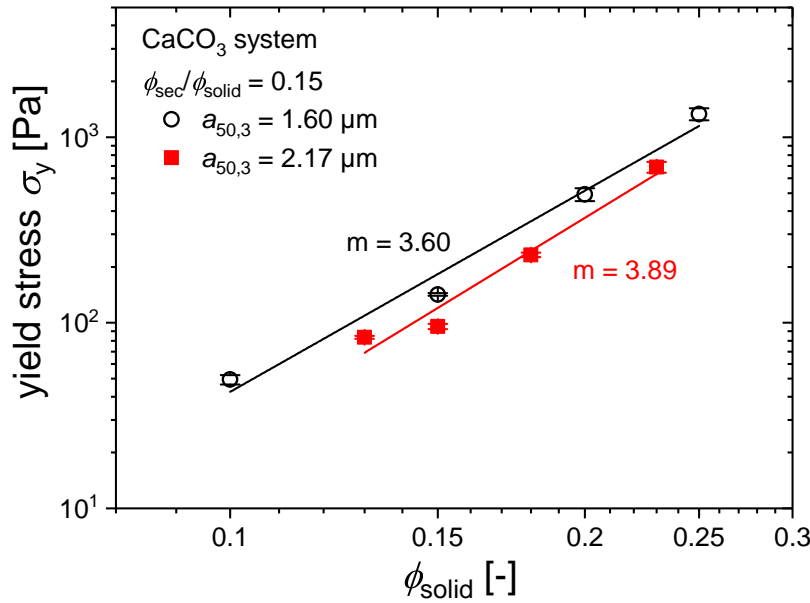
Overall, composition C1 is physically very different from compositions C5 and C6. For example, the particles are from a different material and they are porous, the bulk and secondary fluids are different, and the C1 samples without secondary fluid do not show a yield stress while the C5 and C6 samples do. Finally, the yield stress was measured using oscillatory rather than steady shear, which should further impede a direct comparison. In other words, there are many differences between the systems and many uncertainties in the rescaling factors themselves, so that a priori the attempt to produce such a general master curve was expected to fail. This makes the result of Fig. 6.40 even more remarkable. The very different C1 sample fits very well into the master curve in the funicular state plateau region and even in the ensuing stress decrease from agglomeration when compared to the other two sample systems. This is an excellent indication of sufficient correctness for many of the hypotheses, scalings and transition peculiarities of capillary suspensions found in all parts of chapter 6 as well as the applicability of the determined

relations to a broad range of different capillary suspension sample systems.

There is, however, one obvious property, namely the behavior of samples toward zero secondary fluid that is not captured by this master curve. The samples that already exhibit a yield stress without any addition of secondary fluid (composition C5 and C6) have a much higher rescaled stress than does composition C1, which does not show a yield stress before secondary fluid addition. The first three data points of composition C1, nevertheless, signal an increase in the yield stress caused by an incremental creation and then strengthening of the pendular state microstructure. These first three data points represent stronger structures than for a C1 sample without added fluid, but they are still weaker relatively to the maximum plateau value than the samples without added secondary fluid of systems C5 and C6. (Absolute yield stress values obviously cannot be compared with each others in such a rescaled curve.) To also improve the master curve for secondary fluid volumes towards zero, a further rescaling of the yield stress by a characteristic stress difference between the respective sample without added secondary fluid and the sample at maximum strength would be necessary.

### Trends of the Piau yield stress model for the $\text{CaCO}_3$ system

To further compare the  $\text{Al}_2\text{O}_3$  and  $\text{CaCO}_3$  capillary suspensions, the yield stress of  $\text{CaCO}_3$  samples with both particle sizes  $a_{50,3} = 1.60 \mu\text{m}$  and  $a_{50,3} = 2.17 \mu\text{m}$  were evaluated at a constant ratio of  $\phi_{\text{sec}}/\phi_{\text{solid}} = 0.15$ . This ratio is close to the abscissa of the maximum yield stress as extracted from Fig. 6.38. Fig. 6.41 shows these yield stress data as a function of



**Figure 6.41:** Yield stress as function of the solid volume fraction for  $\text{CaCO}_3$  based capillary suspensions with particle sizes  $a_{50,3} = 1.60 \mu\text{m}$  and  $a_{50,3} = 2.17 \mu\text{m}$  at a constant ratio of  $\phi_{\text{sec}}/\phi_{\text{solid}} = 0.15$ . Power law scalings have been fitted to the data points.

$\phi_{\text{solid}}$ . For both particle sizes, the data points are fitted by power law scalings with exponents of 3.60 for the particles with  $a_{50,3} = 1.60 \mu\text{m}$  and 3.89 for  $a_{50,3} = 2.17 \mu\text{m}$ . Accordingly, the scaling model from Piau et al. [58] can be applied here to calculate fractal dimensions of  $D = 1.89$  and  $D = 1.97$  for  $a_{50,3} = 1.60 \mu\text{m}$  and  $a_{50,3} = 2.17 \mu\text{m}$ , respectively.



These values both lie in the same range as found for the  $\text{Al}_2\text{O}_3$  system using the same scaling model. Even more importantly, the calculated fractal dimension values for the  $\text{CaCO}_3$  samples also increase with increasing particle size. Therefore, this trend is reproducible with different methods of fractal dimension determination, as well as for different capillary suspension sample systems.

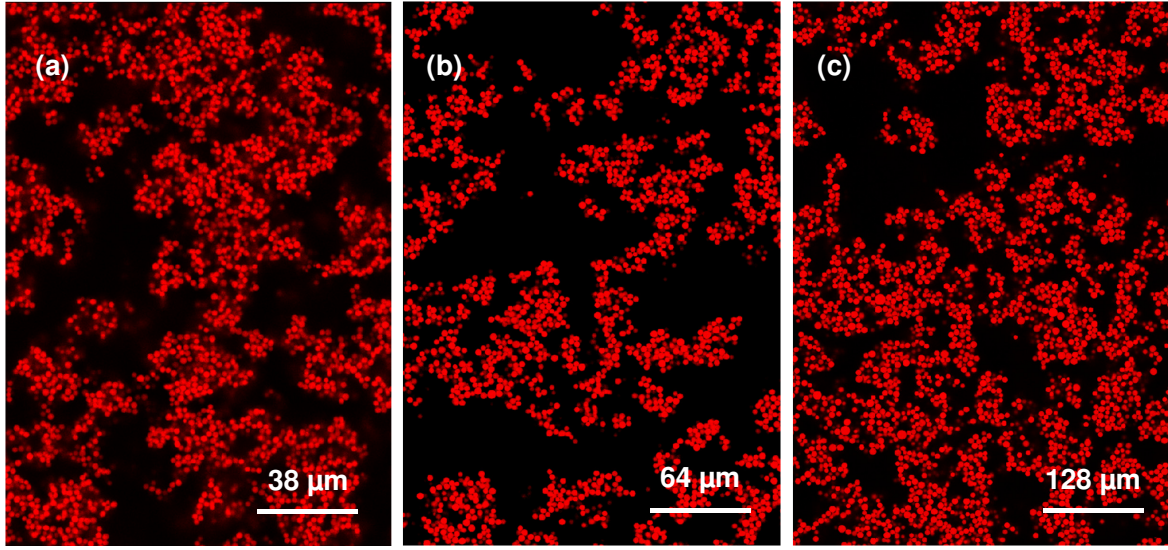
#### 6.3.4 Reassessing the fractal dimensions using confocal microscopy

When understanding the structure of capillary suspensions as a system of flocs, which are interconnected to form a backbone, we can now re-assess the fractal dimension determination from confocal image analysis methods on samples of composition C1 that has been first tried at the end of section 6.2.3. Due to its small volumes the silica sample system could not be used for such extensive rheological measurements as done for the  $\text{Al}_2\text{O}_3$  and  $\text{CaCO}_3$  systems of composition C5 and C6 presented in sections 6.3.1 to 6.3.3. However, the surprisingly well-fitting master curve of Fig. 6.40 is a good foundation for justifying a further comparison of compositions C5 and C6 with composition C1. The rheologically determined apparent fractal dimensions of compositions C5 and C6 therefore may be compared to confocally determined apparent fractal dimensions of composition C1, while each of the methods is not applicable to the other composition, respectively.

#### Imaging the proposed inter- and intra-floc structure

First, capillary suspensions using composition C1 are imaged to see the differences between the proposed compact clusters and sparse backbone. To avoid any problems with badly defined solid and secondary fluid volume fractions, nonporous batches of dyed Kromasil silica were used here, see the three batches “9.3 nonporous” in table 3.4. Three different sizes of silica were used to check if the obtained trends of increasing fractal dimensions with increasing particle size still can be reproduced with this different sample system and method. The usage of nonporous silica allows to set the C1 samples to the same volume ratio,  $\phi_{\text{sec,set}}/\phi_{\text{solid,set}} = 0.12$  as has been used with composition C5 for obtaining the rheological scalings in section 6.3.2. With nonporous particles in composition C1, the position of the yield stress maximum may then be expected to be at roughly the same position as for composition C5, see Fig. 6.40, and thus all presented apparent fractal dimension data of all different compositions is expected to represent funicular structures.

Large-sized 2D confocal images of capillary suspensions of composition C1 based on the nonporous silica particles with the three different sizes  $a_{50,3}$  and (effective) volume fraction  $\phi_{\text{solid}} = 0.26 \pm 0.06$  are shown in Fig. 6.42. The three confocal images have been rescaled in size to allow better visual comparability so that the scale bar in each of the three images denotes a length of  $40 \cdot a_{50,3}$ . These rather large-scaled images, in comparison to the images of smaller extent presented in Fig. 6.14 and 6.15, do not show particle gels that are homogeneous at these scales, but a structure consisting of relatively compact agglomerates with large (sparsely populated) voids. Thus, the model structure shown in Fig. 2.5 is indeed an appropriate representation of the structure of capillary suspensions. This means that making a distinction in the strength and structure between the backbone and agglomerate obtained using the rheological models in section 6.3.2 is appropriate.

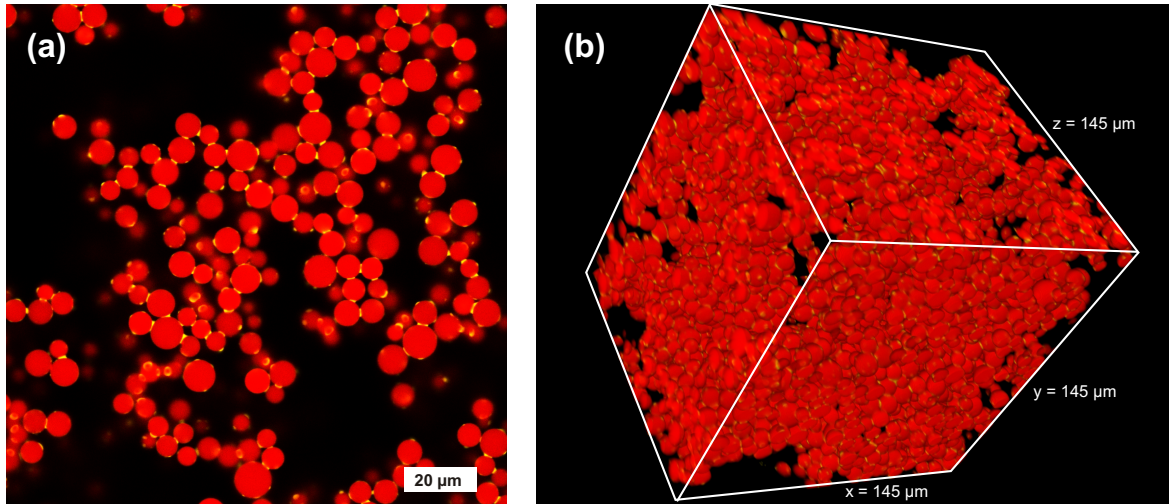


**Figure 6.42:** Confocal 2D images of capillary suspensions based on silica particles of composition C1 ( $\theta = 66 \pm 12^\circ$ ,  $\phi_{\text{solid}} = 0.26 \pm 0.06$ ) with three different mean particle radii (a)  $a_{50,3} = 0.95 \mu\text{m}$ , (b)  $a = 1.59_{50,3} \mu\text{m}$  and (c)  $a = 3.21_{50,3} \mu\text{m}$ , all at  $\phi_{\text{sec}}/\phi_{\text{solid}} = 0.12$ . The silica particles are shown in red. The undyed bulk liquid and secondary liquid are not shown. Image sizes and scale bars have been adjusted so that the scale bar equals  $40 \cdot a_{50,3}$  in each image. Figure reproduced with permission from SOR [46].

### Apparent fractal dimensions from confocal image analysis

The total number of particles  $N$  around a reference particle in the 3D images can be determined as function of the normalized radial distance  $R/a$  to the reference particle by detecting the particle positions. This function  $N(R/a)$  then is used to calculate the fractal dimension using eq. 2.29 as is described in section 4.4. For enabling correct image analysis, 3D confocal images, however, have to be taken at a much higher resolution than shown in Fig. 6.42. Therefore, images with sizes of approximately  $45 \cdot a_{50,3}$  in all three spatial dimensions were taken, and the secondary fluid was also imaged. In other words, for the particles with  $a_{50,3} = 3.21 \mu\text{m}$  this is the same image size as already has been used for the analyses of chapter 6.2. Fig. 6.43 shows an example confocal image of this size, where Fig. 6.43a shows a  $x$ - $y$ -slice of the image. Fig. 6.43b shows a 3D visualization of the whole image that was constructed using the 3D viewer plug-in in ImageJ. These images contain an average of  $3300 \pm 850$  particles and the corresponding local particle volume fraction  $\phi_{\text{solid}} = 0.26 \pm 0.06$  was directly evaluated from the 3D images. While these images are appropriate for image analysis, the easy-to-see structural inhomogeneity of Fig. 6.42 often is not recognized on these smaller scales any more. However, one has to keep in mind that the inhomogeneity of course nevertheless is present in the samples.

Since the clusters have a limited size,  $N(R/a)$  is not calculated for distances longer than the correlation length  $\xi/a$ , which is estimated from eq. 2.30 using the dimension  $D$  from the rheological results at first. The lowest floc dimension calculated from the oscillatory data using the Wu and Morbidelli model in section 6.3.2 was  $D \approx 2.6$ . The measured  $\phi_{\text{solid}} = 0.26 \pm 0.06$  leads to  $\xi/a \approx 29 \pm 12$  (with the error in  $\xi/a$  being estimated based on the error only in  $\phi_{\text{solid}}$  and not in  $D$ ). This value roughly matches the cluster sizes visible in Fig. 6.42. When using the same  $\phi_{\text{solid}}$ , but  $D = 2.0$ , which is in the range predicted from



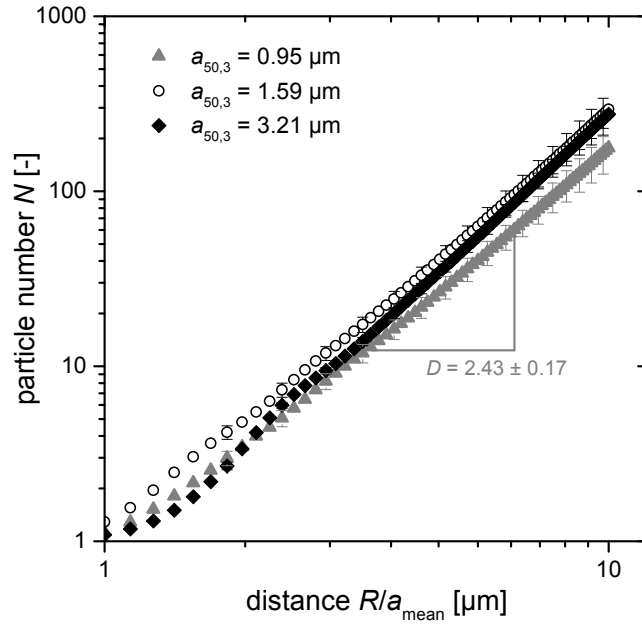
**Figure 6.43:** Confocal image of a silica based capillary suspension with mean particle size  $a_{50,3} = 3.21 \mu\text{m}$ . (a) Two-dimensional  $x$ - $y$ -slice. (b) Three-dimensional reconstruction of the confocal image.

the Piau model, the calculated correlation length drastically shrinks to  $\xi/a \approx 3.85 \pm 0.65$ . However, using  $\phi_{\text{solid}} = 0.26$  is incorrect in the latter calculation. While the relevant solid volume fraction for the backbone cannot be directly defined, the number of contributing particles is clearly lower than the total particle number in the sample. Thus, the relevant  $\xi/a$  value for the backbone should be larger in reality.

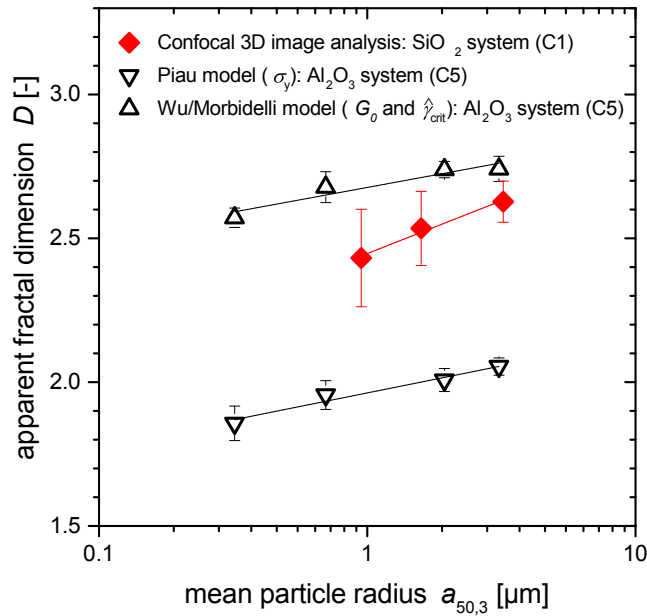
Due to the large variation in volume fraction and particle number caused by the network inhomogeneity, as seen in Fig. 6.42, the  $N(R/a)$  function is strongly influenced by the position inside of the sample where these relatively small 3D images are taken. Furthermore, the arbitrarily chosen reference particles ( $R = 0$ ) also cannot be expected to coincide with the center of gyration of a cluster. Therefore, eight such images were taken for each particle size and the  $N(R/a)$  function in each image was calculated using between 350 and 550 reference particles, randomly distributed in the volume not intersecting the edges, to decrease the influence of these errors. Additionally, the maximum radial distance was set to  $R/a = 10$ , considerably lower than the estimated cluster size of  $\xi/a \approx 29 \pm 12$ , in order to ensure many of these calculations were made inside of a cluster. The mean  $N(R/a)$  functions of all these calculations are shown in Fig. 6.44 for the three different particle sizes. The arithmetic instead of volumetric mean radii,  $a_{\text{mean}}$  are taken as representative  $a$  values for the calculations, see line 27 of Alg. 4.1 in section 4.4, where  $a_{\text{mean}}$  was obtained during the calculations.

The mean  $N(R/a)$  functions show a power law increase where the exponent is evaluated for  $2 < R/a_{\text{mean}} < 10$  and the fractal dimension  $D$  equals the exponent following eq. 2.29. The dimensions, calculated from the image sets for each particle size, are shown in Fig. 6.45 as red diamonds.

This method captures mixed contributions from both the internal aggregate as well as the backbone structure as not all reference particles are close to the gyration center of the clusters, and can also include a portion of the voids, thereby reducing the effective particle density. Thus the optically determined  $D$  values are larger than the calculations from the rheological scaling model of Piau, but smaller than the ones from the Wu and Morbidelli



**Figure 6.44:** Particle number function  $N(R/a_{\text{mean}})$  for silica based capillary suspensions with  $a_{50,3} = 0.95 \mu\text{m}$  (gray triangles),  $a_{50,3} = 1.59 \mu\text{m}$  (black open circles) and  $a_{50,3} = 3.21 \mu\text{m}$  (black filled diamonds), all with  $\phi_{\text{solid}} = 0.26 \pm 0.06$  and  $\phi_{\text{sec}}/\phi_{\text{solid}} = 0.12 \pm 0.03$  as determined from 3D confocal image data. Error bars are only shown at every fourth data point for the sake of clarity. The exponent of the  $N(R/a_{\text{mean}})$  function equals the fractal dimension  $D$  as exemplified in the figure for the particles with  $a_{50,3} = 0.95 \mu\text{m}$ . Figure reproduced with permission from SOR [46].



**Figure 6.45:** Apparent fractal dimensions  $D$  as function of particle size  $a_{50,3}$  determined from confocal image analysis of silica based capillary suspensions (red diamonds). For comparison, the results from the rheological scaling models presented in section 6.3.2 are reproduced in this diagram, where the backbone dimension was calculated using the model of Piau et al. and the aggregate dimension with the model of Wu and Morbidelli. Figure reproduced with permission from SOR [46].

scaling model, representing backbone and aggregate dimensions, respectively. The inhomogeneity of the particle networks leads to scattered data in the calculations of  $D$  from  $N(R/a)$  functions, as local structures will vary significantly between different 3D images and around different reference particles. This scatter is seen in the significant size of the error bars in Fig. 6.44 and 6.45. So, while this scatter is aggravating for the unsuccessful attempt of deriving any trends of the fractal dimension on secondary fluid volume fraction at the end of chapter 6.2, the scatter is inherent to the method and is physically explainable on these length scales. Therefore, it cannot easily be avoided. Nevertheless, as with the dimension determined from rheological data, the apparent fractal dimension values from microscopy image analysis increase with increasing particle size. This is true even though a different method and sample system were used here. There is an increase from  $D = 2.43 \pm 0.17$  at  $a_{50,3} = 0.95 \mu\text{m}$  to  $D = 2.63 \pm 0.07$  at  $a_{50,3} = 3.21 \mu\text{m}$ . Corresponding correlation lengths can be estimated, lying between  $11 \lesssim \xi/a \lesssim 38$ .

Some caveats should be kept in mind when directly comparing the three curves of Fig. 6.45, as there are some differences between the data obtainment from rheology and from confocal microscopy. Most obvious is the usage of two sample systems, especially the difference between perfectly spherical glass beads and more irregularly shaped  $\text{Al}_2\text{O}_3$  particles. Further, the silica samples seem to be in binary-bridged pendular rather than in a funicular configuration as can be seen in Fig. 6.43a while they before had been expected to be funicular, same as the  $\text{Al}_2\text{O}_3$  systems should be. Also, different mixing protocols had to be used to prepare the samples, which has been shown to influence the strength of capillary suspensions [5, 108], see chapter 5. Closely related to the issue of mixing protocols is the general pre-shear history of the samples, including the loading into the measuring device for the rheometer which also differs from the microscope slide. Such different pre-shear protocols may also lead to different structures. Indeed, the rheological response itself might be altered by this pre-shear, as was shown for shear rate dependent thixotropic time scales in silica suspensions by Dullaert and Mewis [184]. Thus, comparing the absolute values of the fractal dimensions determined through confocal microscopy with the values deduced from rheology may not be valid. However, the approximate values and trends in the fractal dimensions from the different approaches are still expected to be valid.

It is clear from both the rheological data and the microscopic data that these capillary suspensions exhibit a heterogeneous gel structure with fractal dimensions that increase with increasing particle size. This increase can be regarded as transitional behavior between characteristic particle size regimes of colloidal two-phase suspensions and wet granular matter. Attractive colloidal suspensions, with typical particle sizes  $\ll 1 \mu\text{m}$ , can arrange their percolating network structure solely by Brownian motion. This leads to the lower limit  $D \approx 1.85$  of accessible fractal dimension values in 3D, given by DLCA kinetics. Wet granular materials, with typical particle sizes  $\gg 20 - 50 \mu\text{m}$ , on the other hand are fully governed by gravitation leading to non-fractal compact structures. This denotes the upper limit of  $D = 3$ .







## 7 Conclusion

### 7.1 Summary

Capillary suspensions with six different compositions have been investigated to elucidate their microstructure and to relate the insights gained from the microstructural analysis to the rheological properties. While the latter are of salient interest for industrial processing as well as customer acceptance of products based on capillary suspensions, a simultaneous understanding of the microstructure is of utmost importance as it enables directed design of the product properties. The six capillary suspension compositions evaluated here range from the glass-bead-based model systems designed for fundamental research to the application-relevant aluminum-oxide-based systems. Different physical properties of the suspensions, like contact angle and particle size, as well as processing parameters, such as mixing conditions during sample preparation, were varied in this thesis and the influence of these properties and parameters on the structure and rheology, especially on the sample yield stress, were evaluated.

#### **Influence of energy input and mixing during sample preparation**

The structure and strength of ternary liquid-liquid-solid systems strongly depends on the sample preparation method and the energy input during mixing of the sample. This is especially true for capillary suspensions, where the secondary liquid only represents a small volume fraction of the sample. A variety of pendular state and capillary state model systems, based on glass beads,  $\alpha$ -Al<sub>2</sub>O<sub>3</sub>, or hydrophobic CaCO<sub>3</sub> (compositions C2–C5 in Table 3.1), were examined while varying the preparation conditions in chapter 5. Enhanced droplet breakup of the secondary fluid leads to stronger particle networks with more homogeneous network structures (section 5.1). Using a dissolver stirrer in capillary state systems, this can be achieved by increasing the energy input by either applying faster mixing speeds or longer mixing times using turbulent mixing. In the pendular state, increased mixing speed also leads to better droplet breakup using the same stirrer, but spherical agglomeration is found to be favored at longer times. This agglomeration decreases the yield stress and leads to severe sample inhomogeneities.

The additional use of a ball mill after turbulent stirring (section 5.2.1) is beneficial for the sample strength as it leads to a minimization of spherical agglomerates. This is attributed to the different breakup mechanism dominated by impact forces of the balls instead of viscous shear forces. However, agglomeration is not fully avoided in the ball mill as the tendency towards agglomeration is inherent to pendular state systems. Emulsification of the secondary fluid before particle addition (section 5.2.2) can also lead to stronger particle networks if coalescence of the secondary fluid droplets before the parti-

cles are well distributed is sufficiently slow. This may be achieved by using small amounts of added surfactant. Using ultrasound for sample preparation (section 5.2.3) enables superlative droplet breakup, leading to very small droplets of secondary fluid that is beneficial compared to the other preparation methods. On the other hand, sonication is limited to samples of very small size due to the very local energy input of the ultrasonic horn, which leads to inhomogeneous sample structures when volumes are too large.

Experiments with a model system containing viscosity-matched fluids covering the entire saturation range from  $S = 0$  to 1 were also performed (section 5.3). These experiments showed that the capillary state competes with the formation of large Pickering emulsion droplets and is often more difficult to achieve than the pendular state.

### **In-situ 3D imaging and influence of contact angle and particle porosity**

Model capillary suspension systems based on chemically treated Kromasil glass beads covering a wide range of three-phase contact angles between  $38^\circ$  and  $147^\circ$  were examined by confocal microscopy and rheology in chapter 6. The confocal measurements made it possible, for the first time, to image entire unmodified sample volumes of capillary suspensions and gain insight into the 3D network structure. A large range of systems could be imaged due to the broad variability of contact angles and porosity, made possible by chemical surface modifications of the particles. Using the confocal microscope, structural differences that occur with the variation in the contact angle were elucidated in section 6.1. For nonporous particles, the confocal images prove the existence of the capillary state for three-phase contact angles slightly higher than  $90^\circ$ . Clusters with small numbers of particles, held together by the secondary phase, are visible. Images of such structures clearly show a sample-spanning, clustered network, as was previously proposed using simulations [30]. The pendular state was imaged for samples with contact angles lower than  $90^\circ$ . The images demonstrate the transition between systems consisting of only binary bridges to systems with bridges binding more than two particles, a state that is analogous to the funicular state in wet granular media. The transition from a binary bridge pendular state to a funicular-like pendular state occurs either from an increase in the secondary fluid volume or due to geometrical reasons when the contact angle is decreased at constant secondary fluid volume. A contact-angle-dependent criterion to calculate the amount of secondary fluid needed for this transition is derived in section 6.1.1 based on the capillary bridge volume equations of Megias-Alguacil et al. [94]. Calculations of individual secondary fluid droplet sphericities additionally offer a possibility to quantify the structural differences observed in the confocal images.

For highly porous particles, the transition from pendular to capillary state changes from  $90^\circ$  to a much higher apparent contact angle near  $130^\circ$  (section 6.1.2). The reason for this shift is not known, but is likely due to a change in wetting behavior caused by surface roughness, or possibly chemical inhomogeneity, inducing contact angle hysteresis. For samples with porous particles and contact angles below  $90^\circ$ , a strong network caused by the capillary force is not formed as the added secondary fluid is rapidly absorbed into the particle pores. There is a slight increase in the shear modulus at angles less than  $90^\circ$  due to small microdroplets that remain on the surface in the asperities, but this increase is dwarfed by the change at  $\theta > 90^\circ$ . Confocal images show numerous pendular bridges at apparent contact angles above  $90^\circ$  and the elastic modulus dramatically increases by three decades compared to the suspension without secondary fluid. Samples that are identified

as being in the capillary state by the confocal measurements also showed an increase in shear modulus when compared to the pure suspensions, but have a modulus one decade lower than the maximal pendular state samples.

### **Elucidation of the influence of different amounts of secondary fluid**

Having shown that 3D confocal imaging is a powerful tool for structure elucidation in the capillary suspension model system based on Kromasil silica particles, further experiments were conducted where the amount of secondary fluid was varied (section 6.2). Two systems containing porous particles, having apparent contact angles of  $87^\circ$  and  $115^\circ$ , were used for these experiments. The rheology of these systems is governed by effective – rather than the set – volume fractions of secondary fluid and solid particles, as the effective volume fractions incorporate the imbibition of some secondary and bulk fluid into the particle pores. The effective volume fractions were directly calculated from the 3D confocal images.

Representative stress values, i.e. the plateau modulus and apparent yield stress, show the same dependence on the effective secondary fluid volume fraction as was shown by Dittmann et al. [10]. With addition of secondary fluid, the stress first increases due to the formation of bridges in the pendular state transmitting capillary forces, then goes through a maximum denoting funicular state structures and finally decreases again when the amount of secondary fluid is large enough that the samples agglomerate even under optimized sample preparation conditions. The confocal images are used to directly visualize each of these structures. Overall, the  $115^\circ$  samples show lower stress values than for  $87^\circ$ , which is related to the difference in energy needed to detach particles from the fluid-fluid interface. This detachment energy is maximal at  $90^\circ$  and decreases for higher (or lower) contact angles.

Using a primarily self-programmed algorithm to analyze the 3D confocal images, the particle positions and individual sizes were detected at varying effective amounts of secondary fluid for the two apparent contact angles of  $87^\circ$  and  $115^\circ$ . With the ascertained particle positions and sizes, different structural parameters can be calculated. Of the many possible parameters, the pair correlation functions  $g(R/a)$ , the coordination numbers  $z$  (as histogram and as mean value) and an apparent fractal dimension  $D$  were chosen in this thesis. The pair correlation functions show a well defined peak at a particle center distance of  $2R$ , i.e. at particle surface contact. The height of this first peak was evaluated as function of the effective secondary fluid content. Settled samples without added secondary fluid and samples with large amounts of secondary fluid, leading to spherical agglomeration, were discussed separately due to their divergent structure. For the capillary suspensions, with intermediate secondary fluid volumes, the height of the first peak of the pair correlation function increases with the amount of secondary fluid for both contact angles. This is related to the increased attraction between particles, which is also reflected in the rheological data.

The same correlation is found for the coordination numbers. The mean coordination number  $z$  also increases with the amount of added secondary fluid, again only taking the samples with a capillary suspension structure into account. Differences in the slopes of the coordination number rise with increasing secondary fluid volume between samples with  $87^\circ$  and  $115^\circ$  are found and these differences closely resemble similar variations in slope found using the rheological data. The clear link between the number of bridges

per particle and the strength as measured using the elastic modulus and the yield stress is shown. However, the coordination numbers are higher for the 115° samples than for the 87° samples. Therefore, the rheological behavior cannot be explained by differences in the coordination number alone. There are no equations to predict the coordination number of capillary suspensions as function of the secondary or solid volume fractions. Empirical equations that predict the relationship between the coordination number and solid content for wet granular materials (i.e. solid volume fractions  $> 0.52$ ) are fitted to the capillary suspension data (solid volume fractions  $\approx 0.15 - 0.25$ ) but, as expected, do not provide satisfactory results.

The determination of fractal dimensions as function of the secondary fluid volume fraction also provides unsatisfactory results. While the fractal dimension can be calculated, the data is accompanied by very large error bars that impede the deduction of any significant trends. However, an increase in the fractal dimension with increasing solid volume fraction is found. A more detailed analysis of fractal dimensions was explicitly performed in section 6.3, summarized below.

### **Rheological and optical approaches to determine the fractal dimension**

Due to the difficulties in determining meaningful values for the fractal dimension solely from confocal imaging, several other approaches to determine the fractal dimension of capillary suspensions have been performed in section 6.3. Rheological scaling laws that are based on different structural and aggregation models were used and either the yield stress data or the elastic plateau modulus and the critical strain amplitude analyzed. A broad variation of particle sizes and solid volume fractions was executed in this set of experiments. Due to the small sample volumes available for the Kromasil silica based model systems, the rheological studies were performed with  $\text{CaCO}_3$  and  $\text{Al}_2\text{O}_3$  based capillary suspensions (composition C5 and C6 in Table 3.1). The latter particles are used for the production of porous ceramics [10, 142]. The approaches based on rheological scaling laws led to different fractal dimensions, which capture structural features on different length scales of the particle networks (section 6.3.2). Fractal dimensions in the range from 1.86 to 2.05 were determined using the yield stress scaling model from Piau et al. [58] assuming a uniform fractal structure, while distinctly higher  $D$  values in the range from 2.57 to 2.74 were obtained for the same capillary suspensions from the rheological scaling model of Wu and Morbidelli [59] applied to critical strain amplitudes and elastic moduli obtained from oscillatory rheology. This marked difference is explained by an inhomogeneous microstructure, where relatively dense agglomerates are linked to form a relatively sparse backbone transmitting the forces. Taking into account the origin of the two applied rheological scaling models, the fractal dimension calculated with the Piau model is then expected to be a measure of the network backbone structure while the model from Wu and Morbidelli describes the fractal dimension inside the aggregates. Due to the locally higher particle volume fraction and more compact structure, the floc dimension is much higher than the backbone dimension.

This hypothesis for interconnected dense flocs is confirmed by confocal images where particle-laden areas are separated by voids with few particles (section 6.3.4). The confocal experiments are again conducted using the Kromasil glass bead based capillary suspensions. Fractal dimensions were directly determined from particle positions obtained from 3D confocal images of these index-matched capillary suspension model systems, as was

shown in the previous section of this thesis. This approach is generally more straightforward since the structural parameter  $D$  is directly obtained from the particle positions rather than using the indirect method of deducing  $D$  from rheological data. While such a direct approach avoids complications and questions regarding approximations and assumptions made to relate structure to rheology, it does not necessarily capture the inhomogeneity of the network structure. Based on structural considerations of the inhomogeneous sample structure, it indeed should be more appropriate to make distinctions between two different dimensionalities – one for the backbone at long length scales and one for the internal aggregate dimensionality at short length scales. This latter value should be the parameter most closely related to the classical definition of fractal dimensions (eq. 2.28). Due to the presence of such different length scales, the direct approach to determine a single dimension  $D$  using particle number functions from microscopy can only provide an apparent fractal dimension containing mixed contributions of both length scales. Due to the short length  $R/a < 10$  used to evaluate the data, the contribution of the internal cluster structure is expected to dominate, however. Accordingly, the optically determined  $D$  values lie between the results obtained from the different rheological approaches, but closer to the intra-floc values than to the backbone dimensions. The appearance of these two different length scales also explains why the error bars in using the optical approach to calculate the fractal dimension in the previous part of the thesis were too large to deduce any clear trends of  $D$  as function of the secondary fluid content.

Regardless of the method used, the fractal dimension of capillary suspensions increases with increasing particle size. This trend is confirmed by all of the sample systems at the various length scales provided by each method. Therefore, capillary suspensions with larger particles exhibit more compact particle arrangements. This can be explained by the weakening of the capillary force in comparison to both the inertial and hydrodynamic forces with increasing particle size. This should reduce the sticking probability of an incoming particle attaching to an aggregate during the preparation of the capillary suspension samples.

### **Yield stress master curve**

A master curve for the yield stress as function of the secondary fluid content could be constructed as an incidental result from the fractal studies (sections 6.3.1 and 6.3.3). This master curve is a very helpful tool to predict the sample yield stress for any given combination of secondary fluid volume, particle size and solid volume fraction for a given composition, as was demonstrated for the  $\text{Al}_2\text{O}_3$ -based system. However, the master curve can also be further generalized, including the interfacial tension as well as the contact angle and the transition from pendular to funicular structures, which itself depends on the contact angle. The generalized master curve then enables the yield stress of samples with different composition to also be predicted, as was shown by including systems based on  $\text{CaCO}_3$  and Kromasil glass beads in addition to the  $\text{Al}_2\text{O}_3$ . The resulting generalized master curve, Fig. 6.40, is primarily deduced from equation 6.1 and, therefore, validates the use of this equation for capillary suspensions in the pendular state while also partially providing results for the heretofore unknown functions included in this equation.

## 7.2 Outlook

While this thesis provides many new insights into the microstructure of capillary suspension in combination with their rheology, there remain many possibilities for further research.

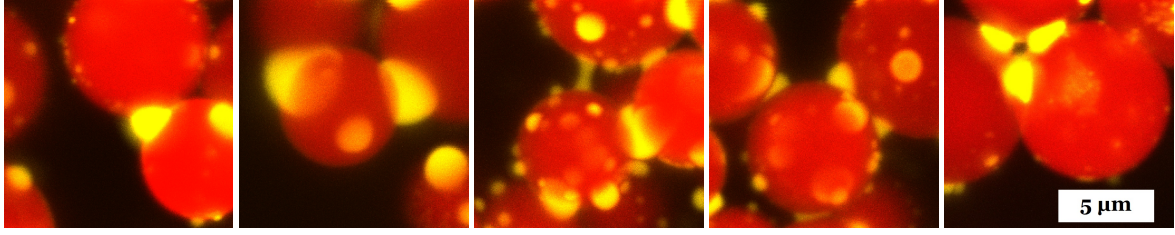
When examining the influence of the droplet breakup and mixing conditions during sample preparation, the capillary state appeared to be much more difficult to prepare than the pendular state. This is true even if the bulk and secondary fluids are viscosity-matched. It can be hypothesized that the formation of a capillary state is enabled or enhanced if the capillary force is not the only attractive interaction present between particles. Further studies may be conducted to prove this hypothesis and to examine the nature of additional attractive or repulsive forces. The contribution of, e.g., electrostatic, friction or van der Waals forces remains unclear at present and a thorough investigation of such forces in the concurrent presence of a capillary attraction is certainly worth further examination.

In general, the structural evaluation in this thesis has mainly focused on the pendular state (in combination with funicular and aggregated structures), while the capillary state was treated in a more cursory manner. Therefore, an analysis of e.g. coordination numbers and fractal dimensions of capillary state systems should also be conducted and the results compared to the results obtained for the pendular state here. In particular, a yield stress master curve for the capillary state, similar as obtained for the pendular state in this thesis, might be searched, or even a general master curve that is valid for both systems.

A peculiarity of the capillary state found in the confocal images (e.g. Fig. 6.5c) were the droplets of secondary fluid that are only connected to a single particle. The loss in the efficacious secondary phase volume due to these singly-connected droplets leads to a reduction in the binding force and the corresponding macroscopic rheological parameters. However, these droplets could also play an important role in aging processes of capillary state systems. If these droplets can migrate to other positions and gradually bind additional particles, an increase in the network strength with time should be observed. Such an increase in the shear modulus over hours and even days was documented in a previous study using a capillary state system containing calcium carbonate particles [127]. Confocal observation of such samples over a long term could help to elucidate the underlying processes and confirm the role of these droplets in this aging. However, this change must be balanced against any possible absorption of secondary fluid into the particles, which weakens the network.

In general, secondary fluid droplets and bridge shapes should be evaluated further in the capillary as well as in the pendular state. This is especially true for binary bridges observed for the  $115^\circ$  sample in section 6.2, as such bridges are unexpected at such a high contact angle. Fig. 7.1 shows confocal close-up views of single secondary fluid entities in this sample between the particles. It is obvious that some odd bridge shapes, like non-axisymmetric bridges or bridges with nonzero particle separation appear here. While such bridges are mathematically difficult to model and the capillary force transmitted by them is not easy to predict, such bridges nevertheless will contribute to the sample structure and strength, and thereby will also directly influence the rheological properties. The existence of such bridges is not yet captured by the approaches used in this thesis, especially for the bridges with nonzero particle distance. Such an attractive interaction without





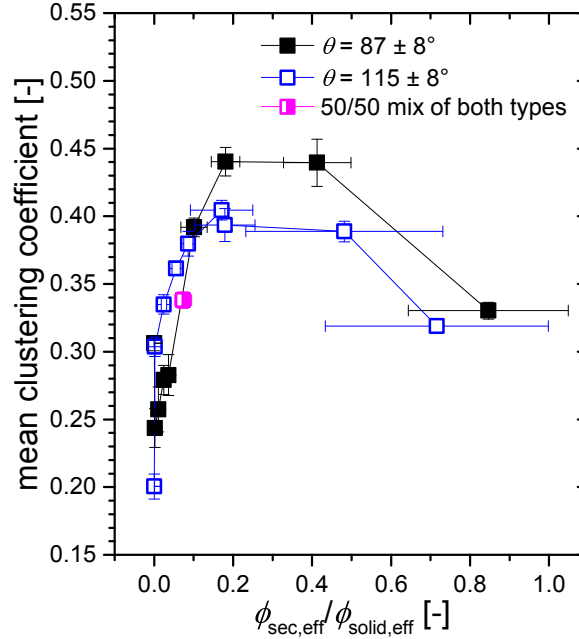
**Figure 7.1:** Confocal images of secondary fluid entities interconnecting the particles in capillary suspensions of composition C1 with an apparent contact angle of  $\theta = 115 \pm 8^\circ$  and  $\phi_{\text{sec,set}}/\phi_{\text{solid,set}} = 0.16$ . The images disclose bridges with non-axisymmetric shape or bridges interconnecting particles with a nonzero surface distance. The 3D reconstruction was made with ImageJ. The size of each 3D image is  $\approx 12 \times 12 \times 7 \mu\text{m}^3$ .

particle contact neither appears in the coordination number histograms computed from the 3D images nor is it correctly represented by the simplification of the yield stress equation 6.1 when a particle separation  $\tilde{s} = 0$  is assumed. One option to tackle these nontrivial problems could be force measurements of individual capillary bridges with an AFM setup using a range of contact angles, bridge shapes and particle separations.

Additionally, the inhomogeneous sample structure and refinement of the optically determined fractal dimension should be investigated further. In particular, the results of section 6.3 showed that the fractal dimension might not be the most meaningful property for a comprehensive and complete insight into the microstructure of capillary suspensions due to their heterogeneous nature. Other characterization approaches provide additional options that can be combined with the fractal dimension to get structural information for such heterogeneous, high volume fraction particle gels. One promising method is that of Wyss et al., who evaluated a similar heterogeneous particle gel by describing it as a two-component system with one phase being represented by large voids of bulk liquid and the second component by the compact particle gel (aggregates and backbone) [70]. This second component is described by a solid volume fraction  $\phi_2$  that is larger than  $\phi_{\text{solid}}$  and is calculated as  $\phi_2 = \phi_{\text{solid}}/(1-\phi_1)$  with  $\phi_1$  representing the estimated volume fraction of the bulk liquid void pores. While it is difficult to precisely determine  $\phi_1$ , it nevertheless should be possible to estimate this value from confocal images in future studies and then determine local aggregate structures represented by  $\phi_2$ . A second promising method to characterize heterogeneous suspensions, first introduced by Varadan and Solomon, is based on the determination of Voronoi volumes around the individual particles. The broadness and the skewness of the distribution of Voronoi volumes can be used to identify the degree of structural heterogeneity [185]. With regard to rheological methods, measurements of space-resolved stress distributions could be used to help one understand the details of the yielding mechanism. Yielding of heterogeneous gels occurs by highly localized breaking of a very small fraction of the network connections [186]. This might also elucidate the relative importance and strength of inter- and intra-floc bonds, which emerged from the discussion of Fig. 6.36. Finally, another promising approach could be to perform simulations of the network structure and compare these simulations to data determined optically. This approach would allow structural information to be determined as the sample conditions are independently varied.

The microstructure of capillary suspensions was mainly characterized in this thesis by

pair correlation functions, fractal dimensions and coordination numbers. Amongst the many other possibilities to characterize the structure for future studies is the promising approach shown in Fig. 7.2. Here, the clustering coefficient of all samples studied in chapter 6.2 is shown as function of the effective secondary fluid volume fraction. This method shows clear trends, which will not be discussed further, but this result demonstrates the potential in using the clustering coefficient in subsequent investigations.



**Figure 7.2:** Mean clustering coefficient as function of the ratio  $\phi_{\text{sec,eff}}/\phi_{\text{solid,eff}}$  of C1 samples. The data was obtained by computational evaluation of confocal 3D images of samples containing porous particles showing  $\theta = 87 \pm 8^\circ$  or  $115 \pm 8^\circ$  as well as a 50/50 mixture of both of these particle types (i.e. all samples summarized in Table 6.1). The calculation of this data was provided by Sebastian Bindgen, KU Leuven.

Finally, it is important to note that this thesis has clarified the structure of capillary suspensions at rest, but did not examine the structure under shear, which is of equal importance, especially during the processing of capillary suspensions. While the quiescent structure and the structure under shear should be closely linked, it is, nevertheless, impossible to easily predict the structure under shear from the rest structure alone. Therefore, an extremely important issue for further research is the elucidation of the structure under shear, e.g., by using a shear cell on the confocal microscope or optical systems on a rotational rheometer. The structure under shear then also has to be coupled to rheological sample properties. In contrast to the rest structure, which was related to the yield stress and viscoelastic properties in the linear viscoelastic region, the structure under shear should instead be coupled to the shear-rate dependent viscosity and the oscillatory rheological properties beyond the linear viscoelastic region.

Thus, while this thesis includes ample, interesting information about the structure and rheology of capillary suspensions, there remain many additional options for promising future research studies.

## 8 Bibliography

- [1] E. Koos and N. Willenbacher, “Capillary forces in suspension rheology,” *Science*, vol. 331, no. 6019, pp. 897–900, 2011.
- [2] E. Koos, “Capillary suspensions: Particle networks formed through the capillary force,” *Current Opinion in Colloid & Interface Science*, vol. 19, no. 6, pp. 575–684, 2014.
- [3] S. van Kao, L. E. Nielsen, and C. T. Hill, “Rheology of concentrated suspensions of spheres. II. Suspensions agglomerated by an immiscible second liquid,” *Journal of Colloid and Interface Science*, vol. 53, no. 3, pp. 367–373, 1975.
- [4] J. McCulfor, P. Himes, and M. R. Anklam, “The effects of capillary forces on the flow properties of glass particle suspensions in mineral oil,” *AIChE Journal*, vol. 57, no. 9, pp. 2334–2340, 2011.
- [5] T. Domenech and S. Velankar, “Capillary-driven percolating networks in ternary blends of immiscible polymers and silica particles,” *Rheologica Acta*, vol. 53, no. 8, pp. 593–605, 2014.
- [6] T. Domenech and S. S. Velankar, “On the rheology of pendular gels and morphological developments in paste-like ternary systems based on capillary attraction,” *Soft Matter*, vol. 11, pp. 1500–1516, 2015.
- [7] E. Koos, J. Johannsmeier, L. Schwebler, and N. Willenbacher, “Tuning suspension rheology using capillary forces,” *Soft Matter*, vol. 8, no. 24, pp. 6620–6628, 2012.
- [8] E. Koos and N. Willenbacher, “Particle configurations and gelation in capillary suspensions,” *Soft Matter*, vol. 8, no. 14, pp. 3988–3994, 2012.
- [9] J. Dittmann, E. Koos, and N. Willenbacher, “Ceramic capillary suspensions: Novel processing route for macroporous ceramic materials,” *Journal of the American Ceramic Society*, vol. 96, no. 2, pp. 391–397, 2013.
- [10] J. Dittmann and N. Willenbacher, “Micro structural investigations and mechanical properties of macro porous ceramic materials from capillary suspensions,” *Journal of the American Ceramic Society*, vol. 97, no. 12, pp. 3787–3792, 2014.
- [11] J. Maurath, J. Dittmann, N. Schultz, and N. Willenbacher, “Fabrication of highly porous glass filters using capillary suspension processing,” *Separation and Purification Technology*, vol. 149, pp. 470–478, 2015.

- [12] J. Dittmann, J. Maurath, B. Bitsch, and N. Willenbacher, “Highly porous materials with unique mechanical properties from smart capillary suspensions,” *Advanced Materials*, vol. 28, no. 8, pp. 1689–1696, 2016.
- [13] K. Hauf, K. Riazi, N. Willenbacher, and E. Koos, “Radical polymerization of capillary bridges between micron-sized particles in liquid bulk phase as a low-temperature route to produce porous solid materials,” *Colloid and Polymer Science*, vol. 295, no. 10, pp. 1773–1785, 2017.
- [14] S. Heidlebaugh, T. Domenech, S. Iasella, and S. S. Velankar, “Aggregation and separation in ternary particle/oil/water systems with fully-wettable particles,” *Langmuir*, vol. 30, no. 1, pp. 63–74, 2014.
- [15] W. Dapeng, X. Wang, Y. Yuan, W. Li, H. Tian, and S. Zhao, “Increasing the apparent shear viscosity of polymer composites by uptake of a small amount of water,” *RSC Advances*, vol. 4, pp. 24686–24691, 2014.
- [16] B. Bitsch, J. Dittmann, M. Schmitt, P. Scharfer, W. Schabel, and N. Willenbacher, “A novel slurry concept for the fabrication of lithium-ion battery electrodes with beneficial properties,” *Journal of Power Sources*, vol. 265, pp. 81–90, 2014.
- [17] M. Schneider, E. Koos, and N. Willenbacher, “Highly conductive, printable pastes from capillary suspensions,” *Scientific Reports*, vol. 6, p. 31367, 2016.
- [18] B. Bitsch, T. Gallasch, M. Schroeder, M. Börner, M. Winter, and N. Willenbacher, “Capillary suspensions as beneficial formulation concept for high energy density Li-ion battery electrodes,” *Journal of Power Sources*, vol. 328, pp. 114–123, 2016.
- [19] M. Schneider, J. Maurath, S. B. Fischer, M. Weiß, N. Willenbacher, and E. Koos, “Suppressing crack formation in particulate systems by utilizing capillary forces,” *ACS Applied Materials and Interfaces*, vol. 9, no. 12, pp. 11095–11105, 2017.
- [20] H. Sun, X. Zhang, and M. M. Yuen, “Enhanced conductivity induced by attractive capillary force in ternary conductive adhesive,” *Composites Science and Technology*, vol. 137, pp. 109–117, 2016.
- [21] L. Jampolski, A. Sanger, T. Jakobs, G. Guthausen, T. Kolb, and N. Willenbacher, “Improving the processability of coke water slurries for entrained flow gasification,” *Fuel*, vol. 185, pp. 102–111, 2016.
- [22] S. Hoffmann, E. Koos, and N. Willenbacher, “Using capillary bridges to tune stability and flow behavior of food suspensions,” *Food Hydrocolloids*, vol. 40, pp. 44–52, 2014.
- [23] J. Maurath and N. Willenbacher, “3D printing of open-porous cellular ceramics with high specific strength,” *Journal of the European Ceramic Society*, vol. 37, no. 15, pp. 4833–4842, 2017.
- [24] S. Roh, D. P. Parekh, B. Bharti, S. D. Stoyanov, and O. D. Velev, “3D printing by multiphase silicone/water capillary inks,” *Advanced Materials*, vol. 29, no. 30, p. 1701554, 2017.

- [25] G. Zylyftari, J. W. Lee, and J. F. Morris, "Salt effects on thermodynamic and rheological properties of hydrate forming emulsions," *Chemical Engineering Science*, vol. 95, pp. 148–160, 2013.
- [26] E. B. Webb, C. A. Koh, and M. W. Liberatore, "High pressure rheology of hydrate slurries formed from water-in-mineral oil emulsions," *Industrial & Engineering Chemistry Research*, vol. 53, no. 17, pp. 6998–7007, 2014.
- [27] S. Velankar, "A non-equilibrium state diagram for liquid/fluid/particle mixtures," *Soft Matter*, vol. 11, pp. 8393–8403, 2015.
- [28] J. Yang and S. S. Velankar, "Preparation and yielding behavior of pendular network suspensions," *Journal of Rheology*, vol. 61, no. 2, pp. 217–228, 2017.
- [29] J. Yang, D. Roell, M. Echavarria, and S. S. Velankar, "A microstructure-composition map of a ternary liquid/liquid/particle system with partially-wetting particles," *Soft Matter*, vol. 13, pp. 8579–8589, 2017.
- [30] A. Fortini, "Clustering and gelation of hard spheres induced by the Pickering effect," *Physical Review E*, vol. 85, no. 4, p. 040401, 2012.
- [31] M. H. Chestnut, "Confocal microscopy of colloids," *Current Opinion in Colloid & Interface Science*, vol. 2, no. 2, pp. 158–161, 1997.
- [32] V. Prasad, D. Semwogerere, and E. R. Weeks, "Confocal microscopy of colloids," *Journal of Physics: Condensed Matter*, vol. 19, no. 11, p. 113102, 2007.
- [33] C. Gögelein, M. Brinkmann, M. Schröter, and S. Herminghaus, "Controlling the formation of capillary bridges in binary liquid mixtures," *Langmuir*, vol. 26, no. 22, pp. 17184–17189, 2010.
- [34] M. N. Lee, H. K. Chan, and A. Mohraz, "Characteristics of Pickering emulsion gels formed by droplet bridging," *Langmuir*, vol. 28, no. 6, pp. 3085–3091, 2011.
- [35] M. E. Leunissen, A. van Blaaderen, A. D. Hollingsworth, M. T. Sullivan, and P. M. Chaikin, "Electrostatics at the oil–water interface, stability, and order in emulsions and colloids," *Proceedings of the National Academy of Sciences*, vol. 104, no. 8, pp. 2585–2590, 2007.
- [36] J. Wenzl, "Wet and dry model granulates under mechanical load: A confocal microscopy study," *PhD thesis, Johannes-Gutenberg-Universität Mainz*, 2014.
- [37] H.-J. Butt, "Controlling the flow of suspensions," *Science*, vol. 331, no. 6019, pp. 868–869, 2011.
- [38] J. Mewis and N. Wagner, *Colloidal Suspension Rheology*. Cambridge: Cambridge University Press, 2012.
- [39] H. A. Barnes, "The yield stress—a review or 'παντα ρει'—everything flows?," *Journal of Non-Newtonian Fluid Mechanics*, vol. 81, no. 1, pp. 133–178, 1999.

- [40] P. C. Møller, J. Mewis, and D. Bonn, “Yield stress and thixotropy: on the difficulty of measuring yield stresses in practice,” *Soft Matter*, vol. 2, no. 4, pp. 274–283, 2006.
- [41] D. Bonn, M. M. Denn, L. Berthier, T. Divoux, and S. Manneville, “Yield stress materials in soft condensed matter,” *Reviews of Modern Physics*, vol. 89, no. 3, p. 035005, 2017.
- [42] Q. Nguyen and D. Boger, “Measuring the flow properties of yield stress fluids,” *Annual Review of Fluid Mechanics*, vol. 24, no. 1, pp. 47–88, 1992.
- [43] F. L. Leite, C. C. Bueno, A. L. Da Róz, E. C. Ziemath, and O. N. Oliveira, “Theoretical models for surface forces and adhesion and their measurement using atomic force microscopy,” *International Journal of Molecular Sciences*, vol. 13, no. 10, pp. 12773–12856, 2012.
- [44] R. G. Larson, *The Structure and Rheology of Complex Fluids*. Oxford: Oxford University Press, 1999.
- [45] M. T. Georgiev, K. D. Danov, P. A. Kralchevsky, T. D. Gurkov, D. P. Krusteva, L. N. Arnaudov, S. D. Stoyanov, and E. G. Pelan, “Rheology of particle/water/oil three-phase dispersions: Electrostatic vs. capillary bridge forces,” *Journal of Colloid and Interface Science*, vol. 513, pp. 515–526, 2018.
- [46] F. Bossler, J. Maurath, K. Dyhr, N. Willenbacher, and E. Koos, “Fractal approaches to characterize the structure of capillary suspensions using rheology and confocal microscopy,” *Journal of Rheology*, vol. 62, no. 1, pp. 183–196, 2018.
- [47] R. Jullien, “Aggregation phenomena and fractal aggregates,” *Contemporary Physics*, vol. 28, no. 5, pp. 477–493, 1987.
- [48] T. Witten Jr and L. M. Sander, “Diffusion-limited aggregation, a kinetic critical phenomenon,” *Physical Review Letters*, vol. 47, no. 19, pp. 1400–1403, 1981.
- [49] R. De Rooij, A. Potanin, D. Van den Ende, and J. Mellema, “Steady shear viscosity of weakly aggregating polystyrene latex dispersions,” *The Journal of Chemical Physics*, vol. 99, no. 11, pp. 9213–9223, 1993.
- [50] M. Kolb and R. Jullien, “Chemically limited versus diffusion limited aggregation,” *Journal de Physique Lettres*, vol. 45, no. 20, pp. 977–981, 1984.
- [51] M. Lin, H. Lindsay, D. Weitz, R. Ball, R. Klein, and P. Meakin, “Universality in colloid aggregation,” *Nature*, vol. 339, pp. 360–362, 1989.
- [52] A. D. Dinsmore, E. R. Weeks, V. Prasad, A. C. Levitt, and D. A. Weitz, “Three-dimensional confocal microscopy of colloids,” *Applied Optics*, vol. 40, no. 24, pp. 4152–4159, 2001.
- [53] C. Mobuchon, P. J. Carreau, and M.-C. Heuzey, “Structural analysis of non-aqueous layered silicate suspensions subjected to shear flow,” *Journal of Rheology*, vol. 53, no. 5, pp. 1025–1048, 2009.



- [54] M. Mellema, J. Van Opheusden, and T. Van Vliet, "Relating colloidal particle interactions to gel structure using Brownian dynamics simulations and the Fuchs stability ratio," *The Journal of Chemical Physics*, vol. 111, no. 13, pp. 6129–6135, 1999.
- [55] L. G. Bremer, T. van Vliet, and P. Walstra, "Theoretical and experimental study of the fractal nature of the structure of casein gels," *Journal of the Chemical Society, Faraday Transactions 1: Physical Chemistry in Condensed Phases*, vol. 85, no. 10, pp. 3359–3372, 1989.
- [56] R. Jullien and R. Botet, *Aggregation and Fractal Aggregates*. Singapore: World Scientific, 1987.
- [57] W.-H. Shih, W. Y. Shih, S.-I. Kim, J. Liu, and I. A. Aksay, "Scaling behavior of the elastic properties of colloidal gels," *Physical Review A*, vol. 42, no. 8, pp. 4772–4779, 1990.
- [58] J. Piau, M. Dorget, and J. Palierne, "Shear elasticity and yield stress of silica-silicone physical gels: Fractal approach," *Journal of Rheology*, vol. 43, no. 2, pp. 305–314, 1999.
- [59] H. Wu and M. Morbidelli, "A model relating structure of colloidal gels to their elastic properties," *Langmuir*, vol. 17, no. 4, pp. 1030–1036, 2001.
- [60] Y. Xi, J. Chen, Y. Xu, F. Chu, and C. Liu, "Yield stress of fractal aggregates," *Fractals*, vol. 23, no. 3, p. 1550028, 2015.
- [61] N. Uriev and I. Y. Ladyzhinsky, "Fractal models in rheology of colloidal gels," *Colloids and Surfaces A: Physicochemical and Engineering Aspects*, vol. 108, no. 1, pp. 1–11, 1996.
- [62] A. R. Studart, E. Amstad, and L. J. Gauckler, "Yielding of weakly attractive nanoparticle networks," *Soft Matter*, vol. 7, no. 14, pp. 6408–6412, 2011.
- [63] W. Y. Shih, W. Shih, and I. A. Aksay, "Elastic and yield behavior of strongly flocculated colloids," *Journal of the American Ceramic Society*, vol. 82, no. 3, pp. 616–624, 1999.
- [64] R. Wessel and R. Ball, "Fractal aggregates and gels in shear flow," *Physical Review A*, vol. 46, no. 6, pp. R3008–R3011, 1992.
- [65] P.-G. De Gennes, *Scaling Concepts in Polymer Physics*. Ithaca: Cornell University Press, 1979.
- [66] F. Saint-Michel, F. Pignon, and A. Magnin, "Fractal behavior and scaling law of hydrophobic silica in polyol," *Journal of Colloid and Interface Science*, vol. 267, no. 2, pp. 314–319, 2003.
- [67] A. Loiseau and J.-F. Tassin, "Model nanocomposites based on laponite and poly (ethylene oxide): preparation and rheology," *Macromolecules*, vol. 39, no. 26, pp. 9185–9191, 2006.

- [68] M. Gareche, A. Allal, N. Zeraibi, F. Roby, N. Azril, and L. Saoudi, "Relationship between the fractal structure with the shear complex modulus of montmorillonite suspensions," *Applied Clay Science*, vol. 123, pp. 11–17, 2016.
- [69] A. Zacccone, H. Wu, and E. Del Gado, "Elasticity of arrested short-ranged attractive colloids: Homogeneous and heterogeneous glasses," *Physical Review Letters*, vol. 103, no. 20, p. 208301, 2009.
- [70] H. M. Wyss, E. Tervoort, L. P. Meier, M. Müller, and L. J. Gauckler, "Relation between microstructure and mechanical behavior of concentrated silica gels," *Journal of Colloid and Interface Science*, vol. 273, no. 2, pp. 455–462, 2004.
- [71] F. Pignon, A. Magnin, J.-M. Piau, B. Cabane, P. Lindner, and O. Diat, "Yield stress thixotropic clay suspension: Investigations of structure by light, neutron, and x-ray scattering," *Physical Review E*, vol. 56, no. 3, pp. 3281–3289, 1997.
- [72] A. Marmur, "Soft contact: Measurement and interpretation of contact angles," *Soft Matter*, vol. 2, no. 1, pp. 12–17, 2006.
- [73] R. N. Wenzel, "Resistance of solid surfaces to wetting by water," *Industrial & Engineering Chemistry*, vol. 28, no. 8, pp. 988–994, 1936.
- [74] A. Marmur, "Wetting on hydrophobic rough surfaces: to be heterogeneous or not to be?," *Langmuir*, vol. 19, no. 20, pp. 8343–8348, 2003.
- [75] A. Cassie and S. Baxter, "Wettability of porous surfaces," *Transactions of the Faraday Society*, vol. 40, pp. 546–551, 1944.
- [76] A. Detrich, M. Nyári, E. Volentiru, and Z. Hórvölgyi, "Estimation of contact angle for hydrophobic silica nanoparticles in their hexagonally ordered layer," *Materials Chemistry and Physics*, vol. 140, pp. 602–609, 2013.
- [77] S. Herminghaus, M. Brinkmann, and R. Seemann, "Wetting and dewetting of complex surface geometries," *Annual Reviews of Materials Research*, vol. 38, pp. 101–121, 2008.
- [78] R. Tadmor, "Line energy and the relation between advancing, receding, and Young contact angles," *Langmuir*, vol. 20, no. 18, pp. 7659–7664, 2004.
- [79] C. Snoeyink, S. Barman, and G. F. Christopher, "Contact angle distribution of particles at fluid interfaces," *Langmuir*, vol. 31, no. 3, pp. 891–897, 2014.
- [80] J. Drelich, "The significance and magnitude of the line tension in three-phase (solid-liquid-fluid) systems," *Colloids and Surfaces A: Physicochemical and Engineering Aspects*, vol. 116, no. 1, pp. 43–54, 1996.
- [81] A. Marmur and B. Krasovitski, "Line tension on curved surfaces: Liquid drops on solid micro- and nanospheres," *Langmuir*, vol. 18, no. 23, pp. 8919–8923, 2002.
- [82] A. Marmur and E. Bittoun, "When Wenzel and Cassie are right: reconciling local and global considerations," *Langmuir*, vol. 25, no. 3, pp. 1277–1281, 2009.

- [83] L. Gao and T. J. McCarthy, "How Wenzel and Cassie were wrong," *Langmuir*, vol. 23, no. 7, pp. 3762–3765, 2007.
- [84] N. Mitarai and F. Nori, "Wet granular materials," *Advances in Physics*, vol. 55, no. 1-2, pp. 1–45, 2006.
- [85] S. Herminghaus, *Wet Granular Matter: A Truly Complex Fluid*. Series in Soft Condensed Matter, Singapore: World Scientific, 2013.
- [86] J. C. Melrose and G. C. Wallick, "Exact geometrical parameters for pendular ring fluid," *The Journal of Physical Chemistry*, vol. 71, no. 11, pp. 3676–3678, 1967.
- [87] D. Megias-Alguacil and L. J. Gauckler, "Accuracy of the toroidal approximation for the calculus of concave and convex liquid bridges between particles," *Granular Matter*, vol. 13, no. 4, pp. 487–492, 2011.
- [88] W. Pietsch and H. Rumpf, "Haftkraft, Kapillardruck, Flüssigkeitsvolumen und Grenzwinkel einer Flüssigkeitsbrücke zwischen zwei Kugeln," *Chemie Ingenieur Technik*, vol. 39, no. 15, pp. 885–893, 1967.
- [89] D. Megias-Alguacil and L. J. Gauckler, "Analysis of the capillary forces between two small solid spheres binded by a convex liquid bridge," *Powder Technology*, vol. 198, no. 2, pp. 211–218, 2010.
- [90] C. D. Willett, M. J. Adams, S. A. Johnson, and J. P. Seville, "Capillary bridges between two spherical bodies," *Langmuir*, vol. 16, no. 24, pp. 9396–9405, 2000.
- [91] S. Strauch and S. Herminghaus, "Wet granular matter: A truly complex fluid," *Soft Matter*, vol. 8, no. 32, pp. 8271–8280, 2012.
- [92] H.-J. Butt, "Capillary forces: Influence of roughness and heterogeneity," *Langmuir*, vol. 24, no. 9, pp. 4715–4721, 2008.
- [93] H.-J. Butt and M. Kappl, "Normal capillary forces," *Advances in Colloid and Interface Science*, vol. 146, no. 1, pp. 48–60, 2009.
- [94] D. Megias-Alguacil and L. J. Gauckler, "Capillary forces between two solid spheres linked by a concave liquid bridge: Regions of existence and forces mapping," *AIChE Journal*, vol. 55, no. 5, pp. 1103–1109, 2009.
- [95] J. Bernal and J. Mason, "Packing of spheres: Co-ordination of randomly packed spheres," *Nature*, vol. 188, pp. 910–911, 1960.
- [96] L. E. Silbert, D. Ertas, G. S. Grest, T. C. Halsey, and D. Levine, "Geometry of frictionless and frictional sphere packings," *Physical Review E*, vol. 65, no. 3, p. 031304, 2002.
- [97] M. Scheel, "Experimental investigations of the mechanical properties of wet granular matter," *PhD thesis, Georg-August-Universität Göttingen*, 2009.

- [98] M. M. Kohonen, D. Geromichalos, M. Scheel, C. Schier, and S. Herminghaus, "On capillary bridges in wet granular materials," *Physica A: Statistical Mechanics and its Applications*, vol. 339, no. 1, pp. 7–15, 2004.
- [99] W. Pietsch, E. Hoffman, and H. Rumpf, "Tensile strength of moist agglomerates," *Industrial & Engineering Chemistry Product Research and Development*, vol. 8, no. 1, pp. 58–62, 1969.
- [100] M. Scheel, R. Seemann, M. Brinkmann, M. Di Michiel, A. Sheppard, and S. Herminghaus, "Liquid distribution and cohesion in wet granular assemblies beyond the capillary bridge regime," *Journal of Physics: Condensed Matter*, vol. 20, no. 49, p. 494236, 2008.
- [101] M. Scheel, R. Seemann, M. Brinkmann, M. Di Michiel, A. Sheppard, B. Breidenbach, and S. Herminghaus, "Morphological clues to wet granular pile stability," *Nature Materials*, vol. 7, no. 3, pp. 189–193, 2008.
- [102] C. L. Flemmer, "On the regime boundaries of moisture in granular materials," *Powder Technology*, vol. 66, pp. 191–194, 1991.
- [103] T. Domenech and S. S. Velankar, "Microstructure, phase inversion and yielding in immiscible polymer blends with selectively wetting silica particles," *Journal of Rheology*, vol. 61, no. 2, pp. 363–377, 2017.
- [104] R. Aveyard, B. P. Binks, and J. H. Clint, "Emulsions stabilised solely by colloidal particles," *Advances in Colloid and Interface Science*, vol. 100, pp. 503–546, 2003.
- [105] B. P. Binks and J. H. Clint, "Solid wettability from surface energy components: relevance to pickering emulsions," *Langmuir*, vol. 18, no. 4, pp. 1270–1273, 2002.
- [106] E. Herzig, K. White, A. Schofield, W. Poon, and P. Clegg, "Bicontinuous emulsions stabilized solely by colloidal particles," *Nature Materials*, vol. 6, no. 12, pp. 966–971, 2007.
- [107] M. Lin, R. Klein, H. Lindsay, D. Weitz, R. Ball, and P. Meakin, "The structure of fractal colloidal aggregates of finite extent," *Journal of Colloid and Interface Science*, vol. 137, no. 1, pp. 263–280, 1990.
- [108] F. Bossler, L. Weyrauch, R. Schmidt, and E. Koos, "Influence of mixing conditions on the rheological properties and structure of capillary suspensions," *Colloids and Surfaces A: Physicochemical and Engineering Aspects*, vol. 518, pp. 85–97, 2017.
- [109] G. I. Taylor, "The viscosity of a fluid containing small drops of another fluid," *Proceedings of the Royal Society of London. Series A*, vol. 138, no. 834, pp. 41–48, 1932.
- [110] G. Taylor, "The formation of emulsions in definable fields of flow," *Proceedings of the Royal Society of London. Series A*, vol. 146, no. 858, pp. 501–523, 1934.
- [111] H. P. Grace, "Dispersion phenomena in high viscosity immiscible fluid systems and application of static mixers as dispersion devices in such systems," *Chemical Engineering Communications*, vol. 14, no. 3-6, pp. 225–277, 1982.

- [112] B. Bentley and L. Leal, "An experimental investigation of drop deformation and breakup in steady, two-dimensional linear flows," *Journal of Fluid Mechanics*, vol. 167, pp. 241–283, 1986.
- [113] S. Caserta, S. Reynaud, M. Simeone, and S. Guido, "Drop deformation in sheared polymer blends," *Journal of Rheology*, vol. 51, pp. 761–774, 2007.
- [114] K. Jansen, W. Agterof, and J. Mellema, "Droplet breakup in concentrated emulsions," *Journal of Rheology*, vol. 45, pp. 227–236, 2001.
- [115] A. Vananroye, P. Van Puyvelde, and P. Moldenaers, "Effect of confinement on droplet breakup in sheared emulsions," *Langmuir*, vol. 22, no. 9, pp. 3972–3974, 2006.
- [116] C. Mabilie, F. Leal-Calderon, J. Bibette, and V. Schmitt, "Monodisperse fragmentation in emulsions: Mechanisms and kinetics," *EPL (Europhysics Letters)*, vol. 61, no. 5, pp. 708–714, 2003.
- [117] S. Guido, "Shear-induced droplet deformation: effects of confined geometry and viscoelasticity," *Current Opinion in Colloid & Interface Science*, vol. 16, no. 1, pp. 61–70, 2011.
- [118] S. Kaur and L. G. Leal, "Drop deformation and break-up in concentrated suspensions," *Journal of Rheology*, vol. 54, pp. 981–1008, 2010.
- [119] K. Arai, M. Konno, Y. Matunaga, and S. Saito, "Effect of dispersed-phase viscosity on the maximum stable drop size for breakup in turbulent flow," *Journal of Chemical Engineering of Japan*, vol. 10, no. 4, pp. 325–330, 1977.
- [120] A. Gupta, H. B. Eral, T. A. Hatton, and P. S. Doyle, "Controlling and predicting droplet size of nanoemulsions: scaling relations with experimental validation," *Soft Matter*, vol. 12, pp. 1452–1458, 2016.
- [121] J. Hinze, "Fundamentals of the hydrodynamic mechanism of splitting in dispersion processes," *AIChE Journal*, vol. 1, no. 3, pp. 289–295, 1955.
- [122] R. Andersson and B. Andersson, "On the breakup of fluid particles in turbulent flows," *AIChE Journal*, vol. 52, no. 6, pp. 2020–2030, 2006.
- [123] M. Zlokarnik, *Rührtechnik - Theorie und Praxis*. Berlin: Springer-Verlag, 1999.
- [124] H. P. Schuchmann and T. Danner, "Emulgieren: mehr als nur Zerkleinern," *Chemie Ingenieur Technik*, vol. 76, no. 4, pp. 364–375, 2004.
- [125] Glycerine Producers' Association, "Physical properties of glycerine and its solutions; retrieved from [http://www.aciscience.org/docs/physical\\_properties\\_of\\_glycerine\\_and\\_its\\_solutions.pdf](http://www.aciscience.org/docs/physical_properties_of_glycerine_and_its_solutions.pdf)," 1963.
- [126] H. Li, "Refractive index of alkali halides and its wavelength and temperature derivatives," *Journal of Physical and Chemical Reference Data*, vol. 5, no. 2, pp. 329–528, 1976.

- [127] E. Koos, W. Kannowade, and N. Willenbacher, "Restructuring and aging in a capillary suspension," *Rheologica Acta*, vol. 53, no. 12, pp. 947–957, 2014.
- [128] W. Stöber, A. Fink, and E. Bohn, "Controlled growth of monodisperse silica spheres in the micron size range," *Journal of Colloid and Interface Science*, vol. 26, no. 1, pp. 62–69, 1968.
- [129] N. A. M. Verhaegh and A. van Blaaderen, "Dispersions of rhodamine-labeled silica spheres: Synthesis, characterization, and fluorescence confocal scanning laser microscopy," *Langmuir*, vol. 10, no. 5, pp. 1427–1438, 1994.
- [130] A. van Blaaderen and A. Vrij, "Synthesis and characterization of colloidal dispersions of fluorescent, monodisperse silica spheres," *Langmuir*, vol. 8, no. 12, pp. 2921–2931, 1992.
- [131] J. Wenzl, R. Seto, M. Roth, H.-J. Butt, and G. K. Auernhammer, "Measurement of rotation of individual spherical particles in cohesive granulates," *Granular Matter*, vol. 15, pp. 391–400, 2012.
- [132] K. Nozawa, H. Gailhanou, L. Raison, P. Panizza, H. Ushiki, E. Sellier, J. Delville, and M. Delville, "Smart control of monodisperse Stöber silica particles: effect of reactant addition rate on growth process," *Langmuir*, vol. 21, no. 4, pp. 1516–1523, 2005.
- [133] S. Li, Q. Wan, Z. Qin, Y. Fu, and Y. Gu, "Understanding Stöber silica's pore characteristics measured by gas adsorption," *Langmuir*, vol. 31, no. 2, pp. 824–832, 2015.
- [134] M. Fuji, H. Fujimori, T. Takei, T. Watanabe, and M. Chikazawa, "Wettability of glass-bead surface modified by trimethylchlorosilane," *The Journal of Physical Chemistry B*, vol. 102, no. 51, pp. 10498–10504, 1998.
- [135] T. Suratwala, M. Hanna, E. Miller, P. Whitman, I. Thomas, P. Ehrmann, R. Maxwell, and A. Burnham, "Surface chemistry and trimethylsilyl functionalization of Stöber silica sols," *Journal of Non-Crystalline Solids*, vol. 316, no. 2, pp. 349–363, 2003.
- [136] S. Brandriss and S. Margel, "Synthesis and characterization of self-assembled hydrophobic monolayer coatings on silica colloids," *Langmuir*, vol. 9, no. 5, pp. 1232–1240, 1993.
- [137] J. Canselier, H. Delmas, A. Wilhelm, and B. Abismail, "Ultrasound emulsification—an overview," *Journal of Dispersion Science and Technology*, vol. 23, no. 1-3, pp. 333–349, 2002.
- [138] H. Walls, S. B. Caines, A. M. Sanchez, and S. A. Khan, "Yield stress and wall slip phenomena in colloidal silica gels," *Journal of Rheology*, vol. 47, no. 4, pp. 847–868, 2003.
- [139] R. Buscall, "Letter to the editor: Wall slip in dispersion rheometry," *Journal of Rheology*, vol. 54, no. 6, pp. 1177–1183, 2010.
- [140] A. Yoshimura and R. K. Prud'homme, "Wall slip corrections for Couette and parallel disk viscometers," *Journal of Rheology*, vol. 32, pp. 53–67, 1988.



- [141] R. Brummer, *Rheology Essentials of Cosmetic and Food Emulsions*. Berlin: Springer Science & Business Media, 2006.
- [142] J. Maurath, B. Bitsch, Y. Schwegler, and N. Willenbacher, "Influence of particle shape on the rheological behavior of three-phase non-brownian suspensions," *Colloids and Surfaces A: Physicochemical and Engineering Aspects*, vol. 497, pp. 316–326, 2016.
- [143] T. Wilson, "Resolution and optical sectioning in the confocal microscope," *Journal of Microscopy*, vol. 244, no. 2, pp. 113–121, 2011.
- [144] S. N. S. Reihani and L. B. Oddershede, "Confocal microscopy of thick specimens," *Journal of Biomedical Optics*, vol. 14, no. 3, p. 030513, 2009.
- [145] K. C. Neuman, E. A. Abbondanzieri, and S. M. Block, "Measurement of the effective focal shift in an optical trap," *Optics Letters*, vol. 30, no. 11, pp. 1318–1320, 2005.
- [146] S. H. Wiersma, P. Török, T. D. Visser, and P. Varga, "Comparison of different theories for focusing through a plane interface," *Journal of the Optical Society of America A*, vol. 14, no. 7, pp. 1482–1490, 1997.
- [147] PromoCell GmbH, "Promofluor 488 Premium, Reactive Dyes; retrieved from [http://www.promokine.info/fileadmin/PDFs/All\\_PDFs/PK-PF488P-0-01.pdf](http://www.promokine.info/fileadmin/PDFs/All_PDFs/PK-PF488P-0-01.pdf)," 2014.
- [148] Z. Gan, J. Ju, T. Zhang, and D. Wu, "Preparation of rhodamine B fluorescent poly (methacrylic acid) coated gelatin nanoparticles," *Journal of Nanomaterials*, vol. 2011, pp. 231–238, 2011.
- [149] K. Dunn and E. Wang, "Optical aberrations and objective choice in multicolor confocal microscopy," *Biotechniques*, vol. 28, no. 3, pp. 542–550, 2000.
- [150] F. Bossler and E. Koos, "Structure of particle networks in capillary suspensions with wetting and nonwetting fluids," *Langmuir*, vol. 32, no. 6, pp. 1489–1501, 2016.
- [151] M. Bortolotti, M. Brugnara, C. Della Volpe, and S. Siboni, "Numerical models for the evaluation of the contact angle from axisymmetric drop profiles: a statistical comparison," *Journal of Colloid and Interface Science*, vol. 336, no. 1, pp. 285–297, 2009.
- [152] E. R. Weeks, J. C. Crocker, A. C. Levitt, A. Schofield, and D. A. Weitz, "Three-dimensional direct imaging of structural relaxation near the colloidal glass transition," *Science*, vol. 287, no. 5453, pp. 627–631, 2000.
- [153] J. C. Crocker and E. R. Weeks, "Particle tracking using IDL; retrieved from <http://www.physics.emory.edu/faculty/weeks/idl/>."
- [154] J. C. Crocker and D. G. Grier, "Methods of digital video microscopy for colloidal studies," *Journal of Colloid and Interface Science*, vol. 179, no. 1, pp. 298–310, 1996.

- [155] E. R. Weeks, "Download IDL macros for particle tracking and analysis; retrieved from <http://www.physics.emory.edu/faculty/weeks//idl/download.html>."
- [156] W.-H. Tsai, "Moment-preserving thresholding: A new approach," *Computer Vision, Graphics, and Image Processing*, vol. 29, no. 3, pp. 377–393, 1985.
- [157] E. R. Weeks, "How to calculate the pair correlation function  $g(r)$ ; retrieved from <http://www.physics.emory.edu/faculty/weeks//idl/gofr2.html>."
- [158] M. Leocmach and H. Tanaka, "A novel particle tracking method with individual particle size measurement and its application to ordering in glassy hard sphere colloids," *Soft Matter*, vol. 9, no. 5, pp. 1447–1457, 2013.
- [159] P. Knight, T. Instone, J. Pearson, and M. Hounslow, "An investigation into the kinetics of liquid distribution and growth in high shear mixer agglomeration," *Powder Technology*, vol. 97, no. 3, pp. 246–257, 1998.
- [160] A. Scott, M. Hounslow, and T. Instone, "Direct evidence of heterogeneity during high-shear granulation," *Powder Technology*, vol. 113, no. 1, pp. 205–213, 2000.
- [161] T. Schæfer and C. Mathiesen, "Melt pelletization in a high shear mixer. IX. Effects of binder particle size," *International Journal of Pharmaceutics*, vol. 139, no. 1, pp. 139–148, 1996.
- [162] T. Domenech, J. Yang, S. Heidlebaugh, and S. Velankar, "Three distinct open-pore morphologies from a single particle-filled polymer blend," *Physical Chemistry Chemical Physics*, vol. 18, pp. 4310–4315, 2016.
- [163] F. Bossler and E. Koos, "Online Supplementary Information to [150], <http://pubs.acs.org/doi/suppl/10.1021/acs.langmuir.5b04246>," 2016.
- [164] F. P. Cordelières, "3D object counter; retrieved from: [http://imagejdocu.tudor.lu/doku.php?id=plugin:analysis:3d\\_object\\_counter:start](http://imagejdocu.tudor.lu/doku.php?id=plugin:analysis:3d_object_counter:start)."
- [165] S. Bolte and F. Cordelières, "A guided tour into subcellular colocalization analysis in light microscopy," *Journal of Microscopy*, vol. 224, no. 3, pp. 213–232, 2006.
- [166] V. N. Manoharan, M. T. Elsesser, and D. J. Pine, "Dense packing and symmetry in small clusters of microspheres," *Science*, vol. 301, no. 5632, pp. 483–487, 2003.
- [167] T. Gambaryan-Roisman, "Liquids on porous layers: Wetting, imbibition and transport processes," *Current Opinion in Colloid & Interface Science*, vol. 19, no. 4, pp. 320–335, 2014.
- [168] I. Ametov and C. A. Prestidge, "Hydrophobic interactions in concentrated colloidal suspensions: A rheological investigation," *The Journal of Physical Chemistry B*, vol. 108, no. 32, pp. 12116–12122, 2004.
- [169] S. Chen, G. Øye, and J. Sjöblom, "Rheological properties of silica particle suspensions in mineral oil," *Journal of Dispersion Science and Technology*, vol. 26, no. 6, pp. 791–798, 2005.

- [170] G. B. Davies, T. Krüger, P. V. Coveney, and J. Harting, “Detachment energies of spheroidal particles from fluid-fluid interfaces,” *The Journal of Chemical Physics*, vol. 141, p. 154902, 2014.
- [171] F. Mahaut, X. Chateau, P. Coussot, and G. Ovarlez, “Yield stress and elastic modulus of suspensions of noncolloidal particles in yield stress fluids,” *Journal of Rheology*, vol. 52, no. 1, pp. 287–313, 2008.
- [172] O. Uche, F. Stillinger, and S. Torquato, “On the realizability of pair correlation functions,” *Physica A: Statistical Mechanics and its Applications*, vol. 360, no. 1, pp. 21–36, 2006.
- [173] C. P. Royall, W. C. Poon, and E. R. Weeks, “In search of colloidal hard spheres,” *Soft Matter*, vol. 9, no. 1, pp. 17–27, 2013.
- [174] Z. Fournier, D. Geromichalos, S. Herminghaus, M. Kohonen, F. Mugele, M. Scheel, M. Schulz, B. Schulz, C. Schier, and R. Seemann, “Mechanical properties of wet granular materials,” *Journal of Physics: Condensed Matter*, vol. 17, no. 9, pp. 477–502, 2005.
- [175] M. Lach-Hab, A. E. González, and E. Blaisten-Barojas, “Concentration dependence of structural and dynamical quantities in colloidal aggregation: computer simulations,” *Physical Review E*, vol. 54, no. 5, pp. 5456–5462, 1996.
- [176] A. E. Gonzalez, M. Lach-Hab, and E. Blaisten-Barojas, “On the concentration dependence of the cluster fractal dimension in colloidal aggregation,” *Journal of Sol-Gel Science and Technology*, vol. 15, no. 2, pp. 119–127, 1999.
- [177] P.-I. Au, J. Liu, and Y.-K. Leong, “Yield stress and microstructure of washed oxide suspensions at the isoelectric point: experimental and model fractal structure,” *Rheologica Acta*, vol. 55, no. 10, pp. 847–856, 2016.
- [178] C. Kranenburg, “The fractal structure of cohesive sediment aggregates,” *Estuarine, Coastal and Shelf Science*, vol. 39, no. 6, pp. 451–460, 1994.
- [179] F. E. Torres, W. B. Russel, and W. R. Schowalter, “Floc structure and growth kinetics for rapid shear coagulation of polystyrene colloids,” *Journal of Colloid and Interface Science*, vol. 142, no. 2, pp. 554–574, 1991.
- [180] C. Allain, M. Cloitre, and F. Parisse, “Settling by cluster deposition in aggregating colloidal suspensions,” *Journal of Colloid and Interface Science*, vol. 178, no. 2, pp. 411–416, 1996.
- [181] C. Allain, M. Cloitre, and M. Wafra, “Aggregation and sedimentation in colloidal suspensions,” *Physical Review Letters*, vol. 74, no. 8, pp. 1478–1481, 1995.
- [182] M. Peltomäki, E. Hellén, and M. Alava, “No self-similar aggregates with sedimentation,” *Journal of Statistical Mechanics: Theory and Experiment*, vol. 2004, no. 9, p. P09002, 2004.

- [183] S. Ikeda, E. A. Foegeding, and T. Hagiwara, “Rheological study on the fractal nature of the protein gel structure,” *Langmuir*, vol. 15, no. 25, pp. 8584–8589, 1999.
- [184] K. Dullaert and J. Mewis, “Thixotropy: Build-up and breakdown curves during flow,” *Journal of Rheology*, vol. 49, no. 6, pp. 1213–1230, 2005.
- [185] P. Varadan and M. J. Solomon, “Direct visualization of long-range heterogeneous structure in dense colloidal gels,” *Langmuir*, vol. 19, no. 3, pp. 509–512, 2003.
- [186] J. Colombo and E. Del Gado, “Stress localization, stiffening, and yielding in a model colloidal gel,” *Journal of Rheology*, vol. 58, no. 5, pp. 1089–1116, 2014.

## 9 Appendix

### 9.1 Calculations of partial sphere volumes inside a box

If the center of a sphere with radius  $R$  is placed in a box with edge dimensions  $x_{\text{box}} \times y_{\text{box}} \times z_{\text{box}}$ , parts of the sphere volume can extend beyond the box boundaries. This problem appears during calculations of the pair correlation function  $g(R/a)$ . In this case, the calculation of only the volume lying inside of the box boundaries is needed, see section 4.4. Closed-form equations derived for solving this geometrical problem are given in this appendix section.

**Basic statements on the problem: Calculate the portion of a sphere volume contained within a box**

1. The problem is solved in Cartesian coordinates.
2. The sphere center point C is inside of the box volume.
3. The origin of the coordinates is placed in C, i.e.  $C(x_0, y_0, z_0) = C(0, 0, 0)$ .
4. The distances from C to the six faces of the box are denoted by  $|x_+|$ ,  $|x_-|$ ,  $|y_+|$ ,  $|y_-|$ ,  $|z_+|$  and  $|z_-|$  with  $|x_+| + |x_-| = x_{\text{box}}$ ,  $|y_+| + |y_-| = y_{\text{box}}$  and  $|z_+| + |z_-| = z_{\text{box}}$ .
5. The full sphere volume is  $V_{\text{sphere}} = (4/3) \cdot \pi R^3$ .

#### Possible overlaps

If  $|x_+| < R$ , the sphere is perpendicularly intersected by the box face on the positive  $x$  coordinate axis. Equivalent statements can be made for the other five box faces. More generalized, the criterion is written as  $s < R$  where  $s$  replaces the distance parallel to one of the axes from C to the corresponding box face. The sub-volume of the sphere lying beyond the face is a spherical cap. When calculating the partial sphere volume inside of the box, the volume  $V_{\text{cap}}$  of each cap has to be subtracted from the full volume  $V_{\text{sphere}}$ .

If  $\sqrt{|x_+|^2 + |y_+|^2} < R$ , the sphere also extends beyond the box edge where the adjacent positive  $x$  and positive  $y$  box faces intersect, i.e. part of the sphere volume lies in a wedge beyond this intersection. Equivalent criteria can be drawn for all eleven other adjacent box edges. More generalized, the criterion is written as  $\sqrt{s^2 + t^2} < R$  where  $s$  and  $t$  replace the distances from C to the corresponding adjacent box faces. The existence of such a perpendicular wedge with volume  $V_{\text{wedge}}$  also presupposes the existence of two spherical cap volumes lying beyond the adjacent box faces. As both of these cap volumes are subtracted from the sphere volume, the wedge volume would be subtracted twice as it is part of both cap volumes. Thus,  $V_{\text{wedge}}$  has to be added back to the total (or subtracted from

the sum of the cap volumes to find the volume of their union) when the volume of the partial sphere inside of the box is calculated.

If  $\sqrt{|x_+|^2 + |y_+|^2 + |z_+|^2} < R$ , the sphere extends beyond the box corner where the three adjacent positive  $x$ , positive  $y$  and positive  $z$  box faces intersect, i.e. part of the sphere volume is situated beyond this corner. Equivalent criteria can also be made for all seven other box corners. More generalized, the criterion is written as  $\sqrt{s^2 + t^2 + u^2} < R$  where  $s$ ,  $t$  and  $u$  replace the distances from  $C$  to the corresponding adjacent box faces. Again, the existence of such a corner sub-volume  $V_{\text{corner}}$  necessitates that the intersection between the three cap volumes lies outside of the box, and that three wedges, also lying outside of the box, will also be formed. As all three cap volumes are subtracted from the sphere and all three wedge volumes are added back, the corner sub-volume has already been both subtracted and added three times, since it is part of all three cap and wedge volumes. Thus, when the volume of the partial sphere inside of the box is calculated,  $V_{\text{corner}}$  has to be subtracted once more.

### Calculation

The partial volume of the sphere lying inside of the box  $V_{\text{inside}}$  can be represented by a combination of 27 separately calculated sub-volumes (1 full sphere volume  $V_{\text{sphere}}$ , 6 cap volumes  $V_{\text{cap}}$ , 12 wedge volumes  $V_{\text{wedge}}$  and 8 corner volumes  $V_{\text{corner}}$ ). As noted above, one gets

$$V_{\text{inside}} = V_{\text{sphere}} - \sum_{i=1}^6 V_{\text{cap},i} + \sum_{j=1}^{12} V_{\text{wedge},j} - \sum_{k=1}^8 V_{\text{corner},k} \quad (9.1)$$

with the indices  $i$ ,  $j$  and  $k$  enumerating the possible sub-volumes beyond all 6 faces, 12 edges and 8 corners of the box. For faces, edges, and corners, which do not overlap with the sphere, the corresponding sub-volumes are set to zero. The remaining ones are calculated separately using equations 9.2, 9.4 and 9.6 below. The distance variables  $s$ ,  $t$  and  $u$  behave commutatively in these calculations.

The sub-volume of each spherical cap is calculated via the well-known geometric equation

$$V_{\text{cap}} = \frac{h_{\text{cap}}^2 \pi}{3} (3R - h_{\text{cap}}) \quad (9.2)$$

with the cap height  $h_{\text{cap}}$  being expressed by the distance from  $C$  to the box face as  $h_{\text{cap}} = R - s$  where  $s > 0$  by definition.

The sub-volume of each wedge is calculated by solving the integral

$$V_{\text{wedge}} = \int_s^{\sqrt{R^2-t^2}} \int_t^{\sqrt{R^2-x^2}} \int_{-\sqrt{R^2-x^2-y^2}}^{\sqrt{R^2-x^2-y^2}} dz dy dx. \quad (9.3)$$

This integral is solved in closed form under the assumptions  $R > 0$ ,  $s > 0$ ,  $t > 0$ , and the undefined term  $\arctan(x/0)$ , occurring during integrations, is replaced by  $\arctan(\infty) = \pi/2$ , since  $x > s$  and, by definition,  $s > 0$ . The solved closed form equation of the wedge



volume then reads

$$\begin{aligned}
 V_{\text{wedge}} = & \frac{1}{6}\pi s^3 + \frac{1}{6}\pi t^3 - \frac{1}{2}\pi sR^2 - \frac{1}{2}\pi tR^2 + \frac{2}{3}ts\sqrt{R^2 - s^2 - t^2} \\
 & + \left[ tR^2 - \frac{1}{3}t^3 \right] \arctan\left(\frac{s}{\sqrt{R^2 - s^2 - t^2}}\right) + \left[ sR^2 - \frac{1}{3}s^3 \right] \arctan\left(\frac{t}{\sqrt{R^2 - s^2 - t^2}}\right) \\
 & + \frac{2}{3}R^3 \arctan\left(\frac{R\sqrt{R^2 - s^2 - t^2}}{st}\right). \quad (9.4)
 \end{aligned}$$

The sub-volume of each corner volume is calculated by solving the integral

$$V_{\text{corner}} = \int_s^{\sqrt{R^2 - u^2 - t^2}} \int_t^{\sqrt{R^2 - u^2 - x^2}} \int_u^{\sqrt{R^2 - x^2 - y^2}} dz dy dx. \quad (9.5)$$

This integral is solved in closed form under the assumptions  $R > 0$ ,  $s > 0$ ,  $t > 0$ ,  $u > 0$ , and the undefined term  $\arctan(x/0)$  is again replaced by  $\arctan(\infty) = \pi/2$ . The solved closed form equation of the corner volume then reads

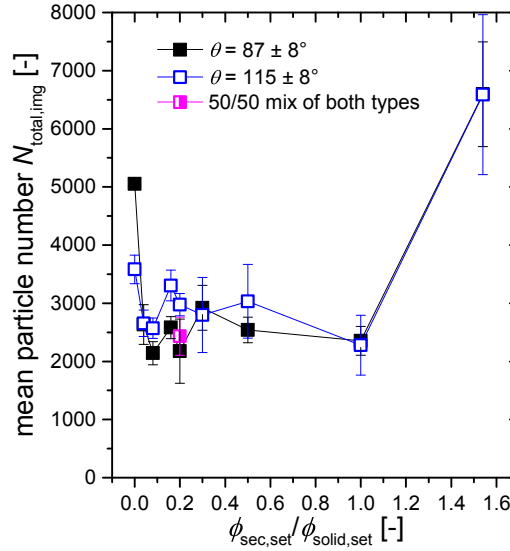
$$\begin{aligned}
 V_{\text{corner}} = & \frac{1}{3}us\sqrt{R^2 - s^2 - u^2} + \frac{1}{3}ut\sqrt{R^2 - t^2 - u^2} + \frac{1}{3}ts\sqrt{R^2 - s^2 - t^2} - stu \\
 & + \frac{1}{3}R^3 \arctan\left(\frac{R\sqrt{R^2 - s^2 - t^2}}{st}\right) + \frac{1}{3}R^3 \arctan\left(\frac{u\sqrt{R^2 - t^2 - u^2}}{tR}\right) \\
 & - \frac{1}{3}R^3 \arctan\left(\frac{us}{R\sqrt{R^2 - s^2 - u^2}}\right) - \frac{1}{3}R^3 \arctan\left(\frac{uR}{t\sqrt{R^2 - t^2 - u^2}}\right) \\
 & + \left[ \frac{1}{2}uR^2 - \frac{1}{6}u^3 \right] \arctan\left(\frac{s}{\sqrt{R^2 - s^2 - u^2}}\right) + \left[ \frac{1}{2}tR^2 - \frac{1}{6}t^3 \right] \arctan\left(\frac{s}{\sqrt{R^2 - s^2 - t^2}}\right) \\
 & + \left[ \frac{1}{2}sR^2 - \frac{1}{6}s^3 \right] \arctan\left(\frac{t}{\sqrt{R^2 - s^2 - t^2}}\right) + \left[ \frac{1}{6}u^3 - \frac{1}{2}uR^2 \right] \arctan\left(\frac{\sqrt{R^2 - t^2 - u^2}}{t}\right) \\
 & + \left[ \frac{1}{6}t^3 - \frac{1}{2}tR^2 \right] \arctan\left(\frac{\sqrt{R^2 - t^2 - u^2}}{u}\right) + \left[ \frac{1}{6}s^3 - \frac{1}{2}sR^2 \right] \arctan\left(\frac{\sqrt{R^2 - s^2 - u^2}}{u}\right). \quad (9.6)
 \end{aligned}$$

This set of equations was included into the self-written IDL algorithm presented in section 4.4. When all cap, wedge, and corner sub-volumes are not equal to zero, the box is fully incorporated in the sphere and  $V_{\text{inside}} = V_{\text{box}}$ . This equality was checked by calculating several of such fully overlapping test spheres via the cumbersome equation 9.1 and comparing them to the easy calculation  $V_{\text{box}} = x_{\text{box}} \cdot y_{\text{box}} \cdot z_{\text{box}}$ . Despite the many necessary sub-calculations, the differences in results from both equations were on the order of only 0.0001 %, which was accepted as sufficient proof for their correctness and feasibility.

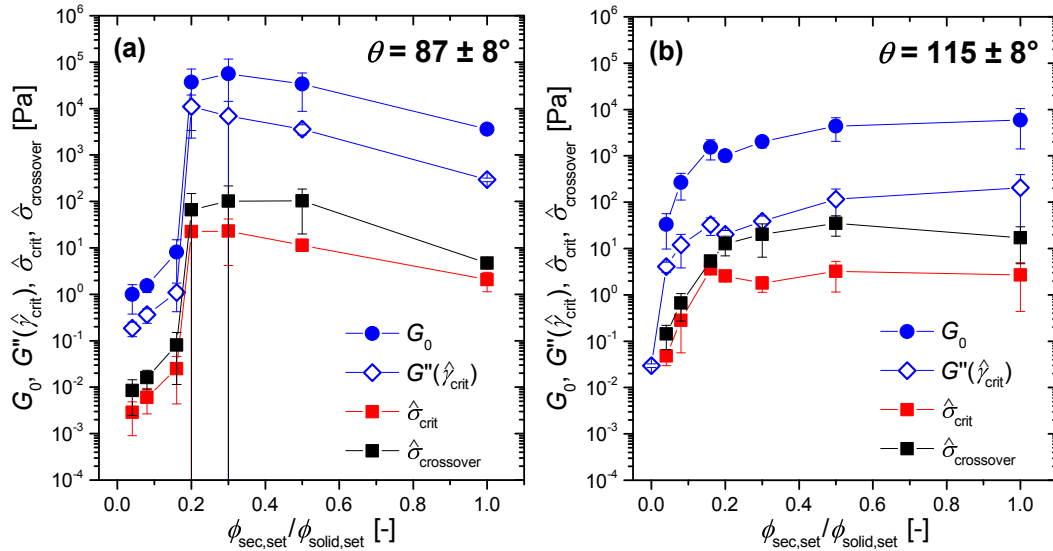
## 9.2 Additional figures to chapter 6.2

In this appendix subsection, six additional figures, related to the results and discussion in chapter 6.2 of the confocal images with composition C1 samples are presented. Each image is referenced and discussed in that section. These appendix figures include a plot of total number of detected particles (Fig. 9.1), rheological data as function of the set

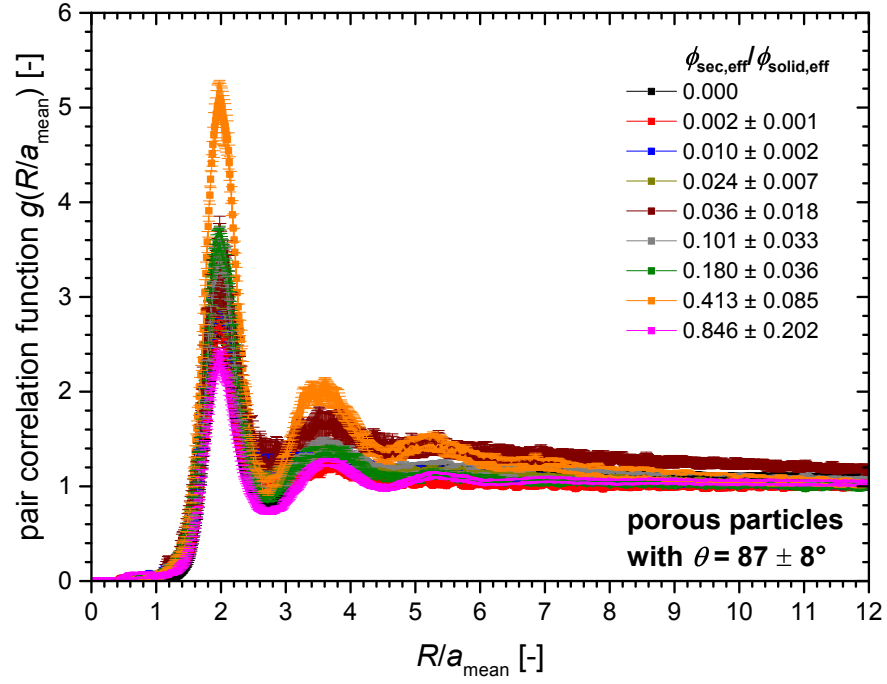
secondary fluid to solid volume ratio (Fig. 9.2), pair correlation functions for samples with  $87^\circ$  (Fig. 9.3) and  $115^\circ$  (Fig. 9.4), as well as for a sample containing a 50/50 mixture of particles with both of these contact angles (Fig. 9.5). Finally, histograms of coordination numbers at a set volume ratio of  $\phi_{\text{sec,set}}/\phi_{\text{solid,set}} = 0.20$  are shown in Fig. 9.6.



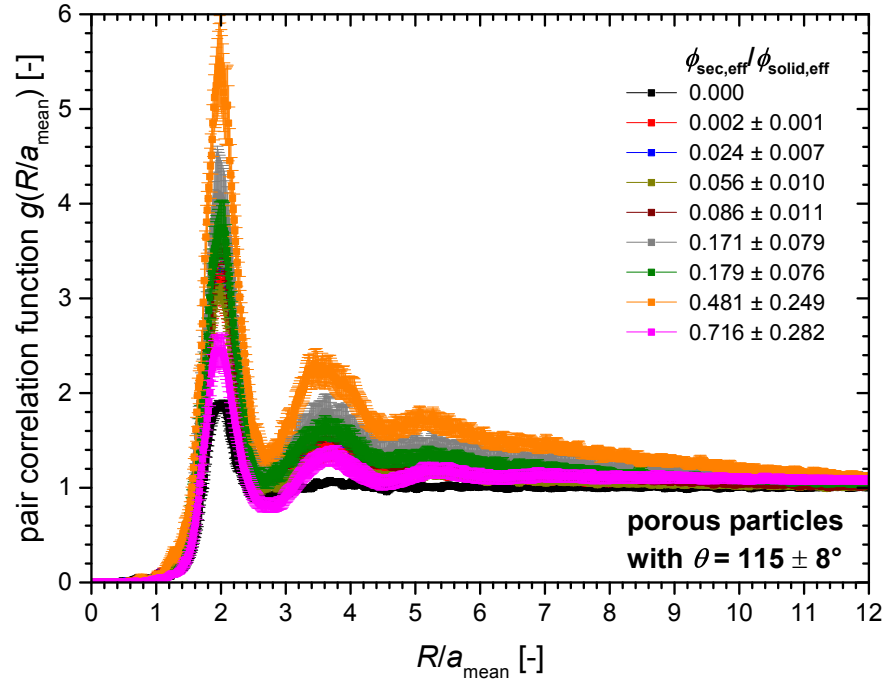
**Figure 9.1:** Detected number of particles per image  $N_{\text{total,img}}$  as function of the ratio  $\phi_{\text{sec,set}}/\phi_{\text{solid,set}}$  of C1 samples. The data was obtained by computational evaluation of confocal 3D images of samples containing porous particles having  $\theta = 87 \pm 8^\circ$  and  $115 \pm 8^\circ$ , as well as a 50/50 mixture of both of these particle types (i.e. all samples summarized in Table 6.1).



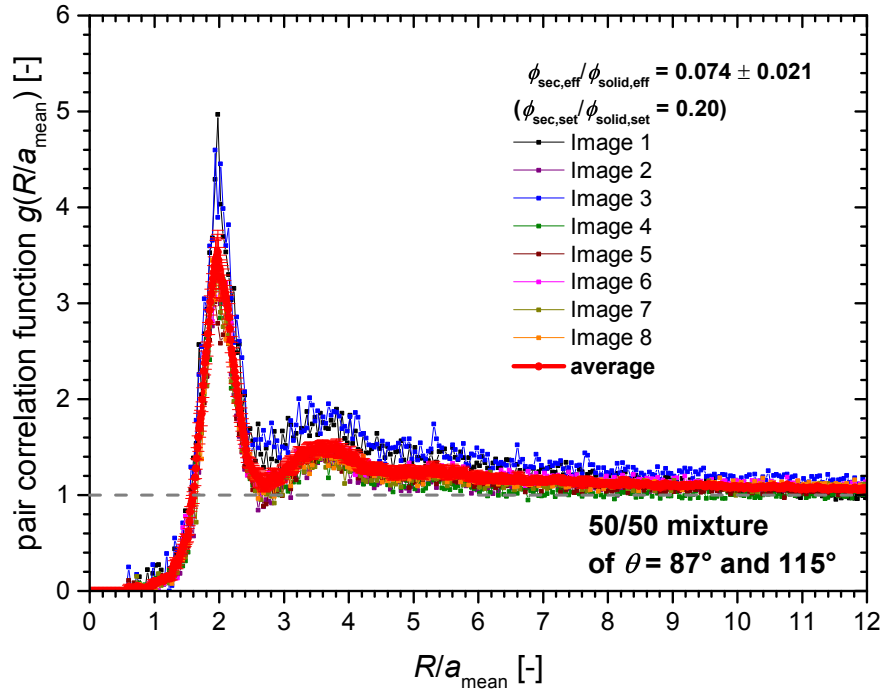
**Figure 9.2:** Plateau modulus  $G_0$ , loss modulus  $G''(\hat{\gamma}_{\text{crit}})$  at the end of the LVE region, stress amplitude  $\hat{\sigma}_{\text{crit}}$  at the end of the LVE region and crossover stress amplitude  $\hat{\sigma}_{\text{crossover}}$  as function of the set secondary fluid to solid volume ratio  $\phi_{\text{sec,set}}/\phi_{\text{solid,set}}$  for the samples with particles having (a)  $\theta = 87 \pm 8^\circ$  and (b)  $\theta = 115 \pm 8^\circ$ . The same data is plotted against the effective ratio  $\phi_{\text{sec,eff}}/\phi_{\text{solid,eff}}$  in Fig. 6.20. The frequency was fixed at  $\omega = 1$  rad/s.



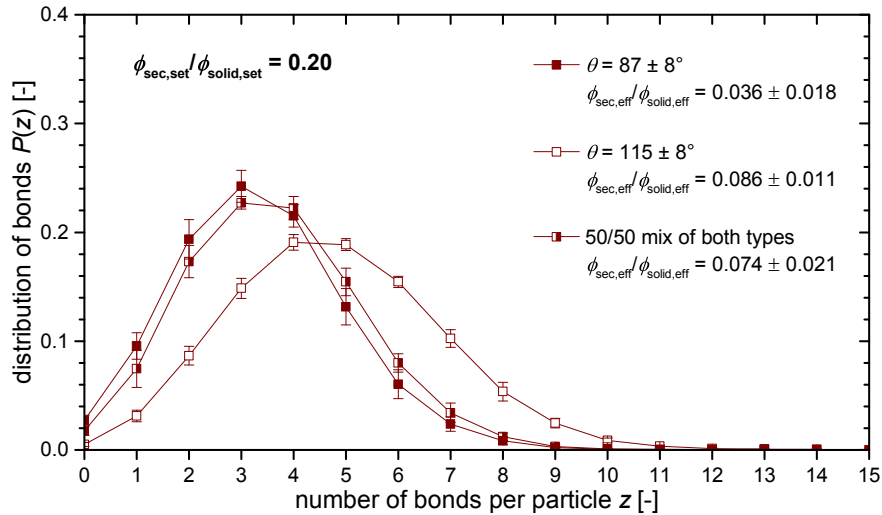
**Figure 9.3:** Pair correlation functions  $g(R/a_{\text{mean}})$  of C1 samples with varied effective secondary fluid to solid volume ratio with particles having  $87 \pm 8^\circ$ . The same diagrams without error bars are shown in Fig. 6.23a. The radial coordinate  $R$  is normalized by the calculated mean radius  $a_{\text{mean}}$  of each individual sample as shown in Fig. 6.17a.



**Figure 9.4:** Pair correlation functions  $g(R/a_{\text{mean}})$  of C1 samples with varied effective secondary fluid to solid volume ratio with particles having  $115 \pm 8^\circ$ . The same diagrams without error bars are shown in Fig. 6.23b. The radial coordinate  $R$  is normalized by the calculated mean radius  $a_{\text{mean}}$  of each individual sample as shown in Fig. 6.17a.



**Figure 9.5:** Pair correlation functions  $g(R/a_{\text{mean}})$  of C1 samples with a set secondary fluid to solid volume ratio  $\phi_{\text{sec,set}}/\phi_{\text{solid,set}} = 0.20$  containing a 50/50 mixture of particles having  $87 \pm 8^\circ$  and  $115 \pm 8^\circ$ . The red curve denotes the average of all eight individual confocal images, where each is also included in the diagram and labeled as “Image 1” to “Image 8”. Therefore, this figure can also be seen as a typical example for the accuracy and deviations inherent to all of the calculated  $g(R/a)$  curves in the main text section 6.2.3, which are shown in a simplified form without error bars therein. The radial coordinate  $R$  is normalized by the calculated mean radius  $a_{\text{mean}}$  of each individual sample as shown in Fig. 6.17a.



**Figure 9.6:** Histograms  $P$  of the coordination number  $z$  (count of contacts per particle) of porous C1 samples with constant set secondary fluid to solid volume ratio  $\phi_{\text{sec,set}}/\phi_{\text{solid,set}} = 0.20$  with particles having  $87 \pm 8^\circ$ ,  $115 \pm 8^\circ$ , and a 50/50 mixture of both particle types. Every particle pair with a surface distance  $< 0.85 \mu\text{m}$  was counted as a contact. Note that the effective solid volume fractions of the three samples are also different.

## 9.3 List of symbols and abbreviations

### Latin Symbols

Symbol	Unit	Description
$A$	$\text{mm}^2$	(surface) area
$A_{\text{actual}}$	$\text{mm}^2$	actually wetted area
$A_{\text{bridge}}$	$\mu\text{m}^2$	surface area of a secondary fluid droplet
$A_{\text{flat}}$	$\text{mm}^2$	ideal flat surface area
$A_{\text{H}}$	J	Hamaker constant
$a$	$\mu\text{m}$	particle radius
$a_{50,3}$	$\mu\text{m}$	volumetric mean particle radius
$a_{\text{agg}}$	$\mu\text{m}$	estimate radius of a particle aggregate
$a_{\text{app}}$	$\mu\text{m}$	detected apparent particle radius obtained from confocal image analysis
$a_{\text{drop}}$	$\mu\text{m}$	droplet radius
$a_{\text{exp}}$	$\mu\text{m}$	expected mean particle radius
$a_{\text{mean}}$	$\mu\text{m}$	arithmetic mean particle radius
$\text{Ca}_{\text{crit}}$	-	critical Capillary number
$c_{\text{NaI}}$	wt %	sodium iodide concentration
$D$	-	fractal dimension
$D_{\text{diff}}$	$\text{m}^2 \text{s}^{-1}$	diffusion coefficient
$\mathbf{D}$		strain-rate tensor
$d_x, d_y, d_z$	nm	resolution limit in $x$ , $y$ , and $z$ direction
$E$	J	energy; or energy input
$E_{\text{detach}}$	J	energy needed to detach a particle from an interface
$E_{\text{V}}$	$\text{J m}^{-3}$	energy density
$e$	C	electronic charge
$F$	N	force
$F_{\text{c}}$	N	capillary force
$F_{\text{h}}$	N	hydrodynamic force
$F_{\text{i}}$	N	inertial force
$F_{\text{max}}$	N	maximal force
$F_{\text{vdW}}$	N	van der Waals force
$f$	Hz	frequency
$f_{\text{coll}}$	$\text{s}^{-1}$	frequency of droplet collisions
$G$	J	Gibbs energy
$G$	Pa	shear modulus
$ G^* $	Pa	complex shear modulus
$G'$	Pa	elastic modulus (= storage modulus)
$G''$	Pa	viscous modulus (= loss modulus)
$G_0$	Pa	frequency-independent plateau value of the elastic modulus
$g$	$\text{m s}^{-2}$	acceleration of gravity
$g(R/a)$	-	pair correlation function
$h$	J s	Planck's constant

$h$	mm	gap height
$h_{\text{blade}}$	mm	height of the blade in the vane geometry
$h_{\text{cyl}}$	mm	height of the cylinder in the Searle geometry
$h_{\text{cap}}$	$\mu\text{m}$	height of a spherical cap
$I$	-	intensity (brightness of a voxel); all used indices are detailed in the text
$K_b$	Pa	elastic constant of the backbone
$K_f$	Pa	intra-floc elastic constant
$k_B$	$\text{J K}^{-1}$	Boltzmann constant
$M$	N m	(stirrer) torque
$M_D$	N m	dissolver stirrer torque
$M_R$	N m	rheometer torque
$m$	g	mass
$m_{\text{solid}}$	g	total particle mass
$m$	-	exponent
$m_\gamma$	-	scaling exponent of the critical strain amplitude
$m_G$	-	scaling exponent of the plateau modulus
$N$	-	particle number
$N_{\text{bridge}}$	-	total number of bridges in a sample
$N_{\text{particle}}$	-	total number of particles in a sample
$N_{\text{total,img}}$	-	total number of particles in the 3D image
$NA$	-	numerical aperture
$n$	rpm	rotational speed of the stirrer
$n_1, n_2$	rpm	rotational stirring speed during the first/second mixing step
$n_d$	rpm	rotational stirring speed during particle dispersion when fluids have been emulsified first
$n$	-	refractive index
$n_b$	-	refractive index of the bulk liquid
$n_{\text{immersion}}$	-	refractive index of the immersion liquid
$n_p$	-	refractive index of the particles
$n_{\text{sample}}$	-	refractive index of the sample
$n$	mol	amount of substance
$Oh$	-	Ohnesorge number
$\mathbf{P}$	-	particle detection matrix
$P$	-	probability
$P_{\text{coa}}$	-	coalescence probability
$P_r$	-	probability of capillary bridge rupture under unity shear
$P_{\text{Watt}}$	W	power
$P_{\text{Watt,m}}$	$\text{W kg}^{-1}$	power per unit mass
$P_{\text{Watt,V}}$	$\text{W m}^{-3}$	power per unit volume
$p$	Pa	pressure
$\Delta p$	Pa	Laplace pressure
$Pe_{\text{gravity}}$	-	Péclet number of gravity
$Q_3$	%	cumulative percent volume
$R$	$\mu\text{m}$	radius; or radial coordinate
$R_1, R_2$	$\mu\text{m}$	principal radii of curvature



$R_{\text{blade}}$	mm	radius of the blade in the vane geometry
$R_{\text{c}}$	$\mu\text{m}$	radius of a particle cluster
$R_{\text{cone}}$	mm	cone radius
$R_{\text{cup}}, R_{\text{cyl}}$	mm	radius of the cup/cylinder in the Searle geometry
$R_{\text{plate}}$	mm	plate radius
$S$	-	saturation
$S$	$\text{J K}^{-1}$	entropy
$s$	$\mu\text{m}$	particle surface distance
$\tilde{s}$	-	relative particle surface distance, $s/a$
$s_{\text{c}}$	$\mu\text{m}$	particle center distance
$s_{\text{plate}}$	mm	distance that the top plate has moved
$s_{\text{true}}, s_{\text{app}}$	$\mu\text{m}$	true and apparent size of an object in $z$ direction
$s, t, u$	$\mu\text{m}$	distances of a point in a box towards the three box faces
$T$	K, or $^{\circ}\text{C}$	temperature
$t$	s	time
$t_{\text{def}}$	s	critical deformation time
$t_{\text{diff}}$	s	particle diffusion timescale
$t_{\text{eff}}$	s	time that a droplet spends in the zone of power input
$t_{\text{sed}}$	s	particle sedimentation timescale
$\Delta t$	min	time interval
$\Delta t_1, \Delta t_2$	min	duration of the first/second mixing step
$\Delta t_3$	h	duration of mixing in the ball mill
$\Delta t_{\text{d}}$	min	duration of particle dispersion step when fluids have been emulsified first
$\Delta t_{\text{mix}}$	min	duration of the particle dispersion step when using ultrasound
$u$	$\text{mm s}^{-1}$	velocity scale inside a droplet
$V$	mL	volume
$V_{\text{bridge}}$	$\mu\text{L}$	volume of a capillary bridge or other secondary fluid entity
$\tilde{V}_{\text{bridge}}$	-	relative capillary bridge volume, $V_{\text{bridge}}/a^3$
$V_{\text{bridge,crit}}$	$\mu\text{L}$	volume of a capillary bridge at which it will coalesce with an adjacent bridge
$V_{\text{box}}$	$\mu\text{L}$	volume of a box
$V_{\text{bulk}}$	mL	total bulk fluid volume
$V_{\text{bulk,in}}$	mL	bulk fluid volume inside of particle pores
$V_{\text{bulk,out}}$	mL	bulk fluid volume outside of particle pores
$V_{\text{cap}}$	$\mu\text{L}$	volume of a spherical cap
$V_{\text{corner}}$	$\mu\text{L}$	volume of a “perpendicular corner” cut from a sphere
$V_{\text{inside}}$	$\mu\text{L}$	partial sphere volume lying inside of a box
$V_{\text{sample}}$	mL	total sample volume
$V_{\text{sec}}$	mL	total secondary fluid volume
$V_{\text{sec,in}}$	mL	secondary fluid volume inside of particle pores
$V_{\text{sec,out}}$	mL	secondary fluid volume outside of particle pores
$V_{\text{solid}}$	mL	total particle volume
$V_{\text{sphere}}$	$\mu\text{L}$	volume of a single spherical particle, or of any other sphere
$V_{\text{pore}}$	mL	pore volume

$V_{\text{wedge}}$	$\mu\text{L}$	volume of a perpendicular spherical wedge
$v_{\text{sed}}$	$\text{mm s}^{-1}$	sedimentation velocity
$v_{\text{plate}}$	$\text{mm s}^{-1}$	plate velocity
$v_x, v_y, v_z$	$\text{mm s}^{-1}$	flow velocities in spatial $x$ , $y$ and $z$ directions
$W$	-	ratio of added liquid volume to the total volume (including interstitial air) of wet granular matter
$W^*$	-	volume ratio $W$ at the pendular-funicular transition in wet granular matter
$W_{\text{cb}}$	-	volume ratio $W$ at onset of pendular bridge formation in wet granular matter
$We_{\text{crit}}$	-	critical Weber number
$x, y, z$	-	spatial directions; or Cartesian coordinates
$x_a$	$\mu\text{m}$	length of the spherical cap formed by a bridge on a particle
$x_{\text{box}}, y_{\text{box}}, z_{\text{box}}$	$\mu\text{m}$	dimensions of a box
$x_{\text{size}}, y_{\text{size}}, z_{\text{size}}$	$\mu\text{m}$	dimensions of a confocal image
$x_v, y_v, z_v$	$\mu\text{m}$	dimensions of a voxel
$z$	-	(mean) coordination number
$z_{\text{el}}$	-	electrolyte valence
$z_{\text{factor}}$	-	ratio of a voxel's dimension in $z$ to $x$ direction
$\Delta z_{\text{focus}}$	$\mu\text{m}$	vertical shift of focal point
$\Delta z_{\text{obj}}$	$\mu\text{m}$	vertical shift of the objective

### Greek Symbols

Symbol	Unit	Description
$\alpha$	$^\circ$	cone angle
$\alpha_{\text{immersion}}$	$^\circ$	angle of refraction in the immersion liquid
$\alpha_{\text{sample}}$	$^\circ$	angle of refraction in the sample
$\beta$	$^\circ$	half-filling angle of a pendular bridge
$\beta_{\text{Wu}}$	-	parameter in the Wu/Morbidelli model denoting the relative inter-floc strength
$\Gamma$	$\text{mN m}^{-1}$	interfacial tension, surface tension, or interfacial energy
$\Gamma_{\text{AB}}$	$\text{mN m}^{-1}$	interfacial tension between liquids A and B
$\Gamma_{\text{SA}}$	$\text{mN m}^{-1}$	interfacial energy between solid S and liquid A
$\Gamma_{\text{SB}}$	$\text{mN m}^{-1}$	interfacial energy between solid S and liquid B
$\gamma$	-	(shear) strain
$\hat{\gamma}$	-	strain amplitude
$\hat{\gamma}_{\text{crit}}$	-	strain amplitude at the end of the LVE region
$\hat{\gamma}_{\text{crossover}}$	-	strain amplitude at intersection of $G'$ and $G''$
$\dot{\gamma}$	$\text{s}^{-1}$	shear rate
$\dot{\gamma}_{\text{crit}}$	$\text{s}^{-1}$	critical shear rate for droplet breakup
$\Delta$	-	difference
$\delta$	rad	phase shift angle

$\epsilon$	-	porosity
$\epsilon_0$	$\text{A s V}^{-1} \text{m}^{-1}$	vacuum permittivity
$\epsilon_b$	-	dielectric constant (= relative permittivity) of the bulk liquid
$\epsilon_p$	-	dielectric constant (= relative permittivity) of the particle
$\eta$	$\text{mPa s}$	(shear) viscosity
$\eta_b$	$\text{mPa s}$	viscosity of the bulk liquid
$\eta_d$	$\text{mPa s}$	viscosity of the droplet; or viscosity of the secondary liquid
$\theta$	$^\circ$	three-phase contact angle
$\theta_{\text{adv}}$	$^\circ$	advancing contact angle
$\theta_{\text{CB}}$	$^\circ$	Cassie-Baxter contact angle
$\theta_{\text{eq}}$	$^\circ$	equilibrium contact angle
$\theta_{\text{mean}}$	$^\circ$	mean contact angle of several experimental values
$\theta_{\text{rec}}$	$^\circ$	receding contact angle
$\theta_{\text{Wenzel}}$	$^\circ$	Wenzel contact angle
$\theta_{\text{Young}}$	$^\circ$	Young contact angle
$\kappa$	$\mu\text{m}^{-1}$	inverse Debye length
$\lambda$	-	viscosity ratio, $\eta_d/\eta_b$
$\lambda$	$\text{nm}$	wavelength of light
$\mu$	-	friction coefficient
$\mu$	$\text{J}$	chemical potential
$\nu_e$	$\text{s}^{-1}$	main ultraviolet absorption frequency
$\xi$	$\mu\text{m}$	correlation length
$\rho$	$\text{g mL}^{-1}$	mass density
$\rho_b$	$\text{g mL}^{-1}$	density of the bulk liquid
$\rho_{\text{solid}}$	$\text{g mL}^{-1}$	density of the particles
$\Delta\rho$	$\text{g mL}^{-1}$	density difference
$\sigma$		stress tensor
$\sigma$	$\text{Pa}$	(shear) stress
$\hat{\sigma}$	$\text{Pa}$	stress amplitude
$\hat{\sigma}_{\text{crit}}$	$\text{Pa}$	stress amplitude at the end of the LVE region
$\hat{\sigma}_{\text{crossover}}$	$\text{Pa}$	stress amplitude at intersection of $G'$ and $G''$
$\sigma_{\text{bridge}}$	$\text{Pa}$	stress in a capillary bridge
$\sigma_{\text{cb}}$	$\text{Pa}$	capillary force contribution to the yield stress
$\sigma_{\text{crit}}$	$\text{Pa}$	critical stress for droplet breakup
$\sigma_{\text{detach}}$	$\text{Pa}$	stress needed to detach a particle from an interface
$\sigma_{\mu}$	$\text{Pa}$	interparticle friction contribution to the yield stress
$\sigma_y$	$\text{Pa}$	yield stress
$\phi_{\text{Hex}}$	-	volume fraction of Hexamoll DINCH
$\phi_{\text{max}}$	-	maximum packing fraction
$\phi_{\text{sec}}$	-	secondary fluid volume fraction
$\phi_{\text{sec,eff}}$	-	effective secondary fluid volume fraction
$\phi_{\text{sec,set}}$	-	set secondary fluid volume fraction
$\phi_{\text{solid}}$	-	solid volume fraction
$\phi_{\text{solid,eff}}$	-	effective solid volume fraction
$\phi_{\text{solid,set}}$	-	set solid volume fraction
$\Psi$	-	Wadell sphericity

$\Psi$	J	potential
$\Psi_{\text{DLVO}}$	J	DLVO potential
$\Psi_{\text{el}}$	J	electrostatic potential
$\Psi_{\text{min}}$	J	potential minimum
$\Psi_{\text{surf}}$	J	particle surface potential
$\Psi_{\text{vdW}}$	J	van der Waals potential
$\Omega$	$\text{rad s}^{-1}$	angular velocity
$\Omega_{\text{coa}}$	$\text{s}^{-1}$	coalescence rate
$\omega$	$\text{rad s}^{-1}$	angular frequency

### Abbreviations

Abbreviation	Meaning
2D, 3D	two-, three-dimensional
AFM	atomic force microscopy
$(\alpha\text{-})\text{Al}_2\text{O}_3$	aluminum oxide
Alg.	Algorithm
APS	(3-Aminopropyl)-triethoxysilane
BET	Brunauer-Emmett-Teller adsorption method
$\text{CaCO}_3$	calcium carbonate
DINCH	1,2-cyclohexane dicarboxylic acid diisononyl ester
DLCA	diffusion limited cluster aggregation
DLVO theory	a theory postulated by Derjaguin, Landau, Verwey and Overbeek
KPG stirrer	“Kerngezogenes Präzisions-Glasgerät”, a type of laboratory stirrer
LVE	linear viscoelastic
NaI	sodium iodide
PMT	photomultiplier tube
PSF	point spread function
RLCA	reaction limited cluster aggregation
SEM	surface electron microscopy
TEOS	Tetraethoxysilane
TMCS	Trimethylchlorosilane
vol %	volume percent
wt %	weight percent

# 10 Academic CV (shortened version)

## Personal data

Name: Frank Bossler  
Date of birth: March 06, 1987  
Place of birth: Biberach an der Riß, Germany

## Peer-Reviewed Journal Publications

1. F. Bossler, J. Maurath, K. Dyhr, N. Willenbacher, E. Koos: *Fractal Approaches to Characterize the Structure of Capillary Suspensions using Rheology and Confocal Microscopy*; Journal of Rheology, 62 (1), 183–196 (2018). Featured article.
2. F. Bossler, L. Weyrauch, R. Schmidt, E. Koos: *Influence of Mixing Conditions on the Rheological Properties and Structure of Capillary Suspensions*; Colloids and Surfaces A: Physicochemical and Engineering Aspects, 518, 85–97 (2017).
3. F. Bossler, E. Koos: *Structure of Particle Networks in Capillary Suspensions with Wetting and Nonwetting Fluids*; Langmuir, 32 (6), 1489–1501 (2016).
4. C. Oelschlaeger, F. Bossler, N. Willenbacher: *Synthesis, Structural and Micromechanical Properties of 3D Hyaluronic Acid-Based Cryogel Scaffolds*; Biomacromolecules, 17 (2), 580–589 (2016).

## Conference Contributions

1. F. Bossler, I. Natalia, M. Weiß, S. Fischer, E. Koos: *Structure of Capillary Suspensions and their Applications* (talk). 2017 MRS Fall Meeting & Exhibition, Boston (USA), November 26 – December 01, 2017.
2. F. Bossler, S. Bindgen, E. Koos: *Structural Transitions with Variation of the Secondary Fluid Volume Fraction in Liquid-Liquid-Solid Systems* (Keynote presentation). 31st Conference of The European Colloid and Interface Society, Madrid (Spain), September 03–08, 2017.
3. F. Bossler, J. Maurath, N. Willenbacher, E. Koos: *Untersuchung der Mikrostruktur von Kapillarsuspensionen zur Entwicklung innovativer Pasten* (talk). Gemeinsame Diskussionstagung der Deutschen Rheologischen Gesellschaft und der ProcessNet-Fachgruppe "Rheologie", Berlin (Germany), March 13–14, 2017.
4. F. Bossler, J. Maurath, K. Dyhr, N. Willenbacher, E. Koos: *Fractal Dimensions of Capillary Force Induced Particle Networks Determined from Rheology and Confocal Microscopy* (poster). 30th Conference of The European Colloid and Interface Society Rome (Italy), September 04–09, 2016.

5. F. Bossler, J. Maurath, K. Dyhr, N. Willenbacher, E. Koos: *Fractal Dimensions of Capillary Force Induced Particle Networks Determined from Rheology and Confocal Microscopy* (talk). 17th International Congress on Rheology, Kyoto (Japan), August 08–13, 2016.
6. I. Natalia, F. Bossler, E. Koos: *Strength and Deformation of Capillary Suspension Networks* (poster). 17th International Congress on Rheology, Kyoto (Japan), August 08–13, 2016.
7. F. Bossler, J. Maurath, K. Dyhr, N. Willenbacher, E. Koos: *Scaling Behavior of the Yield Stress in Capillary Suspensions* (poster). 89th ACS Colloid & Surface Science Symposium, Pittsburgh (USA), June 15–17, 2015.
8. C. Oelschlaeger, L. Lintis, E. Hnátková, F. Bossler, N. Willenbacher: *Structural, Macro- and Microrheological Properties of Hyaluronic Acid (HA) Cryogels* (poster). 10th Annual Hyaluronan Conference, Florence (Italy), June 07–11, 2015.
9. F. Bossler, I. Natalia, E. Koos: *Networks Induced by the Capillary Force* (talk). 15th Conference of the International Association of Colloid and Interface Scientists, Mainz (Germany), May 24–29, 2015.
10. F. Bossler, J. Maurath, K. Dyhr, N. Willenbacher, E. Koos: *Scaling Behavior of the Yield Stress in Capillary Suspensions* (poster). 15th Conference of the International Association of Colloid and Interface Scientists, Mainz (Germany), May 24–29, 2015.
11. F. Bossler, L. Weyrauch, R. Schmidt, E. Koos: *Influence of Droplet Breakup and Particle Agglomeration on the Rheology of Capillary Suspensions* (talk). 10th Annual European Rheology Conference, Nantes (France), April 14–17, 2015.
12. C. Oelschlaeger, L. Lintis, E. Hnátková, F. Bossler, N. Willenbacher: *Structural, Mechanical and Microrheological Properties of Hyaluronic Acid Cryogels* (talk). 10th Annual European Rheology Conference, Nantes (France), April 14–17, 2015.
13. F. Bossler, E. Koos: *Structure of Networks Induced by the Capillary Force* (Keynote presentation). 28th Conference of The European Colloid and Interface Society, Limassol (Cyprus), September 07–12, 2014.